Trace Element Mobility in Aqueous Fluids and the Cause of Melting in Subduction Zones

Dissertation

Zur Erlangung der Würde eines

Doktors der Naturwissenschaften

- Dr. rer. nat. -

der Bayreuther Graduiertenschule für Mathematik und

Naturwissenschaften

vorgelegt von

Greta Rustioni

aus Voghera (Italien)

Bayreuth 2020

Die vorliegende Arbeit wurde in der Zeit von Oktober 2016 bis September 2020 in Bayreuth am Bayerischen Geoinstitut unter Betreuung von Herrn Professor Dr. Hans Keppler angefertigt.

Vollständiger Abdruck der von der Bayreuther Graduiertenschule für Mathematik und Naturwissenschaften (BayNAT) der Universität Bayreuth genehmigten Dissertation zur Erlangung des akademischen Grades einer Doktorin der Naturwissenschaften (Dr. rer. nat.).

Dissertation eingereicht am: 30.04.2020

Zulassung durch das Leitungsgremium: 30.04.2020

Wissenschaftliches Kolloquium:10.09.2020

Amtierender Direktor: Prof. Dr. Markus Lippitz

Prüfungsausschuss:

Prof. Dr. Hans Keppler (Gutachter)
Prof. Dr. Daniel Frost (Gutachter)
PD. Dr. Catherine McCammon (Vorsitz)
Prof. Dr. David Rubie

(Weiterer Gutachter: Prof. Dr. Michihiko Nakamura)

Table of Contents

Summary

The formation of magmas in subduction zones is the main mechanism for the growth of the continental crust today. Nevertheless, there is still no consensus concerning the mechanism that causes melting in the mantle wedge above the subducted plate. Most recent studies suggest that water-bearing sediment melts infiltrate the mantle wedge and reduce the solidus of the mantle peridotite. However, this idea is difficult to reconcile with the striking similarity of primitive arc basalt compositions in all subduction zones worldwide, irrespective of the presence, amount, and nature of sediment subducted. In this dissertation, I therefore investigated the hypothesis that aqueous fluids released from the basaltic portion of the subducted slab are the main trigger for melting in volcanic arcs. In order to test this hypothesis, I studied the composition of subduction zone fluids in high-pressure experiments and compared them with the trace element enrichment pattern seen in natural subduction zone magmas. In contrast to previous studies, I also investigated in detail the effect of fluid salinity (NaCl content) on the trace element enrichment pattern, as this may be strongly altered by selective complexing with chloride.

For measuring fluid compositions at high pressures and temperatures, the "diamond trap" method was used, where a layer of diamond powder inside an Au or Pt capsule containing the charge is used to trap the fluid inside its pore space. The composition of the fluid is then determined by laser-ablation inductively coupled plasma mass spectroscopy (LA-ICP-MS) after quenching the run and freezing the charge. Since this method was essential for this study, a number of tests were carried out in simple and well-studied model systems to check the reliability of the results. In general, the method yields data within a factor of two of the expected value. However, systems that are highly susceptible to dissolution and re-precipitation in temperature gradients may lead to erroneous results. Freezing the sample before analysis is essential for obtaining high-quality data.

Experiments to determine the fluid/eclogite partition coefficients of a large suite of trace elements were carried out at 700 – 800 ˚C and 4 – 5 GPa in a piston cylinder apparatus. Additional experiments at 6 GPa were done in a multi anvil press. Starting materials were

synthetic glasses of MORB compositions and aqueous solutions with variable NaCl contents. By using periodic oscillations of temperature during the experiments, it was possible to enhance the grain growth of minerals due to Ostwald ripening, such that from all solid phases crystals large enough for laser-ablation ICP-MS analysis could be obtained.

Under run conditions, the starting glasses converted to a well-crystallized eclogitic assemblage of omphacite and garnet, with minor rutile and kyanite. The coexisting aqueous fluid contained typically 30 - 40 wt. % of solutes, mostly silica. With increasing salinity (up to about 7 wt. % Cl), the fluid/eclogite partition coefficients of the large-ion lithophile elements (e.g. Cs, Rb, Ba, Sr), of the light rare earth elements (e.g. La, Ce), of U, Th, and Pb increased up to three orders of magnitude. On the other hand, the partitioning of the typical high-field strength trace elements (e.g. Ti, Nb, Ta) was unaffected by salinity. Attainment of equilibrium was demonstrated by truly reversed experiments; runs starting with the trace elements doped either in the solution or in the solid glass yielded consistent results. Increasing pressure and temperature generally enhances the partitioning into the fluid, but does not fundamentally change the enrichment pattern.

The experimental data were used to quantitatively model the composition of partial melts of the mantle wedge after metasomatic enrichment by an aqueous fluid released from the basaltic part of the subducted slab after amphibole dehydration. The models show that trace element enrichment pattern of primitive arc basalts can be fully reproduced by adding just 2.5 wt. % of a saline fluid with 7 – 10 wt. % Cl to the source. Lower salinities would require higher fractions of fluid additions, while a purely aqueous fluid (without any Cl) is unable to produce the observed trace element enrichment pattern. In contrast to this finding, sediment melts generated under plausible slab-surface conditions have difficulties to yield the trace element pattern in primitive arc basalts.

The present study therefore demonstrates that primitive arc basalts are produced by the partial melting of a mantle peridotite enriched by saline fluids released from the basaltic part of the subducted slab. The contribution of sediment melts to the petrogenesis of these magmas is likely negligible and the importance of sediment melts for magma formation in subduction zones has likely been grossly overestimated.

Zusammenfassung

Die Bildung von Magmen in Subduktionszonen ist der Hauptmechanismus für das Wachstum der kontinentalen Kruste in der jüngeren geologischen Vergangenheit. Es besteht jedoch nach wie vor kein Konsens über den Mechanismus der Schmelzbildung im Mantelkeil über der subduzierten Platte. Neuere Arbeiten nehmen meistens an, dass wasserhaltige Sedimentschmelzen in den Mantelkeil aufsteigen und den Schmelzpunkt des Peridotits herabsetzen. Diese Vorstellung ist jedoch schwer vereinbar mit der weltweiten, auffallenden Ähnlichkeit in der Zusammensetzung von primitiven Magmen aus Inselbögen, unabhängig von der Gegenwart, der Menge und der Zusammensetzung von subduziertem Sediment. Diese Dissertation untersucht daher die Hypothese, dass Wasser-reiche Fluide aus dem basaltischen Teil der subduzierten Platte die Schmelzbildung in Subduktionszonen auslösen. Um diese Hypothese zu testen, wurde die Zusammensetzung von Fluiden in Subduktionszonen mit Hilfe von Hochdruckexperimenten im Labor untersucht und die Daten mit dem Spurenelement-Muster in natürlichen Magmen aus Subduktionszonen verglichen. Im Gegensatz zu früheren Untersuchungen wurde auch der Effekt der Salinität des Fluids (d.h. des NaCl-Gehalts) auf das Spurenelement-Anreicherungsmuster untersucht, da dieses Muster möglicherweise sehr stark durch Komplexbildung mit Chlorid verändert werden könnte.

Zur Bestimmung von Fluid-Zusammensetzungen bei hohem Druck und hoher Temperatur wurde die „Diamond-Trap"-Methode verwendet. Hierbei dient eine Lage von Diamantpulver in der Probenkapsel dazu, Teile des Fluids im Porenraum zwischen den Diamantkörnern einzufangen. Die Zusammensetzung des Fluids wird dann nach Abschrecken des Experiments zu Raumtemperatur und Einfrieren der Probe mit Hilfe von Laser-Ablations-ICP-MS (inductively coupled plasma mass spectroscopy) bestimmt. Da diese Methode für diese Dissertation essentiell war, wurden eine Reihe von Tests in einfachen und gut untersuchten Modellsystemen ausgeführt, um die Zuverlässigkeit der Messwerte zu überprüfen. Im Allgemeinen reproduziert die Methode die erwarteten Messwerte innerhalb eines Faktors von zwei. Bei Systemen, die sehr empfindlich sind in Bezug auf Auflösung und Wiederausfällung in einem Temperaturgradienten können jedoch systematische Fehler auftreten. Das Einfrieren der Proben vor der Analyse ist in jedem Fall essentiell, um zuverlässige Daten zu erhalten.

Experimente zur Messung der Fluid/Eklogit-Verteilungskoeffizienten zahlreicher Spurenelemente wurden bei 700 – 800 ˚C und 4 – 5 GPa in einer Piston-Cylinder-Apparatur ausgeführt. Für weitere Experimente bei 6 GPa diente eine Multi-Anvil-Apparatur. Ausgangsmaterialien waren synthetische Gläser mit MORB-Zusammensetzung sowie wässrige Lösungen mit unterschiedlichen NaCl-Gehalten. Während der Experimente konnte das Kornwachstum aufgrund von Ostwald-Reifung durch periodische Schwankungen in der Temperatur verstärkt werden. Von allen festen Phasen konnten dadurch Kristalle erhalten wurden, die groß genug waren für die Messung mit Laser-Ablations- ICP-MS.

Während der Experimente bildete sich aus den Gläsern eine gut kristallisierte Eklogit - Paragenese mit Omphacit, Granat und geringen Mengen von Rutil und Disthen. Die koexistierende wässrige Fluidphase enthielt typischerweise 30 – 40 Gew. % gelöste Stoffe, überwiegend SiO_2. Mit steigender Salinität (bis etwa 7 Gew. % Cl) erhöhten sich die Fluid/Eklogit-Verteilungskoeffizienten der LILE (large-ion lithophile elements, wie Cs, Rb, Ba, Sr), der leichten seltenen Erden (wie La, Ce) sowie von U, Th und Pb um bis zu drei Zehnerpotenzen. Andererseits wurde das Verteilungsverhalten der typischen HFSE (high field strength elements, wie Ti, Nb, Ta) durch die Salinität nicht beeinflusst. Gleichgewicht wurde durch reversible Experimente nachgewiesen. Versuche, in denen die Spurenelemente ursprünglich nur im Glas oder nur in der Flüssigkeit vorhanden waren, lieferten konsistente Resultate. Steigende Temperatur und steigender Druck verstärken die Verteilung von Spurenelementen in das Fluid. Das grundsätzliche Verteilungsmuster ändert sich jedoch nicht.

Mit Hilfe der experimentellen Daten wurde die Zusammensetzung von Teilschmelzen des Mantels nach metasomatischer Anreicherung durch wässrige Fluide aus dem basaltischen Teil der subduzierten Platte quantitativ modelliert. Die Modelle zeigen, dass das Spurenelement-Anreicherungsmuster von primitiven Inselbogen-Basalten vollständig erklärt werden kann durch die Anreicherung der Schmelzzone mit 2.5 Gew. % eines Fluids mit 7 – 10 Gew. % Cl aus dem basaltischen Teil der subduzierten Platte. Niedrigere Salinitäten würden eine stärkere Fluid-Zufuhr erfordern. Fluide ohne Chlorid können das beobachtete Anreicherungsmuster nicht erzeugen. Im Gegensatz zu Chlorid-haltigen wässrigen Fluiden können Sedimentschmelzen, die unter plausiblen Bedingungen nahe der Oberfläche der subduzierten Platte gebildet wurden, das beobachtete Anreicherungsmuster in primitiven Inselbogen-Basalten nicht voll reproduzieren.

Die vorliegende Arbeit zeigt daher, dass primitive Inselbogen-Basalte durch das partielle Schmelzen eines Mantel-Peridotits entstehen, der metasomatisch angereichert wurde durch salzhaltige Fluide aus dem basaltischen Teil der subduzierten Platte. Sedimentschmelzen sind an der Bildung dieser Magmen wahrscheinlich nicht beteiligt. Generell ist die Bedeutung von Sedimentschmelzen für die Bildung von Magmen in Subduktionszonen wahrscheinlich weit überschätzt worden.

1. Introduction

1.1.   Subduction zones

In subduction zones, relatively dense oceanic crust is recycled into the mantle (Figure 1.1). The slab pull of the dense crust is one of the driving forces of global plate movements (e.g. Höink et al. 2011). Because of its lower density, continental crust is subducted only under exceptional circumstances (e.g. Zheng and Chen 2016). Since the subducted oceanic crust was in contact with seawater, it contains hydrous minerals that become unstable at greater depth (Schmidt and Poli 1998). The water released from these minerals must play an important role in magma formation in subduction zones, as they are colder than the surrounding mantle (Syracuse et al. 2010) and therefore, some solidus depression due to water is required for melting (e.g. Kawamoto and Holloway 1997). Indeed, the water contents observed in basalts and andesites from volcanic arcs are much higher than those typically seen in mid-ocean ridge basalts (MORB) or in ocean island basalts (OIB; Métrich and Wallace 2008).
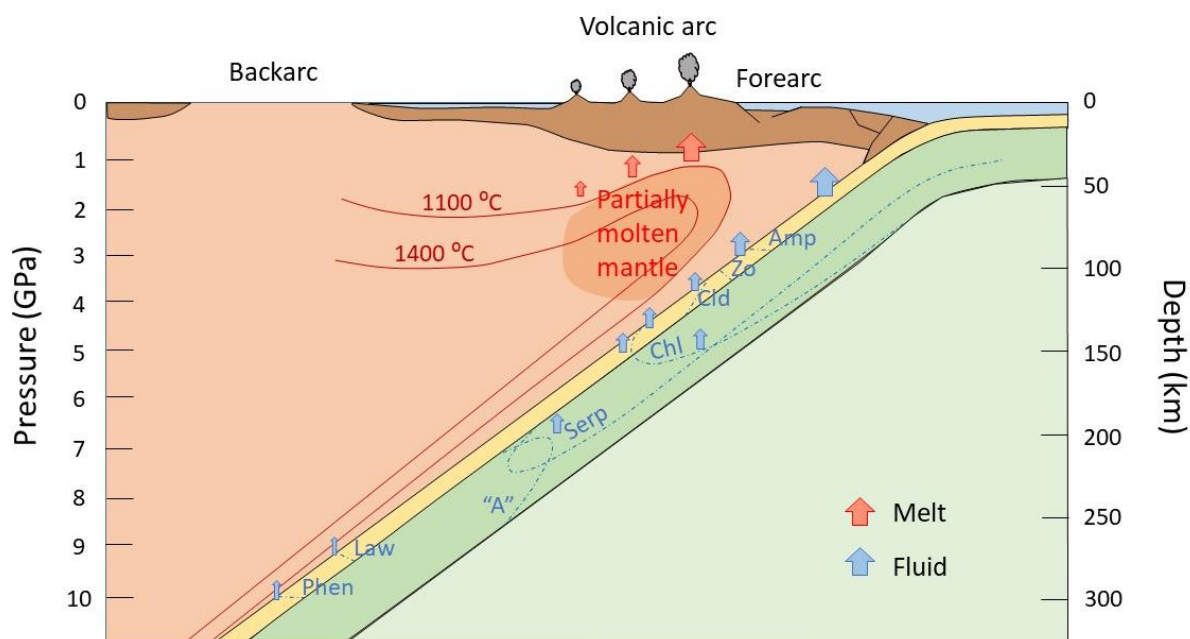
Figure 1.1. *Schematic diagram of a subduction zone, showing the stability range of various hydrous phases. Modified after Schmidt and Poli (1998)*

9

While the modern concept of subduction zones is intimately connected to the theory of plate tectonics, some of the related geological observations were already familiar to geologists more than a century ago. Already Alfred Wegener (1920) noted the concentration of earthquake epicenters at the continental margins around the Pacific. However, he interpreted this as evidence for continents sliding over the ocean floor, rather than the ocean floor being subducted under the continents. The location of many volcanoes close to the sea also intrigued many geologists and made them believe that there may be some causal relationship. Svante Arrhenius (1900) assumed that the seafloor acts as some kind of semipermeable membrane, which allows seawater to enter the zone of melting below active arc volcanoes such as Stromboli. He referred to the water-rich nature of volcanic gases as additional line of evidence for this theory.

Direct evidence for subducting slabs was first provided by the observations of Wadati-Benioff zones, i.e. of earthquake foci that are located on a dipping plane tracing the subducting slab (Benioff 1949). These earthquakes appear to arise in the cold, brittle interior of the slab (Brodholt and Stein 1988). With modern tomographic methods, subducting slabs can be imaged down to the lower mantle (e.g. van der Hilst et al. 1997). Strong geochemical evidence for the deep subduction of sediments is provided by the detection of ^{10}Be in arc lavas (Brown et al. 1982). ^{10}Be is radioactive and has a half-life of 1.39 million years. It is continuously produced on Earth´s surface by nuclear spallation reactions induced by cosmic rays.

It is still uncertain at what time plate tectonics and therefore subduction started in Earth´s history. The TTG (tonalite-trondjemite-granodiorite) suite that was an important component of the Archean crust may have been produced by direct melting of a subducted basaltic slab (e.g. Rapp et al. 2003), but other interpretations are also possible (e.g. Johnson et al. 2017). Holder et al. (2019) recently suggested that the paired metamorphic belts, which are typical for subduction zones, gradually emerged in the Neoarchean. However, subduction in the Archean may have been short-lived and episodic due to frequent slab breakoff (Moyen and van Hunen 2012).

1.2. Magma generation in subduction zones

Magma generation in subduction zones is the main mechanism for the growth of the continental crust since the onset of plate tectonics (e.g. Hawkesworth et al. 2019). However, the process of subduction itself does not only create crust, but it may also destroy some existing crust by "subduction erosion", essentially by scraping off some crustal material from the overriding plate and transporting it back into the mantle. The relative magnitude of crustal growth by the formation of new magmas and of subduction erosion is not always easy to assess (e.g. Huene and Scholl 1991). Magmas produced in subduction zones typically range from basaltic to andesitic compositions (e.g. Kelemen et al. 2005). However, at continental margins very large granitic plutons may be produced as well. These magmas, as well as at least some of the andesites, likely represent mixtures of mantle-derived melts with extensive crustal contamination (e.g. Hildreth and Moorbath 1988). For understanding magma generation in subduction zones, primitive arc basalts are of particular interest. They have high Mg-numbers, as well as high Ni and Cr contents suggesting that they are primary melts from the mantle, unaffected by fractional crystallization of crustal contamination. The major element composition of primitive arc basalts is not very different from mid-ocean ridge basalts (MORB) or ocean island basalts (OIB), but the trace element enrichment pattern is strikingly different. Figure 1.2 shows a compilation of trace element abundance data for primitive arc basalts after Kelemen et al. (2005), normalized to the "all MORB average" of Gale et al. (2013). Large-ion lithophile elements (LILE), such as Rb, Ba, or Sr are strongly enriched, as are the light rare earth elements (LREE), such as La and Ce. On the other hand, high field strength trace elements (HFSE, e.g. Nb, Ta, and Ti), are strongly depleted in the melt, the "negative Nb Ta anomaly" being a characteristic feature of these magmas.

Compared to MORB or OIB basalts, the water and Cl contents of primitive arc basalts are much higher. Figure 1.3 compiles some data from undegassed melt inclusions (Métrich and Wallace 2008). Water contents up to 6 wt. % and Cl contents up to 2000 ppm are common. In most cases, the Cl/H_2O ratio could be explained by adding an aqueous fluid containing between 1 and 15 wt. % NaCl to the melt. Subduction zone magmas are also relatively oxidized and the oxidation state appears to correlate with water (Kelley and Cottrell 2009). The high water
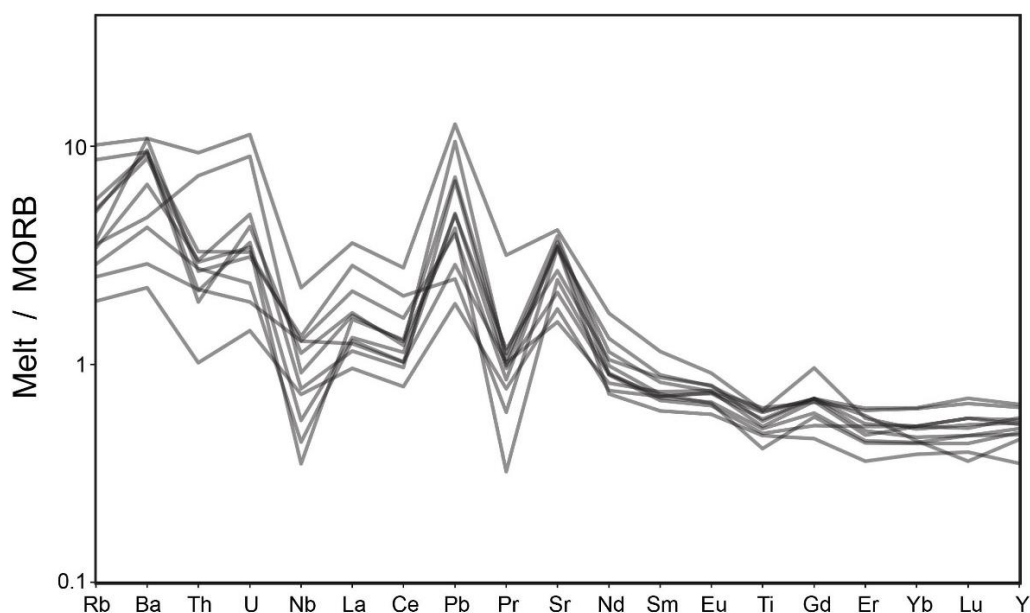
Figure 1.2. *Trace element abundances in primitive arc basalts. This compilation includes data from the Kermadec, Lesser Antilles, Marianas, New Hebrides, Scotia, Tonga, Aleutian, Andean, Cascades, Central America, and Kamchatka arcs. Data are from Kelemen et al. (2005), normalized to the "all MORB average" of Gale et al. (2013).*
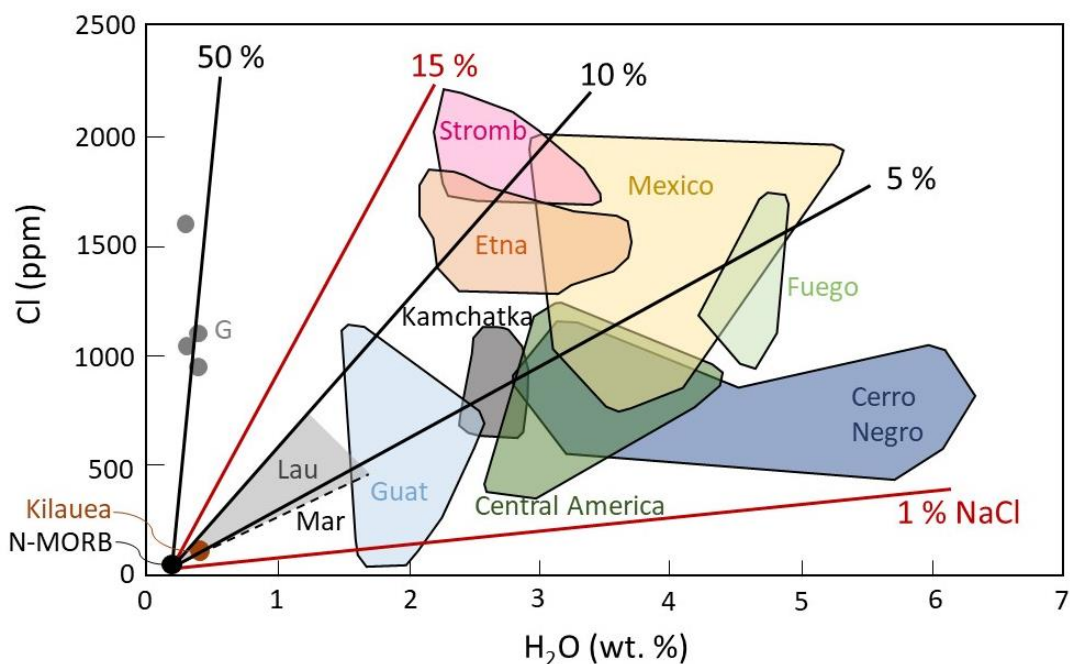
Figure 1.3. *H_2O and Cl contents in olivine-hosted melt inclusions from arc basalts. Modified after Métrich and Wallace (2008). G = Galungung, Indonesia, Guat = Guatamalan volcanoes behind volcanic front; Lau = Lau basin; Mar = Mariana trough basalts (dashed line); Stromb = Stromboli, Italy. Lines give the weight percentage of NaCl in aqueous fluids required to produces the observed Cl/H_2O ratios.*

content of the parental magmas is – together with the elevated viscosity of the andesitic or dacitic melts - the main reason why most of the explosive volcanic activity is concentrated at subduction zones. Prominent recent events include the 1980 eruption of Mt. St. Helens (e.g. Scandone and Malone 1985) and the 1991 eruption of Pinatubo. In particular for the Pinatubo eruption, the atmospheric effects have been carefully studied (McCormick et al.1995). They included a global cooling of surface temperatures by 0.5 ˚C due to the injection of 17 Megatons of SO_2 into the stratosphere, which was photochemically oxidized to sulfate aerosols. The aerosols effectively shielded sunlight for more than a year.

Early models of magma formation in subduction zones assumed direct melting of subducted basaltic crust (Green and Ringwood 1968). According to current estimates of slab temperatures (Syracuse et al. 2010), this mechanism is likely not realistic today, except perhaps if very young, hot oceanic crust is subducted. Direct slab melting within steeper geothermal gradients may, however, have produced the Archean TTG (tonalite-trondjemite-granodiorite) suite that is a main component of the earliest continental crust (Rapp et al. 2003). Modern adakites may be analogues of the TTG. Adakites are a group of andesitic to rhyolitic magmas that occur in some subduction zones (e.g. Martin 1999). They have geochemical characteristics, such as high Sr/Y and La/Yb ratios that are consistent with partial melting of a basaltic source with garnet in the residue.

Any model of magma formation in subduction zones obviously strongly depends on the inferred temperatures inside the slab. Since the slab was subducted from the surface, it is generally colder than the surrounding mantle. Slab temperatures cannot be directly measured and therefore, estimates of slab temperatures depend on geodynamic models. Figure 1.4 shows the range of inferred slab surface temperatures as calculated by Syracuse et al. (2010), using different assumptions. In general, the older the slab, the faster the subduction velocity and the steeper the angle of subduction, the colder is the slab interior at a given depth. These three variables are therefore sometimes combined in the slab thermal parameter $\phi = t\, v\, \sin\theta$, where t is the age of the slab, v is the subduction velocity and θ is the angle of subduction (see Maunder et al. 2019 for discussion). Inspection of Figure 1.4 shows that under most circumstances, at a pressure of 4 GPa, corresponding to a typical depth of the slab of 120 km below the volcanic front, temperatures are too low for melting.
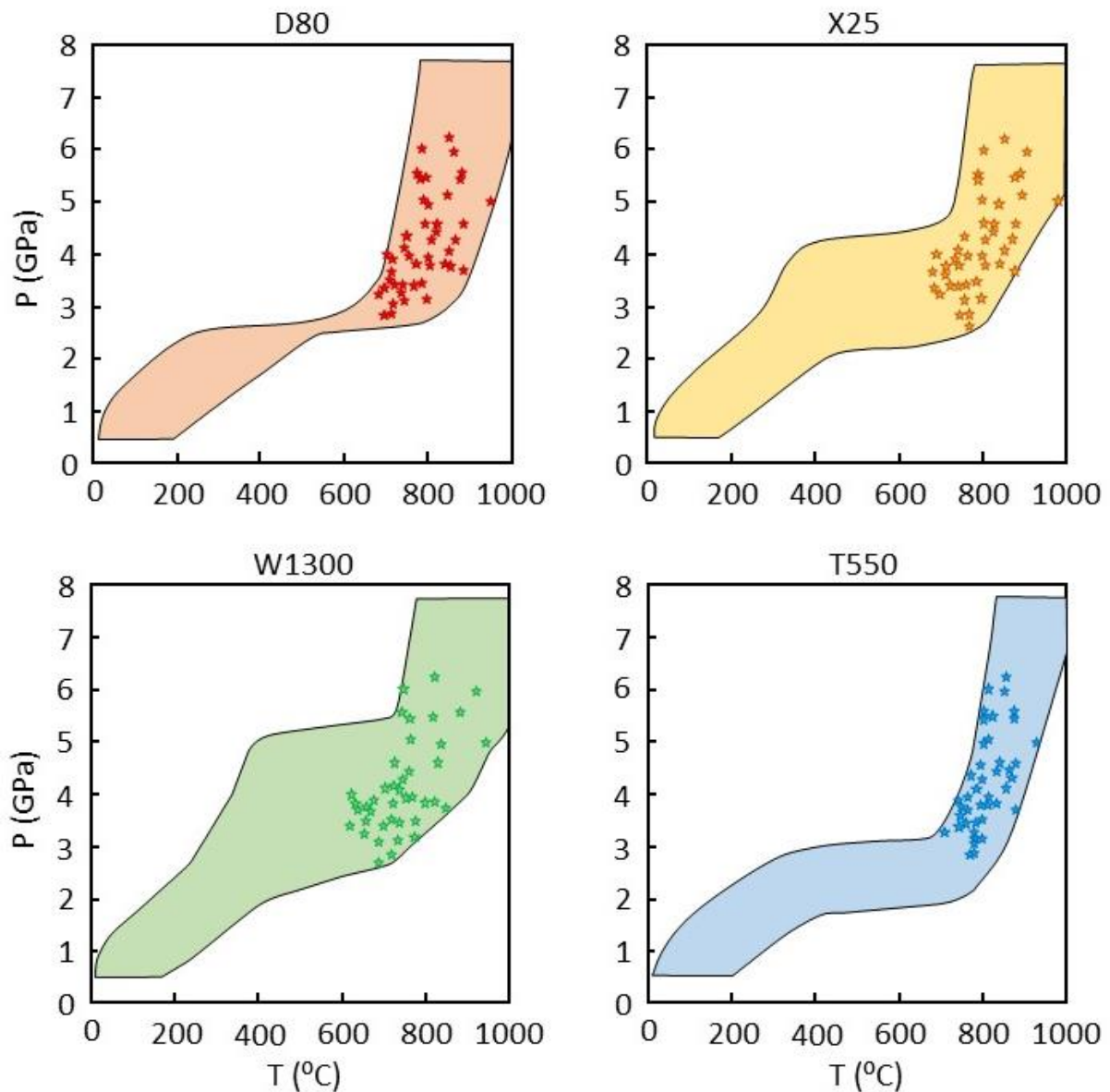
Figure 1.4. *Models of slab surface pressure-temperature paths in subduction zones using various assumptions. Modified after Syracuse et al. (2010). Global ranges of slab surface temperatures are given as colored areas, stars represent projections of the corresponding volcanic front on the slab surface. D80 assumes full mechanical coupling between plate and mantle wedge at a depth of 80 km; X25 assumes that this coupling occurs 25 km trenchward of the arc. W1300 is a model assuming that the maximum temperature directly below the arc is 1300 ˚C. T550 assumes that coupling between plate and mantle wedge occurs at a slab surface temperature of 550 ˚C.*

A widely accepted, alternative model to slab melting is that melting actually takes place in the mantle wedge above the slab. This is consistent with the geochemical characteristics of primitive arc basalts, such as their high Mg numbers, high Ni and Cr content (e.g. Kelemen et

14

al. 2005) that qualify them as partial melts of a mantle peridotite. A plausible mechanism for inducing melting in the mantle wedge is the addition of water released from the subducted slab, which causes a drastic melting point depression (Kawamoto and Holloway 1997). Many models therefore assume that aqueous fluids released by the breakdown of hydrous minerals in the subducted slab infiltrate into the mantle wedge and trigger melting (e.g. Gill 1981, Arculus and Powell 1986, Tatsumi 1989, Peacock 1990). This mechanism would be generally consistent with the typical trace element enrichment pattern seen in arc magmas, as LILE elements, such as heavy alkalis and alkaline earths are likely soluble in water, while HFSE, such as Nb, Ta or Ti, are not. However, a number of experimental studies that looked at the partitioning of trace elements between aqueous fluids and the minerals of the subducted slab appeared to indicate that aqueous fluids are rather inefficient in transporting most of the relevant trace elements (Brenan et al. 1994, 1995, Stalder et al. 1998, Johnson and Plank 1999, Kessel et al. 2005). This has led to the widespread notion that aqueous fluids are "too dilute" to produce the trace element enrichment observed in arc magmas and therefore, melting in subduction zones must be caused by some other mechanism (e.g. Hermann et al. 2006, Spandler and Pirard 2013).

Because of the perceived difficulty with the hypothesis of aqueous fluids triggering melting in subduction zones, in recent years another model has become popular, which assumes that sediment melts transport water from the subducted slab to the mantle wedge and cause the formation of arc magmas (e.g. Kelemen et al. 2005, Hermann et al. 2006, Hermann and Rubatto 2009, Skora and Blundy 2010, Behn et al. 2011, Spandler and Pirard 2013, Skora et al. 2015). The "sediment melt hypothesis", however, also has a number of problems:

Sediment melting is often postulated by comparing water-saturated melting curves with inferred geotherms (e.g. Syracuse et al. 2010). However, at the depths below the volcanic front, the sediment is likely not water-saturated anymore, since most of the water is already lost by a series of dehydration reactions occurring at shallow depths (e.g. Hacker 2008). Some water may still be contained in minerals such as phengite. However, the solidus for "dehydration melting" of phengite-bearing metapelites is 200 – 300 ˚C above the water-saturated solidus (Schmidt et al. 2004). These temperatures would likely only be reached under very unusual circumstances. Sediment melting would therefore require supply of water from below, e.g. by serpentine dehydration. It is uncertain to what extent the peridotite below the oceanic crust is

actually hydrated to serpentinite. Estimates vary widely and the degree of serpentinization likely depends very much on the formation of deep fractures during the bending of the slab when it enters the subduction zone. These fractures allow deep circulation of seawater (e.g. Faccenda et al. 2009; Canales et al. 2017). Moreover, if the upward migration of water was mostly channelized, only a small fraction of the sediment layer would be affected. Indeed, while fluids may originally be released by diffusive flow near the source, with larger distance from the source the flow is likely to become channelized (e.g. Zack and John 2007, John et al. 2012, Plümper et al. 2017).

Another problem with sediment melting is the striking similarity in the trace element pattern of primitive arc basalts worldwide, irrespective of the presence, absence, nature, or amount of sediment present. Figure 1.2 includes data from arcs with little or no sediment subduction (e.g. Kamchatka) as well as arcs with massive sediment subduction. Also, the nature of the sediment subducted changes, from mostly pelites in some arcs (e.g. Tonga) to mostly carbonates in other arcs (e.g. Central America). If sediment melting was responsible for the formation of the trace element enrichment of these magmas, one would expect major variation in the enrichment patterns. This effect is not observed.

"Supercritical fluids" intermediate in composition between silicate melts and aqueous fluids have sometimes also been discussed as possible agents for transporting water and trace elements from the subducted slab to the zone of melting. This is because at relatively high temperatures and pressures, silicate melts (particularly the silica-rich sediment melts) may become completely miscible with water, such that under some circumstances, the distinction between melt and aqueous fluid will disappear. This effect was first postulated by Niggli (1920), and directly demonstrated in experiments by Shen and Keppler (1997) and Bureau and Keppler (1999). These data suggest that for silica-rich systems (such as pelitic sediments), complete miscibility between silicate melt and fluid may indeed be reached in the deeper parts of the subducted slab. However, the study of Kessel et al. (2005) suggest that such "supercritical fluids" would have difficulties producing the strong fractionation between LILE and HFSE elements that is a hallmark of arc magmas.

1.3. Subduction zones and volatile fluxes

In subduction zones, water, carbon, and nitrogen are recycled back into the mantle. This process is therefore important for controlling the evolution of sea level (Rüpke et al. 2004, Karlsen et al. 2019), atmospheric composition (Mallik et al. 2018), and climate in deep geologic time (Plank and Manning 2019). For water, current models suggest that the subduction efficiency very much depends on the stability of serpentine in the slab. Since lower mantle temperatures are favorable for the preservation of serpentine, the subduction efficiency for water may have increased over geologic time, leading to a secular decrease of sea level by several hundred meters in the Phanerozoic eon (Rüpke et al. 2004). These models are, however, possibly oversimplified as they for example do not consider water transport by nominally anhydrous minerals.

The efficiency of carbon and nitrogen recycling depends very much on how water is transported from the subducted slab to the zone of melting. For nitrogen, aqueous fluids are much more efficient than silicate melts in returning nitrogen to the surface, therefore limiting the nitrogen flux back into the mantle (Mallik et al. 2018). While carbonates are thermally stable during a normal subduction path, the dilution of CO_2 in the coexisting fluid phase by water could cause the breakdown of carbonates and therefore return carbon to the surface before it can be deeply subducted. A major possible mechanism for carbon release at shallow depth is therefore fluxing by aqueous fluids from below (Plank and Manning 2019). These examples show that the question whether sediment melts or aqueous fluids trigger melting in the mantle wedge has very important implications for the efficiency of volatile recycling and for the global volatile cycles in general.

1.4. Aims of this thesis

The aim of this thesis is to provide new experimental constraints on the chemical transport by aqueous fluids in subduction zones by measuring the partitioning of a large suite of trace elements between fluid and eclogite. These data will be used to answer the question whether aqueous fluids or sediment melts are responsible for the generation of arc magmas.

In contrast to previous studies, the experiments reported here will investigate the fluid/eclogite partitioning for aqueous fluids containing chloride at concentration levels compatible with those inferred from the Cl/H_2O ratios of arc magmas (Métrich and Wallace 2008). At the pressures and temperatures of the subducted slab, the dielectric constant of water is reduced to about half the value at ambient conditions (e.g. Keppler 2017). Therefore, solutes cannot easily be dissolved as dissociated species and the effective transport of trace elements may require some complexing by chloride. From experiments at lower pressures, it is very well known that chloride complexing can greatly enhance the partitioning of many trace elements into aqueous fluids. In the discussion about aqueous fluid transport in subduction zones, this effect has largely been ignored.

2. Experimental and analytical methods

2.1. Measuring fluid/mineral partition coefficients

The direct determination of fluid/mineral partitioning presents several challenges. One of the main difficulties is to attain chemical equilibrium between the fluid and the mineral phases in the typical timescale of an experiment. In most cases, it is impossible to reach equilibrium by solid-state diffusion in reasonable experimental durations (e.g. Keppler 2017). A possibility to establish equilibrium is to crystallize the solid mineral phases from the fluid and in equilibrium with it. However, due to the low solubility of most silicate minerals in aqueous fluids, complete dissolution and reprecipitation of the crystals is unattainable in experiments. One possible way to overcome this problem is to employ a metastable phase, such as glass, as solid starting material in order to promote dissolution and precipitation of the mineral assemblage stable at the run conditions. However, even this approach is not free of shortcomings and some complications may emerge when a glass is chosen as starting material, as discussed in further detail in Section 2.2.

Another major issue in this kind of experiments is to accurately determine the composition of the fluid at high pressure and temperature while it is in equilibrium with the minerals. The difficulty arises from the compositional changes that the fluid experiences during quenching due to the precipitation of solid phases. In many cases, it is not straightforward to distinguish these precipitates, which should be regarded as fluid components as they were originally dissolved into the fluid, from those minerals that were actually stable at the conditions of the experiment. Several experimental techniques have been developed to overcome this problem. One possible approach is to try to determine fluid/mineral partitioning behavior avoiding direct measurements of the fluid phase. Brenan et al. (1995) for example, performed experiments with a large excess of fluid with respect to the amount crystalline starting material. Therefore, they only analyzed the recrystallized minerals, assuming for calculations that the fluid represent an infinite reservoir of trace elements and hence did not undergo any substantial compositional change during the experiment. Another method that allows to bypass fluid measurements is to

determine fluid/mineral partition coefficients through mineral solubilities. This can be achieved by accurately measuring the weight loss of crystals, usually inserted in an inner perforated capsule, loaded together with a large amount of fluid in an outer sealed capsule (e.g. Anderson and Burnham, 1965; Manning 1994, Tropper and Manning 2007). Generally, this method gives rather precise results for minerals that dissolve congruently. However, its application may be problematic in multi-component systems. The weight loss approach also has limitations when applied to minerals for which the solubility in water is strongly affected by temperature. In this case, temperature gradients along the capsule may cause dissolution of material in the hot portion and re-precipitation in the colder parts, leading to major errors in the solubility determination. One further possibility is to observe in-situ the complete dissolution of minerals of known weight in a known amount of fluid using externally heated diamond-anvil cells (Audetat and Keppler 2005).

Despite the difficulties described, several techniques also enable a direct determination of the fluid composition. This is for example possible employing an externally heated diamond-anvil cell combined with in situ synchrotron-radiation X-ray fluorescence (e.g. Manning et al. 2008; Wilke et al. 2012). However, the applicability of this method is limited to the study of simple systems and only provides information about elements for which absorption energies do not overlap with those of diamond, thus precluding quantification of elements such as Si, Al, Cl, Na and Mg. Also, in most cases the detection limits are too high to adequately quantify trace element solubilities in the fluid. Lastly, as the duration of diamond-anvil cell experiments is typically limited to a few hours, this method can only be applied to those systems that require a short time for equilibration. Other methods that do not adopt in-situ measurements, have been proposed to overcome problems related to the precipitation occurring during the quench of a fluid. Such experiments mostly rely on the idea of physically separating a portion of the fluid from the solid phases, while ensuring that chemical exchange and equilibration is possible during the run. One way to achieve such separation is to synthesize fluid inclusions during the experiment (e.g. Spandler et al. 2007; Bali et al. 2011, 2012; Tsay et al. 2014, 2017). These inclusions are produced as dissolution and recrystallization of a host mineral (typically quartz or olivine) occurs. If the conditions of the experiments are close to the α-β quartz or the α quartz-coesite transition, it is also possible to control to some extent the time of formation of the fluid inclusions to ensure that equilibrium is achieved before the sealing (Zajacz et al. 2010; Tsay et al. 2016). By briefly crossing the phase transition boundary, extensive cracks can be

developed in-situ due to the large volume change between the two polymorphs. Bringing again the run to the initial conditions in the α quartz stability field, the cracks start to heal to minimize surface energy, trapping in the process several fluid inclusions. As the fluid is isolated by the host, the bulk fluid composition, including eventual solid precipitates formed upon quenching, can be analyzed at room conditions by Laser Ablation Inductively Coupled Plasma Mass Spectrometry (LA-ICP-MS). An advantage of this method is that it provides several separated samples of the fluid, allowing to eventually identify and discard contaminated inclusions. On the other hand, the synthetic fluid inclusion approach precludes any quantification of solutes contained in the host mineral (e.g. SiO_2 if quartz is used). Moreover, for systems that reach chemical equilibrium slowly, it is not always possible to achieve equilibrium before the inclusions are isolated. In the framework of this thesis, an alternative experimental approach, the diamond trap method, was applied and tested for the direct measurement of fluid/mineral partition coefficients and of mineral solubilities.

2.2. The diamond trap method

The basic idea of the diamond trap method is to fill a portion of the capsule with a fine-grained diamond powder. Since diamond is mostly chemically inert and mechanically strong, this kind of trap provides some pores, preserved at high pressure, which are available for circulation of the fluid only. In this way, equilibration of the fluid with the mineral phases is facilitated as the system remains open for the entire duration of the experiment, unlike for synthetic fluid inclusions. At the same time, an efficient segregation of the fluid is attained since the solid starting material is unlikely to enter and contaminate the diamond trap if some precautions are taken. It is therefore reasonable to assume that in general, solid materials found inside the diamond trap represent fluid components precipitated upon quenching. This, however, may not be true in systems that are particularly sensitive to temperature. In these cases, the temperature gradients that typically develop in high-pressure experiments may lead to dissolution of minerals and their reprecipitation in the diamond trap. Moreover, this phenomenon is likely to be more severe when a metastable starting material is used, as a supersaturated solution that reaches equilibrium by precipitating crystals is expected to form during the early stages of the experiment. As these crystalline phases could also contaminate the diamond trap, they will be

erroneously considered to be fluid components, resulting in an overestimation of the solute concentrations in the fluid. This problem may be reduced, if the crystalline mineral assemblage stable at the experimental conditions is used as starting material. However, as discussed above, this would hinder the attainment of chemical equilibrium between fluid and minerals.

The diamond trap technique was first proposed by Ryabchikov et al. (1989). These authors introduced diamond powder, enclosed in a perforated inner capsule, inside an outer capsule also containing the solid starting material and distilled water. A later development of the method was proposed to study the composition of low fractions of partial melting (e.g. Johnson and Kushiro 1992, Kushiro and Hirose 1992, Hirose and Kushiro 1993, Baker and Stolper 1994, Baker et al 1995). In these experiments, to enhance the segregation of small amounts of melt, the diamond powder was inserted directly inside the outer capsule and different geometries were tested. The results from Kushiro and Hirose (1992) showed that one of the best designs is a thin layer of diamond sandwiched at the center of the capsule between the solid starting material. One important observation of this study is that the liquid must completely fill the pores between the diamonds in order to avoid the development of negative pressure gradients in the trap, which would prevent the attainment of equilibrium at the desired experimental conditions. Later, Stalder et al. (1997, 1998) used the diamond trap method combined with LA-ICP-MS for the determination of trace element partition coefficients between aqueous fluids and minerals. After high pressure experiments, the capsules were pierced and dried. Fluid compositions were therefore derived from analysis of the diamond trap portion containing the solid precipitates, assuming that none of the fluid components remained dissolved in the fluid that was lost from the capsule. However, this assumption is not always valid and may introduce large errors in the measured concentrations. This problem was largely solved by Kessel et al (2004), who introduced a new approach for the analysis of the diamond trap. These authors opened the capsules in frozen state and performed measurements of the diamond trap containing both the solid precipitates and the frozen fluid by LA-ICP-MS equipped with a freezing chamber. In this way, the bulk composition of the fluid, as it was at high pressure and temperature during the experiment, can be directly measured. This approach was tested through measurements of quartz solubilities in water by Aerts et al. (2010), who showed that for this system, the accuracy and precision of the method is similar to weight-loss experiments.

In the present study, the method developed by Kessel et al (2004) was used for the determination of fluid/eclogite partition coefficients. Moreover, in order to test the reliability of the method, the following three different analytical approaches were compared in simplified experiments conducted at 2 kbar and room temperature loaded with a fluid of known composition. Measurements of the diamond trap layer were performed in such experiments either: (a) after evaporation of the fluid at ambient condition, (b) after freeze-drying the sample, or (c) after opening the capsule in frozen state to directly analyze the fluid in solid state. In addition, mineral solubilities in simple and well-studied systems (quartz-water, forsterite-enstatite-water, albite-water, rutile-water and corundum-water) were determined using the diamond trap technique and compared to literature values in order to assess the reliability of the method. (see Chapter 6 for further details). Moreover, to confirm that equilibrium was attained in the fluid/eclogite partitioning experiments, several reversed experiments were performed. In such experiments, the trace elements were completely doped into the fluid phase instead of the solid starting material.

Figure 2.1. *Picture of an experimental charge after a piston cylinder high-pressure and high-temperature diamond trap experiment. After LA-ICP-MS analysis of the fluid in frozen state, the sample was mounted in epoxy and polished for mineral analyses.*

2.3.   **Starting materials and capsule preparation**

For the solubility experiments conducted to test the diamond trap method, crystalline phases were used as starting materials. Both olivine (Fo_{90}) and enstatite ($En_{89}Fs_{09}Wo_{02}Ac_{00}$) used for experiments in the forsterite-enstatite-water system are from San Carlos peridotite. Also for albite, a natural crystal from Brazil was selected. On the other hand, synthetic crystals were used for quartz, corundum and rutile solubility experiments. Powders were prepared from each of these crystals.

For eclogite-water partitioning experiments, synthetic glasses were used as starting material. All the glasses have a major element composition close to the starting material used in Schmidt and Poli (1998) and Kessel et al. (2004, 2005), which is considered to be representative of mid ocean ridge basalts (MORB). To produce the basic glass, SiO_2, TiO_2, $Al(OH)_3$, Fe_2O_3, $Mg(OH)_2$, $CaCO_3$ and Na_2CO_3 powders, which were previously dried at 140 ˚C overnight, were mixed in an agate mortar under ethanol for 1 hour. The resulting material was dried under an IR lamp and inserted in a Pt crucible to be decarbonated trough a gradual heating over 12 hours to a final temperature of 1100 ˚C, which was maintained for other 12 hours. The mixture was then melted at 1600 ˚C and rapidly quenched in distilled water to obtain a homogeneous glass. A similar procedure was used to synthesize two glasses with diopside composition, which were doped with 26 trace elements (Li, Be, B, Sc, Rb, Sr, Y, Zr, Nb, Cs, Ba, La, Ce, Nd, Sm, Eu, Gd, Dy, Er, Yb, Lu, Hf, Ta, Pb, Th, and U) in different concentrations. After crushing all the glasses into fine powders, the MORB starting material was mixed with a small quantity (0.4, 1 or 2 wt. %) of one of the two diopside glasses in order to obtain different trace element concentrations. Before experiments, all starting materials were also mixed with ~ 1 wt. % of natural garnet seeds selected from Grytting (Norway) eclogite in order to facilitate garnet growth during the experiments.

In order to understand the effect of chlorine on the partitioning behavior of trace elements in the eclogite-water system, several aqueous solutions were prepared by mixing 1, 5, 10 or 15 wt. % of NaCl to distilled water. Trace element doped solutions were also produced to be used in experiments loaded with the undoped MORB glass to test the attainment of equilibrium through reversed experiments. To obtain such fluids, a mixture of equal amounts of certified ICP-MS calibration solutions containing each 1000 ppm of trace element in 5 % HNO_3 was

prepared. The resulting solution was placed under an infrared lamp to evaporate and the solid residue was then re-dissolved in a smaller quantity of 5 % HNO_3. This produced a milky solution with higher concentration of trace elements, which was left to rest for 1 month. After the sedimentation of the insoluble residue, the clear solution at the top was separated and analyzed by ICP-MS.

Lastly, an aqueous solution of known composition was used in experiments to determine the best approach for diamond trap measurements. This solution was prepared by mixing a CsOH-Na_2SiO_3-water and a NaCl-KCl-water solution.

Final compositions in terms of major and trace elements of the different solid starting materials and doped aqueous solutions used in the eclogite-water experiments, and more details about their preparation can be found in Chapters 6 and 7.

In all the diamond trap experiments, the capsule design and preparation was similar. Au or Pt capsules with a diameter of 5 mm and 10 mm length were used for piston cylinder experiments. About 1/3 of the total amount of aqueous fluid was first pipetted into the capsule, followed by half of the total amount of solid starting material. A relatively thin layer (~ 2 mm thick) of diamond powder with grain size of 10 – 20 μm was then inserted followed by the remaining amount of fluid. This two-steps fluid addition procedure was used to prevent an eventual contamination of the diamond trap due to suspension of some of the material from the bottom layer. This is particularly important when a fine grained powder is used as solid starting material. Lastly, the second half of solid starting material was added, so that the diamond trap layer is sandwiched between two layers of solid starting material (see Figure 2.1). The total fluid/solid starting materials weight ratio was typically between 0.30 and 0.45. An empty space of about 1 mm was left between the starting material and the top lid in order to avoid severe fluid loss due to heating upon welding of the lid to the capsule. To check that major fluid loss did not occur during the sealing, the capsules were weighed before and after welding the top lid and again after leaving the capsules several hours at 130 ˚C.

For multi-anvil experiments, the procedure was essentially the same, but smaller capsules containing less starting material were used, while retaining the same proportions between fluid, glass, and diamond. The maximum capsule size that could be accommodated in the multi-anvil assembly used in these experiments is 4 mm in diameter and 4 mm long. However, capsules

with initial length of 5 mm were filled as described above and successively pre-shrinked before the high-pressure experiments to the desired length of 4 mm to eliminate the empty space left during the preparation of the capsule as described above for piston cylinder capsules. This method was used to increase the amount of material that could be inserted into the capsule, while facilitating the welding of the top lid.

2.4.   Piston cylinder apparatus

The piston cylinder press is an apparatus for high pressure and temperature experiments developed by Boyd and England (1960). The greatest advantage of this high-pressure device is the possibility to work with relatively large volumes of samples (typically ~200 mm^3) over long periods of time (days to weeks). On the other hand, the main limitation is represented by the rather low range of pressure accessible with piston cylinder, which for a routine set-up, ranges from 0.5 to 5 GPa, thus covering typical conditions from the deep crust to the uppermost mantle.
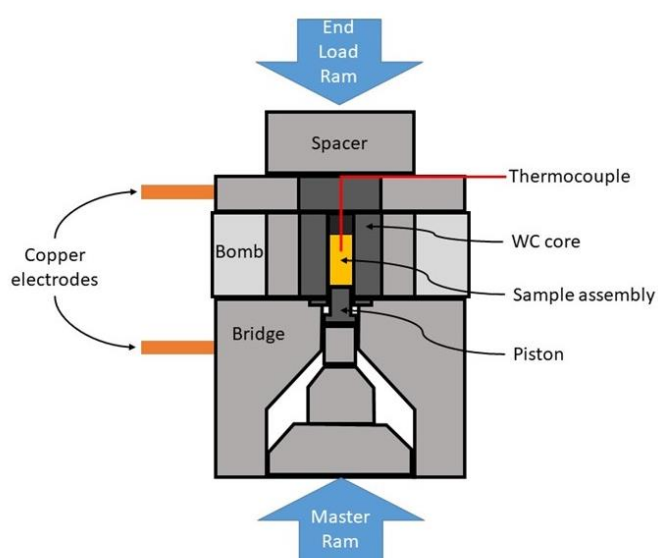
Figure 2.2. *Piston cylinder apparatus used in BGI (on the left) and schematic diagram of an end-loaded piston cylinder and its components (on the right).*

As many other high-pressure devices, the piston cylinder relies on the relationship existing between force (F), the area to which it is applied (A), and pressure (P): P = F / A. Therefore, even with relatively small loads, it is possible to amplify the pressure exerted on the sample by reducing the area of the pushing piston. Depending on the piston cylinder type, one (non end-loaded) or two (end-loaded) hydraulic rams arranged are used to deliver the load and to contain the sample. The first ram (master ram) drives the piston that applies the pressure on the sample. The optional second ram (end-load ram) is positioned opposite to the master ram (see Figure 2.2) and is used to strengthen the pressure vessel, thus extending the maximum high pressure limit from ~ 2 to 5 GPa. The pressure vessel, also called "bomb", consists of a supporting steel ring containing a tungsten carbide core with a central cylindrical cavity for the assembly. Soft materials, such as NaCl, MgO, talc, pyrex, alumina, pyrophyllite, that flow under mild shear stresses, are used for the assembly to make the stress field acting on the sample quasi-hydrostatic despite the uniaxial load applied by the piston cylinder press itself. The difference between the nominal pressure (i.e. the pressure based purely on geometrical consideration calculated as $P_{nominal} = \frac{A_{ram}}{A_{piston}} P_{oil\ ram}$) and the "real pressure" that the sample experiences, is the friction correction. Most of this pressure loss is thought to be due to the different shear strength of the materials chosen for the assembly (Johannes 1978) and calibration experiments should be performed to quantify the appropriate friction corrections needed to convert the nominal pressure to the real pressure. Frictional effects also depend on the method employed to reach the desired pressure. The standard approach ("hot piston-in") consists in applying only 90 % of the target pressure first, then increase the temperature at constant pressure, and finally increase the pressure to the desired conditions. This method helps especially when materials with high thermal expansion, such as NaCl, are used as pressure medium, as during heating a marked increase in pressure can occur.

To achieve high temperatures, up to 2200 °C, a current is passed through a graphite furnace located in the assembly (Figure 2.3). The temperature is monitored with an accuracy of ±1 °C by a thermocouple placed close to the top of the capsule. Uncertainties in the determination of the run temperature are usually introduced by thermal gradients that develop within the assembly. In order to reduce this problem, tapered or stepped graphite furnaces can be used instead of straight graphite tubes. During experiments, a cooling system that makes use of water
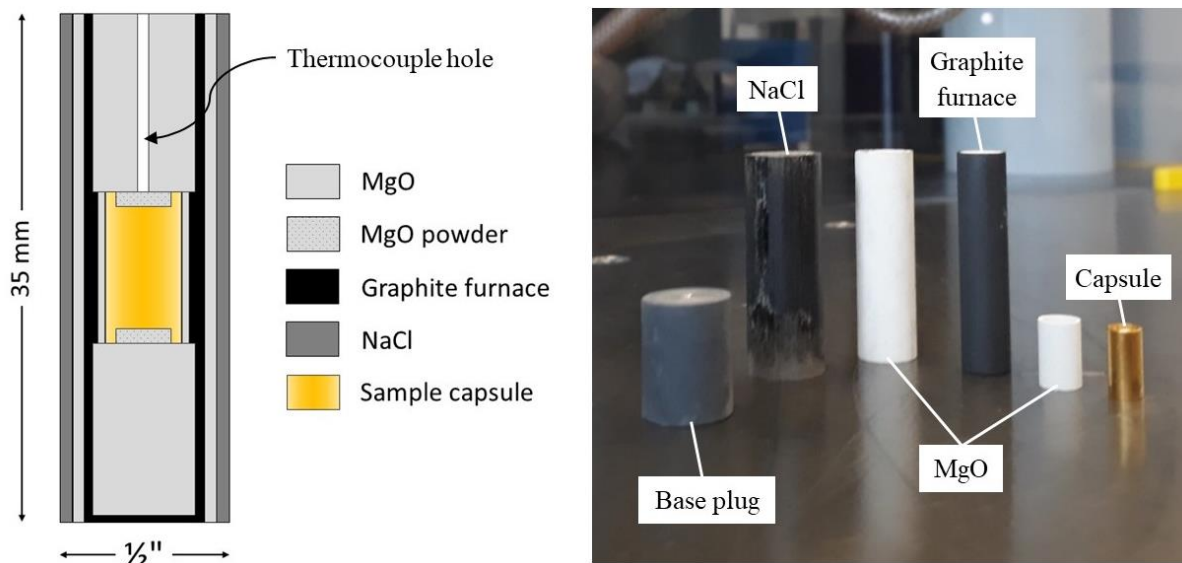
Figure 2.3. *Piston cylinder assembly used in this study.*

circulating through the bridge, the bomb and the upper plate is activated. This cooling water also helps to achieve rapid quench to room temperature by shutting off the electrical power at the end of the experiment.

For the purposes of this study, a piston cylinder apparatus was used to conduct partitioning and solubility experiments in the pressure and temperature range of 1 to 5 GPa and 700 to 1000 °C. A ½ inch assembly, consisting of an outer cylinder of NaCl and an inner cylinder of MgO containing the stepped graphite furnace was used in all experiments (see Figure 2.3). MgO plugs and sleeve ensure that the capsule stays at the center of the assembly, where the thermal gradient should be at its minimum. A hole in the top plug allows placing the thermocouple as close as possible to the capsule to have a realistic constraint on the temperature applied to the sample. An S-type thermocouple ($Pt – Pt_{90}Rh_{10}$) connected to a Eurotherm controller was used to monitor the temperature. Experiment durations ranged from 1 to 7 days depending on the time necessary to reach full equilibrium in the investigated system. In some experiments, ± 30 °C cycles around the target temperature were applied to enhance mineral growth by Ostwald ripening (i.e. dissolution of the smaller crystals at high temperature and re-precipitation of material around bigger crystals at low temperature). Compression and decompression duration varied from 30 minutes for experiments conducted at relatively low pressures, to 20 hours for experiments conducted at 4 - 5 GPa, in order to minimize capsule deformation and maximize

the longevity of the pressure vessel. More details about the experimental procedures followed in these experiments can be found in Chapter 6 and 7.

2.5.   Multi-anvil apparatus

The multi-anvil press allows reaching higher pressures (up to 25 GPa with standard setups) than the piston cylinder apparatus while maintaining relatively large volume samples. In contrast to the piston cylinder, which first applies a uniaxial load to the assembly inside a stiff pressure container, the multi-anvil apparatus delivers pressure onto the sample from different directions, without using a passive container. Several geometries of multi-anvil presses exist (e.g. Huppertz 2004), and for the purposes of this study, a 6/8 Walker-type multi-anvil press was used. The 6/8 multi-anvil was first described by Kawai and Endo (1970) and consisted of six steel anvils that together formed a spherical outer shape with a cubic cavity at the center. In this cavity a second set of eight cubic-shaped tungsten carbide inner anvils is located. Each of the tungsten carbide cubes has a triangular corner truncation that creates an octahedral cavity at the center, where a ceramic pressure medium containing the sample is placed. Pyrophyllite gaskets are also arranged between the cubic anvils in order to support the truncations and to seal the high-pressure volume. While the inner anvils and assembly remain similar to the Kawai-type multi-anvil, Walker et al (1990) introduced a split-cylinder shape for the outer steel anvils, where each of the anvils is free to float inside a ring. This allowed a considerable reduction in production costs for the device.

Different types of assembly can be used depending on the pressure and temperature range and sample volumes needed. The larger the sample volume, the smaller is in general the pressure achievable. A particular type of assembly is described by two numbers: the truncation edge length (TEL) and the octahedral edge length (OEL) using the OEL/TEL notation (i.e. a 25/15 assembly has an octahedron with 25 mm long edge and an anvil truncation of 15 mm). In general, MgO is used for the octahedral assembly. A stepped tubular resistance heater typically made of graphite, lanthanum chromite or metal foils, is inserted into the MgO octahedron. An insulator material (e.g. ZrO_2) should be placed around the furnace to prevent heating of the tungsten carbide anvils and the pyrophyllite gaskets that could enhance plastic deformation.

MgO spacers are used to keep the capsule at the center of the assembly, while Mo lids ensure contact between the WC anvils and the furnace.

Similarly to the piston cylinder apparatus, also in multi-anvil devices a significant portion of the force applied by the anvils is lost during experiments due to friction losses in the gaskets and the assembly. Therefore, it is very important also in this case to perform calibration experiments in order to estimate the real pressure experienced by the sample.

In this study, I performed multi-anvil experiments at 6 GPa and 800 °C to investigate the effect of pressure on the partitioning behavior of trace elements with respect to fluid salinity. A Walker-type multi-anvil with 25/15 assembly (see Figure 2.4) was used following the pressure calibration curve from Keppler and Frost (2005). A D-type thermocouple ($W_{97}Re_3$ - $W_{75}Re_{25}$) was used to monitor the temperature during the experiments. Compression and decompression were carried out within 15 hours, and high pressure and temperature conditions were maintained for 3 days.
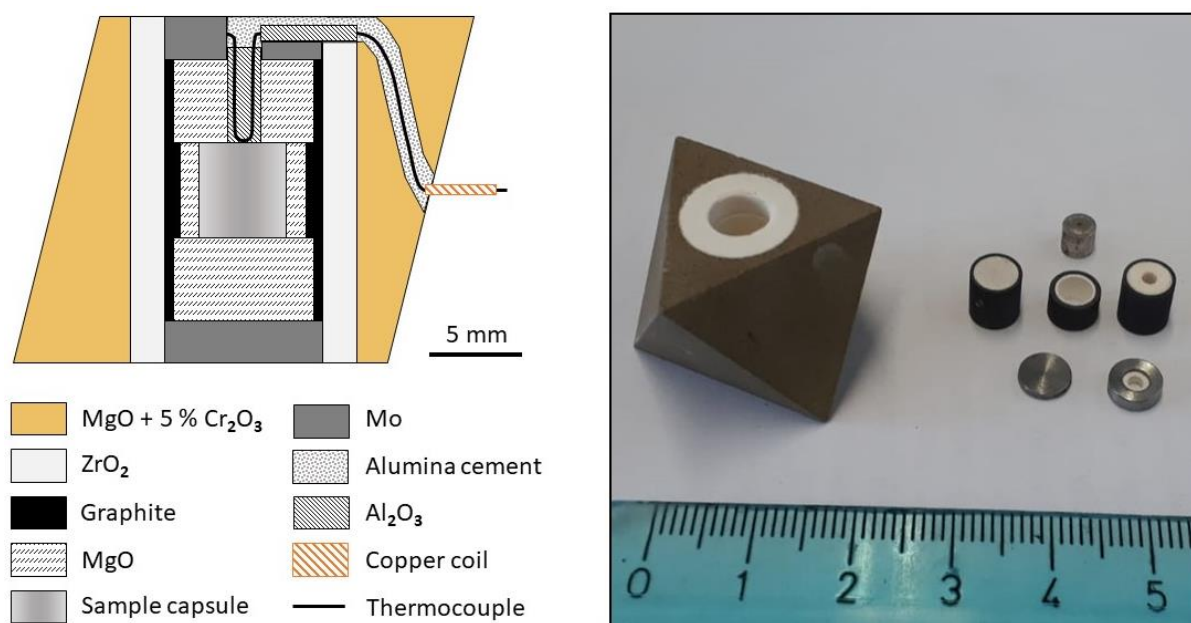
Figure 2.4. Multi-anvil assembly used in this study

2.6. Laser ablation inductively coupled plasma mass spectrometry

The Laser Ablation Inductively Coupled Plasma Mass Spectrometry (LA-ICP-MS) is an analytical technique for the determination of major, minor and trace elements, including the quantification of isotopic ratios. This method allows measuring most of the elements (with the exception of H, C, N, O, F, S and some noble gases) in any kind of matrix, but it only gives information about elemental abundances (i.e. it does not provide any information on valence state, molecular species or crystal structure of the sample). Due to its high spatial resolution (at the μm level) and high sensitivity (detection limits to sub-ppm), in combination with fast analytical procedures and minimal sample preparation, LA-ICP-MS has become a popular analytical method, which found one of its greatest successes in application to geological sciences. The idea of combining laser ablation sampling with ICP excitation source and mass spectrometry was first introduced by Gray (1985).

A schematic setup of LA-ICP-MS is shown in Figure 2.5. Different lasers can be used, and almost all the available laser wavelengths have been tested for this application (Günther and Hattendorf, 2005). The first instruments made use of lasers in the infrared or visible range, while today the most common wavelengths employed are in the ultraviolet (266, 213 and 193 nm). This shift towards shorter wavelengths was driven by the better quality of ablation achieved with them. UV wavelengths produce a smaller thermal alteration of the sample and generate particles of smaller size during ablation as compared to lasers having longer wavelength. This helps to prevent elemental fractionation processes during the analysis (Günther and Hattendorf, 2005). The laser beam initially has an inhomogeneous power distribution. However, to ensure an even sampling, a "flat top" energy distribution is required at the ablation spot. Therefore, optical lenses are used to homogenize the beam. A mask with different apertures is then used to control the final pit size on the sample, which may be regulated to be between 5 and 200 μm in diameter. After being homogenized and shaped, the pulsed laser enters a petrographic microscope, which directs and focuses the beam on the sample. The analysis can be monitored and directed in real time using a CCD camera that shares the same focal point as the beam. The quantity of material removed from the sample at each laser pulse depends on the laser energy and on the nature and transparency of the sample.
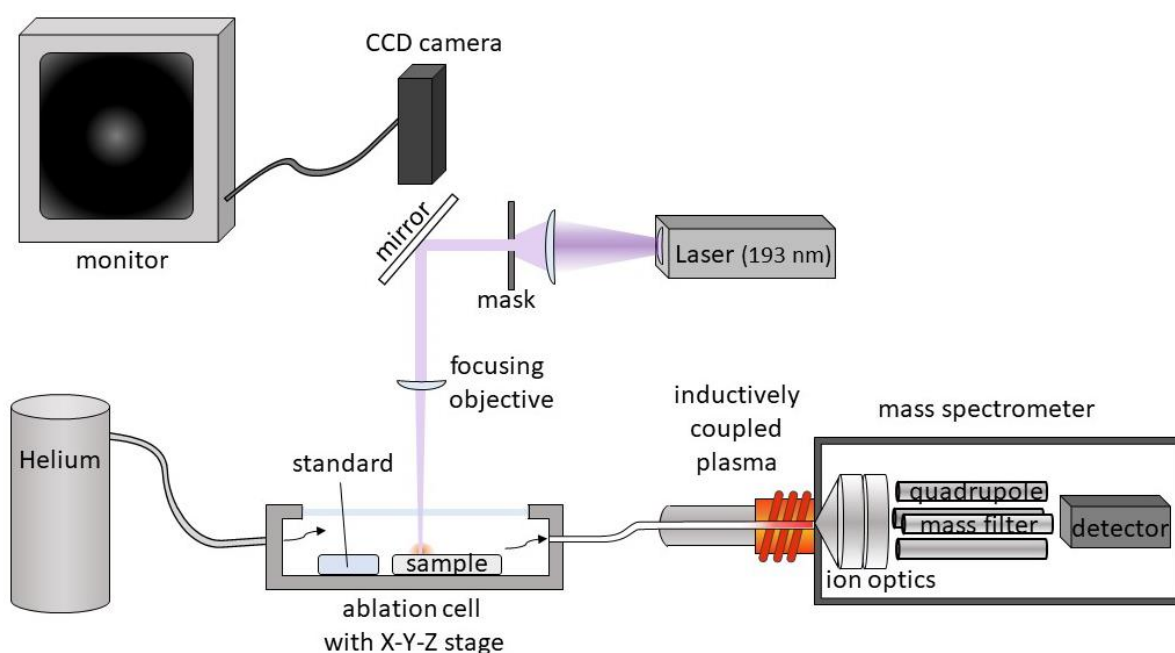
Figure 2.5. *Schematic Laser Ablation Inductively Coupled Plasma Mass Spectrometry instrument diagram. Modified from Günther and Hattendorf (2005).*

The typical thickness of the layer removed by a single pulse is about 0.1 - 0.3 μm, and the analysis is usually interrupted when the ablation crater reaches a depth of 20 - 50 μm. The ablation cell in which the sample is accommodated during analysis is constantly flushed with argon or helium. When the laser hits the sample, the material is converted to plasma, and tiny particles (usually smaller than 1 μm) that form from condensation of the plasma cloud are transferred to the ICP by the flushing gas. The transport efficiency is about 10 – 40 % (Günther and Hattendorf, 2005). The volume of the ablation cell can affect the signal/background ratio of the resulting signals. Also, the use of He instead of Ar as flushing gas when using a 193 nm laser, has been demonstrated to enhance the signals by a factor of five, as well as reducing elemental fractionation in silicate analysis (Eggins et al. 1998). The addition of minor quantities of H_2 to the gas stream can help to prevent most of the Ar-based interferences (Günther et al. 2001, Mason and Kraan 2002) and increases the sensitivity for most elements by a factor of 2 – 4 when added to the He carrier (Guillong and Heinrich 2007). In the ICP, the temperature is increased to 5000 - 7000 °C in order to ionize all the particles transported by the gas. For complete ionization, it is important that the particles generated by the laser are as small as possible (Guillong and Günther 2002). The ions are then transferred to the mass spectrometer,

where ion lenses accelerate them. The majority of MS make use of a quadrupole mass analyzer. This device is made of four cylindrical metal rods of which each opposing pair is connected electrically. When ions travel between the rods, an oscillating electrical field selectively stabilizes or destabilizes their path, depending on their mass/charge ratio. Quadrupole mass filters therefore allow the arrival at the detector of only one specific mass at a given time. Changes to the potentials on the rods, and hence to the selected mass/charge ratio to measure, can however be performed very fast (typically 3 ms). Usually each mass is measured for a time of 10-20 ms, implying that even when analyzing multiple elements together, an entire cycle of mass measurements will last far less than one second. A typical LA-ICP-MS analysis takes between 2 and 5 minutes. Of these, the first 40 seconds are generally used for background measurements. At the beginning of the analysis, the formation of refractory oxide ions such as ThO^+, is monitored and operating parameters are adjusted to minimize the abundance of such oxides trying at the same time to maximize the signal/background ratio.

Relative intensities in the signals collected from the sample are compared to those obtained from an "external standard" (i.e. a well characterized reference material). An advantage of LA-ICP-MS is the possibility to use external standards that are not matrix-matched to the sample, so that the same standard analysis can be used for the quantification of multiple elements in different phases. In order to obtain absolute concentrations of elements, also an "internal standard" is required. This can be any element contained in the sample for which the absolute concentration is known (e.g. it has been determined through another independent analytical method) or it can be assumed based on the nature of the sample itself. For example, if all of the major element that constitute the sample are analyzed, it is possible to assume that the sum of all the measured major oxides should close at 100 wt. %. The most important parameters that influence the detection limits achieved by LA-ICP-MS are the amount of material ablated (i.e. the pit size employed) and the mass of the element (higher masses are more sensitive than lower masses).

For the aim of this study, both fluid and mineral compositions, retrieved after high pressure and temperature experiments, were characterized by LA-ICP-MS. The instrument present at the Bayerisches Geoinstitut is similar to that described by Günther et al. (1998) and uses a GeolasPro 193 nm ArF Excimer Laser (Coherent, USA) together with an Elan DRC-e (Perkin Elmer, Canada). The ICP-MS was tuned to a thorium oxide production rate of 0.05 – 0.10 %

and a rate of doubly charged Ca ions of 0.15 - 0.25 % according to measurements on NIST SRM 610 glass (Jochum et al. 2011). The sample chamber was flushed with He gas with a flow rate of 0.4 l/min, to which 5 ml/min H_2 was admixed on the way to the ICP-MS (Guillong and Heinrich, 2007). Measured isotopes included ^{7}Li, ^{9}Be, ^{11}B, ^{23}Na, ^{25}Mg, ^{27}Al, ^{30}Si, ^{35}Cl, ^{39}K, ^{43}Ca, ^{45}Sc, ^{49}Ti, ^{57}Fe, ^{85}Rb, ^{88}Sr, ^{89}Y, ^{90}Zr, ^{93}Nb, ^{133}Cs, ^{137}Ba, ^{139}La, ^{140}Ce, ^{146}Nd, ^{147}Sm, ^{153}Eu, ^{157}Gd, ^{163}Dy, ^{167}Er, ^{172}Yb, ^{175}Lu, ^{178}Hf, ^{181}Ta, ^{208}Pb, ^{232}Th, and ^{238}U, using a dwell time of 10 ms.

For the analysis of the fluid phase, the capsules, which were stored in a freezer at -18 °C immediately after experiments, were cooled in liquid nitrogen and cut open longitudinally with a razor blade attached to an opening device. After cutting, one half of the capsule was quickly placed in a LA-ICP-MS ablation chamber equipped with a Peltier-cooling element. Tests with H_2O-ethanol mixtures showed that the temperature within this sample chamber is maintained at about -30 °C. This ensured that the aqueous fluid present in the capsule remained in frozen state during the entire duration of the analysis. The diamond trap layer was analyzed along two perpendicular transects with a repetition rate of 7 Hz and a large laser spot size of 50 - 70 μm to obtain the best average of the bulk fluid composition. External standardization was mostly based on NIST SRM 610 glass (Jochum et al., 2011), except for chlorine quantification for which a well characterized natural afghanite crystal (Seo et al. 2011) was used. Each fluid analytical sequence was bracketed by two measurements of NIST SRM 610 and one of afghanite both before and after analysis on the sample. The two measured transects were divided into 3 – 6 separate integration intervals to check homogeneity and reproducibility in the calculated element concentrations. Either Cl or Cs were used as internal standard for the fluid, as both these elements are expected to strongly partition into the fluid in all the considered systems. Internal standard concentrations were also corrected for the dilution effect produced by the dissolution of major elements during the high-pressure experiments.

For the partitioning experiments conducted in the fluid-eclogite system, after measurements of the diamond trap layer, the fluid contained in the capsules was allowed to evaporate at room condition. The dry samples were impregnated in epoxy and the surface was polished to expose the minerals. Single crystals were analyzed with spot sizes of 7 – 20 µm, trying to avoid inclusion and the garnet seeds at the core of many garnets. NIST SRM 610 glass was again used for external standardization, while internal standardization was in this case done by

normalizing the sum of measured major oxides to 100 wt. %. Values obtained from the average of 4 – 7 different crystals of the same mineral located in different portions of the capsules were considered representative for the composition of garnet, omphacite and rutile. Measurements from kyanite crystals resulted in trace element concentrations below LA-ICP-MS detection limits, and the presence of this mineral was therefore ignored in the calculation of fluid/eclogite partition coefficients. Fluid/eclogite partition coefficients were obtained by normalizing the individual fluid/mineral partition coefficients to a bulk rock composition of 59 % omphacite, 39 % garnet and 2 % rutile, considered to be representative for the mafic portion of a subducting oceanic slab at the studied P and T conditions.

2.7.   Electron microscopy

In partitioning experiments between fluid and eclogite, the mineral assemblage was also characterized by means of scanning electron microscopy (SEM) and electron microprobe (EMP).

2.7.1. Scanning electron microscopy

In SEM, a beam of focused electrons is used to scan the sample surface. Several interactions, observed using different detectors, can occur when the beam hits the sample (Figure 2.6). When high-energy electrons interact elastically with the deep regions of the atoms constituting the sample, these electrons can be backscattered in a proportion strongly dependent on the atomic masses (heavier atoms generate more of these interactions than light atoms). Using this principle, it is possible to produce back scattered electrons (BSE) images, in which bright colors represent phases that are able to back scatter more electrons, hence having an higher molar mass, while regions presenting darker colors reflect areas characterized by atoms with lower masses. On the other hand, when the electrons of the beam interact inelastically with the sample, it may cause the ejection of an electron from an inner atomic shell. The vacancy produced by this process is then filled by an electron from one of the outer, higher-energy shells, thus releasing an X-ray photon. The energy of this radiation is characteristic for each
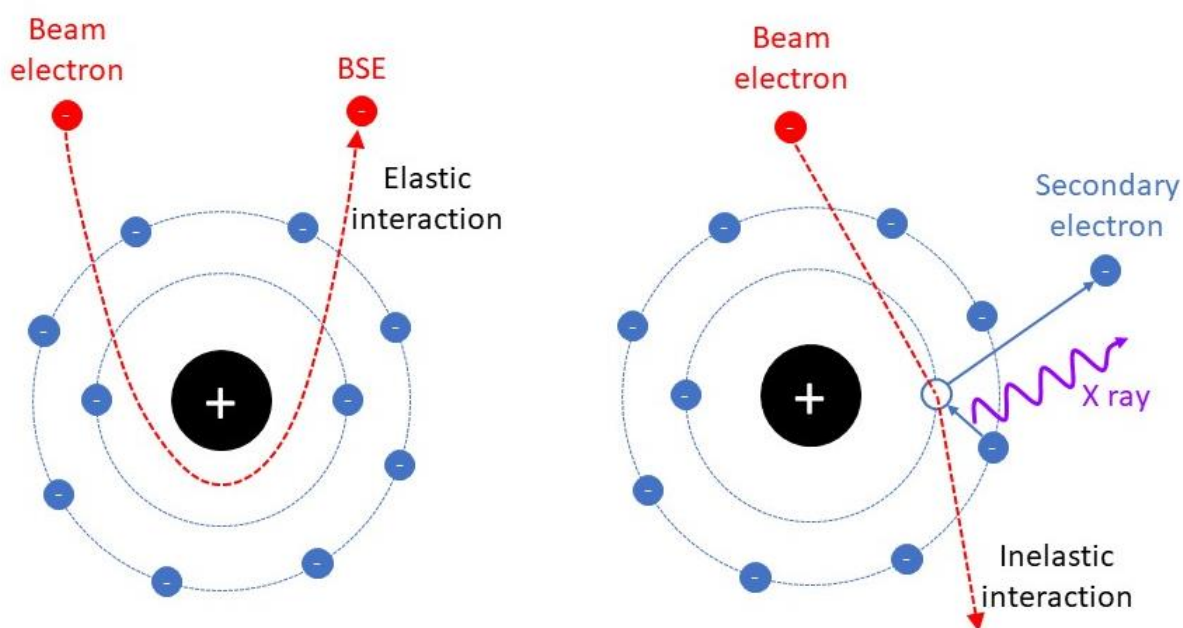
Figure 2.6. *Schematic mechanisms of interactions that produce backscattered electrons (BSE) and characteristic X ray emissions detected by energy dispersive spectrometer (EDS).*

element and depends on the jump in energy that occurred when the electron filled the inner shell vacancy. The X-rays released are collected by an energy dispersive spectrometer (EDS) that provides a semi-quantitative measurement of the element abundance in the sample.

BSE images complemented by EDS analysis for the identification of mineralogical phases were acquired using a Zeiss Gemini Leo 1530 scanning electron microscope (SEM). The samples were mounted in epoxy resin, polished on one side to maximize the exposure of the eclogitic portion, and coated with a carbon layer 14 nm thick. The instrument was operated with an accelerating voltage of 20 kV, a working distance of 14 mm and an aperture of 60 μm. The sample maps generated from the BSE images were used to select and locate crystals for subsequent LA-ICP-MS analysis.

2.7.2. Electron microprobe

Similarly to SEM, the electron microprobe makes use of the characteristic X-rays emitted after inelastic interactions occurring between the electron beam and the sample. In this case, a wavelength dispersive spectrometer (WDS) is used to collect such radiations. The X-rays

emitted from the sample are focused on a single crystal, whose d-spacings are known. The single crystal diffracts the X-rays according to the Bragg's law. Therefore, the wavelength of the diffracted beam may be calculated from the lattice spacing of the crystal and the diffraction angle, which can be varied during a measurement. The WDS mode thus allows a comparison, in terms of both position and intensity, between the spectra collected from the sample and from matrix-matched standard materials, yielding an accurate quantification of major element abundances in the analyzed sample.

Major element compositions of garnet, omphacite, kyanite and rutile produced in high-pressure experiments, were quantified using a JEOL JXA 8200 microprobe. The instrument was operated with a focused beam, 15 kV of acceleration voltage, a beam current of 15 nA and counting times of 10 sec on the background and 20 sec on the peak. Calibration was performed using the following standards: Diopside for Si, Mg, Ca; $MnTiO_3$ for Ti; Fe_2O_3 for Fe, albite for Na, and corundum for Al.

3. Results and discussion

3.1. Testing the diamond trap method

The diamond trap method was used in this study in order to determine the composition of aqueous fluids coexisting with eclogite at typical subduction zone conditions. While this method had been previously used in different variations, systematic tests of the method had never been carried out. Therefore, a number of experiments were performed out to assess the reliability of the method.

First, a diamond trap was prepared containing a fluid of known composition. This diamond trap was then analyzed by laser-ablation ICP-MS either after opening the trap and drying it at ambient conditions, or after freeze-drying it. Alternatively, the entire trap containing the fluid was frozen in liquid nitrogen, then sectioned and analyzed in frozen state. Results are shown in Figure 3.1. Only the analyses of the trap in frozen state returned the correct concentrations of the various elements in solution, while both drying the trap at ambient conditions and freeze-drying yielded widely scattered data, which even after averaging significantly diverged from the expected result. The most likely reason for this is some inhomogeneous re-distribution of dissolved material inside the trap during drying. The results clearly show that data obtained in some previous studies without freezing the trap are unreliable (e.g. Stalder et al. 1998).

In order to test whether the diamond trap method yields correct fluid compositions in high pressure and high temperature experiments, several piston cylinder experiments were carried out to determine mineral solubilities in water in some well-studied systems. These were the systems quartz-H_2O (Manning 1994), forsterite-enstatite-H_2O (Newton and Manning 2002), rutile-H_2O (Audetat and Keppler 2005), and corundum-H_2O (Tropper and Manning 2007). Moreover, an experiment was carried out in the system albite-H_2O at conditions beyond the critical curve (Shen and Keppler 1997), such that the entire trap was filled with a homogeneous fluid of known composition (equivalent to the bulk composition of the charge). The results of the analyses are shown in Figure 3.2. In general, for most systems, the expected concentrations are reproduced within a factor of two or better. However, there are problems in the systems

rutile-H_2O and corundum-H_2O, which are known to be difficult to investigate. Previous studies have produced results diverging by many orders of magnitude (see Audetat and Keppler 2005). The reason for this is likely that dissolution and re-precipitation of crystals in these systems occurs already as a result of very minor temperature gradients. This may cause some local contamination of the diamond trap by crystals that were stable during run conditions and therefore, the analysis of the trap yields scattered data that are above the expected value.
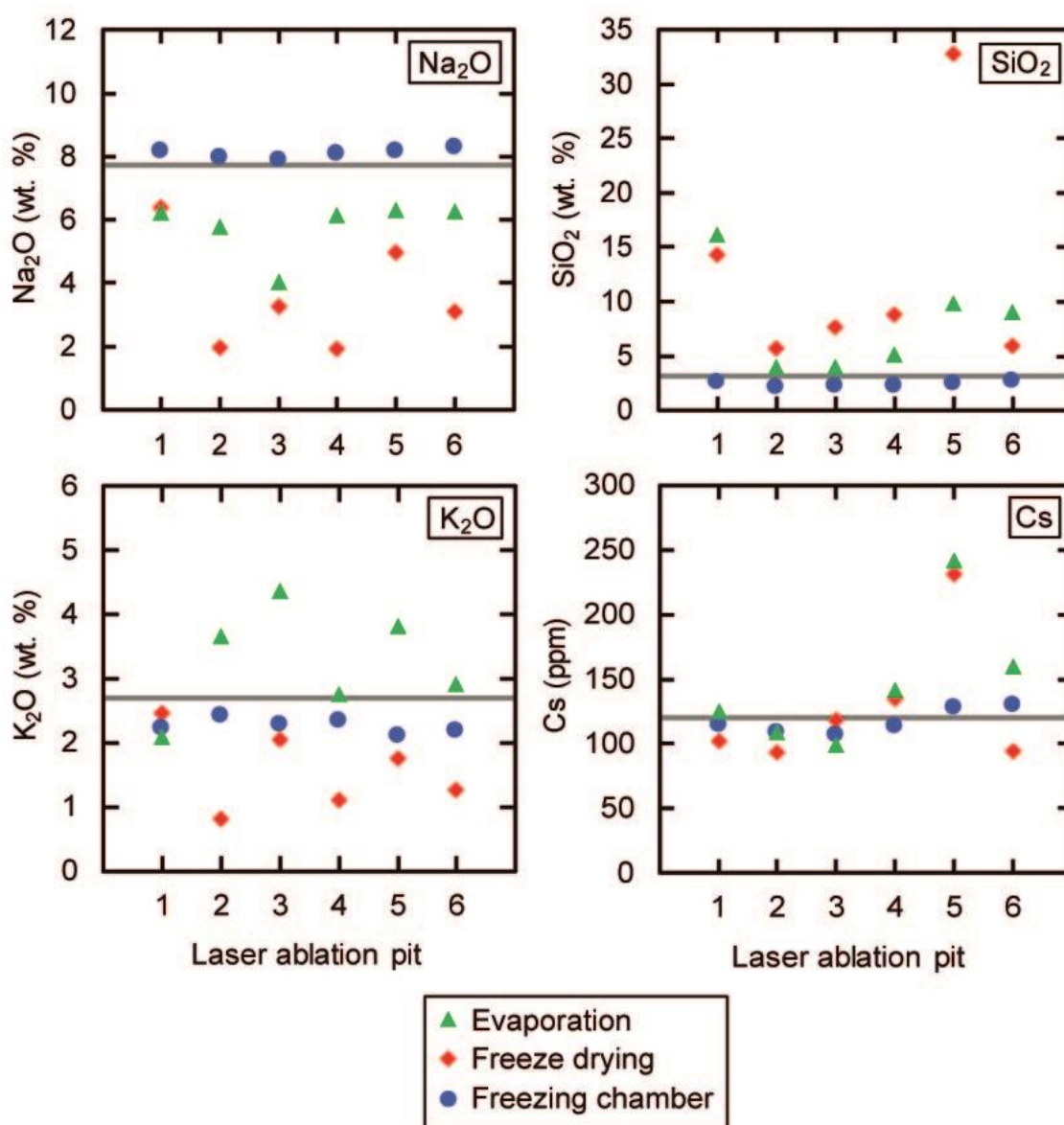
Figure 3.1. Test of laser ablation ICP-MS analyses of a diamond trap loaded with a solution of known composition. The trap as analyzed after drying the solution at ambient temperature, after freeze-drying, or in frozen state after freezing the entire trap. The expected (true) concentration is shown as a gray line.
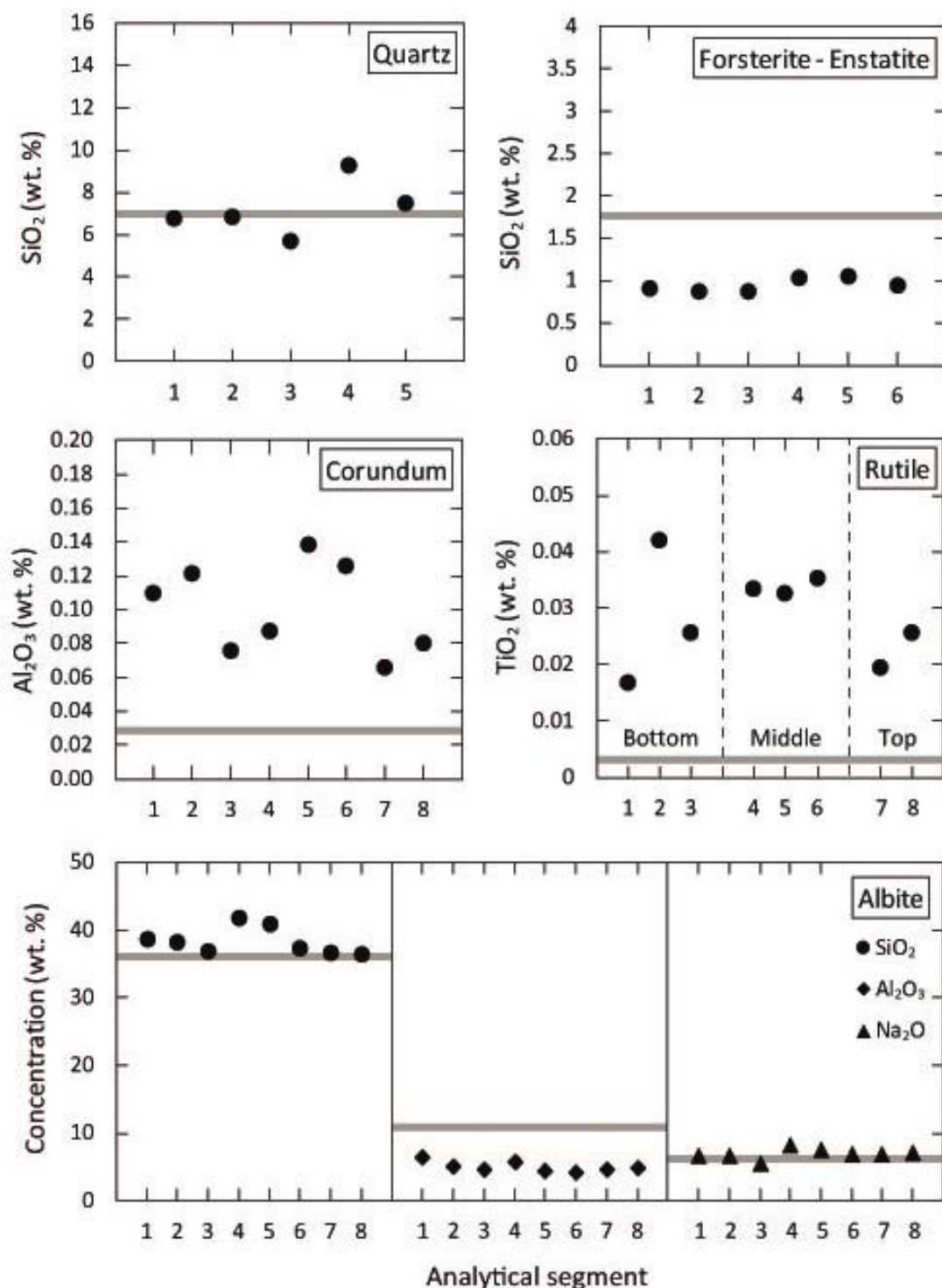
Figure 3.2. *Test of the diamond trap method by solubility experiments in well-studied systems. The concentrations expected from independent measurements as reported in the literature are indicated as grey lines. Quartz solubility in water was studied at 1 GPa and 800 ℃, the solubility of silica in water in equilibrium with forsterite and enstatite at 1 GPa and 800 ℃, corundum solubility in water at 2 GPa and 700 ℃, and rutile solubility in water at 2 GPa and 1000 ℃. The albite-water system was studied at 1.8 GPa and 800, which is beyond the critical cure in this system, such that the entire capsule should have been filled with a fluid identical to the bulk composition of the charge.*

In general, the tests carried out here show that the diamond trap method used to determine fluid compositions in piston cylinder experiments yields in most cases results that are accurate within a factor of two. While the method is therefore not optimal for high-precision solubility studies, it is completely appropriate for fluid/mineral partitioning experiments, as these numbers may vary by many orders of magnitude and an accuracy within a factor of two is acceptable. Attention has to be paid, however, to possible problems caused by the precipitation of accessory phases within the trap resulting from slight temperature gradients. This process could lead to erroneously high estimates of fluid solubilities. Such effects will, however, usually be detectable as strong heterogeneities within the diamond trap.

3.2.   Experimental results on trace element partitioning between saline fluids and eclogite

The main aim of this study was to provide data on the partitioning of trace elements between eclogite and aqueous fluids, in order to model the trace elements signature of fluids released from the basaltic part of the subducted slab. In order to do this, piston cylinder experiments using the diamond trap method were carried out at 4 GPa and 800 ˚C. These are conditions that fall in the middle of the expected slab surface P, T conditions at a typical depth of 120 km below the volcanic arc. They likely also correspond to conditions just after the dehydration of amphibole, which is the main water carrier in the basaltic part of the slab. In order to assess the P, T dependence of partitioning, additional piston cylinder experiments were carried out at 4 GPa and 700 ˚C and 5 GPa and 800 ˚C, as well as some multi anvil experiments at 6 GPa and 800 ˚C.

Starting materials in the experiments were basaltic glasses of MORB composition and aqueous solutions containing some dissolved NaCl. In most experiments, the trace elements were initially doped into the basaltic glass, but some reversed experiments with trace elements doped into the solution were also carried out. In general, there was good agreement between forward and reversed experiments, demonstrating attainment of equilibrium. During the runs, the basaltic glass always recrystallized to an eclogitic assemblage of omphacite + garnet + rutile + kyanite. Mineral compositions were uniform throughout the charge, again demonstrating

attainment of equilibrium. A problem encountered was, however, the difficulty to grow omphacite crystals large enough for chemical analysis by laser-ablation ICP-MS. This problem was solved by applying some periodic temperature fluctuations by $\pm$ 30 ˚C during the run. This method helped to increase grain size, particularly of the omphacite by Ostwald ripening, i.e. by the dissolution of smaller grains and the growth of larger crystals (Figure 3.3).

Bulk fluid compositions coexisting with eclogite at various P, T conditions are compiled in Figure 3.4. Total solute contents are typically around 30 – 40 wt. %. The most important solute is SiO_2. Na_2O, CaO, FeO, and MgO contents increase with salinity, while SiO_2 and Al_2O_3 do not.

Figure 3.5 shows the effect of fluid salinity on the fluid/eclogite partition coefficients of several trace elements at 4 GPa and 800 ˚C. The partition coefficients for the light rare earth elements (e.g. La) increase by up to three orders of magnitude with salinity, probably due to complexing with chloride. Similar effects are seen in the large-ion lithophile elements (e.g. Rb, Cs, Sr) as well as for Pb, Th, and U. On the other hand, the partitioning of the heavy rare earths (e.g. Lu) and of the typical high field strength trace elements Nb and Ta is independent of salinity. The data in Figure 3.5 indicate very good agreement between forward and reversed experiments as
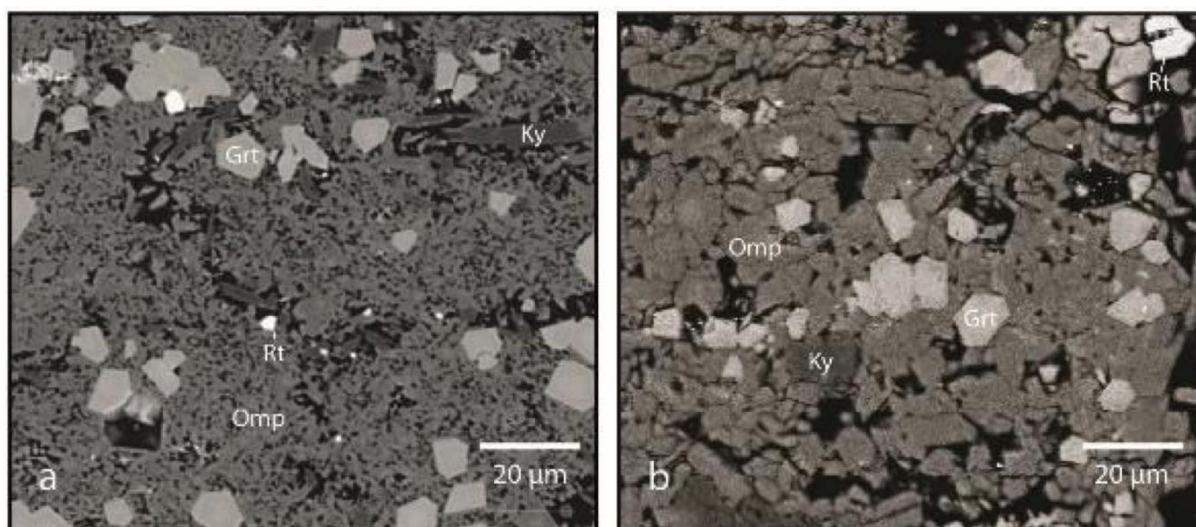
Figure 3.3. *Effect of temperature cycling on grain growth. Shown are SEM images of eclogites synthesized in the presence of an aqueous fluid at 4 GPa and 800 ˚C. The sample on the left side (a) was synthesized at constant temperature, the one on the right side (b) with 30 ˚C temperature cycling. An increase in the size of the omphacite crystals applying temperature cycling is obvious.*
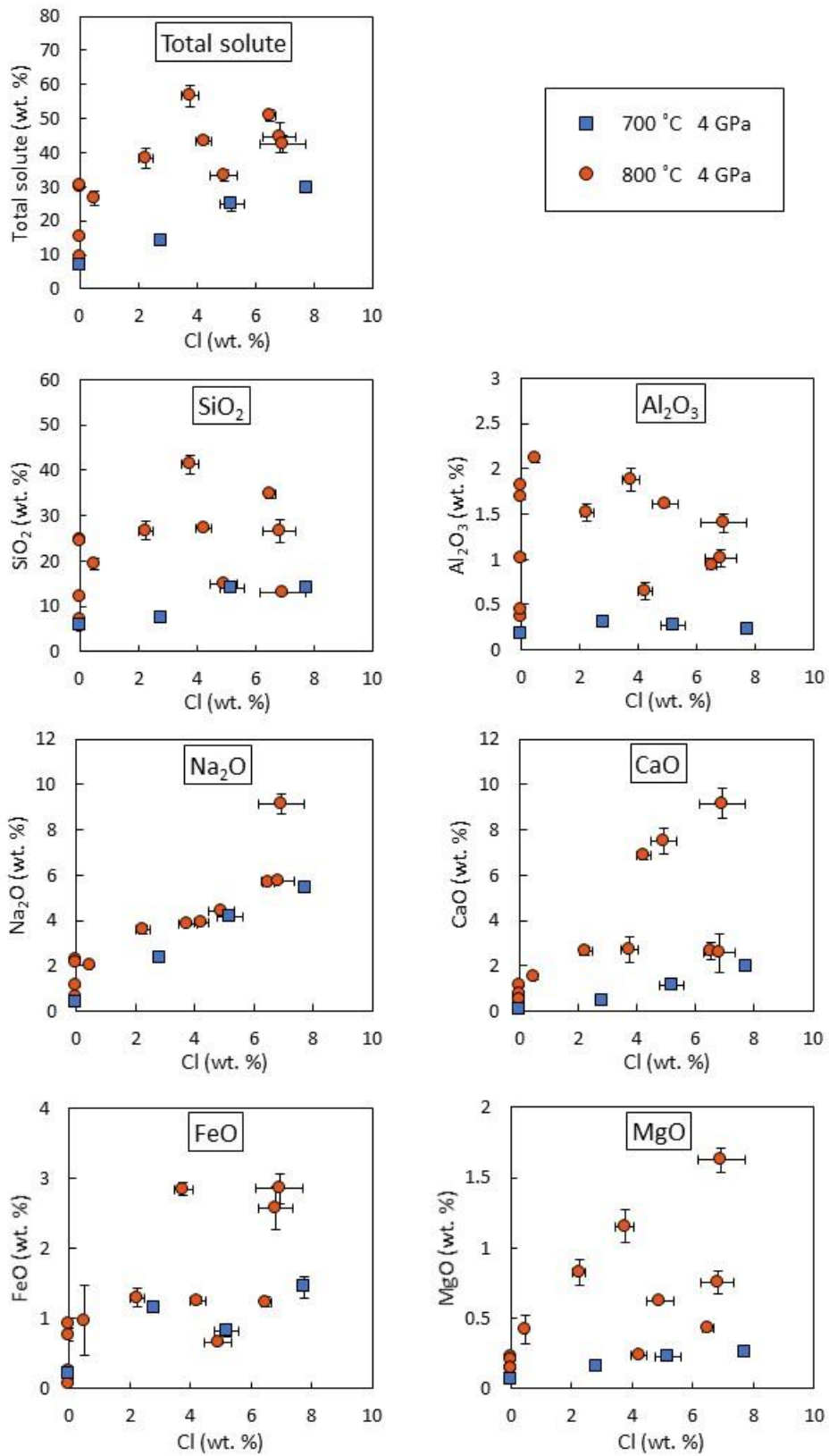
3. Results and discussion
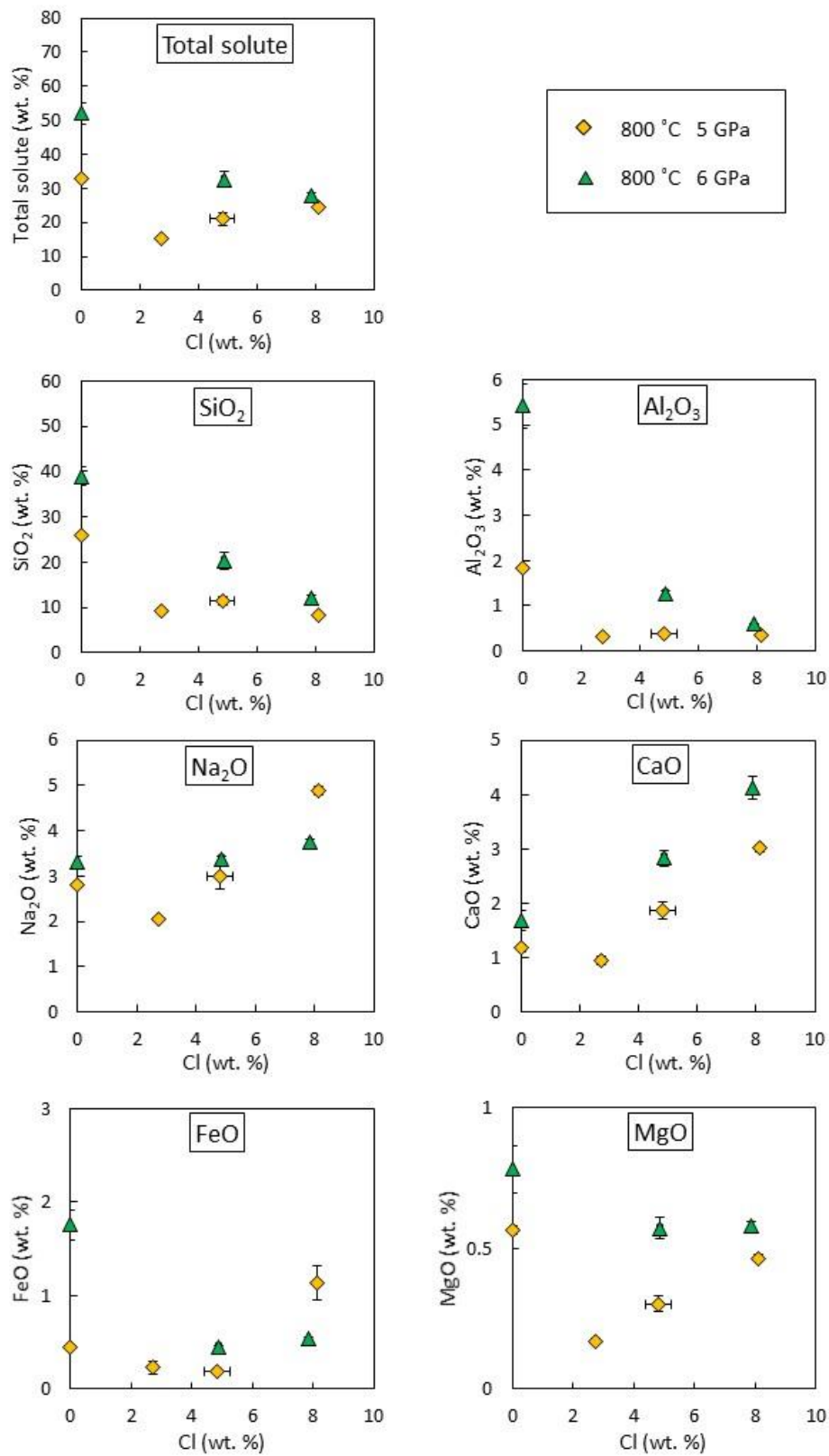
Figure 3.4. *Bulk composition of aqueous fluid coexisting with eclogite at 4 – 6 GPa and 700 – 800 ˚C*
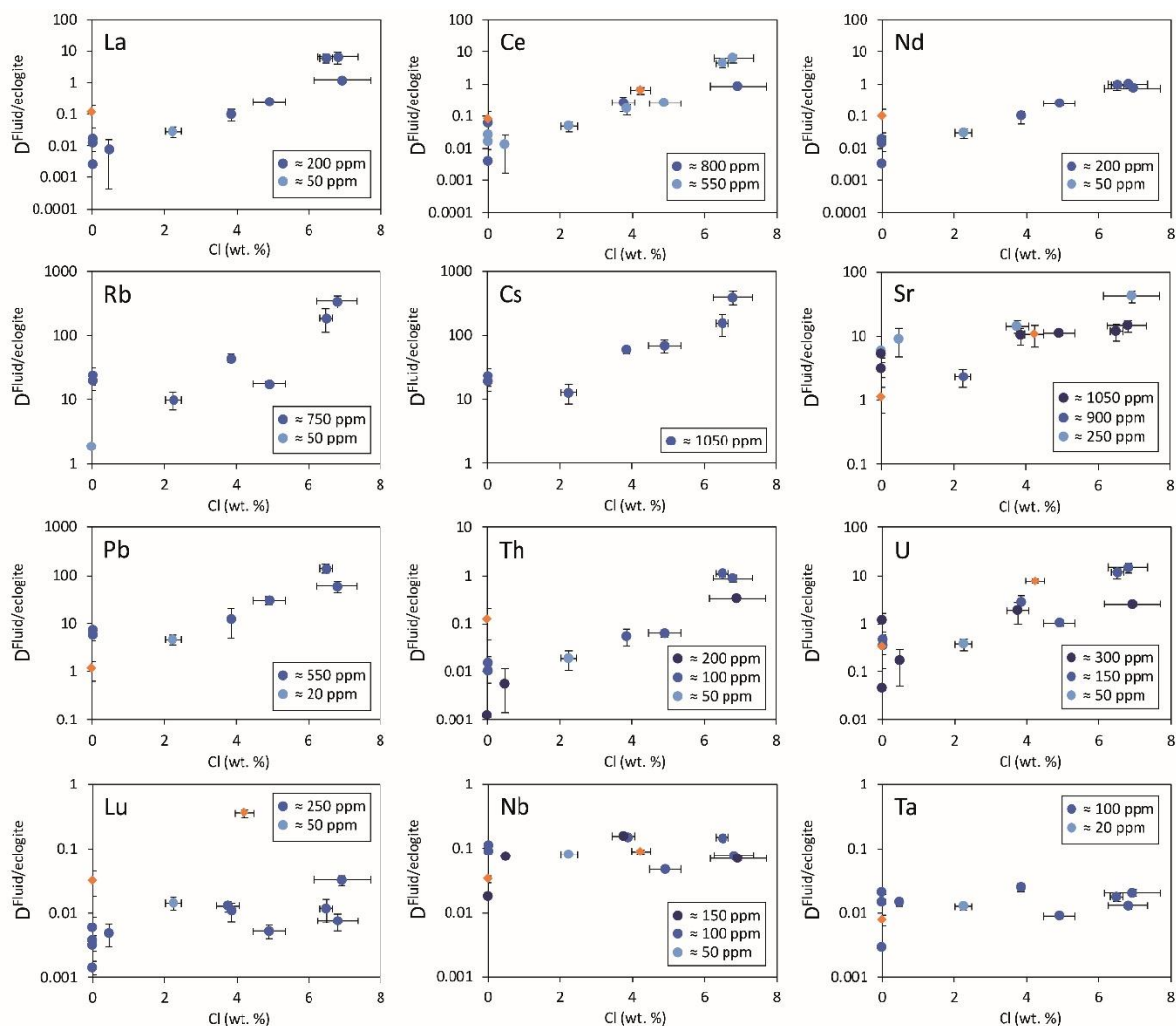
Figure 3.5. Dependence of fluid/eclogite partition coefficients of various trace elements on fluid salinity at 4 GPa and 800 ˚C. Orange dots refer to reversed experiments, blue dots with different shading refer to forward experiments with different levels of trace element doping in the starting material.

well as consistency of results for different levels trace element doping. This implies that equilibrium was achieved and that the trace element concentration range studied falls within Henry´s law.

The trace element enrichment patter in the fluid is shown in Figure 3.6. With increasing salinity, the pattern more and more resembles the fingerprint seen in typical arc magmas, with a strong enrichment of large-ion lithophile elements and light rare earths, of Pb, U, and Th, relative to the heavy rare earths and the high field strength elements.
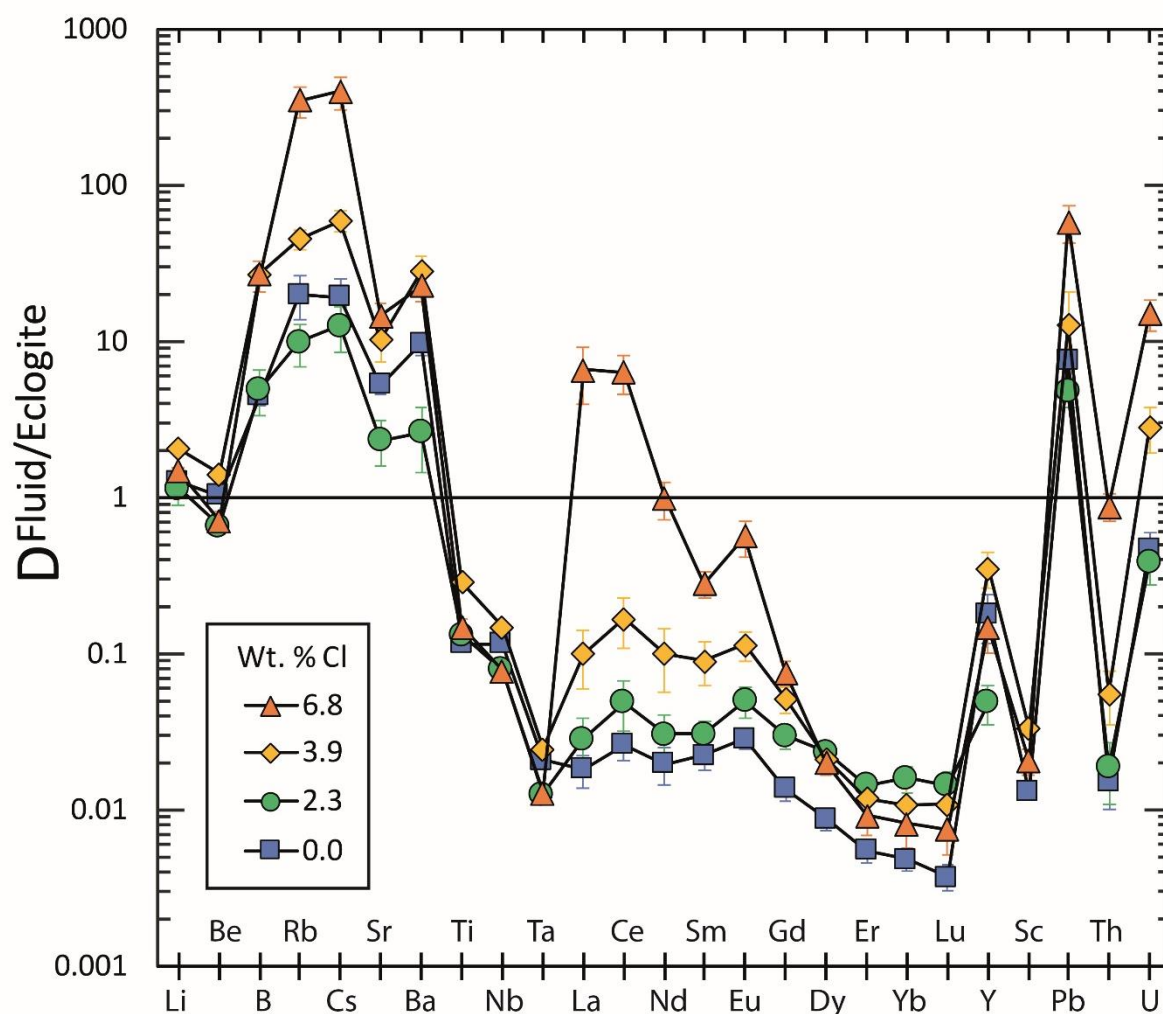
Figure 3.6. *Trace element enrichment pattern of fluids coexisting with an eclogitic assemblage at 4 GPa and 800 ˚C.*

3.3. The cause of melting in subduction zones

The experimental data for the fluid/eclogite partitioning of trace elements were used in order to test whether partial melting of a mantle source enriched by a saline, aqueous fluid released from the basaltic part of the subducted slab could reproduce the trace element abundance pattern seen in primitive arc basalts. For modeling, we assumed batch equilibrium between the fluid and the eclogite of the subducted slab and batch equilibrium during melting of the mantle wedge. The composition of the slab was assumed to be the "all MORB average" of Gale et al. (2013). The composition of the depleted mantle in the mantle wedge was taken from Salters

and Stracke (2004). Most of the mineral/melt partition coefficients during mantle melting were taken from Salters et al. (2002). The fraction of fluid in the slab was assumed to be 2 wt. %, while 20 % of melting was assumed in the mantle wedge. The influence of these two parameters on the final result is, however, relatively small. The enrichment pattern produced depends mostly on fluid salinity and on the fraction of fluid added to the mantle wedge.
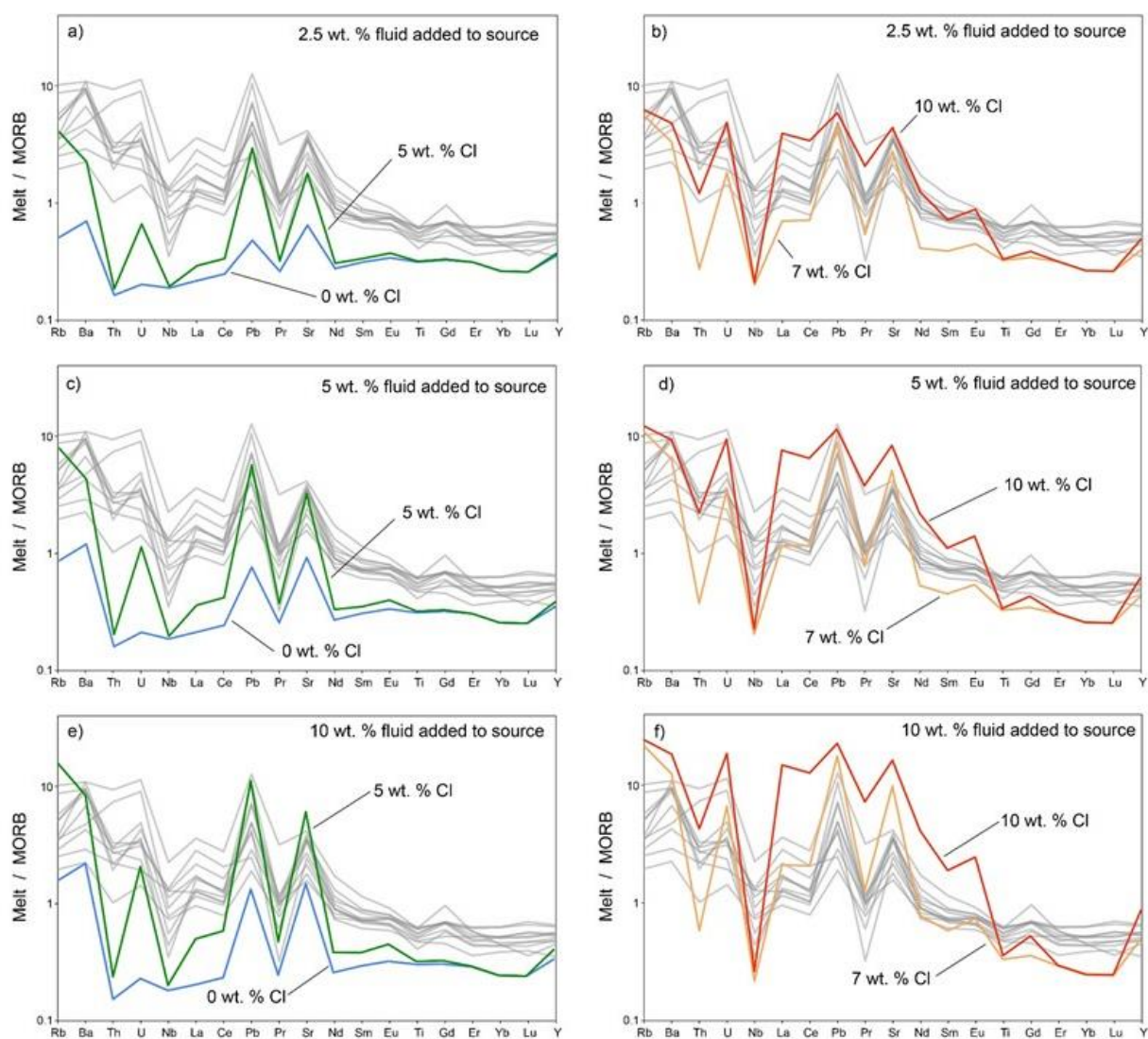
Figure 3.7. *Predicted trace element enrichment pattern for partial melts of the mantle wedge metasomatized by aqueous fluids released from the basaltic part of the subducted slab. Compositions for primitive arc basalts as compiled by Kelemen et al. (2005) are shown for comparison as grey lines.*

Figure 3.7 shows the modeling results for a range of these parameters and compares them to a compilation of data from primitive arc basalts worldwide. The data clearly show that a pure aqueous fluid without Cl cannot produce the observed enrichment pattern. However, already the addition of a few wt. % of a fluid containing between 7 and 10 wt. % Cl to the mantle wedge reproduces the enrichment pattern nearly completely. One interesting observation in Figure 3.7 is that the predicted negative Nb anomaly is more pronounced that in most natural arc basalts. This is, however, due to the fact that in the calculation of the bulk fluid/eclogite partition coefficients, we assumed 2 wt. % rutile in the eclogite. Reducing this fraction would diminish the negative Nb anomaly. The data therefore suggest that likely in the eclogites of the subducted slab, the rutile fraction is rather small.

In order to test whether the addition of sediment melts to the mantle wedge could generate the trace element enrichment pattern in primitive arc basalts, the resulting melt compositions were also calculated. For this, the compositions of near-solidus partial melts of various sediments were taken from the experimental studies of Hermann & Rubatto (2009), Skora and Blundy (2010), and Skora et al. (2015). The results are shown in Figure 3.8. In general, these models have difficulties reproducing the entire trace element abundance pattern of primitive arc basalts. In particular, they are unable to enrich the light rare earths to the required concentration level and the fractionation of Nb relative to the light rare earths is not correctly predicted. Most sediment melts also have difficulties in enriching Sr to the required level. The closest match is achieved with partial melts of GLOSS (global subducting sediment, Plank and Langmuir 1988). However, the reason for this is simple: GLOSS is very similar in composition to the average continental crust and therefore, it has already inherited a subduction-like trace element enrichment pattern. Obviously, this pattern cannot have originated in the first place, if it requires metasomatism by a partial melt of a sediment, which already contains this pattern. In contrast to this, the mechanism proposed here produces the trace element enrichment pattern in primitive arc basalts de novo by metasomatic enrichment of the mantle wedge with a saline fluid released from the subducted slab.

Another obvious observation from Figure 3.8 is that the enrichment pattern for many trace elements, e.g. thorium, is strikingly different for different types of sedimentary material. Therefore, arc with mostly carbonate subduction should produce a very different pattern from
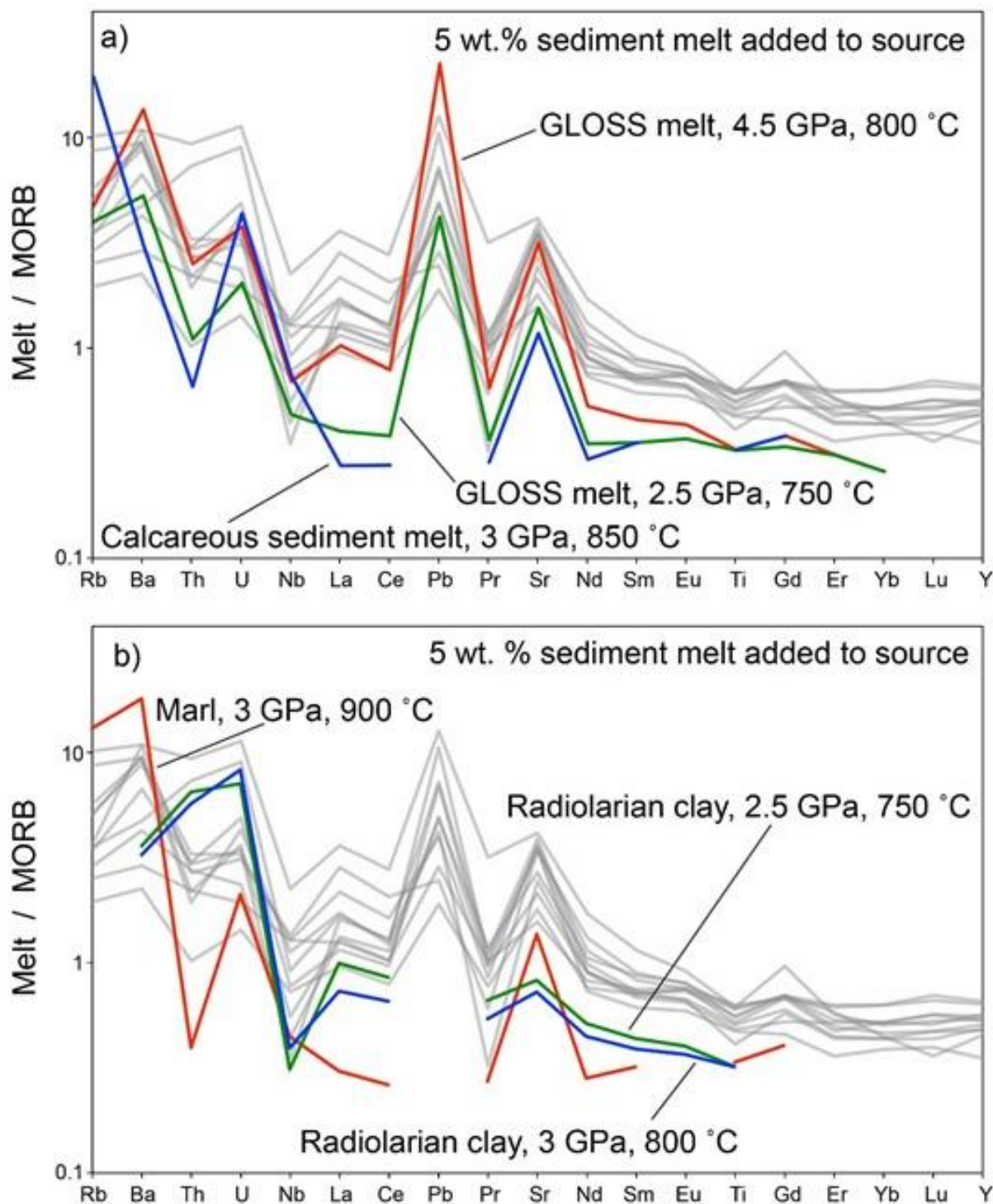
Figure 3.8. *Predicted trace element enrichment patterns for partial melts of the mantle wedge enriched by 5 wt. % of sediment melts. Near-solidus melt compositions were taken from the experimental studies of Hermann and Rubatto (2009) for GLOSS (global subducting sediment), Skora and Blundy (2010) for radiolarian clay and Skora et al. (2015) for calcareous sediment and marl. Compositions for primitive arc basalts as compiled by Kelemen et al. (2005) are shown for comparison as grey lines.*

arcs with mostly pelite subduction or no sediment subduction. However, this is not observed. The patterns of natural arc basalts shown as background in Figures 3.7 and 3.8 are all strikingly similar.

The present study therefore provides strong evidence that aqueous fluids released from the basaltic part of the subducted slab are the main trigger for melting in subduction zones. The contribution of sediment melts to the generation of primitive arc basalts is likely negligible. They may well contribute to the origin of other types of subduction-related magmas, in particular the ultrapotassic melts. However, in general, the importance of sediment melting for arc magmatism has likely been grossly overestimated.

4. References

Aerts M, Hack AC, Reusser E, Ulmer P (2010) Assessment of the diamond-trap method for studying high-pressure fluids and melts and an improved freezing stage design for laser ablation ICP-MS analysis. American Mineralogist, 95, 1523-1526

Anderson, G., & Burnham, C. W. (1965) The solubility of quartz in super-critical water. American Journal of Science, 263(6), 494-511.

Arculus RJ, Powell R (1986) Source component mixing in the regions of arc magma generation. J Geophys Res 91: 5913–5926

Arrhenius S (1900) Zur Physik des Vulkanismus. Geologiska Föreningen i Stockholm Förhandlingar 22: 395-420.

Audétat A, Keppler H (2005) Solubility of rutile in subduction zone fluids, as determined by experiments in the hydrothermal diamond anvil cell. Earth Planet Sci Lett 232: 393– 402

Baker MB, Stolper EM (1994) Determining the composition of high-pressure mantle melts using diamond aggregates. Geochimica et Cosmochimica Acta, 58(13), 2811-2827.

Baker MB, Hirschmann MM, Ghiorso MS, Stolper EM (1995) Compositions of near-solidus peridotite melts from experiments and thermodynamic calculations. Nature, 375(6529), 308-311.

Bali E, Audetat A, and Keppler H (2011) The mobility of U and Th in subduction zone fluids: an indicator of oxygen fugacity and fluid salinity. Contributions to Mineralogy and Petrology, 161, 597–613.

Bali, E., Keppler, H., and Audetat, A. (2012) The mobility of W and Mo in subduction zone fluids and the Mo-W-Th-U systematics of island arc magmas. Earth and Planetary Science Letters, 351, 195–207.

Behn MD, Kelemen PB, Hirth G, Hacker BR, Massonne HJ (2011) Diapirs as the source of the sediment signature in arc lavas. Nature Geoscience 4: 641–646

Benioff H (1949) Seismic evidence for the fault origin of oceanic deeps. GSA Bulletin 60: 1837–1856.

Boyd FR, England JL (1960) Apparatus for phase-equilibrium measurements at pressures up to 50 kilobars and temperatures up to 1750 °C. Journal of Geophysical Research, 65(2), 741-748.

Brenan JM, Shaw HF, Phinney DL, Ryerson FJ (1994) Rutile-aqueous fluid partitioning of Nb, Ta, Hf, Zr, U and Th: implications for high-field strength element depletions in island arc basalts. Earth Planet Sci Lett 128: 327–339

Brenan JM, Shaw HF, Ryerson FJ, Phinney DL (1995) Mineral-aqueous fluid partitioning of trace elements at 900 °C and 2.0 GPa: Constraints on the trace element chemistry of mantle and deep crustal fluids. Geochim Cosmochim Acta 59: 3331–3350

Brodholt J, Stein S (1988) Rheological control of Wadati-Benioff seismicity. Geophys Res Lett 15: 1081-1084

Brown L, Klein J, Middleton R, Sacks IS, Tera F (1982) 10Be in island-arc volcanoes and implications for subduction. Nature 229: 718–720.

Bureau H, Keppler H (1999) Complete miscibility between silicate melts and hydrous fluids in the upper mantle: experimental evidence and geochemical implications. Earth Planet Sci Lett 165: 187-196

Canales JP, Carbotte SM, Nedimović MR, Carton H (2017) Dry Juan de Fuca slab revealed by quantification of water entering Cascadia subduction zone. Nature Geosci 10: 864–870

Eggins SM, Kinsley LPJ, Shelley JMG (1998) Deposition and element fractionation processes during atmospheric pressure laser sampling for analysis by ICP-MS. Applied Surface Science, 127, 278-286.

Faccenda M, Gerya TV, Burlini L (2009) Deep slab hydration induced by bending-related variations in tectonic pressure. Nature Geosci 2: 790–793

Gale A, Dalton CA, Langmuir CH, Su Y, Schilling JG (2013) The mean composition of ocean ridge basalts. Geochem Geophys Geosyst 14: 489–518

Gill J (1981) Orogenic Andesites and Plate Tectonics. Springer, Berlin.

Gray AL (1985) Solid sample introduction by laser ablation for inductively coupled plasma source mass spectrometry. Analyst, 110(5), 551-556.

Green TH, Ringwood TE (1968) Genesis of the calc-alkaline igneous rock suite. Contrib Mineral Petrol 18: 105–162

Guillong M, Günther D (2002) Effect of particle size distribution on ICP-induced elemental fractionation in laser ablation-inductively coupled plasma-mass spectrometry. Journal of Analytical Atomic Spectrometry, 17(8), 831-837.

Guillong M, Heinrich CA (2007) Sensitivity enhancement in laser ablation ICP-MS using small amounts of hydrogen in the carrier gas. Journal of Analytical Atomic Spectrometry, 22(12), 1488-1494.

Günther D, Audétat A, Frischknecht R, Heinrich CA (1998) Quantitative analysis of major, minor and trace elements in fluid inclusions using laser ablation–inductively coupled plasmamass spectrometry. J. Anal. At. Spectrom. 13, 263-270.

Günther D, Hattendorf B, Audétat A (2001) Multi-element analysis of melt and fluid inclusions with improved detection capabilities for Ca and Fe using laser ablation with a dynamic reaction cell ICP-MSPresented at the 2001 European Winter Conference on Plasma Spectrochemistry, Lillehammer, Norway, February 4–8, 2001. Journal of Analytical Atomic Spectrometry, 16(9), 1085-1090.

Günther D, Hattendorf B (2005) Solid sample analysis using laser ablation inductively coupled plasma mass spectrometry. TrAC Trends in Analytical Chemistry, 24(3), 255-265.

Hacker BR (2008) H_2O subduction beyond arcs. Geochemistry, Geophysics, Geosystems 9: Q03001

Hawkesworth C, Cawood PA, Dhuime B (2019) Rates of generation and growth of the continental crust. Geoscience Frontiers 10: 165-173

Hermann J, Spandler C, Hack A, Korsakov AV (2006) Aqueous fluids and hydrous melts in high-pressure and ultra-high pressure rocks: implications for element transfer in subduction zones. Lithos 92: 399–417

Hermann J, Rubatto D (2009) Accessory phase control on the trace element signature of sediment melts in subduction zones. Chem Geol 265: 512-526

Hildreth W, Moorbath S (1988) Crustal contribution to arc magmatism in the Andes of Central Chile. Contr Mineral Petrol 98: 455-489

Hirose K, Kushiro I (1993) Partial melting of dry peridotites at high pressures: determination of compositions of melts segregated from peridotite using aggregates of diamond. Earth and Planetary Science Letters, 114(4), 477-489.

Höink T, Jellinek AM, Lenardic A (2011) Viscous coupling at the lithosphere asthenosphere boundary. Geochem Geophys Geosystems 12: Article Number: Q0AK02

Holder RM, Viete DR, Brown M, Johnson TE (2019) Metamorphism and the evolution of plate tectonics. Nature 572: 378–381

Huppertz H (2004) Multianvil high-pressure/high-temperature synthesis in solid state chemistry. Zeitschrift für Kristallographie-Crystalline Materials, 219(6), 330-338.

Jochum KP, Weis U, Stoll B, Kuzmin D, Yang QC, Raczek I, Jacob DE, Stracke A, Birbaum K, Frick DA, Gunther D, Enzweiler J (2011) Determination of reference values for NIST SRM 610-617 glasses following ISO guidelines. Geostandards and Geoanalytical Research, 35, 397-429.

John T, Gussone N, Podladchikov YY, Bebout GE, Dohmen R, Halama R, Klemd R, Magna T, Seitz HM (2012) Volcanic arcs fed by rapid pulsed fluid flow through subducting slabs. Nature Geosci 5: 489–492

Johnson, K. T., & Kushiro, I. (1992). Segregation of high pressure partial melts from peridotite using aggregates of diamond: a new experimental approach. Geophysical Research Letters, 19(16), 1703-1706.

Johnson MC, Plank T (1999) Dehydration and melting experiments constrain the fate of subducted sediments. Geochemistry, Geophysics, Geosystems 1: Article Number: 1007

Johnson TE, Brown M, Gardiner NJ, Kirkland CL, Smithies RH (2017) Earth's first stable continents did not form by subduction. Nature 543: 239–242

Karlsen KS, Conrad CP, Magni V (2019) Deep water cycling and sea level change since the breakup of Pangea. Geochem, Geophys, Geosystems 20: 2919–2935

Kawai N, Endo S (1970) The generation of ultrahigh hydrostatic pressures by a split sphere apparatus. Review of Scientific Instruments, 41(8), 1178-1181.

Kawamoto T, Holloway JR (1997) Melting temperature and partial melt chemistry of H_2O-saturated mantle peridotite to 11 gigapascals. Science 276: 240-243

Kelemen PB, Hanghøj K, Greene AR (2005) One view of the geochemistry of subduction-related magmatic arcs, with an emphasis on primitive andesite and lower crust. In R.L. Rudnick, Ed., Treatise of Geochemistry, vol. 3, The Crust: 593-659 (Elsevier, Amsterdam).

Kelley KA, Cottrell E (2009) Water and the oxidation state of subduction zone magmas. Science 325: 605–607.

Keppler H, Frost DJ, (2005) Introduction to minerals under extreme conditions. In: Miletich, R. (Ed.), Mineral Behaviour at Extreme Conditions. In: European Mineralogical Union Lecture Notes in Mineralogy, vol. 7, pp. 1–30.

Keppler H (2017) Fluids and trace element transport in subduction zones. American Mineralogist, 102, 5–20.

Kessel R, Ulmer P, Pettke T, Schmidt MW, Thompson AB (2004) A novel approach to determine high-pressure high-temperature fluid and melt compositions using diamond-trap experiments. American Mineralogist, 89, 1078-1086.

Kessel R, Schmidt MW, Ulmer P, Pettke T (2005) Trace element signature of subduction-zone fluids, melts and supercritical liquids at 120–180 km depth. Nature 437: 724–727

Kushiro I., Hirose K. (1992) Experimental determination of composition of melt formed by equilibrium partial melting of peridotite at high pressures using aggregates of diamond grains. Proceedings of the Japan Academy, Series B, 68(5), 63-68.

Mallik A, Li Y, Wiedenbeck M (2018) Nitrogen evolution within the Earth's atmosphere–mantle system assessed by recycling in subduction zones. Earth Planet Sci Lett 482: 556–566

Manning CE (1994) The solubility of quartz in H2O in the lower crust and upper mantle. Geochim Cosmochim Acta 58: 4831–4839

Manning, CE., Wilke, M., Schmidt, C., Cauzid, J. (2008). Rutile solubility in albite-H_2O and $Na_2Si_3O_7$-H_2O at high temperatures and pressures by in-situ synchrotron radiation micro-XRF. Earth and Planetary Science Letters, 272(3-4), 730-737.

Martin (1999) Adakitic magmas: modern analogues of Archaean granitoids. Lithos 46: 411–429

Mason PR, Kraan WJ (2002) Attenuation of spectral interferences during laser ablation inductively coupled plasma mass spectrometry (LA-ICP-MS) using an rf only collision and reaction cell. Journal of Analytical Atomic Spectrometry, 17(8), 858-867.

Maunder B, van Hunen J, Bouilhol P, Magni V (2019). Modeling slab temperature: A reevaluation of the thermal parameter. Geochem, Geophys, Geosystems 20: 673–687

McCormick MP, Thomason LW, Trepte CR (1995) Atmospheric effects of the Mt Pinatubo eruption. Nature 373: 399–404

Métrich N, Wallace PJ (2008) Volatile abundances in basaltic magmas and their degassing paths tracked by melt inclusions. Rev Mineral Geochem 69: 363–402

Moyen JF, van Hunen J (2012) Short term episodicity of Archean plate tectonics. Geology 40: 451-454

Newton RC, Manning CE (2002) Solubility of enstatite + forsterite in H_2O at deep crust/upper mantle conditions: 4 to 15 kbar and 700 to 900°C. Geochim Cosmochim Acta 66: 4165–4176

Niggli P (1920) Die leichtflüchtigen Bestandteile im Magma. Teubner, Leipzig.

Peacock SM (1990) Fluid processes in subduction zones. Science 248: 329–337.

Plank T, Langmuir CH (1988) The chemical composition of subducting sediment and its consequences for the crust and mantle. Chem Geol 145: 325–394

Plank T, Manning CE (2019) Subducting carbon. Nature 574: 343-352

Plümper O, John T, Podladchikov YY, Vrijmoed JC, Scambelluri M (2017) Fluid escape from subduction zones controlled by channel-forming reactive porosity. Nature Geosci 10: 150-156

Rapp RP, Shimizu N, Norman MD (2003) Growth of early continental crust by partial melting of eclogite. Nature 425: 605-609

Rüpke LH, Phipps Morgan J, Hort M, Connolly JAD (2004) Serpentine and the subduction zone water cycle. Earth Planet Sci Lett 223: 17–34

Salters VJM, Stracke A (2004), Composition of the depleted mantle. Geochem Geophys Geosyst 5: Article Number 5

Salters VJM, Longhi JE, Bizimis M (2002) Near mantle solidus trace element partitioning at pressures up to 3.4 GPa. Geochem Geophys, Geosyst 3: Article Number 7

Scandone R, Malone SD (1985) Magma supply, magma discharge and readjustment of the feeding system of mount St. Helens during 1980. J Volcanol Geothermal Res 23: 239-262

Schmidt MW, Poli S (1998) Experimentally based water budgets for dehydrating slabs and consequences for arc magma generation. Earth Planet Sci Lett 163: 361–379

Schmidt MW, Vielzeuf D, Auzanneau E (2004) Melting and dissolution of subducting crust at high pressures: the key role of white mica. Earth Planet Sci Lett 228: 65–84

Seo JH, Guillong M, Aerts M, Zajacz Z, Heinrich CA (2011) Microanalysis of S, Cl, and Br in fluid inclusions by LA-ICP-MS. Chemical Geology, 284, 35-44.

Shen AH, Keppler H (1997) Direct observation of complete miscibility in the albite–H_2O system. Nature 385: 710-712

Skora S, Blundy J (2010) High-pressure hydrous phase relations of radiolarian clay and implications for the involvement of subducted sediment in arc magmatism. J Petrol 51: 2211–2243

Skora S, Blundy J D, Brooker R A, Green ECR, de Hoog JCM, Connolly JAD (2015) Hydrous phase relations and trace element partitioning behaviour in calcareous sediments at subduction-zone conditions. J Petrol 56: 953–980

Spandler, C., Mavrogenes, J., & Hermann, J. (2007). Experimental constraints on element mobility from subducted sediments using high-P synthetic fluid/melt inclusions. Chemical Geology, 239(3-4), 228-249.

Spandler C, Pirard C (2013) Element recycling from subducting slabs to arc crust: A review. Lithos 170-171: 208–223

Stalder, R., Foley, S. F., Brey, G. P., Forsythe, L. M., & Horn, I. (1997). First results from a new experimental technique to determine fluid/solid trace element partition coefficients using diamond aggregate extraction traps. Neues Jahrbuch fur Mineralogie, Abhandlungen, 172(1), 117-132.

Stalder R, Foley SF, Brey GP, Horn I (1998) Mineral aqueous fluid partitioning of trace elements at 900–1200 °C and 3.0–5.7 GPa: New experimental data for garnet, clinopyroxene, and rutile, and implications for mantle metasomatism. Geochim Cosmochim Acta 62: 1781–1801

Syracuse EM, van Keken, PE, Abers GA (2010) The global range of subduction zone thermal models. Phys Earth Planet Interiors 183: 73–90

Tatsumi Y (1989) Migration of fluid phases and genesis of basalt magmas in subduction zones. J Geophys Res 94: 4697–4707

Tropper P, Manning CE (2007) The solubility of corundum in H_2O at high pressure and temperature and its implications for Al mobility in the deep crust and upper mantle. Chem Geol 240: 54–60

Tsay, A., Zajacz, Z., and Sanchez-Valle, C. (2014) Efficient mobilization and fractionation of rare-earth elements by aqueous fluids upon slab dehydration. Earth and Planetary Science Letters, 398, 101–112.

Tsay, A., Zajacz, Z., Ulmer, P., Waelle, M., & Sanchez-Valle, C. (2016) A new experimental approach to study fluid–rock equilibria at the slab-mantle interface based on the synthetic fluid inclusion technique. American Mineralogist, 101(10), 2199-2209.

Tsay, A., Zajacz, Z., Ulmer, P., & Sanchez-Valle, C. (2017) Mobility of major and trace elements in the eclogite-fluid system and element fluxes upon slab dehydration. Geochimica et Cosmochimica Acta, 198, 70-91.

van der Hilst RD, Widiyantoro S, Engdahl ER (1997) Evidence for deep mantle circulation from global tomography. Nature 386: 578-584

von Huene R, Scholl DW (1991) Observations at convergent margins concerning sediment subduction, subduction erosion, and the growth of continental-crust. Rev Geophys 29: 279-316

Walker D, Carpenter MA, Hitch CM (1990) Some simplifications to multianvil devices for high pressure experiments. American Mineralogist, 75(9-10), 1020-1028.

Wegener A (1920) Die Entstehung der Kontinente und Ozeane. Vieweg, Braunschweig.

Wilke M, Schmidt C, Dubrail J, Appel K, Borchert M, Kvashnina K, Manning CE (2012) Zircon solubility and zirconium complexation in $H_2O + Na_2O + SiO_2 \pm Al_2O_3$ fluids at high pressure and temperature. Earth and Planetary Science Letters, 349, 15-25.

Zack T, John T (2007) An evaluation of reactive fluid flow and trace element mobility in subducting slabs. Chemical Geol 239: 199–216

Zajacz, Z., Seo, J. H., Candela, P. A., Piccoli, P. M., Heinrich, C. A., & Guillong, M. (2010) Alkali metals control the release of gold from volatile-rich magmas. Earth and Planetary Science Letters, 297(1-2), 50-56.

Zheng YF, Chen YX (2016) Continental versus oceanic subduction zones. National Science Review 3: 495–519

5. List of manuscripts and individual contributions

a) Rustioni G, Audetat A, Keppler H (2019) Experimental evidence for fluid-induced melting in subduction zones. Geochemical Perspectives Letters 11:49-54

GR carried out all high-pressure experiments and analyzed them by laser-ablation ICP-MS with the help of AA. All authors discussed the results together. GR prepared all figures and tables for the publication. HK wrote a first draft of the text, with further refinement by GR and AA.

b) Rustioni G, Audetat A, Keppler H (2021) A systematic assessment of the diamond trap method for measuring fluid compositions in high-pressure experiments. American Mineralogist: Journal of Earth and Planetary Materials, 2021, 106.1: 28-37.

GR carried out all high-pressure experiments and analyzed them by laser-ablation ICP-MS with the help of AA. All authors discussed the results together. GR prepared all figures and tables for the publication. GR and HK wrote a first draft of the text, with further refinement by AA.

c) Rustioni G, Audetat A, Keppler H (2021) The composition of subduction zone fluids and the origin of the trace element enrichment in arc magmas. Manuscript submitted to Contributions to Mineralogy and Petrology

GR carried out all high-pressure experiments and analyzed them by laser-ablation ICP-MS with the help of AA. All authors discussed the results together. GR and HK prepared figures and tables for the publication and wrote a first draft of the text, with further refinement by AA.

6. Experimental evidence for fluid-induced melting in subduction zones

Greta Rustioni, Andreas Audétat, Hans Keppler

Bayerisches Geoinstitut, Universität Bayreuth, D-95440 Bayreuth, Germany

6.1. Abstract

Although subduction zones are the main source of seismic and volcanic hazards on Earth, the causes of melting in volcanic arcs are still not fully understood. Recent models suggested that melting in the mantle wedge is not caused by hydrous fluids, but by sediment melts ascending from the subducted slab. A main argument for these models was that hydrous fluids are "too dilute" to produce the trace element enrichment observed in arc magmas. Here we demonstrate experimentally that even moderate salinities enhance the partitioning of trace elements such as the light rare earths, alkalis, alkaline earths, Pb, and U into the fluid by several orders of magnitude. Our data therefore show that saline hydrous fluids released from the basaltic part of the oceanic crust may produce the enrichment in LILE and light REE elements, and the negative Nb-Ta anomaly observed in typical arc magmas.

6.2. Introduction

In subduction zones, oceanic crust is recycled into the mantle. Thermal models show that the temperature of the mantle wedge above the subducting slab is actually considerably lower than in other parts of the shallow upper mantle (Syracuse et al., 2010). Melting must therefore be caused by other effects, most likely by the addition of water, which may reduce the melting

61

temperatures of mantle peridotite by several 100 ˚C (Kawamoto and Holloway, 1997; Gaetani and Grove, 1998). Water may be transferred from the subducted oceanic slab to the mantle wedge in the form of aqueous fluids, released by the dehydration of hydrous minerals, or by sediment melts. Already early studies (Perfit et al., 1980; Arculus and Powell, 1986) noted that the trace element enrichment pattern in magmas from volcanic arcs above a subduction zone is distinctly different from that observed in magmas at divergent plate boundaries, e.g., mid-ocean ridges. Typical features of arc magmas include high enrichments of large ion lithophile elements (LILE, such as Rb^+, Cs^+, Sr^{2+}, Ba^{2+}) and light rare earth elements (REE, such as La^{3+} and Ce^{3+}), but strong depletions of high field strength elements (HFSE, such as Ti^{4+}, Nb^{5+} and Ta^{5+}). Some experimental studies (Kessel et al., 2005; Hermann et al., 2006) suggested that trace element transport by aqueous fluids is unable to produce the observed trace element enrichment pattern in arc magmas. This led to the suggestion that sediment melts are the main agents of metasomatism in the mantle wedge above subduction zones (Kelemen et al., 2005; Hermann et al., 2006; Skora and Blundy, 2010; Behn et al., 2011; Spandler and Pirard, 2013). Previous studies, however, did not consider the effect of chloride, which may affect the partition behaviour of various trace elements by the formation of chloride complexes in the fluid. As the subducted oceanic crust was in contact with seawater, it is expected to contain chloride and measurements of the Cl/H_2O ratio of primitive arc magmas (Métrich and Wallace, 2008), as well as other lines of evidence (Kawamoto et al., 2013), are consistent with the incorporation of aqueous fluids (Manning, 2004) containing up to 15 wt. % NaCl. In the present study, we therefore for the first time directly measured the effect of chlorine on the partitioning of trace elements between aqueous fluids and the minerals of the subducted basaltic crust at conditions corresponding to the typical depth of the slab below the volcanic front.

6.3. Methods

Experiments were carried out in an end-loaded piston cylinder apparatus (Boyd and England, 1960) at 4 GPa and 800 ˚C with run durations between 2 and 7 days. Synthetic MORB (mid-ocean ridge basalt) glass doped with a suite of trace elements was loaded together with water or NaCl solutions into platinum capsules. A layer of diamond powder was inserted in the middle of the capsule between the layers of MORB powder to provide some empty pore space

between the diamond grains for trapping the fluid (Ryabchikov et al., 1989). After quenching of the experiments, the sample capsules were cooled to liquid nitrogen temperature and cut in half. Both the compositions of the minerals and of the quenched fluid trapped between the diamond grains were then measured in frozen state (Kessel et al., 2005) by laser ablation ICP-MS. Additional details about the experimental and analytical methods are given in the Supplementary Information.
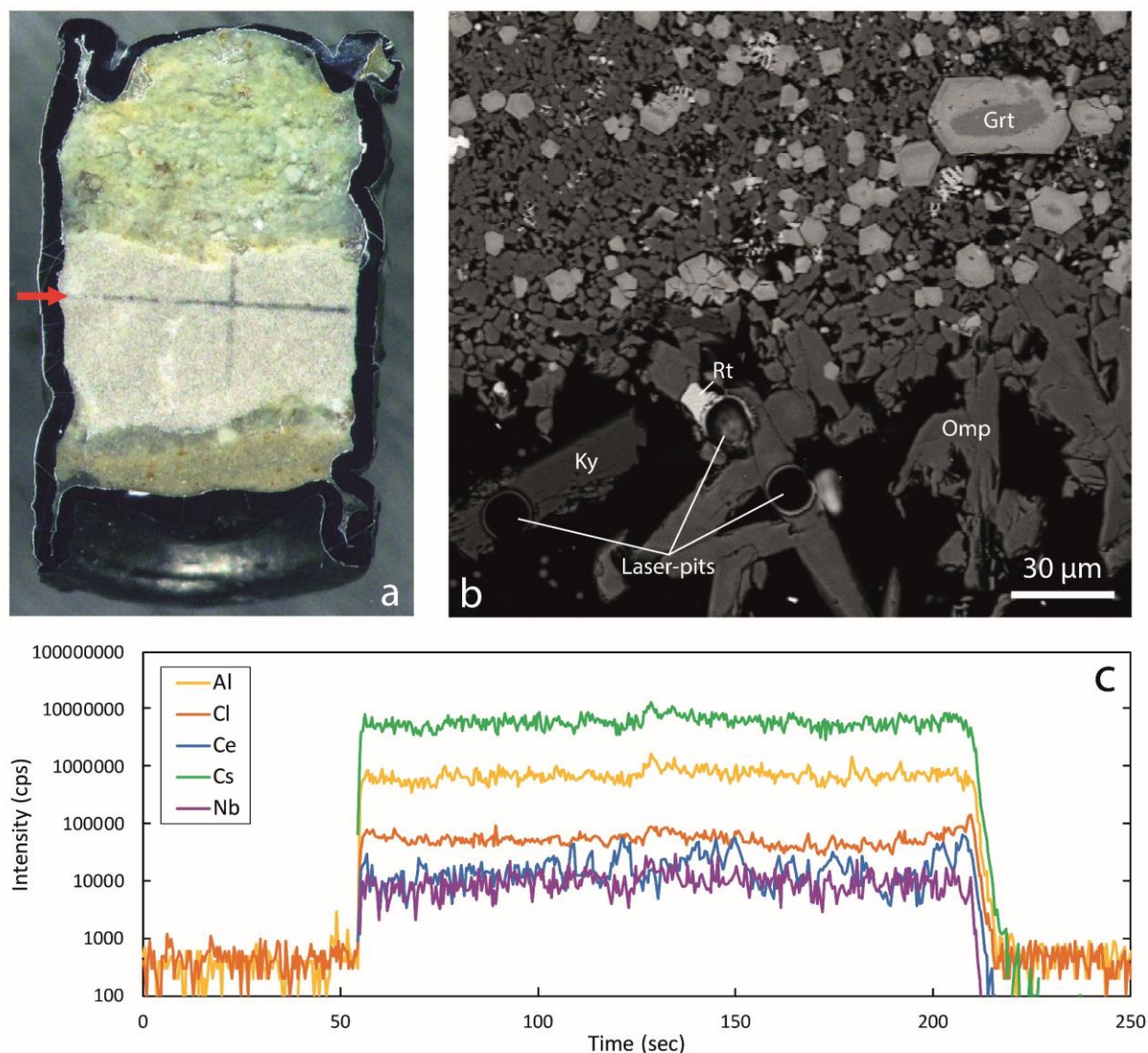
Figure 6.1. *Run products from high pressure experiments. (**a**) Cross section of a sample capsule after an experiment (image width 5 mm). A white layer of diamond powder is sandwiched between the silicate sample. The red arrow points to a laser ablation trace. (**b**) Backscatter electron image of the silicate part of a sample, consisting mostly of omphacite (Omp) and garnet (Grt) with minor kyanite (Ky) and rutile (Rt). In the centre of some garnet crystals, remnants of the garnet seeds are visible. (**c**) Laser ablation analysis of frozen fluid in the diamond trap, demonstrating the homogeneity of the sample.*

6.4. Results and discussion

During the high pressure experiments, the glasses recrystallized to an eclogitic assemblage of omphacite, garnet, rutile, and kyanite, i.e. the same minerals that are expected to be stable in the subducted basaltic oceanic crust below the volcanic arc (Figure 6.1). Other accessory phases likely do not occur in natural MORB at eclogite facies conditions. The solubility of phosphorus in garnet is so high that apatite and other phosphates are unlikely to form (Konzett and Frost, 2009). Due to the very low K_2O content in natural MORB, eclogites of MORB composition either contain no phengite at all or at most traces of this mineral (e.g., Okrusch et al., 1991; see also the Supplementary Information for further discussion). Indeed, in sub-solidus experiments with natural MORB at 3 GPa and 800 ˚C, Carter et al. (2015) did not observe any phengite or apatite.

Mineral compositions in our experiments were found to be uniform in the entire sample, consistent with attainment of equilibrium throughout the entire charge. With a few exceptions, as discussed below, laser ablation ICP-MS analyses of trace element concentrations yielded homogeneous compositions of both the quenched fluid phase and the minerals (see Figure 6.1 for typical laser ablation signals). Fluid/mineral partition coefficients $D^{fluid/mineral} = c^{fluid}/c^{mineral}$ were calculated from the measured trace element concentrations in fluid (c^{fluid}) and coexisting minerals ($c^{mineral}$). Bulk fluid/eclogite partition coefficients were then calculated from the individual fluid/mineral partition coefficients assuming an eclogitic mineralogy with 59 % omphacite, 39 % garnet and 2 % rutile. Experimental details, compositions of all phases and calculated bulk fluid eclogite partition coefficients are compiled in Tables 6.1 to 6.8 of the Supplementary Information.

A major problem in all studies of element partitioning between minerals and fluid is attainment of equilibrium, since the diffusion coefficients of most of the relevant trace elements in the minerals are very low. In order to circumvent this problem, we introduced periodic temperature fluctuations by ± 30 ˚C in our experiments, which enhanced grain growth and equilibration by Ostwald ripening (i.e. the dissolution of smaller grains at higher temperature and the growth of larger grains upon cooling). Indeed, the resulting grain sizes observed after runs with these sinusoidal temperature fluctuations were generally much larger than for experiments at constant temperature, but mineral compositions were not affected. In order to demonstrate

conclusively the attainment of equilibrium, we also performed some reversed experiments, starting with a trace element-free MORB glass and trace element-doped solutions. In general, both the normal "forward" experiments starting with trace element-doped MORB glass and the reversed experiments gave very consistent results. We are therefore confident that the trace element partition coefficients reported here represent true chemical equilibrium between aqueous fluid and minerals. Moreover, results from experiments with different concentration levels of trace elements yielded consistent partition coefficients, implying that Henry´s law is fulfilled.
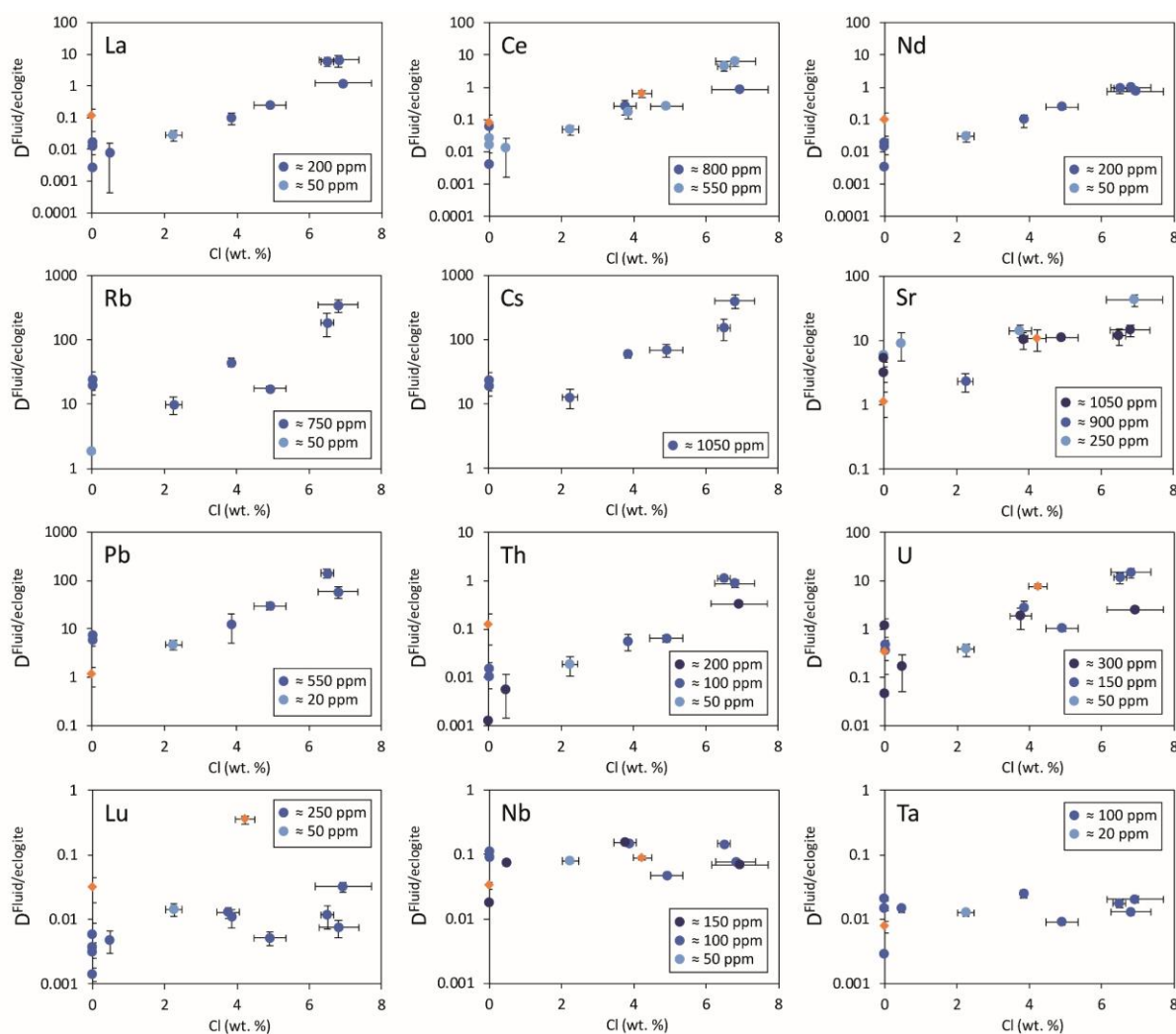
Figure 6.2. *Effect of chloride on fluid/eclogite partition coefficients of trace elements at 4 GPa and 800 ˚C. Blue data points are the results from "forward" experiments, where the trace elements were initially doped into the solid starting material, while orange data points are from "reversed" experiments, which started with all trace elements dissolved in the fluid. For the forward experiments, results for different initial trace element concentrations in the starting material are given. Error bars are one standard deviation. Data for these and additional elements are given in Tables 6.1 to 6.8.*

Figure 6.2 shows the fluid/eclogite partition coefficients for some selected trace elements as a function of the chloride content in the fluid. For the light rare earths, such as La and Ce, there is a striking increase of $D^{fluid/eclogite}$ by up to three orders of magnitude even for moderate salinities (up to 15 wt. % NaCl). Similar, although smaller effects are seen for the alkalis (e.g., Rb and Cs) and the alkaline earths (Sr). Pb, Th, and U also show striking increases with salinity. On the other hand, both the typical high field strength elements, such as Nb and Ta as well as the heavy rare earth (e.g., Lu) appear to be unaffected by chloride.
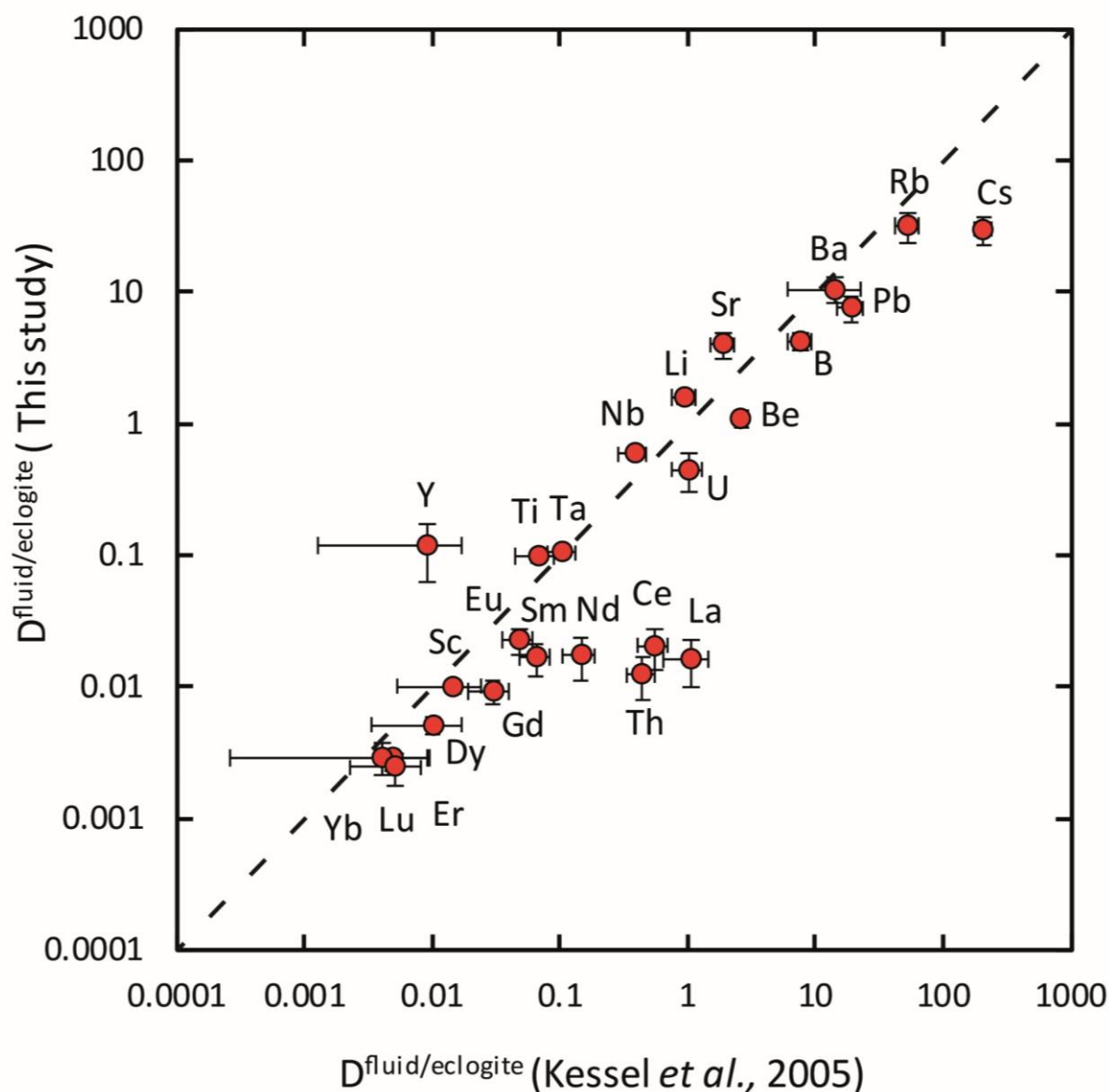
Figure 6.3 *Comparison of the fluid/eclogite partition coefficients for Cl-free fluids measured in this study with those reported by Kessel et al. (2005). Both sets of experiments were carried out at 4 GPa and 800 ˚C, with a bulk composition resembling MORB.*

Our data for Cl-free aqueous fluids are generally consistent with those from a previous study (Kessel et al., 2005), as shown in Figure 6.3. For saline fluids, there are no published data that could be directly compared with our results. However, both studies on mineral solubilities (Bali et al., 2011; Tropper et al., 2011; Tsay et al., 2014) and fluid/melt partitioning (Keppler, 1996; Kawamoto et al., 2014) at lower pressures suggest that those elements that are affected by fluid salinity indeed form stable chloride complexes in aqueous fluids. In particular, Tsay et al. (2014) noted an increase of the solubility of $La_2Si_2O_7$ and $Nd_2Si_2O_7$ in aqueous fluid by one order of magnitude upon addition of 1.5 M NaCl at 800 ˚C and 2.6 GPa. The formation of chloride complexes will tend to stabilise the trace element in the fluid and therefore increase the fluid/eclogite partition coefficient. Only the sensitivity of Th to chloride is unexpected, as it behaves differently from other HFSE trace elements, such as Nb and Ta. However, the ionic radius of Th^{4+} is significantly larger than that of Nb^{5+}, Ta^{5+}, or Ti^{4+}, such that its geochemical behaviour may be transitional between a typical high field strength and a large ion lithophile element. We also tried to measure the fluid/eclogite partitioning of Zr and Hf, two important HFSE trace elements, but here we encountered experimental problems. The distribution of these elements in the quenched fluid inside the diamond trap was always highly inhomogeneous, which precluded the reliable determination of fluid concentrations and partition coefficients. A possible reason could be the very low solubility (Bernini et al., 2013) of zircon $ZrSiO_4$ and hafnon $HfSiO_4$, which may have precipitated early during the experiment inside the diamond trap and may have failed to reach equilibrium.

Figure 6.4 shows the trace element enrichment pattern in the fluid phase from the fluid/eclogite partitioning experiments as a function of salinity. An important observation here is that a pure aqueous fluid would not be able to produce all of the trace element enrichment features observed in arc magmas. While such fluids may effectively transport some large ion lithophile elements, like Rb, Cs, Sr, and Ba (with fluid/eclogite partition coefficients > 1), the light rare earths as well as uranium would be retained in the eclogite. This used to be one of the main arguments why aqueous fluids were considered to be "too dilute" to produce the trace element enrichment observed in arc magmas and why alternative mechanisms, such as metasomatism by sediment melt were proposed. However, for elevated salinities the enrichment pattern in aqueous fluid has a striking similarity to that observed in arc magmas, with the light rare earths and U becoming mobile in the fluid together with the large ion lithophile elements, while at
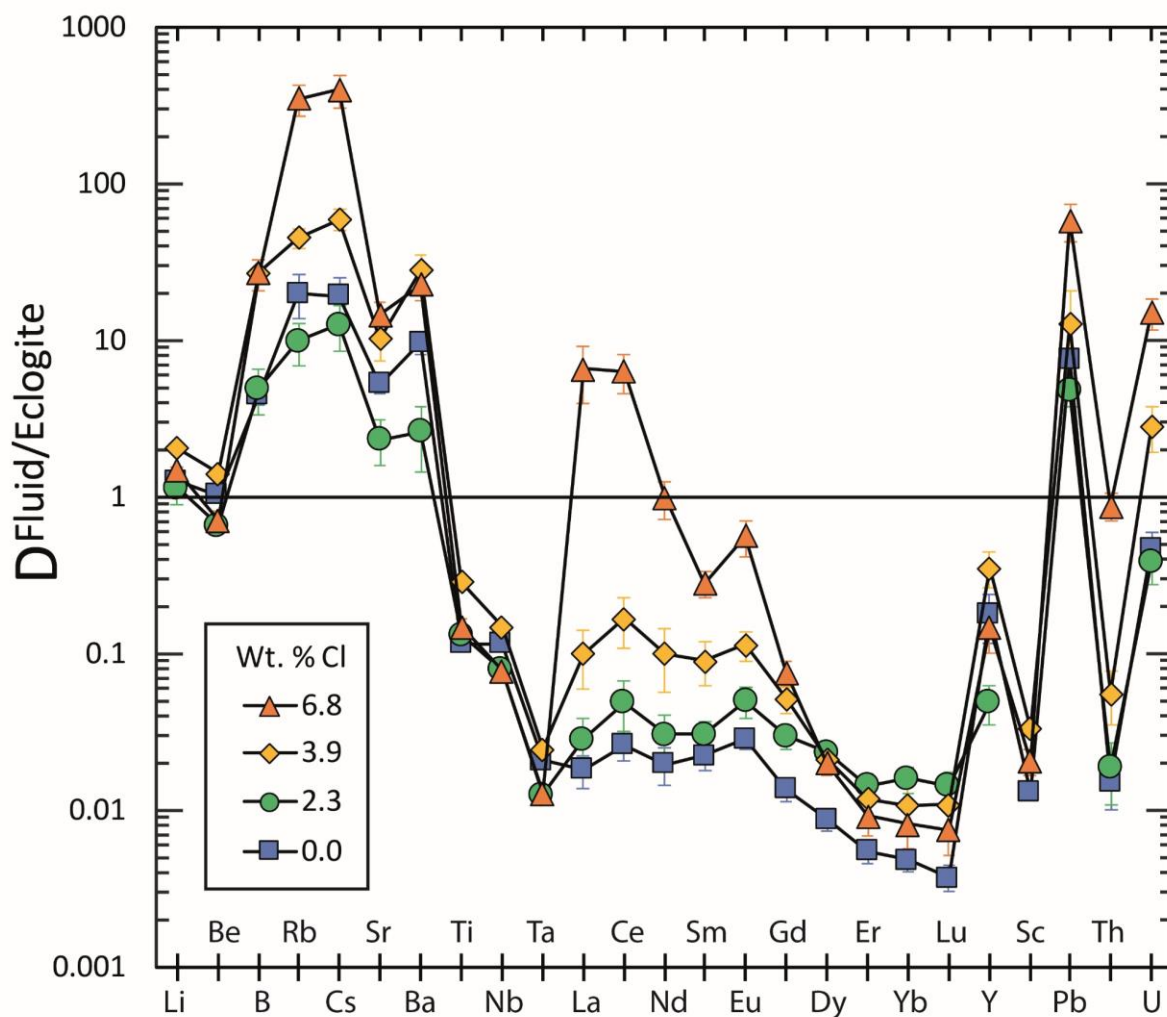
Figure 6.4. *Trace element enrichment patterns in fluids from fluid/eclogite partitioning experiments at 4 GPa and 800 ˚C. Error bars are one standard deviation. Data for these and additional elements are given in Tables 6.1 to 6.8.*

the same time, high field strength elements, such as Nb, Ta, and Ti are nearly completely retained in the eclogite. The high Ba/La, Ba/Nb, and U/Th ratios match well with those inferred from primitive arc basalts (see Supplementary Information for further discussion). In particular, the "negative Nb-Ta anomaly" i.e. the strong depletion of Nb and Ta relative to both light rare earths and large ion lithophile elements is a hallmark of subduction zone magmas. Saline fluids can fractionate these elements by three orders of magnitude, mainly through the effect of Cl on rare earth partitioning. In a chloride-free system, the fluid/eclogite partition coefficient of La and Ce could be increased to a similar value by a temperature increase of several 100 ˚C,

ultimately leading to melting (Kessel et al., 2005). However, in silicate melts, Nb and Ta would also become mobile and therefore, this effect cannot produce the negative Nb Ta anomaly observed in subduction zone magmas.

6.5. Conclusions

Our experimental data show that saline fluids released from the basaltic layer of the subducted slab can account for most features in the trace element enrichment pattern observed in subduction zone magmas. In the light of these experiments, the relative importance of aqueous fluids and sediment melts in the formation of arc magmas needs to be reconsidered. Strong evidence for the involvement of sedimentary material comes from isotopic data; already Armstrong (1971) noted a close correlation between the $^{206}Pb/^{204}Pb$ ratio of arc magmas and the sediments in front of some arcs and similar evidence has been presented for different isotope systems. However, these observations do not necessarily require the involvement of sediment melts. The isotopic signal observed may also have been transported by aqueous fluids; our data suggest that both Pb and Sr may be efficiently transported by saline fluids (Figure 6.4) and even Be and Nd may be significantly mobile under some conditions. High Th/La ratios in arc magmas may be inherited from sediments (Plank, 2005); however, it remains uncertain whether sediment melts could effectively transport these elements, as they are strongly retained in residual monazite and other phases and the fractionation of Th and La between melt and monazite may not always operate in the right direction (Skora and Blundy, 2010). On the other hand, experimental data suggest that mantle metasomatism by sediment melts produces distinctly potassic melts (Mallik et al., 2015) different from average subduction zone magmas. Thermal models of subduction zones (Syracuse et al., 2010) suggest temperatures below the arc that are lower than those required for dehydration melting (e.g., Mann and Schmidt, 2015). Higher temperatures have been inferred from Ce/H_2O ratios. However, the Ce/H_2O geothermometer (Plank et al., 2009) is based on the assumption that the Ce/H_2O ratio in fluids and melts is a function of temperature only. Our data (Figure 6.2) show that at the same temperature, this ratio may vary by three orders of magnitude as a function of salinity.

6.6. References

Arculus, R.J., Powell, R. (1986) Source component mixing in the regions of arc magma generation. Journal of Geophysical Research 91, 5913–5926.

Armstrong, R.L. (1971) Isotopic and chemical constraints on models of magma genesis in volcanic arcs. Earth and Planetary Science Letters 12, 37–142.

Bali, E., Audetat, A., Kepp ler, H. (2011) The mobility of U and Th in subduction zone fluids: an indicator of oxygen fugacity and fluid salinity. Contributions to Mineralogy and Petrology 161, 597–613.

Behn, M.D., Kelemen, P.B., Hirth, G., Hacker, B.R., Massonne, H.J. (2011) Diapirs as the source of the sediment signature in arc lavas. Nature Geoscience 4, 641–646.

Bernini, D., Audetat, A., Dolejs, D., Kepp ler, H. (2013) Zircon solubility in aqueous fluids at high temperatures and pressures. Geochimica et Cosmochimica Acta 119, 178–187.

Boyd, F.R., England, J.L. (1960) Apparatus for phase-equilibrium measurements at pressures up to 50 kilobars and temperatures up to 1750˚C. Journal of Geophysical Research 65, 741–748.

Carter, L.B., Skora, S., Blundy, J.D., De Hoog, J.C.M., Elliott, T. (2015) An experimental study of trace element fluxes from subducted oceanic crust. Journal of Petrology 56, 1585–1606.

Gaetani, G.A., Grove, T.L. (1998) The influence of water on melting of mantle peridotite. Contributions to Mineralogy and Petrology 131,323–346.

Hermann, J., Spa ndler, C., Hack, A., Korsak ov, A.V. (2006) Aqueous fluids and hydrous melts in high-pressure and ultra-high pressure rocks: Implications for element transfer in subduction zones. Lithos 92, 399–417.

Kawamoto, T., Holloway, P.R. (1997) Melting temperature and partial melt chemistry of H_2O-saturated mantle peridotite to 11 gigapascals. Science 276, 240–243.

Kawamoto, T., Yoshika wa, M., Kumagai, Y., Mirab ueno, M.H.T., Okuno, M., Koba yashi, T. (2013) Mantle wedge infiltrated with saline fluids from dehydration and decarbonation of subducting slab. Proceedings of the National Academy of Sciences of the USA 110, 9663–9668.

Kawamoto, T., Mibe, K., Bureau, H., Reguer, S., Mocuta, C., Kubsky, S., Thiaudiere, D., Ono, S., Kogiso, T. (2014) Large-ion lithophile elements delivered by saline fluids to the sub-arc mantle. Earth, Planets and Space 66, doi:10.1186/1880-5981-66-61.

Kelemen, P.B., Hanghøj, K., Greene, A.R. (2005) One view of the geochemistry of subduction-related magmatic arcs, with an emphasis on primitive andesite and lower crust. In: Rudnick, R.L. (Ed.) Treatise of Geochemistry, Volume 3, The Crust. Elsevier, Amsterdam, 593–659.

Keppler, H. (1996) Constraints from partitioning experiments on the composition of subduction-zone fluids. Nature 380, 237–240.

Kessel, R., Schmidt, M.W., Ulmer, P., Pettke, T. (2005) Trace element signature of subduction-zone fluids, melts and supercritical liquids at 120–180 km depth. Nature 437, 724–727.

Konzett, J., Frost, D.J. (2009) The high P-T stability of hydroxyl-apatite in natural and simplified MORB – an experimental study to 15 GPa with implications for transport and storage of phosphorus and halogens in subduction zones. Journal of Petrology 50, 2043–2062.

Mallik, A., Nelson, J., Dasgupta, R. (2015) Partial melting of fertile peridotite fluxed by hydrous rhyolitic melt at 2-3 GPa: implications for mantle wedge hybridization by sediment melt and generation of ultrapotassic magmas in convergent margins. Contributions to Mineralogy and Petrology 169, Article Number 48.

Mann, U., Schmidt, M.W. (2015) Melting of pelitic sediments at subarc depths: 1. Flux vs. fluid-absent melting and a parameterization of melt productivity. Chemical Geology 404, 150–167.

Manning, C.E. (2004) The chemistry of subduction zone fluids. Earth and Planetary Science Letters 223, 1–16.

Métrich, N., Wallace, P.J. (2008) Volatile abundances in basaltic magmas and their degassing paths tracked by melt inclusions. Reviews in Mineralogy and Geochemistry 69, 363–402.

Okrusch, M., Matthes, S., Klemd, R., O'Brien P.J., Schmidt, K. (1991) Eclogites at the north-western margin of the Bohemian Massif: A review. European Journal of Mineralogy 3, 707–730.

Perfit, M.R., Gust, D.A., Bence, A.E., Arculus, R.J., Taylor, S.R. (1980) Chemical characteristics of island-arc basalts - implications for mantle sources. Chemical Geology 30, 227–256.

Plank, T. (2005) Constraints from thorium/lanthanum on sediment recycling at subduction zones and the evolution of the continents. Journal of Petrology 46, 921–944.

Plank, T., Cooper, L.B., Manning, C.E. (2009) Emerging geothermometers for estimating slab surface temperatures. Nature Geoscience, 2, 611–615.

Ryab chikov, I.D., Orlova, G.P., Kalenchuk, G.Y., Ganeyev, I.I., Udovkina, N.G., Nosik, L.P. (1989) Reactions of spinel lherzolite with H2O-CO2 fluids at 20 kbar and 900 °C. Geochemistry International 26, 56–62.

Skora, S., Blundy, J. (2010) High-pressure hydrous phase relations of radiolarian clay and implications for the involvement of subducted sediment in arc magmatism. Journal of Petrology 51, 2211–2243.

Spandler, C., Pirard, C. (2013) Element recycling from subducting slabs to arc crust: A review. Lithos 170-171, 208–223.

Syracuse, E.M., Van Keken, P.E., Abers, G.A. (2010) The global range of subduction zone thermal models. Physics of the Earth and Planetary Interiors 183, 73–90.

Tropper, P., Manning, C.E., Harlov, D.E. (2011) Solubility of CePO4 monazite and YPO4 xenotime in H2O and H2O–NaCl at 800 °C and 1 GPa: Implications for REE and Y transport during high-grade metamorphism. Chemical Geology 282, 58–66.

Tsay, A., Zaja cz, Z., Sanchez-Valle, C. (2014) Efficient mobilization and fractionation of rare-earth elements by aqueous fluids upon slab dehydration. Earth and Planetary Science Letters 398, 101–112.

6.7.   Supplementary information

6.7.1. Starting materials and methods

6.7.1.1. Starting materials

Two glasses with K-free average MORB composition were synthesised at 1600 ˚C. The first one (MORB1) was prepared without trace elements and was used in the reversed experiments. For some forward experiments, part of MORB1 was mixed with 2 wt. % of a synthetic diopside glass (D1) which was doped with 25 trace elements in order to give the final bulk concentrations reported in Supplementary Table 6.2 (MORB1-2D1). A second basaltic glass (MORB2) with similar major element composition but directly doped with LILE was also synthesised. The remaining trace elements were added by mixing 2 wt. % of a second synthetic diopside glass (D2) to MORB2 (MORB2-2D2). In experiment PC23, a starting material prepared by mixing MORB2 with 0.4 wt. % of D1 (MORB2-DD1) was used. To each solid starting material, 1 wt. % of natural garnet seeds selected and crushed from Grytting (Norway) eclogite were added to enhance garnet growth during the experiments. Solutions with 1, 5, 10, or 15 wt. % salinity were prepared by adding pure NaCl to distilled water. For the trace element doped solutions used in the reversed experiments, equal amounts of a certified ICP standard solution for each individual trace element (1000 ppm of trace element in 5 % HNO_3) were mixed and evaporated under an infrared lamp. The solid residue was subsequently dissolved in a smaller amount of 5 % HNO_3 to obtain higher trace element concentrations and the resulting milky solution was left to rest for 1 month. After the deposition of the insoluble residue, the clear solution at the top was separated. The compositions from ICP-MS analyses of the two different doped solutions obtained with this procedure are given in Table 6.2 (SOL1 and SOL2).

6.7.1.2. Experiments

For each experiment, some of the solution was pipetted into a Pt or Au capsule (5 mm outer diameter, 10 mm long, 0.2 mm wall thickness), then a layer of MORB glass powder (~ 55 mg) was added, followed by a layer of diamond powder (with 10 – 20 μm grain diameter). The remaining fluid was added after the diamonds to avoid suspending the first layer of basaltic starting material, which could contaminate the diamond trap. At last, another layer of MORB glass was added. The resulting total fluid/glass weight ratio ranged from 0.30 to 0.45. The capsule was weighed before and after welding of the top lid to assure that no water loss occurred. Each capsule was also left overnight in an oven at 130 ˚C and weighed again to verify the sealing before the experiment. High pressure experiments were carried out at 4 GPa and 800 ˚C in an end-loaded piston cylinder apparatus using ½ inch MgO-NaCl assemblies with a stepped graphite furnace. Temperature was measured with a S-type (Pt/Pt-Rh) thermocouple and monitored by a Eurotherm controller. Long compression and decompression times (16-20 hours) were used to reduce capsule deformation. Temperature was raised at constant pressure after compression with a rate of 100 ˚C/min. In some experiments, a temperature fluctuation of ± 30 ˚C was applied after an initial equilibration at constant temperature for ~ 36 hours to nucleate the stable mineral assemblage. The temperature cycling was terminated ~24 hours before quenching to allow final equilibration. During temperature cycling, linear ramps in temperature (from 770 to 830 ˚C and back) lasted 2 hours each, with dwelling times at both temperatures of 2 hours; a single temperature cycle lasted in total 8 hours. The duration of the experiments at combined high pressure and high temperature was 2 – 7 days. Oxygen fugacity was not controlled, but probably was near the Ni-NiO buffer. The runs were quenched by shutting off the power at constant pressure before starting decompression.

6.7.1.3. Analytics

After the experiments, the retrieved capsules were immediately cooled in liquid nitrogen and then stored in a freezer at -18 °C until the day of the analysis. On that day, each capsule was taken out of the freezer, cooled further to -50 to -100 °C, and then cut longitudinally in half with a razor blade attached to an opening device. One half of the frozen capsule was then quickly transferred to a Laser-Ablation Inductively-Coupled-Plasma Mass-Spectrometry (LA-ICP-MS) sample chamber equipped with a Peltier-cooling element to keep the sample frozen

during the entire measurement. Tests with H2O-ethanol mixtures revealed that the temperature in this sample chamber was ca. -30 °C. Analysing the diamond trap in frozen state is necessary to avoid element fractionation during solution evaporation, which would introduce major uncertainties in the quantification procedure. The LA-ICP-MS measurements were performed with a 193 nm ArF GeolasPro laser ablation unit (Coherent, USA) connected to a Elan DRC-e quadrupole ICP-MS unit (Perkin Elmer, Canada). The sample chamber was flushed with He at a flow rate of 0.4 l/min, to which 5 ml/min H_2 was admixed on the way to the ICP-MS. Measured isotopes included ^{7}Li, ^{9}Be, ^{11}B, ^{23}Na, ^{25}Mg, ^{27}Al, ^{30}Si, ^{35}Cl, ^{43}Ca, ^{45}Sc, ^{49}Ti, ^{57}Fe, ^{85}Rb, ^{88}Sr, ^{89}Y, ^{90}Zr, ^{93}Nb, ^{133}Cs, ^{137}Ba, ^{139}La, ^{140}Ce, ^{146}Nd, ^{147}Sm, ^{153}Eu, ^{157}Gd, ^{163}Dy, ^{167}Er, ^{172}Yb, ^{175}Lu, ^{178}Hf, ^{181}Ta, ^{208}Pb, ^{232}Th, and ^{238}U, using a dwell time of 10 ms. The ICP-MS was tuned to a thorium oxide production rate of 0.05 – 0.10 % and a rate of doubly charged Ca ions of 0.15 – 0.25 % based on measurements on NIST SRM 610 glass (Jochum et al., 2011). The diamond trap layer was analysed by moving the laser beam at constant velocity along two perpendicular transects (parallel and perpendicular to the diamond layer, see Figure 6.1 a) using a laser spot size of 50-70 μm and a repetition rate of 7 Hz. The signals resulting from each transect (Figure 6.1 c) were divided into 3 – 4 separate integration intervals, for which element concentrations were calculated. The NIST SRM 610 glass and a well-characterised, natural afghanite crystal (Seo et al., 2011) were used as external standards. Chlorine (or Cs in experiments conducted with pure water) was used as internal standard, because these elements are expected to partition strongly into the fluid in the K-free eclogite-water system at the experimental conditions. Indeed, chlorine was never detected in any of the crystalline phases. Chlorine contents in the fluid phase were corrected for the dilution effect by dissolved solutes (mostly SiO_2), as determined from the diamond trap analyses. After analysis of the diamond trap, the capsules were left to evaporate at room temperature and subsequently were impregnated with epoxy resin and were polished to expose minerals for LA-ICP-MS measurements. The largest suitable spot sizes to analyse single crystals and the rims in zoned garnets were chosen, usually in the range of 7 – 20 μm. Averages obtained from measurements of 4 to 7 separate crystals within the capsule were used to calculate the compositions of garnet (Supplementary Table 6.5), omphacite (Table 6.6) and rutile (Table 6.7). Special care was taken in the garnet measurements to only analyse inclusion-free rim portions and to avoid the natural garnet seeds, which showed distinctively different composition. To calculate bulk fluid/eclogite partition coefficients, first the fluid/mineral partition coefficients for each

mineral were calculated, and then the results normalised to a representative eclogitic composition of 59 % omphacite, 39 % garnet and 2 % rutile.

Major element compositions of minerals were also measured by electron microprobe. A JEOL JXA 8200 instrument was used with a focused beam, an acceleration voltage of 15kV, a beam current 15nA and counting times of 10 sec on the background and 20 sec on the peak. The following standards were used: Diopside for Si, Mg, Ca; $MnTiO_3$ for Ti; Fe_2O_3 for Fe, albite for Na; corundum for Al.

6.7.2. Supplementary discussion

6.7.2.1. Phase Assemblage in Experiments and in Natural MORB Eclogites

The starting material used in the experiments was designed to be very similar to that of the study of Kessel et al. (2005) in order to facilitate the comparison of the Cl-free experiments. In particular, as in the study of Kessel et al. (2005), the simplified MORB composition used did not contain any phosphorus or potassium. This is well justified, since both P (0.184 wt. % P_2O_5) and K (0.160 wt. % K_2O) concentrations in natural MORB are very low (Gale et al., 2013). Natural eclogites occasionally contain apatite and phengite, which could be important hosts for certain trace elements (REE in apatite, alkalis and Ba in phengite). However, we argue here that due to the low P and K contents of MORB, these phases will either not occur at all or only occur in insignificant traces in eclogites of MORB composition.

Konzett and Frost (2009) measured the solubility of phosphorus in garnet of MORB eclogite. They observed a solubility of P_2O_5 in the garnet phase of about 0.3 wt. % at 4 GPa. They therefore concluded that virtually all P in a MORB eclogite will be contained in garnet. If apatite is observed in MORB eclogites, it is often a secondary alteration product, e.g., formed by low-temperature exsolution from garnet. This effect was already observed by Fung and Haggerty (1995); see also Keller and Ague (2019). Moreover, we note that in the presence of NaCl, apatite becomes quite soluble in aqueous fluids (Mair et al., 2017), such that traces of apatite would readily be dissolved during dehydration of the basaltic crust.

The low average K_2O content of 0.16 wt. % limits the amount of phengite that may form in an eclogite of MORB composition. Therefore, typical MORB eclogites either contain no

(primary) phengite at all or at most traces of this mineral. In the classical eclogite occurrences of the Bohemian Massif in central Europe, Okrusch et al. (1991) distinguished three lithological types, two of which do not contain any phengite. Similar, phengite-free eclogites of MORB composition were also described by Heinrich (1982), Tubia and Ibarguchi (1991), and Imayama et al. (2017). Eclogites from the North Dulan Belt in China, which formed from N-type and E-type MORB may or may not contain phengite; however, in every case the modal abundance is less than 1 % (Song et al., 2003). Very likely, the occurrence of phengite is limited to the more K-enriched E-MORB types. Finally, we note that during interaction with an aqueous fluid, K will partition into the fluid, which should destabilise any traces of phengite.

6.7.2.2. Silica Content of Starting Materials

The silica content of the solid starting material (54 – 55 wt. %, Table 6.2) is higher than in average MORB (50.47 wt. %, Gale et al., 2013). This, however, compensates for the effect that in our experiments, the fluid/solid ratio is 0.3 – 0.5 and therefore much higher than in nature. These high fluid/solid ratios are necessary in order to be able to trap sufficient fluid in the diamond layer for analysis. Silica preferentially partitions into the fluid and is the most abundant solute in the aqueous phase (e.g., Kessel et al., 2005). This has the effect of shifting the composition of the solid residue back to that of MORB. Indeed, our experiments produce a typical eclogite phase assemblage (Figure 6.1, main text) without any excess quartz or coesite.

6.7.2.3. Comparison of Trace Element Ratios in Primitive Arc Basalts With Those Observed in Experiments

Certain trace element ratios are considered to be particularly characteristic for subduction zone magmas; this includes in particular high Ba/Nb (e.g., Pearce et al., 2005), Ba/La (e.g., Rüpke et al., 2002), and U/Th ratios (e.g., Bali et al., 2011). Here, we compare these ratios in natural, primitive arc basalts with those predicted by our experimental data. Average primitive arc basalt compositions for 14 different subduction zones were taken from the compilation in Kelemen and Hanghøj (2005). Fluid compositions released from the basaltic oceanic crust were obtained by assuming average MORB composition for the crust (Gale et al., 2013) and very low fluid/solid ratios. In this limiting case, the concentration ratio of two elements X and Y in the fluid may be estimated from the equation

$$c_X^{fluid}/c_Y^{fluid} = (c_X^{MORB}/c_Y^{MORB}) \, (D_X^{fluid/eclogite}/D_Y^{fluid/eclogite})$$

These element ratios are directly given as ppm/ppm ratios; they are not normalised to MORB compositions. For Ba/Nb, the data compiled by Kelemen et al. (2005) span a range from 47 to 352. For fluid salinities with > 4 wt. % Cl (experiments PC27, PC36, and PC39, Table 6.8), the predicted Ba/Nb ratios in the fluid range from 1280 to 3201. This means that already a small addition of such a fluid to the source of melting may produce the observed high Ba/Nb ratios. For Ba/La, the situation is similar. In average primitive arc basalts, this ratio ranges from 13 to 48, the ratio calculated for the fluid in the same three experiments as above is between 18 and 605. U/Th ratios in arc basalts are usually higher than in MORB (0.29); the average data by Kelemen et al. (2005) suggest a range from 0.11 to 0.65. In the fluids, the calculated ratio is between 3.1 and 5.0, indicating again that already a minor fluid addition to the source of melting will shift the ratio into the right direction. For the U/Th data, however, it has to be considered that U solubility in fluids increases with oxygen fugacity (Bali et al., 2011). Oxygen fugacity in our experiments was not buffered, but is likely close to the Ni-NiO buffer. For a quantitative discussion of the effect of oxygen fugacity on U/Th ratios in subduction zone fluids, see Bali et al. (2011).

6.7.3. Supplementary tables

Table 6.1. Summary of experiments.

Experiment	NaCl in Fluid (wt. %)	Doped Fluid	Solid Starting Material	Capsule Material	Duration (h)	Temperature Fluctuations
PC09	0	-	MORB1-2D1	Au	84	no
PC22	0	-	MORB1-2D1	Pt	120	no
PC37	0	-	MORB2-2D2	Pt	68	yes
PC38	0	-	MORB2-2D2	Pt	128	no
PC14	1	-	MORB1-2D1	Au	69	no
PC23	5	-	MORB2-DD1	Pt	163	yes
PC10	10	-	MORB1-2D1	Au	68	no
PC25	10	-	MORB2-2D2	Pt	102	yes
PC27	10	-	MORB2-2D2	Pt	93	yes
PC36	15	-	MORB2-2D2	Pt	103	yes
PC39	15	-	MORB2-2D2	Pt	126	yes
PC15	15	-	MORB1-2D1	Au	63	no
PC24*	0	SOL1	MORB1	Pt	144	yes
PC18*	10	SOL2	MORB1	Pt	52	no

* reversed experiments

Table 6.2. *Starting material.*

		MORB1	MORB1-2D1	MORB2-2D2	MORB2-DD1	SOL1	SOL2
Major elements (wt. %)	SiO$_2$	54.04 (18)	53.79 (19)	55.62 (17)	55.78 (15)		
	Al$_2$O$_3$	17.38 (6)	17.04 (6)	17.26 (12)	17.54 (11)		
	MgO	5.56 (3)	5.73 (3)	5.41 (3)	5.27 (2)		
	CaO	9.52 (2)	9.75 (2)	8.88 (8)	8.66 (8)		
	FeO	8.30 (12)	8.14 (13)	6.93 (5)	7.04 (6)		
	Na$_2$O	3.90 (2)	3.83 (3)	3.77 (9)	3.83 (8)		
Trace elements (ppm)	Li		236 (2)	1029 (16)	1076 (15)		100
	Be		192 (1)	1000 (11)	1040 (10)	202	100
	B		45 (1)	495 (16)	266 (15)	159	74
	Rb		61 (1)	777 (16)	728 (16)		99
	Cs		6.2 (1)	1077 (16)	1079 (15)	198	95
	Sr		254 (2)	1068 (7)	877 (8)	178	98
	Ba		456 (2)	1092 (4)	1145 (5)	180	98
	Ti	7718 (18)	7565 (20)	7011 (117)	7124 (115)		
	Nb		138 (1)	77.4 (6)	30.7 (2)	103	17
	Ta		75 (1)	82.0 (9)	15.2 (2)	104	8
	Zr		119 (1)	37.8 (3)	33.1 (2)	188	96
	Hf		121 (1)	38.9 (4)	24.5 (2)	186	98
	La		208 (2)	211 (2)	41.8 (4)	142	99
	Ce		818 (5)	519 (3)	562 (4)	146	99
	Nd		222 (1)	221 (2)	44.0 (2)	154	99
	Sm		215 (2)	224 (1)	42.3 (3)	164	99
	Eu		217 (2)	223 (2)	45.9 (5)	166	99
	Gd		239 (2)	248 (1)	47.2 (4)	168	98
	Dy		245 (2)	243 (3)	48.7 (5)	175	98
	Er		240 (2)	310 (4)	47.4 (4)	177	98
	Yb		241 (2)	296 (3)	47.6 (4)	174	98
	Lu		248 (3)	243 (3)	49.5 (6)	177	98
	Y		250 (3)	36.7 (3)	50.5 (7)	161	98
	Sc			261 (5)			
	Pb		92.5 (4)	530 (5)	21.1 (9)	189	97
	Th		198 (3)	106 (1)	39.4 (7)	117	26
	U		275 (2)	134 (1)	54.9 (4)	195	97

Numbers in parentheses are one standard deviation in the last digits. Total iron is given as FeO.

Table 6.3. *Microprobe analyses of garnet and omphacite (in wt. %).*

Garnet								
SiO$_2$	39.17	39.32	39.86	39.43	39.25	38.77	39.02	39.19	39.26
TiO$_2$	0.69	0.69	0.71	0.64	0.63	0.89	0.79	0.63	0.74
Al$_2$O$_3$	22	21.53	21.91	21.93	21.67	20.83	21.33	21.47	20.8
MgO	7.35	7.46	7.36	7.15	7.17	7.29	6.66	8.18	6.69
CaO	11.37	10.82	10.74	10.76	10.18	9.85	11.32	8.5	10.89
FeO	20.04	20.83	21.08	20.57	21.6	22.27	21.21	22.14	21.8
Na$_2$O	0.06	0.06	0.05	0.09	0.06	0.07	0.09	0.06	0.21
Total	100.7	100.7	101.7	100.6	100.6	100	100.4	100.2	100.4

Omphacite				
SiO$_2$	54.57	54.69	55.81	53.81	53.53
TiO$_2$	0.28	0.21	0.13	0.49	0.84
Al$_2$O$_3$	12.23	12.61	10.20	10.50	10.62
MgO	7.80	8.30	9.77	8.90	8.23
CaO	12.91	12.78	14.76	13.55	13.83
FeO	4.13	3.05	5.18	7.64	6.90
Na$_2$O	6.01	6.52	5.81	5.46	5.90
Total	97.9	98.1	101.6	100.3	99.8

Garnet and omphacite compositions were measured on grains across the capsule in one single experiment (PC09). The average garnet composition is $(Ca_{0.29}Mg_{0.27}Fe_{0.44})_3(Al_{0.97}Fe_{0.03})_2(SiO_4)_3$, the average pyroxene composition is $Ca_{0.52}Na_{0.41}Mg_{0.46}Fe_{0.16}Al_{0.44}Si_{1.96}O_6$

Table 6.4. *Fluid compositions.*

Experiment	PC09	PC22	PC37	PC38	PC14	PC23	PC10	PC25	PC27	PC36	PC39	PC15	PC24*	PC18*
Cl (wt. %)	0	0	0	0	0.48	2.25	3.76	3.85	4.91	6.50	6.81	6.93	0	4.23
Li	147 (8)	51.5 (9)	1172 (25)	1044 (11)	286 (15)	1322(109)	314 (14)	1468 (10)	999 (4)	987 (22)	756 (38)	564 (38)	21.6 (14)	54.1 (7)
Be	50 (3)	22.5 (3)	604 (8)	531 (9)	137 (2)	455 (32)	191 (16)	744 (4)	712 (55)	462 (14)	383 (44)	404 (29)	20.3 (16)	106 (3)
B	731 (43)	29.6 (7)	1120 (18)	1046 (14)	282 (10)	1000 (106)	2094 (224)	3668 (67)	2224 (67)	4097 (145)	2234 (201)	259 (17)	80 (5)	440 (6)
Rb	213 (9)	41.3 (3)	1529 (15)	1544 (11)	670 (42)	2266 (180)	710 (51)	5112 (89)	3089 (38)	5671 (196)	2772 (194)	394 (32)	100 (8)	314 (5)
Cs	17.0 (7)	19.3 (1)	2105 (20)	2076 (15)	51 (1)	4725 (431)	81 (6)	9912 (38)	17895 (1467)	7631 (215)	6312 (485)	125 (14)	86 (8)	427 (67)
Sr	194 (8)	90 (2)	1155 (42)	849 (15)	832 (58)	1356 (64)	396 (47)	1914 (365)	2945 (38)	2236 (167)	1235 (97)	1212 (87)	57 (5)	424 (8)
Ba	254 (23)	157 (2)	1606 (16)	1375 (22)	1285 (130)	1885 (135)	1074 (106)	2314 (4)	4542 (69)	4618 (454)	1441 (84)	2384 (173	275 (23)	1785 (23
Ti	162 (10)	74 (3)	387 (4)	331 (7)	280 (24)	435 (56)	414 (64)	702 (5)	272 (21)	481 (25)	367 (68)	254 (24)	133 (16)	376 (23)
Nb	10.9 (7)	4.44 (4)	17.8 (3)	14.3 (1)	19.0 (8)	4.23 (4)	27 (2)	22.7 (4)	8.5 (7)	23.3 (7)	11.7 (13)	17 (4)	0.74 (5)	3.18 (16)
Ta	0.9 (1)	0.41 (2)	3.3 (1)	2.48 (8)	2.07(14)	0.32 (1)	1.5 (2)	3.47 (2)	1.69 (5)	2.73 (12)	1.9 (3)	2.5 (2)	0.09 (2)	0.84 (14)
La	0.23 (2)	0.18 (1)	0.51 (1)	0.39 (5)	1.5 (6)	0.7 (1)	5.8 (7)	2.62 (13)	5.32 (13)	8.4 (9)	6.9 (17)	43 (2)	5.0 (4)	12.1 (6)
Ce	2.6 (2)	1.5 (2)	2.94 (7)	2.39 (14)	10 (3)	29 (5)	41 (6)	14.5 (6)	20 (1)	29.3 (18)	23 (4)	169 (7)	66 (4)	129 (6)
Nd	0.27 (3)	0.226 (4)	0.60 (3)	0.47 (4)	1.9 (8)	0.86 (10)	5.5 (3)	2.9 (4)	6.3 (4)	7.6 (11)	4.8 (11)	31.3 (17)	4.6 (4)	10.9 (6)
Sm	0.50 (5)	0.287 (8)	0.86 (4)	0.62 (2)	1.9 (6)	0.78 (7)	5.1 (11)	3.6 (5)	6.2 (4)	9.2 (13)	5.4 (8)	26.3 (17)	3.9 (3)	10.3 (3)
Eu	1.0 (1)	0.565 (5)	1.83 (3)	1.42 (3)	3.6 (1)	1.67 (23)	11.3 (13)	7.2 (9)	14.6 (9)	25 (3)	22 (5)	100 (7)	4.2 (3)	13.6 (4)
Gd	1.1 (2)	0.420 (9)	1.06 (4)	0.72 (3)	2.1 (4)	0.81 (4)	4.9 (4)	4.2 (5)	5.5 (3)	11.3 (16)	4.7 (5)	20.8 (5)	2.6 (2)	6.6 (3)
Dy	1.9 (3)	0.63 (4)	1.30 (9)	0.90 (5)	1.7 (3)	0.75 (3)	3.7 (2)	4.4 (4)	2.96 (13)	10.0 (11)	3.38 (16)	10.2 (3)	1.35 (9)	3.8 (3)
Er	1.7 (3)	0.59 (6)	1.37 (12)	0.88 (9)	1.2 (2)	0.52 (5)	2.4 (3)	4.8 (6)	1.98 (13)	8.1 (8)	3.3 (5)	6.0 (2)	1.05 (13)	4.8 (5)
Yb	1.5 (2)	0.63 (5)	1.35 (13)	0.99 (14)	1.4 (2)	0.53 (4)	2.2 (2)	5.3 (7)	2.22 (13)	6.2 (7)	4.0 (7)	5.8 (6)	1.4 (3)	7.6 (11)
Lu	1.3 (2)	0.55 (5)	0.9 (1)	0.68 (9)	1.5 (2)	0.47 (5)	1.8 (3)	4.7 (6)	1.54 (19)	4.1 (3)	3.3 (6)	5.8 (3)	1.2 (2)	9.0 (14)
Y	13 (3)	3.7 (4)	9 (2)	6.7 (17)	20 (5)	5.0 (7)	20 (4)	19 (3)	19 (3)	23 (6)	10.6 (17)	64 (20)	5.5 (6)	28 (8)
Sc			3.3 (2)	2.66 (12)				8.4 (2)	3.00 (16)	5.5 (3)	4.4 (6)			
Pb	108 (21)	17.3 (5)	371 (3)	228 (1)	177 (6)	13 (1)	589 (67)	1708 (96)	860 (109)	1428 (110)	1008 (164)	417 (28)	21.7 (11)	438 (9)
Th	0.19 (2)	0.0497 (8)	0,16 (2)	0.116 (12)	0.9 (5)	0.35 (5)	0.67 (9)	0.52 (1)	0.45 (2)	0.71 (4)	0.55 (9)	6.2 (2)	0.81 (5)	1.62 (15)
U	14 (2)	5.0 (3)	11.7 (12)	9.2 (6)	29 (2)	13.7 (16)	58 (7)	50 (2)	20 (2)	63.8 (22)	36 (6)	158 (7)	12.2 (19)	134 (13)

All compositions are given in ppm by weight, except for Cl (wt.%). Numbers in parentheses are one standard deviation in the last digits. * reversed experiments.

Table 6.5. Garnet compositions.

Experiment	PC09	PC22	PC37	PC38	PC14	PC23	PC10	PC25	PC27	PC36	PC39	PC15	PC24*	PC18*
Cl (wt.%)	0	0	0	0	0.48	2.25	3.76	3.85	4.91	6.50	6.81	6.93	0	4.23
Li	< 57	22 (3)	144 (9)	113 (10)	< 188	162 (41)	< 32	112 (26)	270 (66)	76 (12)	66 (10)	124 (23)	< 39	< 69
Be	< 81	< 70	91 (28)	68 (10)	< 35	127 (32)	< 88	111 (5)	160 (37)	57 (12)	35 (3)	< 162	< 101	< 127
B	< 71	< 79	96 (11)	123 (8)	< 528	26 (1)	< 63	81 (2)	44 (2)	84 (11)	51 (6)	< 110	< 74	< 89
Rb	< 4.9	1.11 (18)	13 (9)	3.6 (5)	< 25	2.7 (7)	< 3.00	2.94 (16)	29 (12)	3.6 (0.9)	1.7 (2)	< 4.84	< 2.98	< 4.1
Cs	< 1.46	< 47	15 (11)	3.4 (5)	< 8.35	3.1 (7)	< 1.30	1.57 (12)	28 (10)	3.9 (1.6)	1.4 (2)	< 1.97	< 0.546	< 3.1
Sr	2.92 (5)	< 1.78	38 (7)	25 (6)	14 (4)	18.7 (6)	2.2 (13)	7.3 (4)	61 (11)	21 (12)	9.2 (28)	7.0 (23)	5 (1)	3.51 (14)
Ba	9.9	< 3.38	22 (12)	14 (5)	< 45.4	6.0 (5)	< 7.00	5.50 (7)	46 (29)	15 (7)	9.0 (17)	< 16	< 6.3	< 16.5
Ti	5295 (657)	4545 (517)	4251 (702)	3955 (247)	6038 (1376)	5002	5540 (521)	2998 (432)	5168 (514)	4122 (2160)	2031 (417)	4234 (372)	4486 (224)	2877 (465)
Nb	28 (3)	28 (3)	9.4 (23)	9 (3)	50 (19)	6.1 (25)	33 (7)	11 (6)	29 (3)	31 (18)	5.0 (18)	9.6 (12)	2.4 (2)	3.1 (0.4)
Ta	12.1 (18)	13 (2)	8 (3)	7.5 (23)	22 (9)	1.6 (3)	17 (5)	11 (7)	27 (3)	31 (20)	4.7 (16)	5.7 (16)	1.7 (4)	< 2.70
Zr	80 (1)	74 (6)	106 (10)	101 (9)	76 (4)	86.9 (5)	93.9 (5)	88 (3)	63 (11)	82 (17)	67 (5)	60 (4)	74 (3)	61 (3)
Hf	33 (3)	40 (2)	36 (4)	33 (4)	41 (2)	17 (3)	54 (4)	26 (2)	32 (5)	32 (7)	23 (2)	43 (4)	19 (3)	22.9 (13)
La	< 1.02	0.65 (4)	5.5 (13)	5.7 (17)	12 (2)	0.52 (8)	< 1.13	1.4 (3)	13 (3)	2.0 (0.8)	1.6 (5)	12 (5)	4.7 (1)	< 1.54
Ce	13.1 (4)	7.1 (3)	41 (9)	27 (8)	49 (28)	36 (2)	7.4 (24)	5.0 (14)	56 (12)	9 (4)	5.0 (13)	87 (29)	74 (19)	11 (5)
Nd	< 6.42	3.5 (3)	8 (2)	8.6 (11)	< 27.3	2.1 (4)	6.6 (6)	4.9 (7)	19 (3)	11 (3)	4.7 (6)	21 (5)	8.8 (4)	< 10.8
Sm	20.7 (49)	14 (3)	34 (6)	28 (4)	36 (2)	7.8 (2)	< 21.7	36 (5)	70 (7)	67 (16)	30 (3)	119 (7)	34 (4)	17.87 (8)
Eu	46 (11)	37 (7)	77 (10)	66 (7)	66 (15)	15.2 (13)	68 (1)	82 (10)	151 (14)	141 (33)	72 (9)	205 (8)	55 (8)	47 (4)
Gd	84 (16)	65 (12)	116 (17)	105 (10)	115 (27)	18 (3)	117 (9)	134 (16)	249 (25)	204 (48)	115 (15)	254 (26)	74 (10)	45 (3)
Dy	237 (6)	223 (26)	294 (35)	291 (18)	229 (10)	44 (2)	260 (7)	435 (23)	538 (56)	473 (89)	382 (52)	423 (35)	106 (26)	58 (2)
Er	361 (43)	450 (59)	529 (52)	532 (28)	362 (40)	62 (9)	340 (18)	930 (131)	781 (103)	818 (182)	872 (117)	430 (52)	106 (32)	63 (3)
Yb	470 (121)	705 (115)	608 (48)	594 (48)	527 (127)	59 (11)	354 (9)	1146 (232)	759 (110)	983 (300)	1194 (155)	378 (48)	92 (31)	60 (4)
Lu	534 (181)	826 (148)	511 (46)	491 (47)	561 (176)	59 (11)	328 (18)	1010 (219)	613 (95)	828 (270)	1088 (137)	401 (52)	86 (22)	51.5 (7)
Y	439 (14)	411 (49)	64 (6)	93 (17)	360 (27)	136 (26)	343 (10)	110 (15)	118 (11)	139 (23)	157 (30)	454 (28)	144 (16)	128 (9)
Sc			461 (37)	407 (22)				428 (29)	402 (38)	351 (79)	388 (43)			
Pb	< 3.52	< 1.8	13 (3)	7.3 (7)	< 27	1.22 (6)	4.3 (7)	5.0 (5)	14 (2)	4.8 (8)	4.9 (8)	< 9.6	2.85 (16)	< 9.0
Th	< 1.29	0.52 (5)	1.82 (21)	3.4 (5)	4.7 (3)	0.336 (9)	< 1.28	1.7 (2)	3.6 (8)	1.05 (16)	0.76 (13)	5.4 (16)	1.1 (3)	< 1.59
U	6.9 (22)	8.1 (11)	11.7 (21)	6.0 (6)	13 (5)	3.2 (5)	< 8.0	4.1 (7)	18 (2)	10 (3)	4.2 (5)	60 (9)	11.66 (2)	8.3 (2)

All compositions are given in ppm by weight, except for Cl (wt.%); numbers in parentheses are one standard deviation in the last digits. < Detection limits are reported as maximum values when element concentrations were too low to be measured; * reversed experiments; ** Cl concentrations in the fluid of the same experiment are given for reference.

Table 6.6. Omphacite compositions

Experiment	PC09	PC22	PC37	PC38	PC14	PC23	PC10	PC25	PC27	PC36	PC39	PC15	PC24*	PC18*
Cl (wt.%) **	0	0	0	0	0.48	2.25	3.76	3.85	4.91	6.50	6.81	6.93	0	4.23
Li	293 (54)	329 (10)	1461 (52)	1298 (209)	344 (28)	1812 (285)	32 (6)	1115 (43)	1463 (30)	1044 (37)	810 (13)	204 (7)	85 (2)	126 (6)
Be	204 (9)	200 (4)	921 (39)	974 (172)	276 (13)	1065 (69)	88 (5)	798 (37)	855 (16)	804 (69)	882 (41)	203 (47)	109 (18)	153 (31)
B	106 (24)	45 (3)	353 (54)	395 (81)	157 (111)	320 (74)	63 (4)	172 (6)	140 (12)	114 (10)	104 (21)	< 41	80 (24)	97 (28)
Rb	7.2 (5)	37 (2)	120 (38)	102 (32)	9 (2)	380 (85)	3.0 (2)	186 (25)	273 (19)	49 (18)	12 (2)	24 (4)	38 (11)	38 (7)
Cs	2.1 (4)	19.46 (3)	172 (55)	147 (47)	< 2.07	620 (144)	1.30 (7)	277 (40)	413 (66)	81 (28)	26 (4)	2.1 (5)	36 (12)	32 (5)
Sr	52.4 (2)	173 (6)	341 (32)	438 (115)	146 (60)	958 (268)	2.2 (13)	305 (29)	400 (20)	300 (69)	136 (19)	42 (6)	83 (29)	63 (23)
Ba	109 (15)	260 (46)	261 (39)	271 (73)	148 (65)	1193 (456)	7.0 (3)	133 (32)	248 (45)	215 (58)	100 (17)	15 (3)	169 (38)	146 (58)
Ti	< 80	1449 (37)	2711 (411)	2696 (921)	2188 (358)	2123 (110)	5540 (521)	2088 (45)	3769 (945)	2665 (305)	2747 (171)	3664 (853)	1008 (97)	1371 (209)
Nb	< 2.94	9.6 (6)	15 (6)	12 (3)	57 (26)	2.5 (3)	33 (7)	4.9 (3)	28 (7)	2.0 (8)	1.41 (14)	39 (6)	0.49 (4)	4.00 (14)
Ta	< 2.17	2.8 (3)	14 (7)	9 (3)	24 (12)	0.81 (21)	17 (5)	3.0 (2)	25 (7)	2.8 (8)	1.01 (14)	15 (3)	0.38 (11)	1.6 (3)
Zr	20 (3)	13.9 (4)	14.6 (15)	17 (4)	35 (14)	18 (3)	93.9 (5)	13.4 (9)	22 (8)	35 (12)	8.5 (4)	8.4 (13)	11.6 (4)	20 (3)
Hf	9.1 (5)	7.6 (6)	7.0 (4)	9 (2)	34 (18)	4.3 (2)	54 (4)	9.0 (5)	12 (2)	12 (4)	4.1 (5)	10.8 (16)	2.97 (2)	15 (3)
La	9 (5)	104 (6)	43 (10)	46 (18)	303 (185)	41 (9)	1.13 (6)	43 (15)	27 (2)	1.0 (1)	0.6 (2)	51 (5)	70 (44)	31 (10)
Ce	63 (24)	624 (4)	160 (35)	222 (89)	1179 (677)	963 (168)	7.4 (2.4)	141 (44)	93 (7)	4.8 (8)	2.6 (2)	273 (28)	1305 (827)	326 (68)
Nd	15 (2)	110 (3)	46 (11)	49 (20)	315 (190)	45 (10)	6.6 (06)	45 (15)	29 (3)	6.2 (1.4)	5.0 (8)	56 (5)	74 (47)	33 (12)
Sm	16 (3)	104.7 (5)	41 (10)	49 (18)	316 (201)	37 (6)	22 (4)	43 (14)	34 (2)	19 (2)	12.0 (8)	53 (8)	71 (43)	27.4 (5)
Eu	13.5 (7)	111.3 (5)	56 (13)	59 (21)	289 (176)	46 (6)	68 (1)	51 (13)	50 (4)	27 (3)	18.7 (7)	51 (4)	59 (34)	20.8 (5)
Gd	10.0 (1)	109.8 (1)	52 (12)	47 (16)	265 (161)	33 (6)	117 (9)	46 (9)	60 (6)	41 (5)	25 (2)	41 (7)	45 (27)	16 (2)
Dy	25 (11)	106 (2)	51 (12)	42 (12)	189 (113)	24 (4)	260 (7)	49 (6)	86 (16)	57 (8)	24 (2)	42 (10)	18 (8)	9.9 (7)
Er	28 (15)	100 (6)	63 (17)	46 (14)	160 (94)	19 (4)	340 (18)	61 (8)	115 (21)	60 (12)	20 (1)	38 (9)	7.5 (15)	6.4 (6)
Yb	25 (12)	96 (6)	58 (16)	47 (16)	157 (93)	16 (3)	354 (9)	55 (6)	116 (22)	38 (11)	12.4 (4)	36 (7)	7.1 (14)	10.4 (5)
Lu	25 (14)	92 (9)	46 (12)	35 (11)	139 (79)	15 (3)	328 (18)	44 (5)	92 (16)	28 (9)	9.0 (3)	32 (10)	5.3 (3)	8.4 (6)
Y	65 (34)	118 (9)	43 (15)	14 (4)	204 (112)	75 (25)	343 (10)	17 (2)	24 (4)	40 (6)	15.5 (4)	42 (10)	27 (7)	11.6 (6)
Sc		113 (12)	99 (18)					131 (6)	139 (6)	146 (8)	98 (2)			
Pb	20 (7)	33 (3)	72 (8)	57 (16)	69 (34)	3.8 (7)	4.3 (7)	219 (122)	39 (3)	14 (2)	26 (4)	5.2 (7)	30 (12)	93 (30)
Th	5.0 (22)	67.3 (5)	16 (4)	17 (7)	274 (177)	31 (9)	1.28 (4)	14 (6)	9 (1)	0.36 (4)	0.540 (25)	27 (2)	10 (6)	8.9 (9)
U	15 (5)	179 (2)	34 (7)	38 (14)	274 (177)	57 (10)	8.0 (3)	27 (9)	20 (1)	2.3 (4)	1.14 (8)	64 (6)	52 (31)	23.3 (9)

All compositions are given in ppm by weight, except for Cl (wt.%); numbers in parentheses are one standard deviation in the last digits. < Detection limits are reported as maximum values when element concentrations were too low to be measured; * reversed experiments; ** Cl concentrations in the fluid of the same experiment are given for reference.

Table 6.7. *Rutile compositions*

Experiment	PC09	PC22	PC37	PC38	PC14	PC23	PC10	PC25	PC27	PC36	PC39	PC15	PC24*	PC18*
Cl (wt.%)	0	0	0	0	0.48	2.25	3.76	3.85	4.91	6.50	6.81	6.93	0	4.23
Li	< 100	< 32	< 112	< 93	< 147	< 46	< 61	< 44	< 409	< 179	< 112	< 214	< 74	< 106
Be	< 297	< 118	< 174	< 107	< 498	< 96	< 168	< 117	< 483	< 126	< 174	< 449	< 190	< 197
B	< 164	< 132	< 184	< 251	< 350	< 84	< 75	< 109	< 562	< 188	< 184	< 225	< 155	< 139
Rb	< 11	< 1.5	< 125	< 34	< 11	< 113	< 6	< 16	< 416	< 75	< 125	< 11	< 7	< 9
Cs	< 2	< 0.8	< 220	< 88	< 5	< 156	< 1.6	< 2	< 1250	< 79	< 220	< 5	< 2	< 8
Sr	< 48	< 17	< 96	< 165	< 45	< 75	< 10	< 23	< 490	< 87	< 96	< 15	< 4	< 47
Ba	< 133	< 40	< 126	< 76	< 67	< 94	< 11	< 15	< 521	< 90	< 126	< 31	< 10	< 126
Nb	10584 (608)	11863 (682)	7067 (285)	7257 (219)	10278 (344)	2475 (80)	8164	7306 (244)	7539 (227)	7226 (161)	7067 (285)	11319 (494)	1067 (43)	1611(157)
Ta	6117 (488)	6568 (523)	7363 (362)	7862 (377)	5893 (232)	1223 (32)	4072	6688 (263)	8110 (389)	7095 (364)	7363 (362)	5476 (301)	528.0 (3)	882(97)
Zr	300.8 (3)	243.3 (2)	309 (23)	341 (13)	260 (15)	341 (17)	307 (16)	401 (24)	302 (12)	331 (29)	309 (23)	346 (42)	276 (10)	274(16)
Hf	263 (16)	257 (16)	130 (23)	104 (12)	193 (41)	58 (10)	307 (52)	261 (55)	138 (16)	112 (18)	130 (23)	341 (16)	69 (20)	189(17)
La	< 7	< 14	< 6	< 38	< 37	< 3	< 36	< 10	< 20	< 4	< 6	< 4	< 7	< 122
Ce	< 69	< 104	< 27	< 147	< 307	< 129	< 172	< 51	< 74	< 9	< 27	< 6	< 123	< 1057
Nd	< 12	< 7	< 14	< 48	< 50	< 4	< 32	< 11	< 21	< 9	< 14	< 28	< 16	< 71
Sm	< 22	< 23	< 16	< 49	< 31	< 5	< 16	< 8	< 29	< 14	< 16	< 25	< 11	< 58
Eu	< 5	< 16	< 9	< 44	< 26	< 4	< 26	< 14	< 25	< 6	< 9	< 7	< 9	< 58
Gd	< 12	< 20	< 13	< 37	< 33	< 7	< 14	< 14	< 33	< 14	< 13	< 27	< 12	< 33
Dy	< 12	< 13	7	< 17	< 20	< 3	< 22	< 5	< 19	< 14	< 7	< 23	< 5	< 12
Er	< 11	< 8	< 10	< 9	< 27	< 4	< 10	< 7	< 7	< 18	< 10	< 19	< 6	< 15
Yb	< 9	< 17	< 11	< 12	< 29	< 4	< 19	< 5	< 11	< 18	< 11	< 20	< 9	< 22
Lu	< 2	< 9	< 3	< 3	< 10	< 0.8	< 11	< 2	< 7	< 9	< 3	< 6	< 4	< 4
Y	< 4	< 9	< 3	< 5	< 15	< 4	< 15	< 2	< 8	< 7	< 3	< 8	< 10	< 10
Sc			< 39	< 38				< 36	< 24	< 51	< 39			
Pb	< 17	< 3	< 39	< 34	< 35	< 5	< 13	< 16	< 216	< 54	< 39	< 18	< 6	< 33
Th	< 3	< 8	< 3	< 20	< 26	< 4	< 15	< 4	< 9	< 2	< 3	< 6	< 3	< 18
U	< 31	< 33	< 8	< 39	< 61	< 8	< 59	< 24	< 36	< 19	< 8	< 74	< 20	< 92

All compositions are given in ppm by weight, except for Cl (wt.%); numbers in parentheses are one standard deviation in the last digits. < Detection limits are reported as maximum values when element concentrations were too low to be measured; * reversed experiments; ** Cl concentrations in the fluid of the same experiment are given for reference.

Table 6.8. Fluid/eclogite partition coefficients.

Experiment	PC09	PC22	PC37	PC38	PC14	PC23	PC10	PC25	PC27	PC36	PC39	PC15	PC24*	PC18*
Cl (wt.%) **	0	0	0	0	0.48	2.25	3.76	3.85	4.91	6.50	6.81	6.93	0	4.23
Li	> 0.74	0 (11)	1.25 (7)	1.27 (21)	> 1.01	1.1 (3)	> 1.7	2.06 (9)	1.01 (4)	1.50 (8)	1.48 (9)	3.3 (3)	> 0.32	> 0.52
Be	> 0.32	> 0.15	1.02 (6)	0.87 (16)	> 0.45	0.66 (8)	> 1.3	1.42 (7)	1.23 (11)	0.91 (10)	0.70 (11)	> 2.2	> 0.19	> 0.74
B	> 7.9	> 0.51	4.5 (6)	3.7 (7)	> 0.92	4.9 (16)	> 25	27 (1)	22 (2)	40 (4)	27 (6)	> 3.8	> 1.04	> 4.7
Rb	> 34	1.82 (9)	20 (6)	25 (8)	> 43	10 (3)	> 170	45 (7)	17.6 (14)	185 (73)	349 (77)	> 24	> 4.2	> 17
Cs	> 9.1	> 1.6	19 (6)	23 (7)	> 11	13 (4)	> 88	59 (9)	69 (16)	152 (55)	398 (96)	> 60	> 3.9	> 21
Sr	6.0 (3)	> 0.86	5.3 (6)	3.1 (8)	9 (4)	2.3 (7)	14 (3)	10 (3)	11.1 (7)	12 (3)	15 (3)	43 (9)	1.1 (5)	11(4)
Ba	> 3.6	> 0.99	9.7 (15)	8.2 (23)	> 12	2.6 (12)	> 112	28 (7)	27 (5)	34 (12)	23 (5)	> 153	> 2.6	> 19
Ti	> 0.075	0.0274 (17)	0.116 (8)	0.103 (12)	0.075 (10)	0.133 (13)	0.131	0.287 (13)	0.063 (7)	0.15 (3)	0.149 (19)	0.065 (8)	0.055 (5)	0.191 (18)
Nb	> 0.049	0.01748 (16)	0.116 (7)	0.092 (4)	0.073 (7)	0.079 (6)	0.154	0.148 (12)	0.047 (4)	0.148 (13)	0.078 (6)	0.069 (6)	0.033 (4)	0.089 (6)
Ta	> 0.0067	0.00294 (11)	0.021 (2)	0.015 (1)	0.015 (2)	0.0126 (16)	> 0.017	0.025 (3)	0.009 (1)	0.018 (2)	0.0130 (17)	0.020 (2)	0.0077 (16)	> 0.043
La	> 0.041	0.0028 (2)	0.018 (4)	0.013 (6)	0.0083 (78)	0.028 (10)	> 0.24	0.10 (4)	0.25 (3)	6.0 (18)	7 (3)	1.22 (18)	0.12 (8)	> 0.62
Ce	0.060 (25)	0.0041 (5)	0.026 (5)	0.017 (7)	0.014 (12)	0.049 (17)	0.27	0.17 (6)	0.25 (3)	4.4 (12)	6.3 (17)	0.85 (12)	0.08 (5)	0.64 (16)
Nd	> 0.023	0.0034 (2)	0.020 (5)	0.014 (6)	> 0.0093	0.031 (10)	> 0.22	0.10 (4)	0.25 (3)	0.9 (3)	1.0 (3)	0.74 (10)	0.10 (6)	> 0.46
Sm	0.028 (6)	0.0042 (1)	0.022 (5)	0.015 (5)	0.010 (8)	0.030 (7)	0.16 (7)	0.09 (3)	0.128 (14)	0.24 (7)	0.28 (5)	0.33 (4)	0.07 (4)	0.437 (16)
Eu	0.039 (1)	0.0069 (2)	0.028 (4)	0.023 (5)	0.018 (14)	0.050 (11)	0.23 (5)	0.114 (25)	0.161 (18)	0.34 (10)	0.56 (15)	0.89 (8)	0.07 (3)	0.43 (3)
Gd	0.029 (9)	0.0046 (3)	0.014 (2)	0.010 (2)	0.010 (7)	0.030 (5)	0.071	0.052 (10)	0.040 (5)	0.11 (3)	0.076 (14)	0.165 (18)	0.045 (15)	0.242 (21)
Dy	0.017 (3)	0.0041 (4)	0.0088 (14)	0.0064 (7)	0.008 (4)	0.023 (2)	0.032	0.021 (3)	0.0111 (14)	0.045 (12)	0.020 (3)	0.053 (5)	0.025 (7)	0.129 (11)
Er	0.010 (3)	0.0025 (4)	0.0055 (9)	0.0037 (5)	0.0050 (17)	0.014 (3)	0.017	0.012 (3)	0.0052 (9)	0.022 (7)	0.009 (2)	0.031 (4)	0.022 (9)	0.166 (21)
Yb	0.007 (3)	0.0019 (4)	0.0048 (8)	0.0037 (8)	0.0047 (16)	0.016 (3)	0.0152	0.011 (3)	0.006 (1)	0.015 (6)	0.008 (2)	0.033 (7)	0.033 (16)	0.25 (4)
Lu	0.006 (3)	0.0014 (3)	0.0037 (7)	0.0032 (7)	0.0048 (018)	0.014 (3)	0.0129	0.011 (4)	0.005 (1)	0.012 (5)	0.008 (2)	0.032 (6)	0.031 (13)	0.35 (5)
Y	0.062 (5)	0.016 (3)	0.18 (6)	0.15 (6)	0.07 (3)	0.049 (14)	0.13 (3)	0.35 (9)	0.30 (6)	0.29 (9)	0.15 (5)	0.31 (10)	0.075 (14)	0.47 (15)
Sc			0.0131 (14)	0.0120 (11)				0.033 (2)	0.0123 (13)	0.024 (4)	0.021 (4)			
Pb	> 8.1	> 0.84	7.6 (9)	6.1 (16)	> 3.4	4.7 (10)	> 64	13 (8)	30 (5)	142 (29)	58 (16)	> 60	1.1 (5)	> 7.3
Th	> 0.053	0.00123 (3)	0.015 (5)	0.010 (5)	0.01 (1)	0.019 (8)	> 0.043	0.06 (2)	0.064 (9)	1.12 (16)	0.88 (17)	0.33 (4)	0.12 (8)	> 0.27
U	1.2 (5)	0.045 (3)	0.47 (12)	0.37 (014)	0.17 (12)	0.39 (11)	1.9 (9)	2.8 (9)	1.04 (14)	12 (3)	15 (3)	2.5 (3)	0.34 (22)	7.8 (9)

Numbers in parentheses are one standard deviation in the last digits; > minimum values of D are reported when only maximum concentrations of trace elements were available for garnet and/or omphacite.; * reversed experiments; ** Cl concentrations in the fluid of the same experiment are given for reference.

6.7.4. Supplementary information references

Fung, A.T., Haggerty, S.E. (1995) Petrography and mineral compositions of eclogites from the Koidu kimberlite complex, Sierra-Leone. Journal of Geophysical Research 100, 20451-20473.

Gale, A., Dalton, C.A., Langmuir, C.H., Su, Y.J., Schilling, J.G. (2013) The mean composition of ocean ridge basalts. Geochemistry Geophysics Geosystems 14, 489-518.

Heinrich, C.A. (1982) Kyanite-eclogite to amphibolite facies evolution of hydrous mafic and pelitic rocks, Adula-Nappe, Central Alps. Contributions to Mineralogy and Petrology 81, 30-38

Imayama, T., Oh, C.W., Baltybaev, S.K., Park, C.S., Yi, K., Jung, H. (2017) Paleoproterozoic high-pressure metamorphic history of the Salma eclogite on the Kola Peninsula, Russia. Lithosphere 9, 855–873.

Jochum, K.P. et al. (2011) Determination of reference values for NIST SRM 610-617 glasses following ISO guidelines. Geostandards and Geoanalytical Research 35, 397-429.

Keller, D.S., Ague, J.J. (2019) Crystallographic and textural evidence for precipitation of rutile, ilmenite, corundum, and apatite lamellae from garnet. American Mineralogist 104, 980-995.

Mair, P., Tropper, P., Harlov, D.E., Manning, C.E. (2017) The solubility of apatite in H_2O, KCl-H_2O, $NaCl$-H_2O at 800 ˚C and 1.0 GPa: Implications for REE mobility in high-grade saline brines. Chemical Geology 470, 180-192.

Pearce, J.A., Stern, R.J., Bloomer, S.H., Fryer, P. (2005) Geochemical mapping of the Mariana arc-basin system: Implications for the nature and distribution of subduction components. Geochemistry Geophysics Geosystems 6, Article Number: Q07006.

Rüpke, L.H., Phipps Morgan, J., Hort, M., Connolly, A.D. (2002) Are the regional variations in Central American arc lavas due to differing basaltic versus peridotitic slab sources of fluids? Geology 30, 1035–1038.

Seo, J.H., Guillong, M., Aerts, M., Zajacz, Z., Heinrich, C.A. (2011) Microanalysis of S, Cl, and Br in fluid inclusions by LA-ICP-MS. Chemical Geology 284, 35-44.

Song, S., Yang, J., Liou, J.G., Wu, C., Shi, R., Xu, Z. (2003) Petrology, geochemistry and isotopic ages of eclogites from the Dulan UHPM Terrane, the North Qaidam, NW China. Lithos 70, 195– 211.

Tubia, J.M., Ibarguchi, J.I.G. (1991) Eclogites of the Ojén nappe: a record of subduction in the Alpujárride complex (Betic Cordilleras, southern Spain). Journal of the Geological Society of London 148, 801-804.

7. A systematic assessment of the diamond trap method for measuring fluid compositions in high-pressure experiments

Greta Rustioni, Andreas Audétat, Hans Keppler

Bayerisches Geoinstitut, Universität Bayreuth, D-95440 Bayreuth, Germany

7.1. Abstract

A variety of experimental techniques have been proposed to measure the composition of aqueous fluids in high-pressure experiments. In particular, the "diamond trap method", where the fluid is sampled in the pore space of diamond powder and analyzed by laser-ablation ICP-MS after the experiment, has become a popular tool. Here, we carried out several tests in order to assess the reliability of this method. (i) We prepared several capsules loaded with fluid of known composition and analyzed the fluid by laser-ablation ICP-MS, either (a) after drying the diamond trap at ambient condition, (b) after freezing and subsequent freeze-drying, and (c) after freezing and by analyzing a frozen state. Of these methods, the analysis in the frozen state (c) was most accurate, while the results from the other two methods were poorly reproducible and the averages sometimes deviated from the expected composition by more than a factor of 2. (ii) We tested the reliability of the diamond trap method by using it to measure mineral solubilities in some well-studied systems at high pressure and high temperature in piston cylinder runs. In the systems quartz-H_2O, forsterite-enstatite-H_2O, and albite-H_2O, the results from analyzing the diamond trap in frozen state by laser-ablation ICP-MS generally agreed well with the expected compositions according to literature data. However, in the systems corundum-H_2O and rutile-H_2O, the data from the analysis of the diamond trap were poorly reproducible and appeared to indicate much higher solubilities than expected. We attribute this not to some unreliability of the analytical method, but rather to the fact that in these systems, minor temperature gradients along the capsule may induce the dissolution and re-precipitation

of material during the run, which causes a contamination of the diamond trap by solid phases. (iii) We carried out several tests on the reliability of the diamond trap to measure fluid compositions and trace element partition coefficients in the eclogite-fluid system at 4 GPa and 800 ˚C using piston cylinder experiments. The good agreement between "forward" and "reversed" experiments – with trace elements initially either doped in the solid starting material or the fluid – as well as the independence of partition coefficients on bulk concentrations suggests that the data obtained are reliable in most cases. We also show that the rate of quenching/cooling has little effect on the analytical results, that temperature oscillations during the run can be used to enhance grain growth, and that well equilibrated samples can be obtained in conventional piston cylinder runs. Overall, our results suggest that the diamond trap method combined with laser-ablation ICP-MS in frozen state yields reliable results accurate within a factor of two in most cases; however, the precipitation of accessory minerals in the diamond trap during the run may severely affect the data in some systems and may lead to a gross overestimation of fluid concentrations.

7.2.   Introduction

Aqueous fluids are important agents of metasomatism in Earth´s mantle, particularly above subduction zones (e.g. Tatsumi 1989, Manning 2004, Kelley and Cottrell 2009, Keppler 2017). Traces of such fluids are sometimes sampled as fluid inclusions in mantle xenoliths and in diamonds (e.g. Kawamoto et al. 2013, Weiss et al. 2015). However, in particular the fluids sampled by diamonds may be the result of extensive fractionation processes, which are not easy to unravel. Constraining the primary composition of mantle fluids therefore requires experimental studies. Unfortunately, methods for the direct withdrawal and analysis of fluids are limited to very low pressures (Potter et al. 1987) and cannot be used under typical mantle P, T conditions. Simply quenching fluids equilibrated with minerals at high P and T and analyzing the quenched fluid at ambient conditions is not likely to yield meaningful results, because in most cases, solutes will precipitate as solid phases even during rapid quenching (e.g. Ryabchikov and Boettcher 1980). Various methods have been proposed to solve this problem. In simple systems, where minerals dissolve congruently, the weight loss of single crystals may allow very accurate solubility measurements, since during quenching, solute will precipitate

throughout the fluid, and only a very minor fraction could produce an overgrowth on the original single crystal (e.g. Manning 1994, Tropper and Manning 2007). Separating the charge into different, but connected compartments for solid phases and fluid – by using a double capsule technique (Anderson and Burnham 1965) or folded capsules (Ryabchikov and Boettcher 1980) – may also help to distinguish material precipitated from the fluid from solids that were stable during run conditions.

Synthetic fluid inclusions offer an attractive possibility to trap fluids in high-pressure experiments. The fluid inclusions may be analyzed at ambient conditions by laser-ablation ICP-MS or other methods, such as synchrotron X-ray fluorescence. This technique has been used successfully to study fluid compositions in various systems (Bali et al. 2011, 2012, Tsay et al. 2014). One limitation of the method is that elements contained in the host crystal (typically quartz or olivine) obviously cannot be quantified. Moreover, it is not always possible to accurately control the time at which the inclusions seal off and lose contact to the main fluid reservoir. In systems where chemical equilibrium is attained slowly, this may have the effect that the fluid trapped in the inclusions has not yet fully equilibrated with the other phases present.

Direct observation of mineral dissolution in the externally-heated diamond anvil cell can provide accurate solubility data for minerals that dissolve congruently in the fluid (e.g. Audétat and Keppler 2005, Bernini et al. 2013), but the approach does not allow to determine the solubility of minerals that dissolve incongruently. Solubility studies may also be carried out by directly measuring fluid compositions in-situ by X-ray fluorescence or X-ray absorption spectroscopy (e.g. Wilke et al. 2012). Other spectroscopic methods, in particular Raman spectroscopy, may also be used to infer solute concentrations. However, Raman spectroscopic measurements in the diamond cell require an extremely careful calibration (see Zarei et al. 2018 for discussion). A general limitation of solubility studies in the externally-heated diamond cell is that run durations are usually relatively short, such that systems that require long timescales (more than a few hours) for equilibration cannot be studied. Moreover, controlling oxygen fugacity in the diamond cell is nearly impossible.

The "diamond trap method" for measuring fluid (and melt) compositions was first introduced by Ryabchikov et al. (1989). It may be used in conventional piston cylinder or multi anvil experiments. A layer of diamond powder is placed together with the other starting materials

inside a noble metal capsule. During the experiment, the fluid infiltrates the pore space between the diamond grains. Upon quenching, any material precipitating from the fluid will remain trapped between the diamond grains. Therefore, ideally, it should be possible to determine the bulk composition of the fluid by analyzing the entire diamond trap. Since its first description, the diamond trap method has been used extensively to infer fluid or melt compositions. For analyzing aqueous fluids, in earlier studies (e.g. Stalder et al. 1998, Johnson and Plank 1999) the water was simply allowed to evaporate after opening the capsule and the remaining solid residue was analyzed. Kessel et al. (2004) introduced a more advanced method, where the capsule is first frozen and then cut open and analyzed in frozen state.

Even though the diamond trap method – in various variants (e.g. Stalder et al. 1998, Johnson and Plank 1999, Kessel et al. 2005, Rustioni et al. 2019) – has become rather popular for determining fluid compositions, the accuracy and precision of this method have been evaluated only for a single measurement of quartz solubility in water (Aerts et al. 2010). In this study, we therefore carried out additional tests to verify the reliability of the diamond trap technique: (i) We loaded capsules containing diamond traps with fluids of known composition and analyzed them by laser-ablation ICP-MS, either after simple evaporation of H2O, after freeze-drying, or in frozen state; (ii) we used the diamond trap technique to measure mineral solubilities at high pressure and temperature in several simple systems, where independent, high-quality solubility data exist; and (iii) we used the method to determine fluid compositions and fluid/mineral partition coefficients of trace elements in the eclogite-$H_2O \pm NaCl$ system. In the latter experiments, we tested the attainment of equilibrium by forward and reverse experiments and we investigated the effect of various experimental parameters, such as cooling or quench rates on the analytical results.

7.3.   Experimental methods

7.3.1. Starting materials

Several solid starting materials and solutions were prepared in order to test different aspects of the diamond trap technique. Solubility measurements were carried out for quartz, forsterite-enstatite, corundum, rutile and albite in water. The quartz was a very pure synthetic crystal

from China. Natural, inclusion-free forsterite-rich olivine (Fo$_{90}$) from San Carlos with a composition similar to that used by Newton and Manning (2002), and enstatite (En$_{89}$Fs$_{09}$Wo$_{02}$Ac$_{00}$) from a metasomatic vein in equilibrium with the peridotite also from San Carlos, were used for the forsterite-enstatite-water system. For corundum, we selected a synthetic, optical sapphire crystal that is very pure according to Laser-Ablation Inductively-Coupled-Plasma Mass-Spectrometry (LA-ICP-MS) analyses. Rutile was also a very pure synthetic crystal. For albite, a natural inclusion-free crystal from Brazil, containing only 0.2 wt. % K$_2$O and <0.05 wt. % CaO, was selected. All the different crystals were crushed into fine powders, and for the forsterite-enstatite experiment, a mixture consisting of 15 wt. % olivine and 85 wt. % enstatite was prepared.

For partitioning experiments in the eclogite-water system, we used a K-free synthetic basalt with a composition similar to the starting material of Kessel et al. (2005) to reproduce an average mid ocean ridge basalt (MORB). SiO$_2$, TiO$_2$, Al(OH)$_3$, Fe$_2$O$_3$, Mg(OH)$_2$, CaCO$_3$ and Na$_2$CO$_3$ were ground and mixed in an agate mortar under ethanol. The mixture was decarbonated in a Pt crucible at 1100 ºC for 12 hours. After cooling, the material was melted at 1600 ºC for 80 minutes and quenched in distilled water to prevent crystallization. The recovered glass was ground to a powder except for three pieces from different portions of the crucible that were analyzed by LA-ICP-MS to assess the final composition and homogeneity of the obtained starting material. In order to dope the trace elements into the MORB starting material, two diopside composition glasses with different concentration of trace elements were synthesized. To produce these doped diopside glasses, a procedure similar to that described above for the MORB was used. In the forward experiments, the basaltic starting material was mixed with 0.4, 1 or 2 wt. % of doped diopside glass in order to achieve different trace element concentrations. Circa 1 wt. % of natural garnet seeds from Grytting (Norway) eclogite was also added to enhance garnet growth during the experiments.

Saline aqueous solutions were used in some of the eclogite-fluid partitioning experiments. NaCl was directly added to distilled water to obtain 1, 5, 10 and 15 wt. % NaCl solutions. Also, in order to perform reversed experiments, two trace element-doped solutions were prepared by mixing appropriate amounts of ICP-MS calibration solution (containing 1000 ppm of each trace element in 5 % HNO$_3$). The resulting solution was evaporated under an infrared lamp and the obtained solid residue was dissolved again in a smaller amount of 5 % HNO$_3$ to increase

the trace element concentration. The resulting milky solution was left to rest for 1 month to allow the insoluble residue to sediment out. The top clear portion of the solution was then separated and analyzed by ICP-MS. Compositions of the MORB glasses and of the solutions for reversed experiments are reported in Rustioni et al. (2019).

A solution with known composition was prepared in order to test various analytical approaches. Two separate solutions were produced by dissolving CsOH and Na_2SiO_3 in distilled water in one case and NaCl and KCl in in distilled water for the other solution. The final solution was then produced by mixing the CsOH-Na_2SiO_3 solution with the NaCl-KCl solution to obtain the composition reported in Table 7.1.

7.3.2.   High pressure experiments

In all experiments, a cylindrical Au or Pt capsule with 10 mm length, 5 mm external diameter and 4.6 mm internal diameter was used. A 2 mm thick layer of diamond powder (10 – 20 μm grain size) was placed in the central part of the capsule in between two layers of solid starting material. Fluid was either completely added before the solid starting material, or it was added in several steps during the filling of the capsules. In the second case, about 1/3 of the total fluid was added at the beginning, while the remaining fluid was inserted after the diamond trap layer. This approach is particularly important when a fine-grained powder is used, to prevent the solid starting material from being suspended and contaminating the diamond trap layer during capsule preparation, which would cause an overestimation of solute content in the fluid phase during LA-ICP-MS analysis after the experiments. About 1 mm of empty space was always left at the top of the capsule to avoid fluid loss during the welding of the top lid. The weight of the capsule was always checked before and after welding. Before high pressure experiments, the capsules were also left overnight in an oven at 130 ⁰C and weighed again to test whether complete sealing was achieved.

High pressure and temperature experiments were conducted in an end-loaded piston cylinder apparatus using ½ inch MgO-NaCl assemblies with a stepped graphite furnace. Temperature was measured with a Pt/Pt-Rh (S-type) thermocouple and monitored by a Eurotherm controller. The temperature was raised at constant pressure after compression at a rate of 100 ⁰C/min. Run durations varied depending on the complexity of the system. For experiments on simple systems used in the solubility tests, the typical duration was 16 – 20 hours. In the eclogite-

water $\pm$ NaCl system, experiment duration varied from 2 to 7 days. Most of the runs were quenched by shutting off the power at constant pressure before starting the decompression. In a few experiments conducted in the eclogite-water system, a cooling ramp of 100 ºC/min was applied instead of the temperature quench.

In the eclogite-water $\pm$ NaCl experiments at 4 GPa and 800 ºC, some of the Au capsules appeared very deformed and contained small holes after the experiments. The extent of deformation could be reduced by pre-shrinking the capsule inside a hydrothermal vessel pressurized to 200 MPa before the piston cylinder runs, in order to eliminate the empty space at the top of the capsules that was considered to be mechanically weaker. However, this method did not particularly enhance the resistance of the capsule and tiny holes were still observed after experiments. The problem was eventually solved by changing the capsule material from gold to platinum and by slowly compressing and decompressing the sample over 16-20 hours at the beginning and the end of the experiments. Slow, continuous compression and decompression was achieved using an automated hydraulic spindle press that continuously changed the oil pressure on master ram and end-load according to a pre-set program.

Another challenge in the eclogite-water experiments was to synthetize crystals (in particular omphacite) large enough for LA-ICP-MS analysis. To overcome this problem, the initial fluid/solid starting material ratio in the capsule was increased from ~ 0.3 to ~ 0.4. Moreover, temperature fluctuations of $\pm$ 30 ºC were applied in experiments to enhance grain growth by Ostwald ripening, i.e. the dissolution of smaller crystals upon heating and the growth of larger
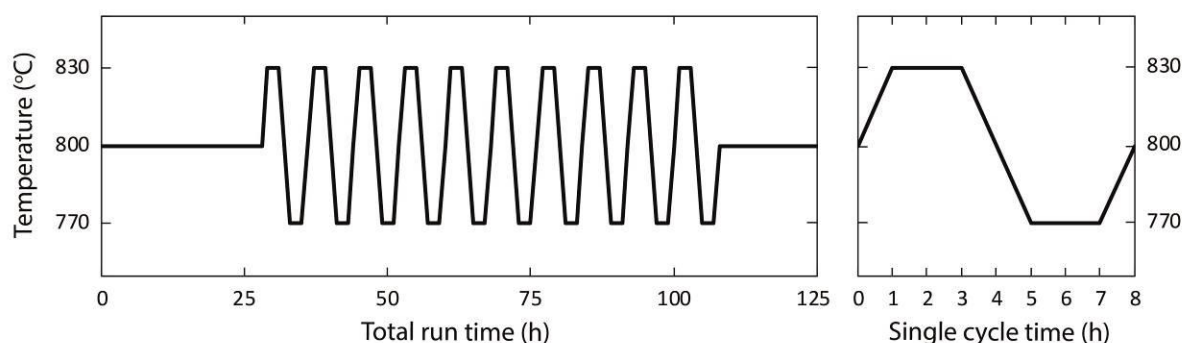

Figure 7.1. *Example of temperature profile in a typical eclogite-water system experiment in which $\pm$ 30 ºC temperature cycling was applied. On the left the entire experiment duration is shown. On the right is the detail of a single temperature cycle with a total duration of 8 hours.*

crystals during cooling. Temperature cycling started after an initial equilibration at constant temperature for ~ 36 hours to nucleate the mineral assemblage stable at 800 ⁰C. The temperature cycling was stopped ~ 24 hours before quenching to let the system equilibrate again. Ramps in temperature (from 770 to 830 ˚C and vice versa) lasted 2 hours each, with dwell times at both temperatures of 2 hours. A single temperature cycle thus lasted 8 hours in total, see Figure 7.1.

7.3.3. Analytical methods

Several analytical approaches were tested, as described below. The best quality of data was obtained when the fluid contained in the diamond trap was directly analyzed in frozen state by LA-ICP-MS following a procedure similar to that described in Kessel et al. (2004). The capsules were cooled in liquid nitrogen and then cut open longitudinally with a razor blade attached to an opening device. One half of the frozen capsule was then quickly transferred to a LA-ICP-MS sample chamber equipped with a Peltier-cooling element to keep the sample frozen during the entire measurement. Tests with H_2O-ethanol mixtures revealed that the temperature within this sample chamber was ca. -30 °C. The LA-ICP-MS measurements were performed with a 193 nm ArF GeolasPro laser ablation unit (Coherent, USA) connected to an Elan DRC-e quadrupole ICP-MS unit (Perkin Elmer, Canada). The sample chamber was flushed with He at a flow rate of 0.4 l/min, to which 5 ml/min H2 was admixed on the way to the ICP-MS. Measured isotopes included ^{7}Li, ^{9}Be, ^{11}B, ^{23}Na, ^{25}Mg, ^{27}Al, ^{30}Si, ^{35}Cl, ^{39}K, ^{43}Ca, ^{45}Sc, ^{49}Ti, ^{57}Fe, ^{85}Rb, ^{88}Sr, ^{89}Y, ^{93}Nb, ^{133}Cs, ^{137}Ba, ^{139}La, ^{140}Ce, ^{146}Nd, ^{147}Sm, ^{153}Eu, ^{157}Gd, ^{163}Dy, ^{167}Er, ^{172}Yb, ^{175}Lu, ^{181}Ta, ^{208}Pb, ^{232}Th, and ^{238}U, using a dwell time of 10 ms. The ICP-MS was tuned to a thorium oxide production rate of 0.05 – 0.10 % and a rate of doubly-charged Ca ions of 0.15 – 0.25 % based on measurements on NIST SRM 610 glass (Jochum et al. 2011). The diamond trap layer was analyzed first by moving the laser beam at constant velocity along a transect perpendicular to the diamond layer in order to locate and subsequently avoid eventual contaminations at the border of the diamond trap. A second transect, parallel to the diamond layer, was measured in the central, homogeneous part of the diamond trap. To obtain the best average of fluid composition, a large laser spot size of 50 – 70 μm and a repetition rate of 7 Hz were used. The signals resulting from each transect (a typical example is shown in Figure 7.2) were divided into 3 – 6 separate integration intervals, for which element concentrations
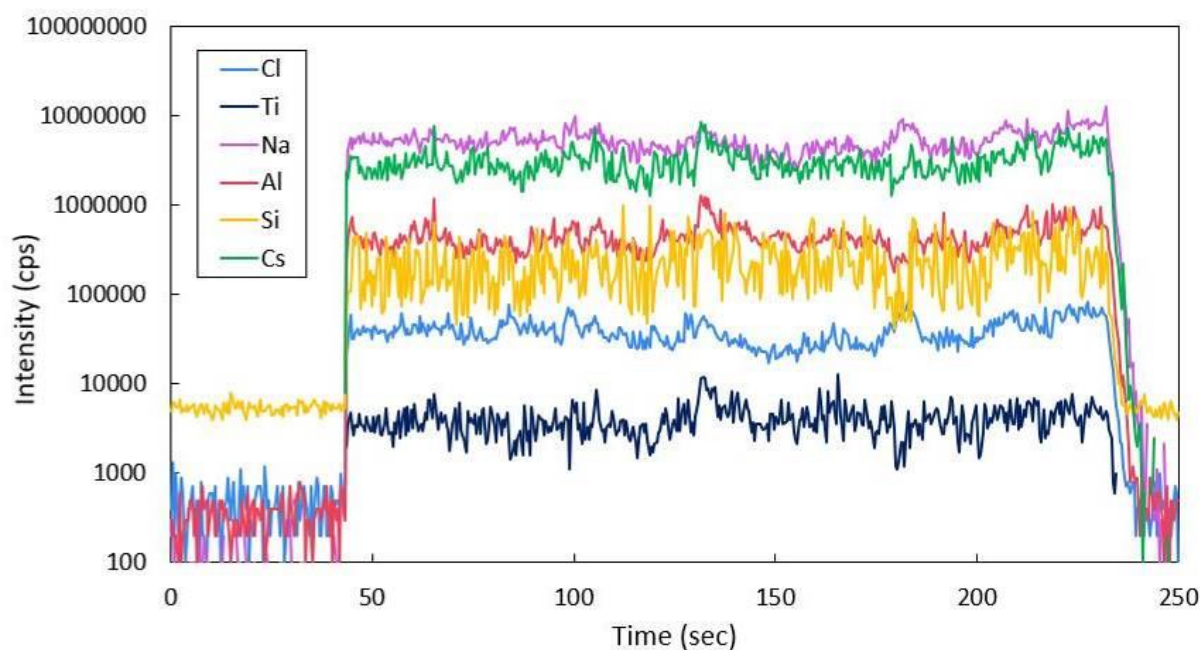
Figure 7.2. *Representative LA-ICP-MS signal collected from the frozen fluid contained in the diamond trap while moving along a transect parallel to the diamond layer from experiment PC39 conducted in the eclogite-water system at 800 °C and 4 GPa. The fluid contained approximately 7 wt. % of Cl, 6 wt. % of Na_2O, 27 wt. % of SiO_2, 1 wt. % Al_2O_3, 370 ppm of Ti and 6300 ppm of Cs.*

were calculated. The average composition of these intervals was considered to be representative of the fluid composition. The NIST SRM 610 glass and a well-characterized, natural afghanite crystal (Seo et al. 2011) were used as external standards. Cesium and/or chlorine were used as internal standard, as these elements are expected to partition strongly into the fluid in all the systems investigated in the present study. Internal standard concentrations used for calculation were corrected considering the dilution effect due to major element dissolution into the fluid during high pressure and temperature experiments.

After analysis of the diamond trap of the eclogite-fluid partitioning experiments, the capsules were left to evaporate at room temperature and subsequently they were impregnated in epoxy resin and polished to expose minerals for LA-ICP-MS measurements. The largest suitable spot sizes to analyze single crystals were typically in the range of 7 – 20 µm. Special care was taken during the garnet measurements to only analyze inclusion-free rim portions and to avoid the natural garnet seeds, which showed distinctively different composition. Averages obtained from measurements of 4 to 7 separate crystals within the capsule were used to calculate the

compositions of garnet, omphacite and rutile. Kyanite crystals were also analyzed, but trace element concentrations were always below the detection limits and thus were considered irrelevant for partitioning calculation. To calculate bulk fluid/eclogite partition coefficients, first the fluid/mineral partition coefficients for each mineral were calculated, and then the results normalized to a representative eclogitic composition of 59 % omphacite, 39 % garnet and 2 % rutile.

7.4.   Results

7.4.1.   Test of various analytical approaches

Simplified diamond trap experiments were carried out to understand which analytical approach provides the most reliable data. Capsules were prepared following the procedure described above. Undoped MORB glass was used as solid starting material, and an aqueous Na-Cl-Si-K-Cs solution of known composition (see Table 7.1) was added to the capsules. Three experiments were conducted in a cold-seal vessel at 200 MPa and room temperature for 1 hour in order to mechanically force the fluid into the pore space between the solid materials and the diamond trap without changing its composition. The retrieved capsules were weighed to check that no fluid loss or gain occurred during experiments. After these experiments, three different procedures were used to analyze the diamond traps. One capsule was cut open longitudinally and let evaporate at room conditions for three days (evaporation approach). The second was frozen in liquid nitrogen, cut open, and then transferred in frozen state into a Christ Alpha 2-4 LDplus freeze-drying apparatus with an ice condensation temperature of -85 °C, where the aqueous liquid sublimated over the course of 2 hours (freeze-drying approach). In both the evaporation and the freeze-drying approaches, after complete drying, one half of the capsule was impregnated in epoxy and polished for further analysis. For the third capsule, the procedure described in the "analytical methods" section was used (freezing chamber approach).

Results of these tests are shown in Figure 7.3 and Table 7.1, together with the original composition of the fluid loaded into the capsule. Assuming that no major change in fluid composition occurred during the experiments, the most accurate and precise method for

Table 7.1. *Tests of different analytical approaches*

Analytical approach	Initial fluid composition	Freeze-drying	Evaporation	Freezing chamber
Na_2O (wt.%)	7.74	2.5 (7)	5.6 (3)	8.02 (6)
SiO_2 (wt.%)	3.12	7 (4)	6 (2)	2.35 (9)
Cl (wt.%)*	7.62	7.62	7.62	7.62
K_2O (wt.%)	2.69	1.3 (2)	3.7 (3)	2.30 (4)
Cs (ppm)	120	110 (20)	148 (19)	115 (4)

One standard deviation is reported in parentheses in terms of the least digit cited; *Cl concentration in the fluid is used as internal standard for calculations
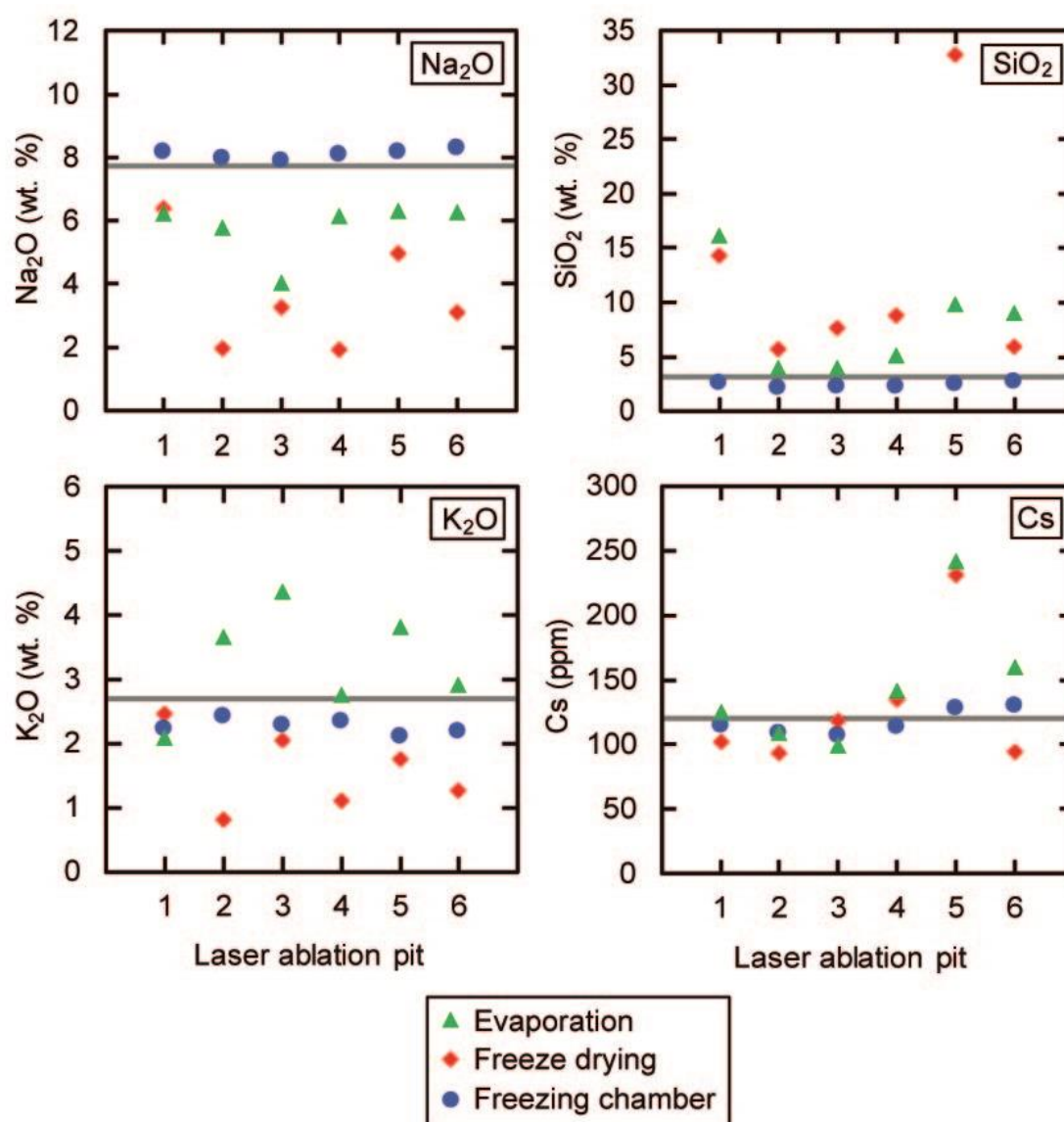
Figure 7.3. *Comparison between measurements of fluid compositions performed using three different methods: "evaporation" (green triangles), "freeze drying" (red diamonds) and "freezing chamber" (blue circles), as described in the text. The initial fluid composition is shown as a grey line.*

analysis is clearly the freezing chamber approach. The concentrations of Na, K, and Cs are reproduced within a relative deviation of 3.6, 14, and 4.2 %. Only for silica, the measured concentration is 25 % below the expected value. This could, however, reflect adsorption of silica on the surface of the glass powder in the charge. While the data obtained with the freezing chamber are very stable and reproducible, both the evaporation and the freeze-drying method give much more scattered results and even the averages sometimes deviate from the expected composition by more than a factor of two (Table 7.1). Since none of the solute components in the fluid is expected to be volatile near ambient temperature, the scatter is unlikely to be due to element loss during evaporation. However, some redistribution of elements inside the diamond trap during evaporation could very well explain the scatter of the data.

7.4.2. Solubility measurements in known systems

Several test experiments were carried out to measure mineral solubilities in water for simple, well-studied systems, in order to compare the diamond trap method with data from literature. Results are shown in Figure 7.4 and Table 7.2.

Two experiments (SC05 and SC06) were performed at 1 GPa and 800 ºC to test quartz solubility in water. This system is very well studied and there is generally a rather good agreement between various experimental data sets (e.g. Anderson and Burnham 1965, Fournier and Potter 1982, Manning 1994). At the conditions of the experiments, SiO_2 concentration in

Table 7.2. *Tests of mineral solubilities in known systems*

Experiment	Type	P (GPa)	T (ºC)	Duration (h)	SiO_2	Al_2O_3	Na_2O	TiO_2
SC05	Quartz	1	800	18	7.2 (5)			
SC06				16	4.2 (5)			
SC02	Forsterite-enstatite	1	800	20	0.94 (3)			
SC12	Corundum	2	700	19		0.101 (9)		
SC07 (top)	Rutile	2	1000	18				0.023 (2)
SC07 (middle)								0.034 (1)
SC07 (bottom)								0.028 (6)
SC03	Albite-water supercritical fluid	1.8	800	16	38.3 (7)	4.9 (2)	6.8 (3)	
SC04				16	37.0 (6)	3.0 (2)	10.6 (3)	

One standard deviation is reported in parentheses in terms of the least digit cited; Concentrations are expressed as wt. % in the fluid phase.
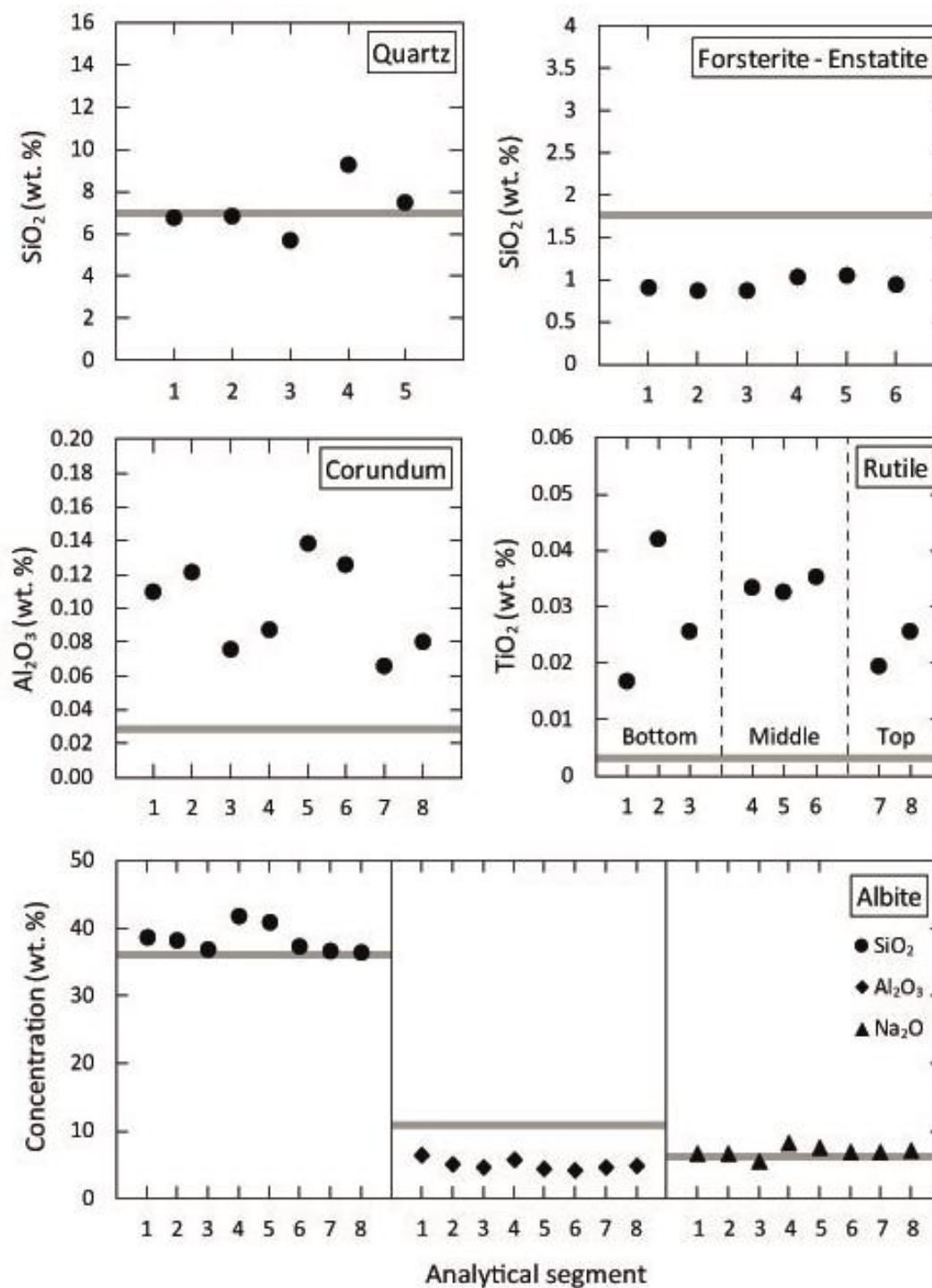
Figure 7.4. *Results of experiments to test mineral solubilities in known systems. Each graph gives the results of a single experiment, and each point represents the integration of a segment of the laser ablation transects performed on the diamond trap portions of the capsule. Expected concentrations in the fluid from the literature are shown as a grey line. The data for quartz are from Manning (1994), for forsterite-enstatite from Newton and Manning (2002), for corundum from Tropper and Manning (2007), and for rutile from Audétat and Keppler (2005). For the albite-H_2O system, the P, T conditions are beyond the critical curve (Shen and Keppler 1997) and therefore the measured composition should equal the bulk composition of the charge.*

the fluid is expected to be 7 wt. % (Manning 1994). The solubility measured in experiment SC05 is 7.2 ± 0.5 wt. %, consistent with literature data. On the other hand, experiment SC06 gave a significantly lower solubility of 4.2 ± 0.5 wt. %. The experimental procedures for SC05 and SC06 were the same, also both diamond traps show relatively homogeneous laser ablation signals along the analyzed transects, resulting in similar precision. Therefore, the reason for the lower solubility obtained from experiment SC06 is not obvious.

The solubility of silica in the forsterite-enstatite-water system at 1 GPa and 800 ºC was tested in experiment SC02. The diamond trap approach yields well-reproducible data with an average of 0.94 ± 0.03 wt. % for the SiO_2 concentration in the fluid. However, this value is significantly below the silica solubility determined by Newton and Manning (2002), who report a value of 1.77 wt. % SiO_2 at the same conditions. A possible reason for the observed low solubility could be incomplete equilibration or perhaps some error associated with the concentration of the Cs standard in the fluid. The run duration of 20 hours is at the low end of those used by Newton and Manning (2002). However, in the latter study, a double capsule technique was used in combination with single crystals, which should make attainment of equilibrium more sluggish than in the present experiments. The high reproducibility in the diamond trap, which reflects a homogeneous fluid and precipitate distribution in the capsule, is consistent with equilibrium throughout the charge.

Corundum solubility tests yielded data with both low precision and low accuracy. The average value for Al_2O_3 concentration in the fluid for a diamond trap experiment (SC12) conducted at 2 GPa and 700 ºC is 0.101 ± 0.009 wt. %. For these conditions, Tropper & Manning (2007) report a much lower corundum solubility of 0.029 wt. %. The scatter in the measured concentrations in the diamond trap may be due to inhomogeneous precipitation of solid materials either during the experiment or upon quench from high temperature. Indeed, such effects are known from previous studies. Corundum solubility increase strongly with temperature and therefore, minute temperature gradients inside a capsule may cause the dissolution and re-precipitation of corundum crystals throughout the charge. Images of such "vapor-transport crystals" are shown by Tropper and Manning (2007). They are likely responsible for the anomalously high apparent solubilities observed in experiment SC12 and for similar order-of-magnitude differences in corundum solubilities reported in previous studies (e.g. Ragnasdottir and Walther 1985, Walther 1997).

Rutile solubility in water is known to be notoriously difficult to measure. Early single-crystal weight-loss experiments in piston cylinder presses suggested very high solubilities up to 1.9 wt. % at 1 GPa and 1100 ˚C (Ayers and Watson 1993). These data were, however, very likely affected by dissolution and re-precipitation effects in a temperature gradient. In later studies, Tropper and Manning (2005) and Antignano and Manning (2008) carefully reduced temperature gradients inside the piston cylinder experiments and obtained solubilities that were orders of magnitude lower. Direct visual observation of rutile dissolution and re-precipitation in an externally-heated diamond cell yielded even lower solubilities in the range of 10 to 25 ppm at 900 to 1050 ˚C and 1 to 2.5 GPa (Audétat and Keppler 2005). As rutile solubility may be strongly affected by temperature gradients, in experiment SC07 three separated diamond traps were placed in the capsule to also test the temperature distribution. Therefore, in addition to the diamond powder layer located at the center, one diamond trap was inserted at the bottom and one at the top of the capsule, with two rutile layers dividing the three diamond layers. TiO_2 concentrations measured in the fluid with this approach are very inhomogeneous, with no systematic difference observed between the three diamond traps. As in previous studies, the measured concentrations are likely affected by dissolution and precipitation in a temperature gradient along the entire capsule. This process also leads to an overestimation of TiO_2 solubility, which at 2 GPa and 1000 ºC is expected to be about 0.003 wt. % (Audétat and Keppler 2005), while in our measurements it ranges between 0.017 and 0.042 wt. %. At face value, these numbers would be more consistent with the rutile solubility model of Antignano and Manning (2008), which predicts 0.026 wt. % TiO_2 under the run conditions. However, the scatter of the data suggests that they are likely affected by some transport process in a thermal gradient.

Two experiments (SC03 and SC04) were conducted at 1.8 GPa and 800 ºC in the albite-water system. At these conditions a supercritical fluid should form (Shen and Keppler 1997), and therefore a single, homogeneous fluid phase should fill the entire pore space in the capsule. The albite starting material was thus directly mixed with diamond and the entire capsule was regarded as a single diamond trap for the fluid. The measured fluid composition turned out to be homogeneous along the entire capsule for both experiments. As the fluid/solid ratio loaded in the two capsules was the same, the expected concentrations in the fluid for both runs are 35.9 wt. % SiO_2, 10.9 wt. % Al_2O_3, and 6 wt. % Na_2O. While SiO_2 and Na_2O show a good agreement between measured concentrations and expected values, particularly for SC03, the

data for Al_2O_3 concentration are considerably lower. As the values for SiO_2 and Na_2O are reasonable, the discrepancy of Al_2O_3 may be caused by a fractionation process. To understand the origin of this problem, we filled a smaller platinum capsule (4 mm high and 4 mm in diameter; sample AbTest) with a mixture of diamond and albite powder in a ratio of about 9:1 plus added water in a similar fluid/solid ratio as in the experiments SC03 and SC04. The capsule was compressed in a cold-seal vessel at 200 MPa without any heating and then analyzed in frozen state in the same way as SC03 and SC04. The SiO_2/Al_2O_3 ratio obtained from this test is 7.5, which is close to that obtained in SC03 and SC04, but significantly different from the theoretical SiO_2/Al_2O_3 weight ratio of 3.54 in albite. In contrast, LA-ICP-MS analyses on a larger fragment of albite using the same laser settings returned the correct SiO_2/Al_2O_3 ratio. Note that the frozen diamond trap ablates in a far less controlled fashion than solids, resulting in deep trenches that are 2-5 times wider than the used beam diameter. The uncontrolled ablation likely causes serious fractionation effects, particularly for refractory elements like Al. We thus believe that the low Al_2O_3 values represent an analytical artifact.

Overall, the data presented here suggest that the analytical precision of the diamond trap technique is high and that the accuracy is commonly within a factor of two or better, except in systems that are highly susceptible to dissolution and re-precipitation of solid phases in minor temperature gradients, such as the systems Al_2O_3-H_2O and TiO_2-H_2O.

7.4.3. Tests in partitioning experiments in the eclogite–water ± NaCl system

Compositions of fluid and minerals, and trace element fluid/eclogite partition coefficients obtained from experiments in the eclogite–water ± NaCl system using the methods described here were reported by Rustioni et al. (2019). A frequent problem in such experiments is the difficulty to obtain crystals large enough for trace element analysis. While in a crystal-melt system this can usually be solved by very slow cooling and slow crystal growth from the melt, this is not possible for a system where crystals coexist with an aqueous fluid only. However, we carried out some tests which suggest that periodic temperature fluctuations can be used to enhance crystal growth through Ostwald ripening, i.e. the dissolution of smaller crystals during heating and the growth of larger crystals during cooling. Figure 7.5 shows a comparison between an eclogite synthesized in an experiment conducted at constant temperature (a) and

one obtained with ± 30 ˚C temperature fluctuations (b). Introducing temperature cycling effectively enhanced omphacite and kyanite growth, while it did not particularly affect the size of garnet and rutile crystals. Table 7.3 reports the average compositions of garnet and omphacite in two different experiments (PC37 and PC38). Both experiments were conducted with pure water for a better comparison, but while in PC38 the temperature was kept constant at 800 ˚C, in PC37 ± 30 ˚C temperature cycling was used. The resulting compositions of both garnet and omphacite from the two experiments are very similar, indicating that although temperature cycling enhanced crystal growth, it did not affect the composition of minerals.
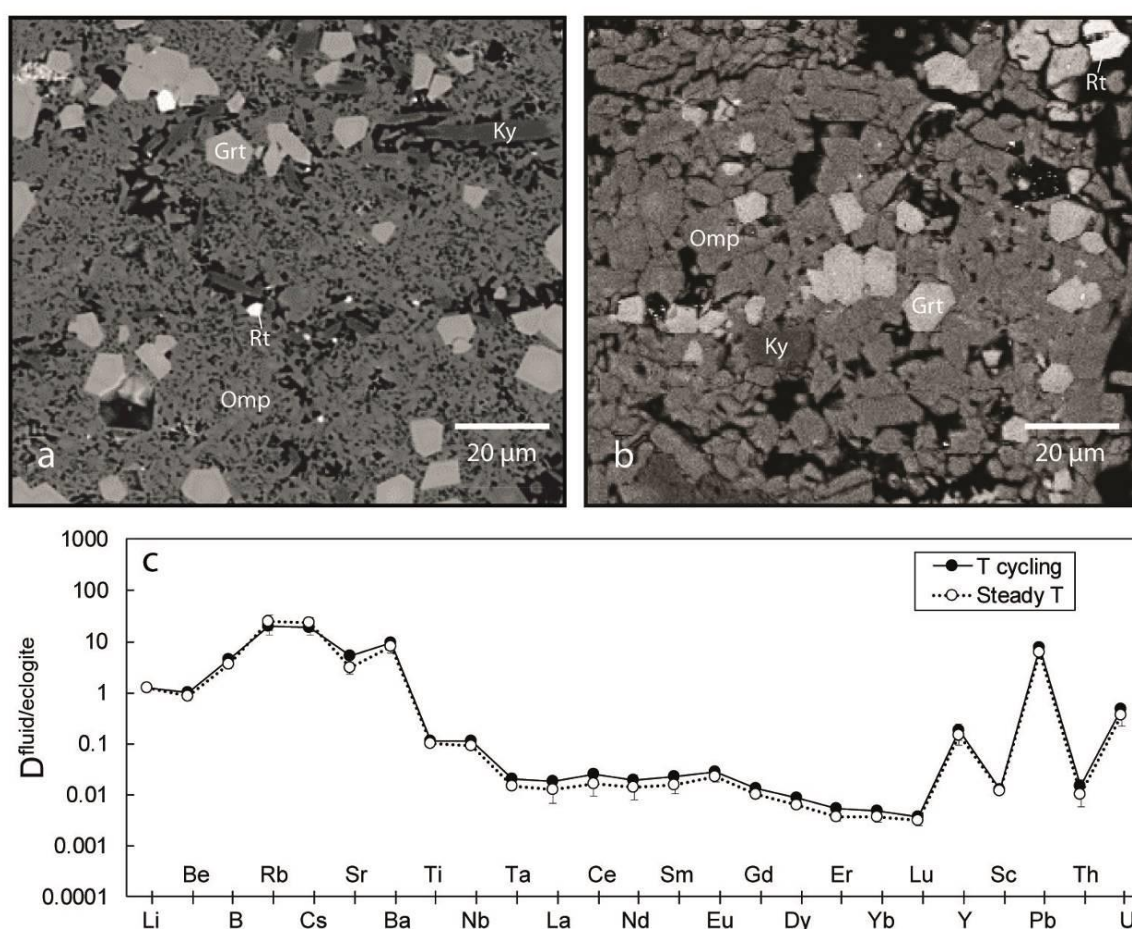
Figure 7.5. *Comparison of experimental results in the eclogite–fluid system at 4 GPa and 800 ˚C conducted with and without temperature fluctuation. (**a**) Eclogite synthetized in an experiment run at constant temperature. (**b**) Eclogite synthetized in an experiment where ± 30 ˚C cycling was used. (**c**) Comparison of trace element fluid/eclogite partition coefficient measured in two experiments conducted at 4 GPa with pure water, one at a steady temperature of 800 ˚C and the other with temperature cycling.*

Table 7.3. Effect of temperature cycling on mineral compositions in the eclogite-H_2O system at 4 GPa and 800 ˚C

Mineral	T cycling	SiO_2	TiO_2	$Al2O_3$	MgO	CaO	FeO	Na_2O
Garnet	No	46.1 (12)	0.67 (2)	19.0 (9)	7.5 (2)	9.2 (7)	17.5 (4)	0.16 (5)
	Yes	46.3 (4)	0.71 (7)	19.2 (4)	8.1 (4)	8.3 (4)	17.4 (2)	0.32 (4)
Omphacite	No	59.3 (4)	0.55 (4)	14.2 (5)	7.5 (2)	13.4 (1)	5.1 (3)	6.73 (1)
	Yes	61.4 (7)	0.45 (4)	14.6 (7)	7.3 (1)	11.8 (4)	4.5 (4)	6.88 (25)

One standard deviation is reported in parentheses in terms of the least digit cited; concentrations are expressed as wt. %.

This observation also applies for trace element compositions. A comparison between trace element $D^{fluid/eclogite}$ between the same two experiments is shown in Figure 5c. Again, the measured partition coefficients in PC37 and PC38 are the same within uncertainties. We therefore conclude that temperature cycling can be a useful technique for enhancing crystal growth in fluid-mineral partitioning experiments without compromising the validity of the measured partition coefficients (see also da Silva et al. 2017). A necessary prerequisite for applying this method is, however, that the amplitude of cycling is within the stability range of the phase assemblage of interest.

The effect of different cooling rates on measured trace element concentrations was tested by comparing experiment PC25, which was quenched from high temperature by shutting off the power resulting in a rapid cooling within 10-15 seconds, to experiment PC27, which was cooled at a constant rate of 100 ˚C/minute. All other parameters in the experimental procedure of PC25 and PC27 were the same. Figure 7.6 shows that the two different cooling rates did not have major effects on the measured partition coefficients for most of the trace elements.

In all experiments, LA-ICP-MS signals obtained from the analysis of frozen fluid in the diamond trap were relatively constant in time for the measured isotopes (Figure 7.2). As the ablation was performed by moving along transects perpendicular and parallel to the diamond layer, this reflects a generally homogeneous distribution of elements inside the trap.

Kessel et al. (2005) used a rocking multi anvil press to measure trace element partitioning in the eclogite-fluid system. Schmidt and Ulmer (2004) suggested that such a device is necessary in order to suppress the formation of extreme chemical zoning (and therefore disequilibrium) in fluid-bearing multi anvil experiments. However, while this technology may indeed offer an
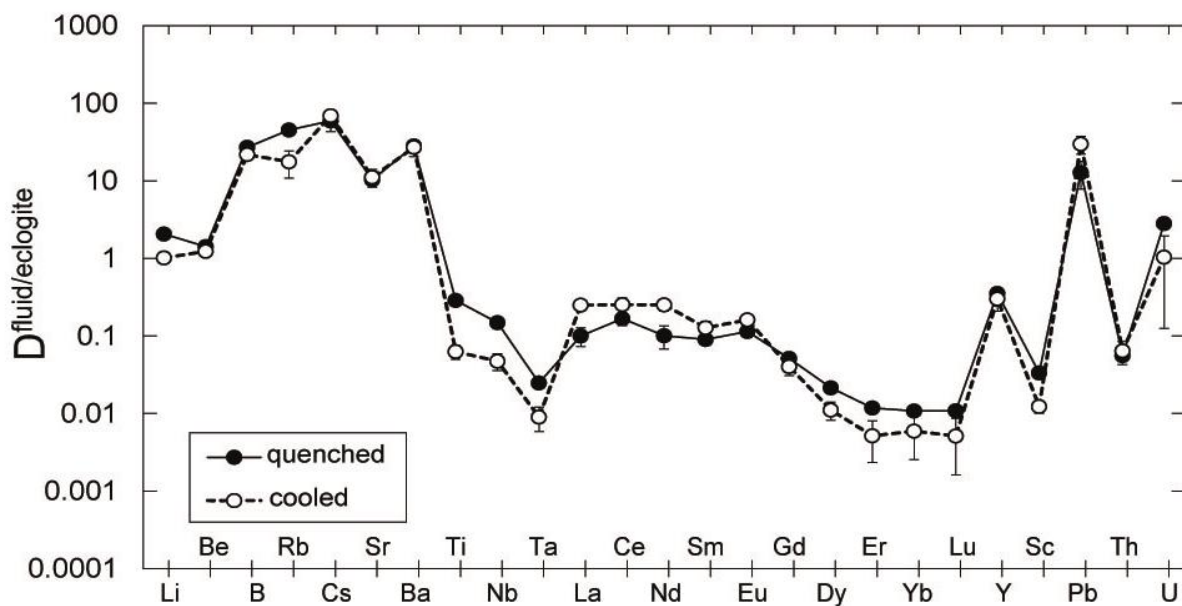
Figure 7.6. *Comparison of fluid/eclogite partition coefficients obtained from an experiment that was rapidly quenched from high temperature, versus one that was cooled down at a rate of 100 ˚C/minute. In general, variations in cooling rate were found to have little effect on the measured fluid compositions.*
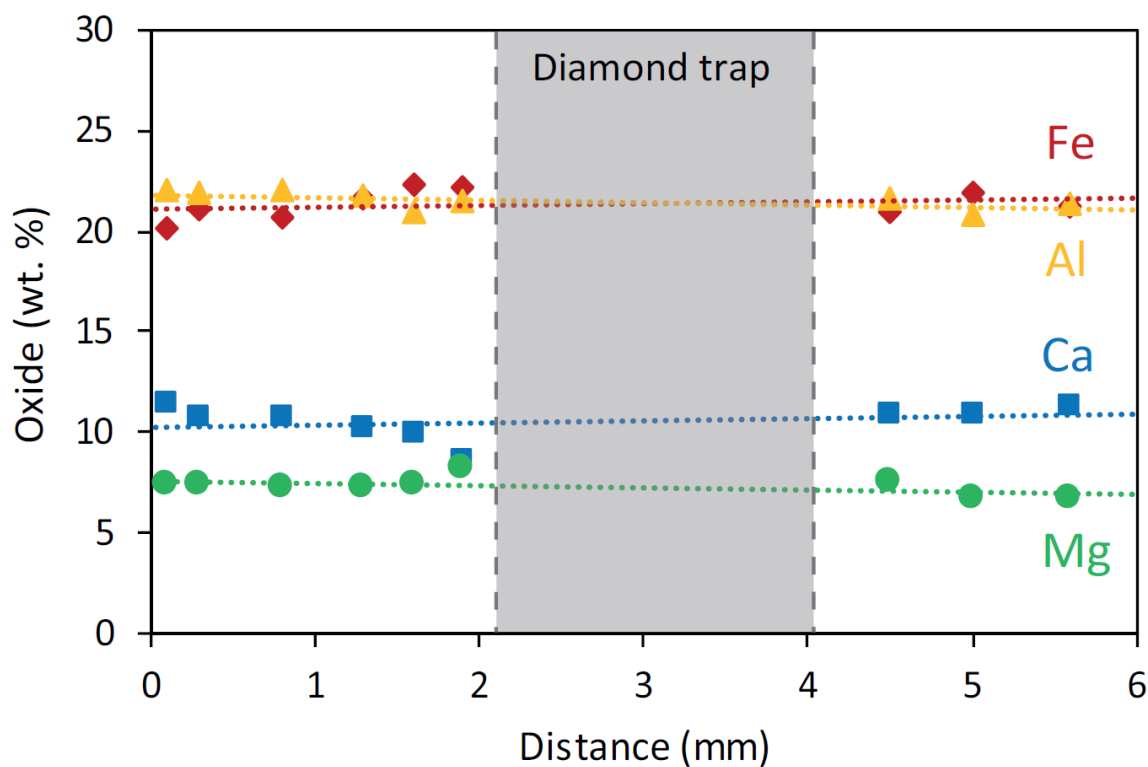
Figure 7.7. *Garnet compositions measured along a single capsule from an experiment in the eclogite-fluid system at 4 GPa and 800 ˚C. Red diamonds are iron, yellow triangles aluminium, blue squares calcium and green circles magnesium oxides.*

106

advantage for multi anvil experiments, where temperature gradients may be rather large, we did not observe any zonation or other evidence for disequilibrium in our piston cylinder experiments. Figure 7.7 shows electron microprobe measurements of garnets that were located in different areas of a capsule recovered from one piston cylinder experiment. The composition is constant throughout the entire length of the recovered charge; moreover, garnet and clinopyroxene appear to be homogeneously distributed, without obvious phase segregation in parts of the capsule. Accordingly, equilibrium was likely achieved throughout the entire charge. We therefore conclude that fluid/mineral partitioning experiments can be carried out with a simple piston cylinder device up to about 5 GPa; the use of a rocking multi anvil in this pressure range is not required.

Unlike for the mineral solubilities in simple model systems, it is not possible to test the accuracy of the data obtained in eclogite-fluid partitioning experiments against independent measurements. However, it was possible to check attainment of equilibrium between mineral and fluid phases by reversed experiments. While in "forward" experiments all the trace elements were doped in the solid starting material, in reversed experiments all the trace elements, except for Ti, were added by means of the fluid phase and an undoped MORB was used. In general, we obtained good agreement between results from forward and reversed experiments, demonstrating attainment of equilibrium in our experiments. Figure 7.8 shows the effect of Cl on the fluid/eclogite partition coefficient of europium. The enhancement of Eu solubility with addition of chlorine is the same for forward and reversed experiments.

In order to be able to measure trace element concentrations in both fluid and solid phases, it may be necessary to dope the starting material with a relatively high concentration of trace elements. At the same time, to measure meaningful partition coefficients, the concentration of trace elements must be low enough to not exceed the boundaries of Henry's law behavior. Figure 7.8 includes results from experiments conducted with different initial concentrations of europium. The fact that all experiments produce a single trend implies that the Eu concentrations used in our experiments fulfill Henry's law. Similar data on reversed experiments and variable trace element concentration for other trace elements are given by Rustioni et al. (2019).

Taken together, the good agreement between forward and reversed experiments and the independence of the measured partition coefficients on the bulk concentration of the trace elements suggests that in most cases, the diamond trap method yields reliable fluid/eclogite partition coefficients.
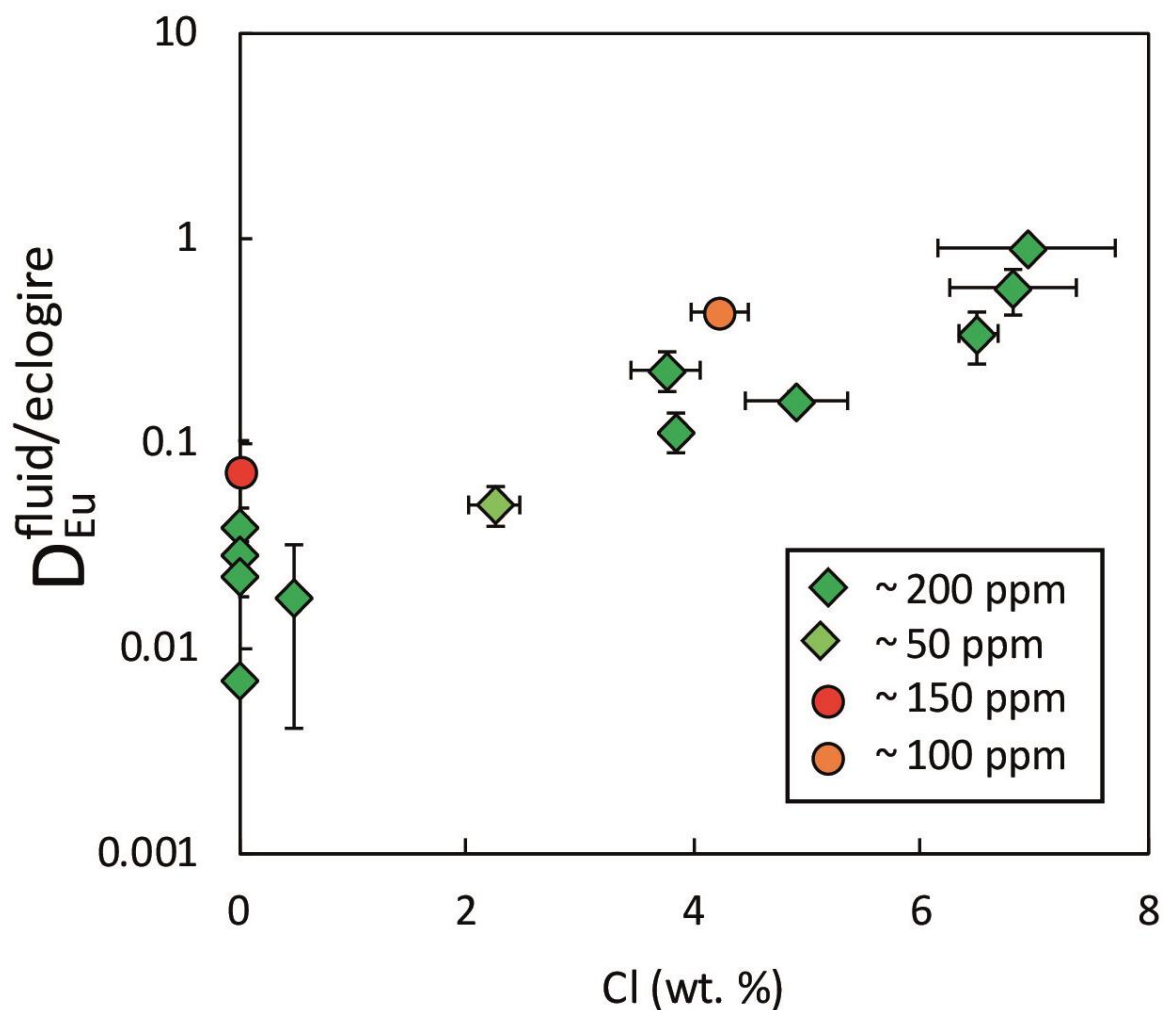
Figure 7.8. Effect of the amount of chlorine dissolved in fluid on the fluid/eclogite partition coefficient of europium. Green diamonds represent data obtained from forward experiments. Red circles are data obtained from reversed experiments. Different shades of color represent different initial concentration of trace elements in the solid starting material (green diamonds) or in the initial fluid (red circles) used in experiments.

7.5.   Implications

The systematic tests carried out in the course of this study show the potential and limitations of the diamond trap technique for studying fluid compositions. In principle, the method is widely applicable for both piston cylinder and multi anvil experiments, covering the entire pressure and temperature range of the upper mantle. At least up to 5 GPa, partitioning and solubility experiments in fluid-bearing systems may be carried out with conventional piston cylinder devices; the use of a rocking multi anvil is not required in this pressure range. Laser ablation ICP-MS analyses of the fluid in the diamond trap should always be carried out in frozen state. The method is particularly suitable for measuring partition coefficients, which may vary by several orders of magnitude and thus do not require very high precision or accuracy. However, particularly in chemically simple systems, measurements of mineral solubilities in fluids using the single-crystal weight-loss techniques, or by direct observation in diamond anvil cells, may yield more accurate results than the diamond trap method. A severe problem can be the dissolution and re-precipitation of solid phases already during the high-pressure and high-temperature experiment, which may lead to erroneously high fluid concentrations. Such effects are to be expected for phases like corundum or rutile with solubilities that are highly temperature dependent, such that dissolution and re-precipitation may occur as a result of minor temperature gradients.

7.6.   References

Aerts, M., Hack, A.C., Reusser, E., and Ulmer, P. (2010) Assessment of the diamond-trap method for studying high-pressure fluids and melts and an improved freezing stage design for laser ablation ICP-MS analysis. American Mineralogist, 95, 1523-1526

Anderson, G.M. and Burnham, C.W. (1965) Solubility of quartz in supercritical water. American Journal of Science, 263, 494-511

Antignano, A. and Manning, C.E. (2008) Rutile solubility in H_2O, H_2O-SiO_2, and H_2O-$NaAlSi_3O_8$ fluids at 0.7-2.0 GPa and 700-1000 ˚C: Implications for mobility of nominally insoluble elements. Chemical Geology, 255, 283-293.

Audétat, A. and Keppler, H. (2005) Solubility of rutile in subduction zone fluids, as determined by experiments in the hydrothermal diamond anvil cell. Earth and Planetary Science Letters, 232, 393– 402.

Ayers, J.C. and Watson, E.B. (1993) Rutile solubility and mobility in supercritical aqueous fluids. Contributions to Mineralogy and Petrology, 114, 321– 330.

Bali, E., Audetat, A., and Keppler, H. (2011) The mobility of U and Th in subduction zone fluids: an indicator of oxygen fugacity and fluid salinity. Contributions to Mineralogy and Petrology, 161, 597–613.

Bali, E., Keppler, H., and Audetat, A. (2012) The mobility of W and Mo in subduction zone fluids and the Mo-W-Th-U systematics of island arc magmas. Earth and Planetary Science Letters, 351, 195–207.

Bernini, D., Audetat, A., Dolejs, D., and Keppler, H (2013) Zircon solubility in aqueous fluids at high temperatures and pressures. Geochimica et Cosmochimica Acta, 119, 178-187

da Silva, M.M., Holtz, F., and Namur, O (2017) Crystallization experiments in rhyolitic systems: The effect of temperature cycling and starting material on crystal size distribution. American Mineralogist, 102, 2284-2294.

Fournier, R.O. and Potter, R.W. (1982) An equation correlating the solubility of quartz in water from 25 ˚C to 900 ˚C at pressures up to 10,000 bars. Geochimica et Cosmochimica Acta, 46, 1969-1973.

Jochum, K.P., Weis, U., Stoll, B., Kuzmin, D., Yang, Q.C., Raczek, I., Jacob, D.E., Stracke, A., Birbaum, K., Frick, D.A., Gunther, D., and Enzweiler, J (2011) Determination of reference values for NIST SRM 610-617 glasses following ISO guidelines. Geostandards and Geoanalytical Research, 35, 397-429.

Johnson, M.C., and Plank, T. (1999) Dehydration and melting experiments constrain the fate of subducted sediments. Geochemistry Geophysics Geosystems, 1, Article Number: 1007

Kawamoto, T., Yoshikawa, M., Kumagai, Y., Mirabueno, M.H.T., Okuno, M., and Kobayashi, T. (2013) Mantle wedge infiltrated with saline fluids from dehydration and decarbonation of subducting slab. Proceedings of the National Academy of Sciences of the USA, 110, 9663–9668.

Kelley, K.A., and Cottrell, E. (2009) Water and the oxidation state of subduction zone magmas. Science, 325, 605–607.

Keppler, H. (2017) Fluids and trace element transport in subduction zones. American Mineralogist, 102, 5–20.

Kessel, R., Ulmer, P., Pettke, T., Schmidt, M.W., and Thompson, A.B. (2004) A novel approach to determine high-pressure high-temperature fluid and melt compositions using diamond-trap experiments. American Mineralogist, 89, 1078-1086.

Kessel, R., Schmidt, M.W., Ulmer, P., and Pettke, T. (2005) Trace element signature of subduction-zone fluids, melts and supercritical liquids at 120–180 km depth. Nature, 437, 724–727.

Manning, C.E. (1994) The solubility of quartz in H_2O in the lower crust and upper mantle. Geochimica et Cosmochimica Acta, 58, 4831–4839.

Manning, C.E. (2004) The chemistry of subduction zone fluids. Earth and Planetary Science Letters, 223, 1–16.

Newton, R.C., and Manning, C.E. (2002) Solubility of enstatite + forsterite in H_2O at deep crust/upper mantle conditions: 4 to 15 kbar and 700 to 900°C. Geochimica et Cosmochimica Acta, 66, No. 23, 4165–4176.

Potter, J.M., Pohl, D.C., and Rimstidt, J.D. (1987) Fluid flow systems for kinetic and solubility studies. In: Hydrothermal Experimental Techniques (G.C. Ulmer, H.L. Barnes, eds.), John Wiley, 240-260.

Ragnarsdottir, K.V., and Walther, J.V. (1985) Experimental determination of corundum solubilities in pure water between 400–700 °C and 1–3 kbar. Geochimica et Cosmochimica Acta, 49, 2109–2115.

Rustioni, G., Audétat, A., and Keppler, H. (2019) Experimental evidence for fluid-induced melting in subduction zones. Geochemical Perspectives Letters, 11, 49-54.

Ryabchikov, I.D., and Boettcher, A.L. (1980) Experimental evidence at high pressure for potassic metasomatism in the mantle of the Earth. American Mineralogist, 65, 915-919.

Ryabchikov, I.D., Orlova, G.P., Kalenchuk, G.Y., Ganeyev, I.I., Udovkina, N.G., and Nosik, L.P. (1989) Reactions of spinel lherzolite with H_2O-CO_2 fluids at 20 kbar and 900 °C. Geochemistry International, 26, 56–62.

Schmidt, M.W., and Ulmer, P. (2004) A rocking multianvil: elimination of chemical segregation in fluid-saturated high-pressure experiments. Geochimica et Cosmochimica Acta, 68, 1889-1899.

Shen, A.H. and Keppler, H. (1997) Direct observation of complete miscibility the albite-H_2O system. Nature, 385, 710-712.

Seo, J.H., Guillong, M., Aerts, M., Zajacz, Z., and Heinrich, C.A. (2011) Microanalysis of S, Cl, and Br in fluid inclusions by LA-ICP-MS. Chemical Geology, 284, 35-44.

Stalder, R., Foley, S.F., Brey, G.P., and Horn, I. (1998) Mineral aqueous fluid partitioning of trace elements at 900–1200 °C and 3.0–5.7 GPa: New experimental data for garnet, clinopyroxene, and rutile, and implications for mantle metasomatism.

Tatsumi, Y. (1989) Migration of fluid phases and genesis of basalt magmas in subduction zones. Journal of Geophysical Research, 94, 4697–4707.

Tropper, P. and Manning, C.E. (2005) Very low solubility of rutile in H_2O at high pressure and temperature, and its implications for Ti mobility in subduction zones. American Mineralogist, 90, 502-505.

Tropper, P., and Manning, C.E. (2007) The solubility of corundum in H_2O at high pressure and temperature and its implications for Al mobility in the deep crust and upper mantle. Chemical Geology, 240, 54–60.

Tsay, A., Zajacz, Z., and Sanchez-Valle, C. (2014) Efficient mobilization and fractionation of rare-earth elements by aqueous fluids upon slab dehydration. Earth and Planetary Science Letters, 398, 101–112.

Walther, J.V. (1997) Experimental determination and interpretation of the solubility of corundum in H_2O between 350 and 600 °C from 0.5 to 2.2 kbar. Geochimica et Cosmochimica Acta, 61, 4955–4964.

Weiss, Y., McNeill, J., Pearson, D.G., Nowell, G.M., and Ottley, C.J. (2015) Highly saline fluids from a subducting slab as the source for fluid-rich diamonds. Nature, 524, 339–342.

Wilke, M., Schmidt, C., Dubrail, J., Appel, K., Borchert, M., Kvashnina, K., and Manning, C.E. (2012) Zircon solubility and zirconium complexation in $H_2O+Na_2O+SiO_2\pm Al_2O_3$ fluids at high pressure and temperature. Earth and Planetary Science Letters, 349, 15–25.

Zarei, A., Klumbach, S., and Keppler, H. (2018) The relative Raman scattering cross sections of H_2O and D_2O, with implications for in situ studies of isotope fractionation. ACS Earth and Space Chemistry, 2, 925−934.

8. The composition of subduction zone fluids and the origin of the trace element enrichment in arc magmas

Greta Rustioni, Andreas Audétat, Hans Keppler

Bayerisches Geoinstitut, Universität Bayreuth, D-95440 Bayreuth, Germany

8.1.   Abstract

The partitioning of major and trace elements between eclogite and aqueous fluids with variable salinity was studied at 700 – 800 ˚C and 4 – 6 GPa in piston cylinder and multi anvil experiments. Fluid compositions were determined using the diamond trap technique combined with laser ablation ICP-MS measurements in frozen state. In addition to NaCl, silica is the main solute in the fluids. The fluid/eclogite partition coefficients of the large ion lithophile elements (LILE), such as Rb, Cs, Sr, and Ba as well as those of the light rare earths (LREE), of Pb and of U increase by up to three orders of magnitude with salinity. These elements will therefore be efficiently transported by saline fluids released from the basaltic layer of the subducted slab. On the other hand, typical high field strength elements, such as Ti, Nb, and Ta are not mobilized by the fluids even at high salinities. Increasing temperature and pressure gradually increases the partitioning into the fluid. In particular, Th is mobilized by silica-rich fluids at 6 GPa already at low salinities. We show that we can fully reproduce the trace element enrichment pattern of primitive arc basalts by adding a few percent of saline fluid (with 5 – 10 wt.% Cl) released from the basaltic slab to the zone of melting in the mantle wedge. Only for thorium, possibly some minor contribution from a silica-rich aqueous fluid released at greater depth is required as an additional component to match the observed enrichment pattern in some cases. Assuming 2 wt. % of rutile in the eclogite equilibrated with the saline fluid produces a negative Nb Ta anomaly that is stronger than in most primitive arc basalts. Therefore, we conclude that the rutile fraction in the subducted eclogite below most arcs is likely < 1 wt. %. In fact, saline

fluids would even produce a noticeable negative Nb Ta anomaly without any rutile in the eclogite residue. Metasomatism by sediment melts alone, on the other hand, is unable to produce the enrichment pattern seen in arc basalts. Sediment melts generated at plausible slab-surface temperatures do not produce the required enrichment of light rare earth elements. Moreover, they often fail to produce the proper fractionation between Nb and the light rare earths. We therefore conclude that at least for primitive arc basalts, the release of hydrous fluids from the basaltic part of the subducted slab is the trigger for melting and the main agent of trace element enrichment. The contribution of sediment melts to the petrogenesis of these magmas is likely negligible. In the supplementary online material, we provide a "Subduction Calculator" in Excel format, which allows to calculate the trace element abundance pattern in primitive arc basalts as function of fluid salinity, the amount of fluid released from the basaltic part of the subducted slab, the fluid fraction added to the source, and the degree of melting.

8.2. Introduction

Magma generation in subduction zones is likely the main mechanism for the growth of the continental crust since the onset of plate tectonics (e.g. Hawkesworth et al. 2019). While early studies assumed that these magmas were formed by direct melting of the subducted basaltic crust (Green and Ringwood 1968), recent thermal models (Syracuse et al. 2010) imply that this is only possible under exceptional circumstances for very young and hot slabs. Direct slab melting within steeper geothermal gradients may, however, have produced the Archean TTG (tonalite trondjemite-granodiorite) suite that is a main component of the earliest continental crust (Rapp et al. 2003). Since the subduction of cold material from Earth´s surface actually reduces the temperature of the surrounding mantle, there is a general consensus that magma formation in subduction zones cannot be caused by elevated temperatures. Rather, melting point depression by the addition of water to the mantle wedge is likely the cause of magmatic activity, consistent with the generally elevated water contents in arc magmas (Métrich and Wallace 2008). Water also appears to correlate with the oxidation state of the magmas (Kelley and Cottrell 2009). Many models therefore assume that aqueous fluids released by the breakdown of hydrous minerals in the subducted slab infiltrate into the mantle wedge and trigger melting (e.g. Gill 1981, Arculus and Powell 1986, Tatsumi 1989, Peacock 1990). This

idea would be generally consistent with the typical trace element enrichment pattern seen in arc magmas (e.g. Kelemen et al. 2005), which features strong enrichments in large ion lithophile (LILE) elements, such as Rb, Cs, Sr, and Ba, which are usually considered to be soluble in aqueous fluids, while the poorly soluble high field strength elements (HFSE), such as Ti, Zr, Hf, Nb, and Ta are depleted. Accordingly, many experimental studies have been carried out in the last decades in order to constrain the composition of aqueous fluids in equilibrium with minerals of the subducted slab at high pressures and temperatures (Brenan et al. 1994, 1995, Keppler 1996, Stalder et al. 1998, Johnson and Plank 1999, Kessel et al. 2005, Bali et al. 2011, 2012, Tsay et al. 2014, 2017). Several of the earlier investigations were hampered by technical problems related to the difficulty in determining fluid compositions quenched from high-pressure experiments. Overall, the available data on the partitioning of trace elements between purely aqueous fluids and eclogite mostly suggest that such fluids are not very efficient in transporting trace elements, with the exception of some alkalis and alkaline earths. Therefore, a common notion in the recent literature is that aqueous fluids are "too dilute" to cause the trace element enrichment pattern seen in typical arc magmas (e.g. Hermann et al. 2006, Spandler and Pirard 2013).

The perceived inability of aqueous fluids to generate the trace element enrichment seen in arc magmas has led to alternative ideas on the nature of the phase that transports water from the subducted slab to the zone of melting in the mantle wedge. One possibility could be supercritical fluids intermediate in composition between aqueous fluids and silicate melts (e.g. Bureau and Keppler 1999, Portnyagin et al. 2007). Indeed, experimental data (Kessel et al. 2005) suggests that the capability of such fluids to transport many trace elements greatly increases with bulk solute content. However, as the composition of the mobile phase becomes more melt-like, the strong fractionation between LILE elements (e.g. Ba) and HFSE elements (e.g. Nb), which is characteristic for arc magmas, also diminishes. Indeed, variations in the Ba/Nb ratio of arc magmas have sometimes be attributed to variable contributions of "shallow" and "deep" fluid components (Pearce et al. 2005), the deep fluid components perhaps being rather silica-rich.

Some recent studies have suggested that sediment melts may be the main agent for the metasomatism of the mantle wedge above the subducted slab and the ultimate trigger for arc magmatism (e.g. Kelemen et al. 2005, Hermann et al. 2006, Hermann and Rubatto 2009, Skora

and Blundy 2010, Behn et al. 2011, Spandler and Pirard 2013, Skora et al. 2015). The correlation of trace element (e.g. Th/La) and isotope ratios of magmas and subducted sediments in some arcs supports some involvement of sediment melts or perhaps of fluids released from the sediment (e.g. Armstrong 1971, Turner and Foden 2001, Plank 2005). Proposing sediment melts as the main trigger of arc magmatism, however, is difficult to reconcile with the striking similarity in the trace element pattern of primitive arc basalts worldwide (see the compilation in Kelemen et al. 2005), irrespective of the presence, absence, nature, and amount of sediment subducted. Also, the rather viscous nature of silica-rich sediment melts does not match with the short timescales for fluid transfer from the slab to the zone of melting inferred from radioactive disequilibria (< 30 000 to 120 000 years, e.g., Hawkesworth et al. 1997; Turner and Foden 2001). However, sediment melts or aqueous fluids released from sediments may contribute to the chemical transport from the subducted slab to the zone of melting in the mantle wedge. Variations in magma composition within a volcanic arc are therefore often interpreted in terms of variable contributions of aqueous fluids and sediment melts (e.g. Elliot et al. 1997, Class et al. 2000, Turner and Foden 2001, Zamboni et al. 2016). On the other hand, a recent study of Klaver et al. (2020) using $\delta^{88/86}$Sr as a tracer of strontium concluded that the slab-derived fluid accounts for >70% of the Sr budget of the Mariana and Aegean arc lavas. Considering that the Aegean arc subducts 3–6 km of Sr-rich calcareous sediments, this observation casts severe doubts on the perceived importance of the sediment melts for arc magma generation.

In a recent study, Rustioni et al. (2019) demonstrated that the fluid/eclogite partition coefficient of many trace elements increases by up to three orders of magnitude upon addition of chloride to the system. Since the Cl/H$_2$O ratio in primitive arc basalts suggests fluid salinities typically ranging between 5 and 15 wt. % NaCl, it is expected that this effect also occurs in natural subduction zone fluids. The experimental data obtained by Rustioni et al. at 4 GPa and 800 ˚C suggest that saline fluids released from the basaltic part of the subducted slab may well account for the typical trace element enrichment pattern seen in primitive arc magmas. This would imply that the relative contribution of aqueous fluids and sediment melts to chemical transport below the arc needs to be reconsidered. In this study, we expand the work by Rustioni et al. (2019) by providing data on the temperature and pressure dependence of fluid/eclogite partitioning for a large suite of trace elements as well as for the major silicate components.

Moreover, we use these data to model the composition of arc magmas as function of fluid salinity, fluid fraction released from the slab and fluid fraction entering the zone of melting.

8.3. Experimental methods

8.3.1. Starting materials and sample preparation

To reproduce the composition of the basaltic portion of subducting oceanic slabs, a K-free MORB glass was synthesized, with a composition similar to that of Kessel et al. (2005). This glass was doped with 26 trace elements by addition of 2 wt. % of a trace element-rich synthetic diopside glass. About 1 wt. % of garnet seeds, selected from Grytting (Norway) eclogite and crushed into a fine powder, were also added to the starting material in order to enhance garnet growth during the experiments. Aqueous solutions with salinities of 1, 5, 10 and 15 wt. % were produced by dissolution of pure NaCl in distilled water. Two trace element doped solutions, obtained by mixing ICP-MS calibration solutions, were used in combination with the undoped MORB glass to carry out reversed experiments. Complete analyses of all starting materials are given in Rustioni et al. (2019).

To perform high-pressure experiments, the starting glass was loaded together with water or saline solutions in platinum or gold capsules. A thin layer of diamond powder was sandwiched between two layers of MORB glass to provide empty pores for fluid circulation. About 1 mm of space was left empty at the top of the capsules in order to avoid fluid losses that may be caused by heating during the welding of the top lid. Each capsule was weighed before and after welding to ensure that no major fluid loss occurred. For piston cylinder experiments, cylindrical capsules with an outer diameter of 5 mm, 0.2 mm wall thickness, and 10 mm length were employed. In the case of multi anvil experiments, Pt tubes with 4 mm outer diameter, 0.15 mm wall thickness, and 5 mm length together with lids were used as capsules. After the sealing of the top lid and before multi anvil experiments, the capsules were pre-compressed to a length of 4 mm to fit into the assembly. This procedure eliminates the empty space originally left at the top of the capsules, thus maximizing the amount of material that can be loaded in each experiment.

8.3.2. Piston cylinder experiments

High-pressure experiments at 4 – 5 GPa and 700 – 800 ˚C were performed using an end-loaded piston cylinder apparatus. ½ inch MgO-NaCl assemblies with a stepped graphite furnace were used. Temperature was measured with an S-type thermocouple (Pt/Pt-Rh) and monitored by a Eurotherm controller. Long compression and decompression durations, up to 20 hours, were applied to reduce the deformation of the capsule. Temperature was increased after compression with a heating rate of 100 ˚C/min. Fluctuations in temperature of $\pm$ 30 ˚C were applied to most of the experiments in order to enhance mineral growth by Ostwald ripening. Experiments were quenched by switching off the electrical power at constant pressure before decompression. Total run durations ranged between 3 and 7 days.

8.3.3. Multi anvil experiments

Experiments at 6 GPa and 800 ˚C were carried out in a Walker-type a multi anvil apparatus following the pressure calibration of Keppler and Frost (2005). We used tungsten carbide cubes as secondary anvils, pyrophyllite gaskets, and a 25/15 (octahedral edge length/truncation edge length in mm) assembly consisting of an outer MgO octahedron that contains a ZrO_2 sleeve, a stepped graphite furnace and an inner MgO sleeve, in which the sample capsule is kept at the center by MgO spacers and Mo caps. All MgO parts were heated to 1000 ˚C for 1 hour to remove eventual moisture before being assembled. Experiments were compressed and decompressed within 15 hours. As for piston cylinder experiments, temperature was raised at a rate of 100 ˚C/min after compression. A D-type ($W_{97}Re_3$ – $W_{75}Re_{25}$) thermocouple was employed to monitor the temperature during experiments. High pressure and temperature conditions were maintained for 3 days. The runs were terminated by rapid quench before decompression.

8.3.4. Laser ablation ICP-MS analyses

Both fluid and mineral compositions were determined by laser ablation inductively coupled plasma mass spectrometry (LA-ICP-MS). After high pressure experiments, the recovered capsules were cooled in liquid nitrogen and cut in half in frozen state to expose the diamond trap. The diamond layer still containing the frozen fluid was then analyzed along two

119

perpendicular transects by means of a LA-ICP-MS equipped with a freezing chamber able to maintain the sample at a temperature of - 30 ˚C during the entire measurement. The instrument used consists of a 193 nm ArF GeolasPro laser ablation unit (Coherent, USA) connected to a Elan DRC-e quadrupole ICP-MS unit (Perkin Elmer, Canada). After the determination of fluid composition, each capsule was impregnated in epoxy and polished. Garnet, omphacite and rutile crystals were then analyzed again using LA-ICP-MS. For further details about the experimental and analytical procedures see Rustioni et al. (2019, 2021).

8.4.   Results

8.4.1.   Bulk fluid compositions

During the runs, the glassy starting material always transformed into a well-crystallized eclogitic assemblage of omphacite + garnet + rutile ± kyanite. Representative microprobe analyses of these phases are given in Rustioni et al. (2019). The major element composition of the fluid coexisting with the eclogitic assemblage are shown in Figures 8.1 and 8.2 for each experiment; see also Table 8.4 in the supplementary online material. The total solute contents shown include SiO_2, Al_2O_3, Na_2O, CaO, FeO, MgO and Cl. These totals are highly dependent on fluid salinity, ranging from an average of about 20 wt. % solutes in experiments conducted at 4 GPa and 800 ˚C without NaCl, to an average of about 40 wt. % in experiments with more than 6 wt. % of Cl at the same conditions. As illustrated by Figure 8.1, an increase in temperature of 100 ˚C at 4 GPa significantly enhances bulk solubility, yielding a total solute content of about 5 wt. % at 700 ˚C, but about 20 wt. % at 800 ˚C for a Cl-free fluid. The effect of salinity is similar at both temperatures.

The major solute in all experiments is SiO_2, which alone represents on average 65 % of the total solute content. At 4 GPa, SiO_2, together with Al_2O_3, does not show a significant increase in solubility upon addition of Cl to the fluid, both oxides being more sensitive to temperature. On the other hand, the solubilities of Na_2O, CaO, FeO, and MgO markedly increase with fluid salinity. In particular, Na_2O concentration is mostly a function of Cl content in the fluid, while CaO, FeO and MgO solubilities are also affected by temperature. The nearly linear increase of
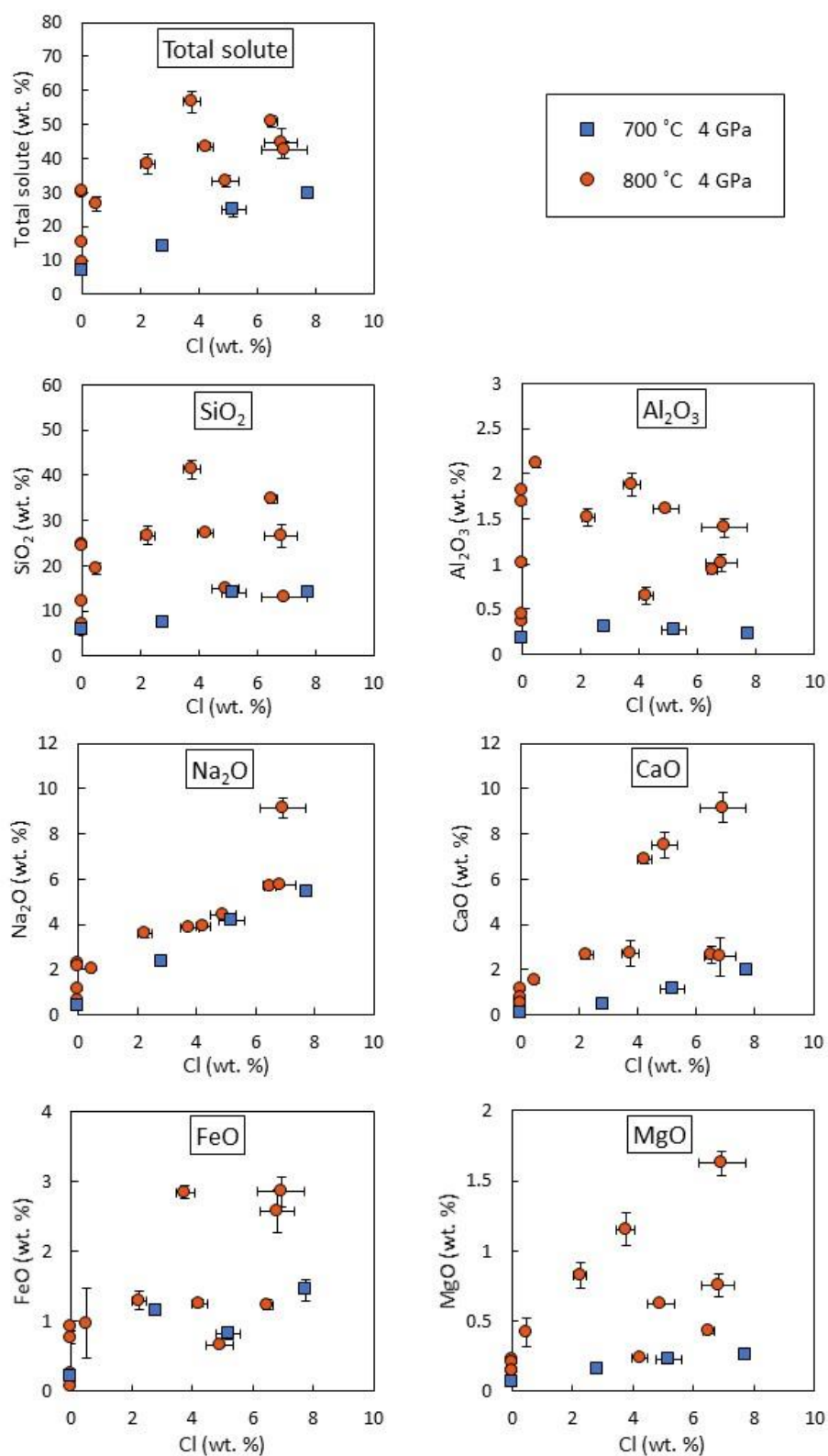
Figure 8.1. *Bulk composition of saline fluids in equilibrium with an eclogitic assemblage from high-pressure experiments at 4 GPa and 700 - 800 ˚C. "Total solute" is the sum of all oxide components plus Cl, with a slight negative correction for the fact that 1 Cl⁻ replaces ½ O²⁻ in the fluid.*
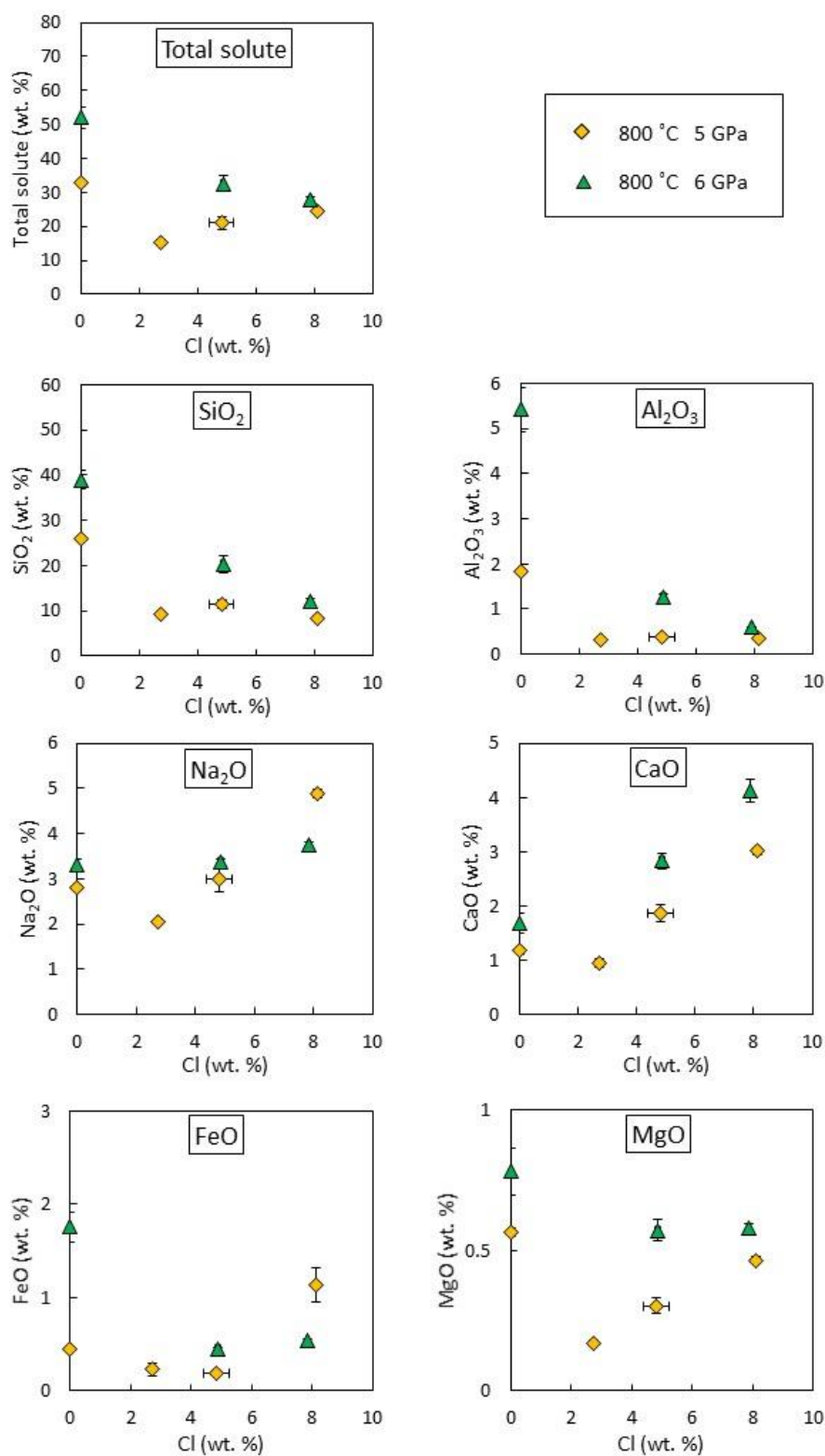
Figure 8.2. *Bulk composition of saline fluids in equilibrium with an eclogitic assemblage from high-pressure experiments at 5 and 6 GPa and 800 ˚C. "Total solute" is the sum of all oxide components plus Cl, with a slight negative correction for the fact that 1 Cl⁻ replaces ½ O²⁻ in the fluid.*

Na_2O, CaO, and MgO concentrations in the fluid at 4 GPa is most likely due to the formation of some undissociated species with a metal:chloride ratio of 1:1 in the fluid, such as NaCl, Ca(OH)Cl, and Mg(OH)Cl.

With pressure increasing to 5 and 6 GPa, the dependence of fluid composition on salinity changes (Figure 8.2). SiO_2 and Al_2O_3 now markedly decrease with salinity, which also translates into a decrease of bulk solute at 6 GPa. While CaO increases with Cl at all pressures, the effect diminishes for Na_2O, FeO and MgO at 5 GPa and nearly disappears or reverts at 6 GPa. Very likely, these effects are due to the high bulk silica contents of Cl-free fluids at 5 and particularly at 6 GPa, where the fluids may be considered to approaching a "supercritical" state, intermediate in composition between typical aqueous fluids and silicate melts. At these high silica contents, cations may dissolve mostly as neutral silicate species or silicate complexes. Upon addition of Cl, silicate anions compete with chloride for cations, such that the effect of Cl on oxide solubilities becomes less pronounced. The negative effect of Cl on silica solubilities is consistent with previous observations Cruz and Manning (2015) in the quartz-H_2O-NaCl system at 1.5 - 2 GPa, but higher temperatures.

As demonstrated by Rustioni et al. (2021), solubilities in aqueous fluids measured with the diamond trap method yield results accurate within a factor of two. While this has a minor effect in the determination of trace element partition coefficients, which may vary by orders of magnitude, this factor may be significant for major element contents and it may explain the significant scatter in some of the data reported in Figures 8.1 and 8.2.

8.4.2.   Trace element partition coefficients

As already observed by Rustioni et al. (2019), fluid/eclogite partition coefficients are highly affected by fluid salinity at 4 GPa and 800 ˚C. In particular, light rare earths show an increase in solubility of up to three orders of magnitude with an addition of 7 wt. % of Cl. A significant, even though smaller, solubility enhancement is observed also for large ion lithophile elements (LILE), as well as for Pb, Th and U. On the other hand, fluid salinity does not have a significant effect on the partitioning behavior of high field strength elements (HFSE). Similar results were found also in experiments conducted at lower temperature (700 ˚C) and higher pressure (5 and 6 GPa). Results from these experiments are shown in Figure 8.3 and 8.4 in comparison to the data from Rustioni et al. (2019). Complete analytical data are compiled in Tables 8.4 to 8.9 in

the supplementary online material. The strong enhancement of the fluid/eclogite partitioning of the light rare earth elements by chloride is seen at all P,T conditions, while the heavy rare earths as well as Nb and Ta are never affected by salinity.

A detailed inspection of the data shows that at 4 GPa, temperature has only a minor effect on the fluid/eclogite partitioning of trace elements (Figure 8.3). The partition coefficients measured at 700 ˚C tend to be slightly lower than at 800 ˚C, but the dependence on fluid salinity
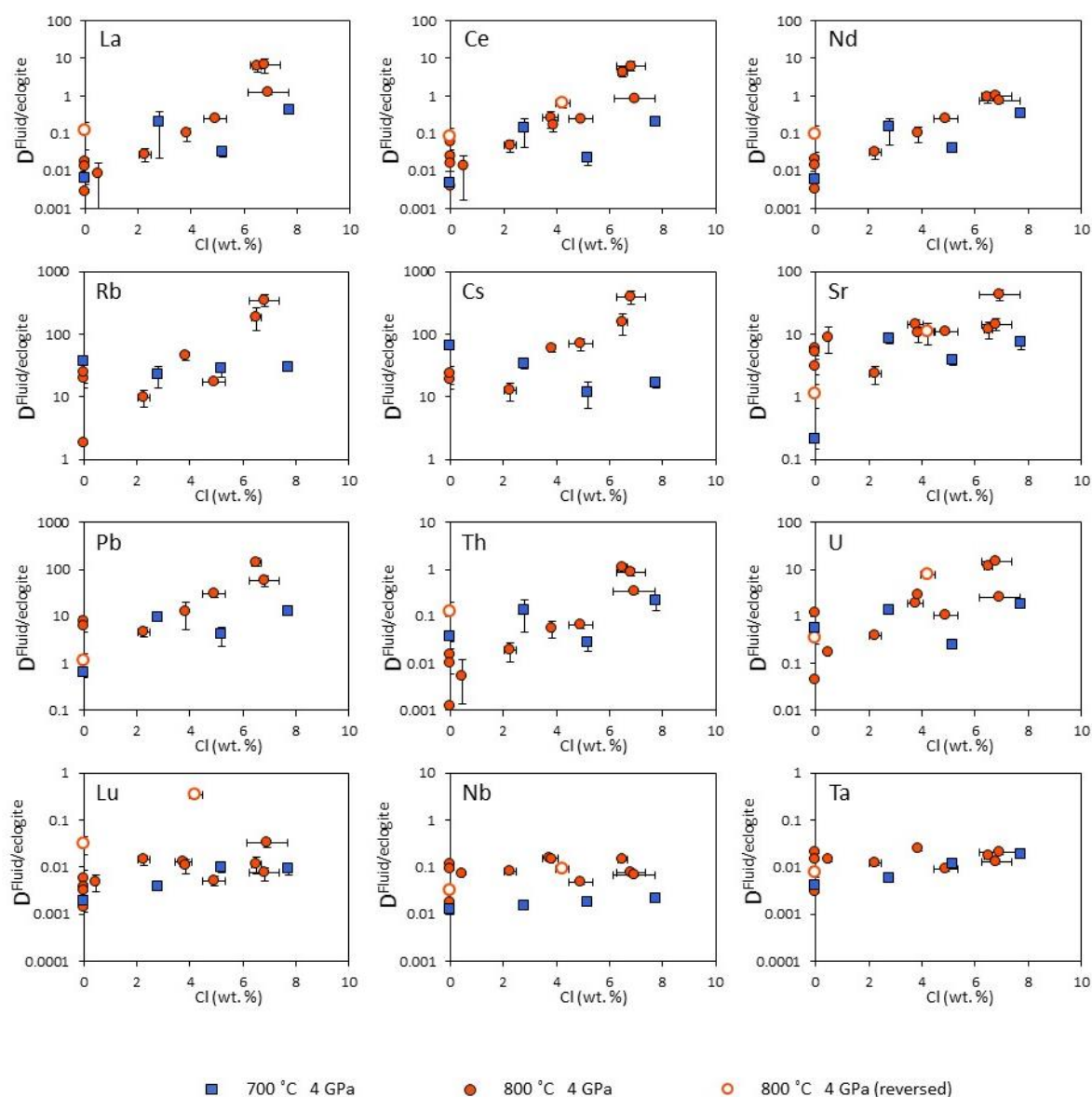
Figure 8.3. *Influence of fluid salinity on the fluid/eclogite partition coefficient of trace elements at 4 GPa and 700 – 800 ˚C.*

is similar. A notable exception are Rb and Cs, where the 700 ˚C data appear to be nearly independent of fluid salinity; very likely, this is an artifact due to incomplete equilibration at the lower temperature. $D_{Nb}^{fluid/eclogite}$ increases by one order of magnitude with temperature increasing from 700 to 800 ˚C. A pressure increase from 4 to 5 or 6 GPa does not fundamentally alter the partition coefficients and their dependence on salinity for most elements. However, notable exceptions from this are Th and U; for both elements, the partitioning into the fluid at low salinity is strongly enhanced by pressure, in agreement with previous observations by
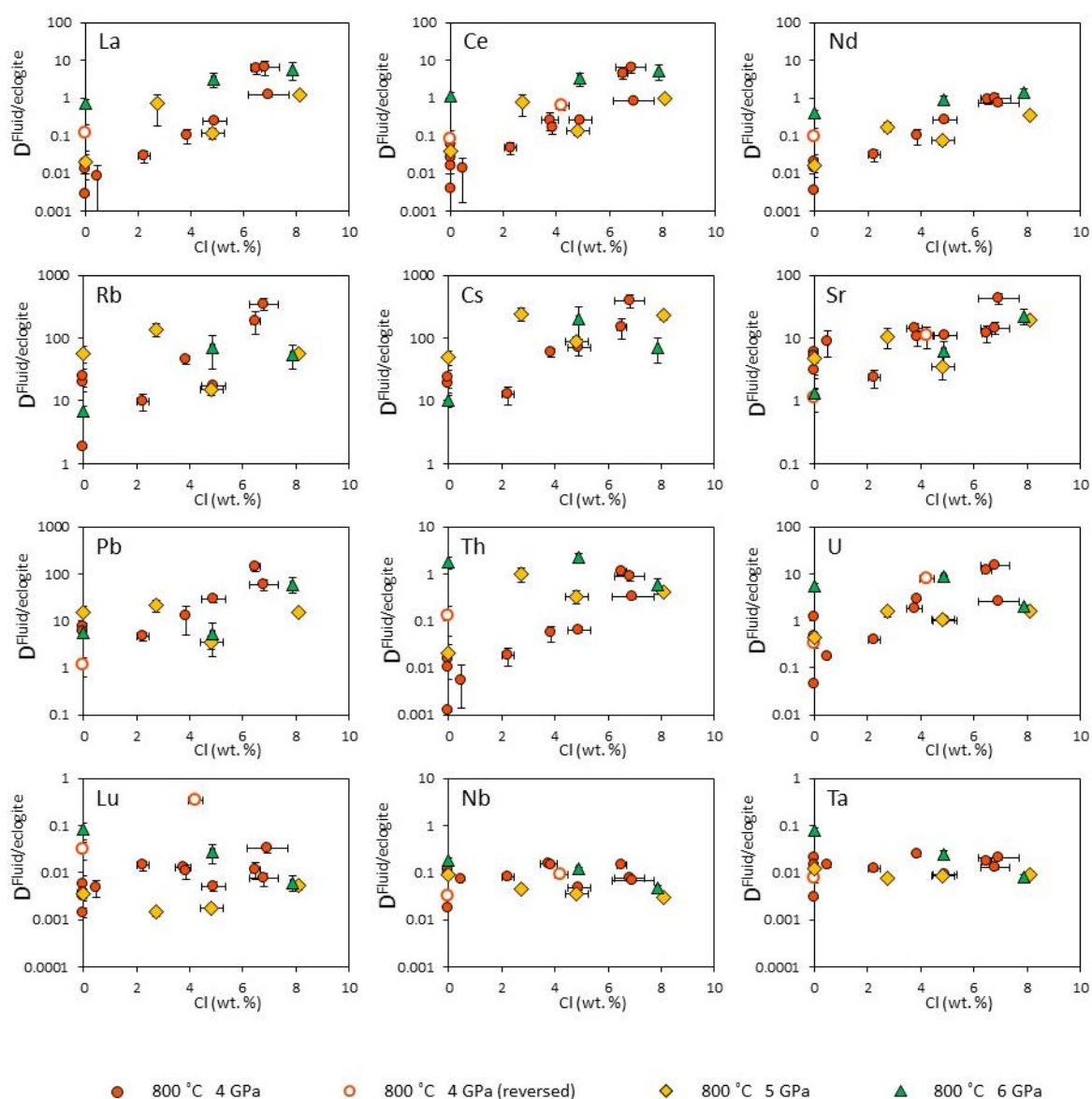
Figure 8.4. *Influence of fluid salinity on the fluid/eclogite partition coefficient of trace elements at 5 - 6 GPa and 800 ˚C.*

Kessel et al. (2005). Very likely, the interaction with silicate species due to the greatly enhanced silica solubility in the fluid (see above) is responsible for this effect. A similar, but weaker enhancement of fluid/eclogite partitioning with pressure at low salinity is also observed for La and Ce.

The reported bulk fluid/eclogite partition coefficients ($D^{fluid/eclogite}$) were calculated from the individual fluid/mineral partition coefficients. In order to constrain the sole effect of changes in fluid salinity on the trace element partitioning behavior, in these calculations the eclogite modal composition is fixed at 59 % omphacite, 39 % garnet and 2 % rutile.
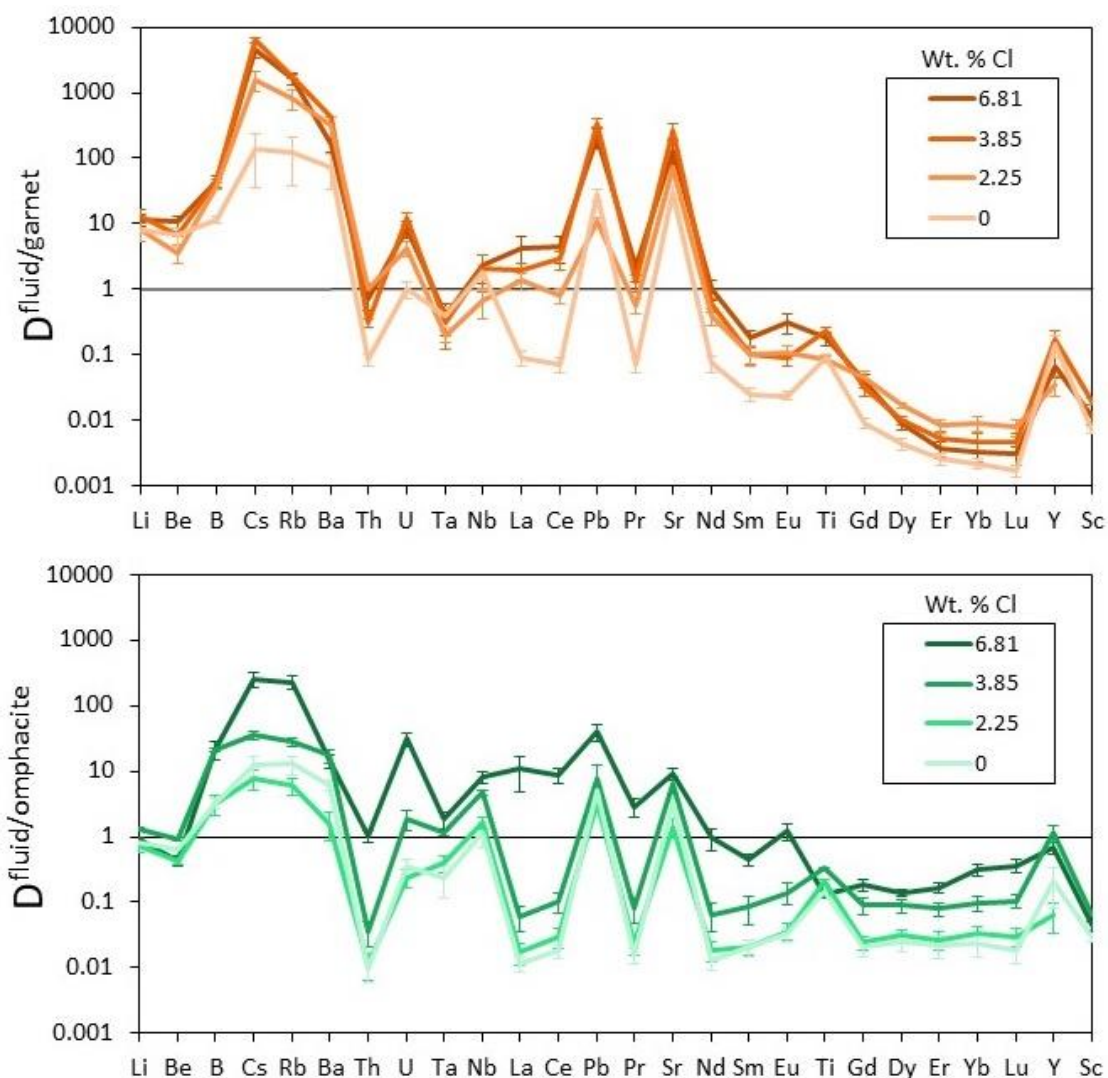
Figure 8.5. *Fluid/garnet (above) and fluid/clinopyroxene (below) partition coefficients of various trace elements at 4 GPa and 800 ˚C.*

Different eclogite modal compositions may also cause changes in the bulk fluid/eclogite partition coefficients. The individual $D^{fluid/mineral}$ for garnet and omphacite and the effect of fluid salinity on those are shown in Figure 8.5. Garnet retains in general less trace elements than omphacite, with the exception of the heavy rare earth elements. Therefore, increasing the modal abundance of garnet relative to omphacite generally enhances $D^{fluid/eclogite}$, except for the heavy rare earth elements.

As rutile is able to retain a large amount high field strength elements, but none of the other investigated trace elements, its presence, even in small proportions, only affects the partitioning
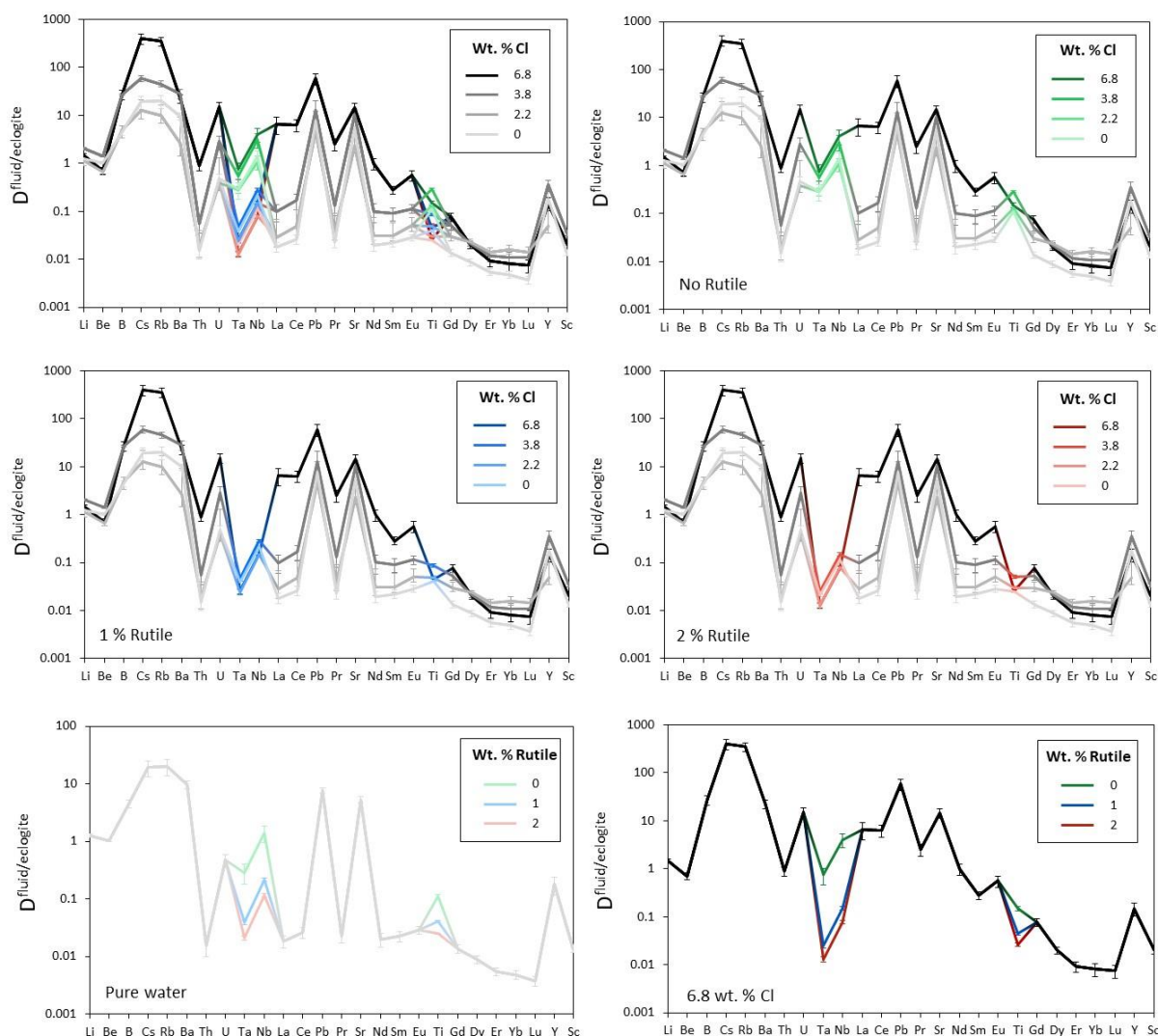
Figure 8.6. *Bulk fluid/eclogite partition coefficients of trace elements at 4 GPa and 800 °C with different rutile contents in the eclogite and for variable fluid salinities. The diagram in the upper left corner summarizes the results from the other diagrams.*

behavior of Nb, Ta, and Ti, leaving the remaining trace element pattern essentially unaltered. Figure 8.6 shows the $D^{fluid/eclogite}$ calculated without and with 1 or 2 % of rutile in the eclogite. These results show that the presence of rutile strongly depletes the fluid in Nb and Ta, especially for high salinities. This effect is similar for the addition of 1 or 2 % rutile, implying that already small proportions of this mineral can greatly affect the $D^{fluid/eclogite}$ for Nb and Ta. Still, a depletion in these elements relative to the light rare earths is never observed for pure water, even with rutile in the eclogitic assemblage. For high salinities on the other hand, a slight negative anomaly in Nb and Ta is already produced even in the absence of rutile.

8.5. Discussion

8.5.1. Comparison with previous studies

As noted by Rustioni et al. (2019), the fluid/eclogite partition coefficients of trace elements measured in this study for pure water (without NaCl) are generally in very good agreement with those obtained by Kessel et al. (2005) using similar methods. However, there is an apparent discrepancy between this study and some previous publications, which suggested that complexing by chlorine does not significantly enhance the fluid/mineral partitioning of trace elements in aqueous fluids under typical subduction zone conditions. Brenan et al. (1995) observed only a minor enhancement of the fluid/clinopyroxene partition coefficients of Sr and Pb upon addition of NaCl at 900 °C and 2 GPa. However, the NaCl concentrations used in that study were rather low, 0.5 molal, which corresponds to just 1.77 wt. % Cl. This concentration is small compared to the concentration range investigated in the present study and it is also at the low end of fluid salinities inferred from the Cl/H$_2$O ratio of primitive arc basalts (Métrich and Wallace 2008). Stalder et al. (1998) claimed that adding up to 5 m HCl has "nearly no effect" on the fluid/garnet partition coefficient of a large suite of trace elements at 10 °C and 4 – 5 GPa. However, they carried out only two experiments with Cl-bearing fluids. Moreover, there is only one single pair of experiments under otherwise equal conditions, where only the HCl content of the fluid varied. If one compares their experiments no. 57 and 64, $D_{Ba}^{fluid/garnet}$ increased from 16 to 59 and $D_{Sr}^{fluid/garnet}$ increased from 13 to 31 upon addition of 1.5 M HCl. Only $D_{Pb}^{fluid/garnet}$ appeared to decrease. Moreover, we note that many of the partition coefficients reported by Stalder et al. (1988) are in striking contrast to more recent experimental

data obtained with improved experimental methods. For example, their data would suggest that Nb always partitions strongly in favor of the fluid in equilibrium with clinopyroxene or garnet, even more so than Sr, while both the data of Kessel et al. (2005) and of Rustioni et al. (2019) suggest much lower fluid/mineral partition coefficients of Nb.

Support for the enhancement of fluid/mineral partition coefficients by chloride complexing under subduction zone conditions comes from a number of recent studies. Both Tsay et al. (2014) and Tropper et al. (2011) observed major increases in the solubilities of $La_2Si_2O_7$ and $CePO_4$, respectively in aqueous fluids at 1 – 2.6 GPa and 600 – 800 ˚C upon addition of chloride. Bali et al. (2001) observed similar effects for UO_2 solubility in aqueous fluids at 1.5 – 2.6 GPa. Kawamoto (2014) studied the fluid/melt partitioning of Pb, Rb, and Sr by direct in-situ synchrotron fluorescence in the hydrothermal diamond anvil cell to 1.3 GPa and 830 ˚C and observed a strong enhancement of the partitioning of these elements into the fluid with increasing chloride concentration. However, Tsay et al. (2017) studied the fluid/eclogite partitioning of a large suite of trace elements at 590 – 800 ˚C and 2.4 – 2.6 GPa and did not observe enhanced fluid/eclogite partitioning of trace elements upon the addition of NaCl. This result is rather curious, as it appears to contradict the study of Tsay et al. (2014) from the same group, which found a major enhancement of the solubility of the light rare earths in aqueous fluids upon addition of NaCl. Possibly, the data reported by Tsay et al. (2017) involve incomplete equilibration between the eclogite and the fluid, perhaps due to early formation and closure of the fluid inclusions used to trap the fluid. While they used some in-situ fracturing method to control the time of inclusion formation, it is not implausible that some fluid inclusions may already have formed rather early during the run, such that the fluid trapped was not in equilibrium with the eclogite.

8.5.2.   A numerical model for the trace element signature of primitive arc basalts

In order to better constrain the mechanism of magma generation in subduction zones, we use our data to quantitatively model the trace element composition of partial melts from a mantle wedge metasomatized by saline fluids released from the basaltic part of the subducted slab. We will then compare these data with the worldwide compilation of primitive arc basalt compositions from Kelemen et al. (2005). For modeling the composition of the fluids released from the slab, we use our fluid/eclogite partitioning data for 4 GPa and 800 ˚C. These

conditions fall right in the middle of the subduction zone thermal profiles as compiled by Syracuse et al. (2010). We argue that they are plausible for an eclogite just after the dehydration of amphibole, which is expected to be the major carrier of water in the basaltic part of the slab. The experimental study of Schmidt and Poli (1998) places the high-pressure stability limit of amphibole near 2.4 GPa. These experiments were, however, carried out with 5 wt.% water added to the system. Mandler and Grove (2016) pointed out that the apparent stability limit of amphibole in mantle peridotite strongly depends on the amount of water added to the charge in experiments. This is because alkalis – which are required to form amphibole – strongly partition into the fluid. High fluid fractions in the charge therefore destabilize amphibole. Mandler and Grove (2016) showed that for water contents < 1 wt. %, the high-pressure stability limit of amphibole approaches 4 GPa. While these data were obtained for a peridotitic bulk composition, a similar effect likely also occurs in basaltic systems, implying that the high-pressure stability limit of amphibole may well be 1 GPa higher than inferred by Schmidt and Poli (1998). Therefore, our experimental data for 4 GPa and 800 ˚C may capture the conditions during or just after amphibole dehydration.

The experimental data on the fluid/eclogite partitioning of trace elements in this study and in Rustioni et al. (2019) were obtained with a starting material free of potassium and phosphorus, very similar to that used in the previous study of Kessel et al. (2005). This is justified, as both K (0.160 wt. % K_2O) and P (0.184 wt. % P_2O_5) are only trace constituents in MORB (Gale et al. 2013). As pointed out by Rustioni et al. (2019), the high phosphorus solubility in garnet (Konzett and Frost 2009) implies that in an eclogite of MORB composition, separate phosphate phases such as apatite are unlikely to be stable. For similar reasons, phengite is expected to be either completely absent or present only in trace amounts. This is supported by an experimental study of Carter et al. (2015) who did not observe any apatite or phengite in an eclogite produced at 3 GPa and 800 ˚C from a natural MORB starting material. Hermann (2002) suggested that allanite may be an important phase retaining light rare earth elements and thorium in subducted eclogites. However, in an experimental study of a natural MORB composition up to 2.8 GPa, Sisson and Kelemen (2018) could not detect any allanite or any other epidote group mineral above 750 ˚C. We are therefore confident that our fluid/eclogite partitioning data, which are based on an eclogite with omphacite + garnet + rutile mineralogy can be directly used to model trace element transport from the basaltic part of the subducted slab to the mantle wedge.

In our model, we assume that the composition of the basaltic part of the subducted slab corresponds to the "all MORB" average from Gale et al. (2013) and the peridotite in the mantle wedge above the slab has the composition of the depleted mantle as estimated by Salters and Stracke (2004). For predicting the partitioning of trace elements between aqueous fluids and eclogite, we used the equation

(1) $$D^{fluid/eclogite} = a\, e^{\,b\, Cl}$$

where $D^{fluid/eclogite}$ is the fluid/eclogite partition coefficient of the element considered and Cl is fluid salinity in wt. % Cl; a and b are regression coefficients calibrated by our experimental data and tabulated for each element in Table 8.1. The concentration of a trace element in fluid c_{fluid} in equilibrium with the MORB eclogite was then calculated assuming batch equilibrium using the equation

(2) $$c_{fluid} = \frac{D^{fluid/eclogite} c_{MORB}}{1 + x_{fluid}(D^{fluid/eclogite} - 1)}$$

where x_{fluid} is the mass fraction of the fluid in the eclogite and c_{MORB} is the concentration of the trace element in the MORB eclogite according to Gale et al. (2013).

The composition of the metasomatized peridotite in the zone of melting in the mantle wedge was then calculated according to

(3) $$c_{source} = x_{fluid}\, c_{fluid} + (1 - x_{fluid})\, c_{peridotite}$$

where c_{source} is the trace element concentration in the source, x_{fluid} is the mass fraction of fluid added and $c_{peridotite}$ is the concentration in the depleted mantle according to Salters and Stracke (2004).

The composition of partial melts from the metasomatized mantle source was then obtained from the following equation, which assumes batch melting:

(4) $$c_{melt} = \frac{c_{source} / D^{peridotite/basalt}}{1 + x_{melt}(1 / D^{peridotite/basalt} - 1)}$$

131

Table 8.1. *Regression coefficients for the dependence of the fluid/eclogite partition coefficient of trace elements at 4 GPa and 800 ℃ on fluid salinity.*

Trace element	a	b	X^2	R^2
Li	0.355 ± 0.215	0.346 ± 0.151	6.12	0.972
Be	1.021 ± 0.176	0.003 ± 0.045	13.14	0.001
B	3.514 ± 1.009	0.379 ± 0.065	1.09	0.991
Rb	3.003 ± 2.243	0.669 ± 0.184	3.08	0.935
Cs	10.202 ± 4.586	0.470 ± 0.103	1.42	0.952
Sr	2.408 ± 0.804	0.368 ± 0.083	2.39	0.928
Ba	4.339 ± 2.570	0.347 ± 0.142	3.66	0.852
Ti	0.007 ± 0.002	0.223 ± 0.109	276.04	0.048
Nb	0.018 ± 0.001	0.233 ± 0.056	91.81	0.337
Ta	0.003 ± 0.006	0.239 ± 0.065	36.10	0.354
La	0.005 ± 0.002	0.961 ± 0.118	0.96	0.976
Ce	0.010 ± 0.004	0.855 ± 0.106	1.10	0.968
Nd	0.008 ± 0.003	0.714 ± 0.076	0.70	0.984
Sm	0.010 ± 0.004	0.588 ± 0.088	1.55	0.985
Eu	0.017 ± 0.005	0.572 ± 0.070	1.15	0.981
Gd	0.005 ± 0.001	0.462 ± 0.053	14.89	0.565
Dy	0.005 ± 0.002	0.456 ± 0.134	4.34	0.920
Er	0.003 ± 0.001	0.171 ± 0.079	12.19	0.214
Yb	0.003 ± 0.009	0.204 ± 0.077	9.47	0.292
Lu	0.002 ± 0.008	0.235 ± 0.085	9.19	0.265
Y	0.035 ± 0.013	0.387 ± 0.091	2.81	0.901
Sc	0.013 ± 0.004	0.056 ± 0.075	18.48	0.123
Pb	2.428 ± 1.137	0.565 ± 0.117	1.75	0.939
Th	0.003 ± 0.002	0.809 ± 0.117	1.30	0.971
U	0.109 ± 0.061	0.727 ± 0.135	2.13	0.949

Data were fitted to equation (1) $D^{fluid/eclogite} = a\,e^{\,b\,Cl}$

For some elements, R^2 is below 0.9; these are typically elements with fluid/eclogite partition coefficients that are nearly independent of Cl, such that equation (1) does not describe the partition behavior well and the scatter in the data may be larger than the variability due to Cl.

where c_{melt} is the concentration of some trace element in the partial melt, x_{melt} is the mass fraction of melt and $D^{peridotite/basalt}$ is the bulk partition coefficient of the trace element between peridotite and melt. $D^{peridotite/basalt}$ was calculated from individual mineral/melt partition coefficients for a mixture of 60 wt. % olivine, 30 wt. % orthopyroxene, 5 wt. % garnet and 5

wt. % clinopyroxene coexisting with the partial melt. Mineral/basalt partition coefficients for REE, Ba, U, Th, Pb, Y, and Nb were taken as averages of the experimental data reported in from Salters et al. (2002). Clinopyroxene/basalt and garnet/basalt partition coefficients for Rb were taken from Klemme et al. (2002), for Sr from Johnson (1994). The partitioning of Sr and Rb into olivine and orthopyroxene was assumed to be zero. Titanium (Ti^{4+}) partition coefficients were taken from Mallmann and O´Neill (2009) and from Johnson (1994). In general, since the trace elements considered here are mostly incompatible in peridotite, variations in the values of the mineral/melt partition coefficients have a rather minor effect on the final result of the calculation. For this reason, possible variations due to the presence of water in the melt (e.g. Sun and Liang 2012) were also ignored.

The results of the calculations outlined above depend on four independent parameters: (i) the fluid salinity, (ii) the fluid fraction in the eclogite, (iii) the fluid fraction added to the source of melting, and (iv) the degree of melting in the mantle wedge. Of these four variables, the fluid salinity is by far the most important parameter, since the fluid/eclogite partition coefficient of some trace elements increases exponentially with salinity, while others are nearly independent of salinity. Fluid salinity therefore does not only produce the strongest absolute variations in final melt composition, but it also changes the fractionation of the various trace elements relative to each other. In contrast to this, the other three parameters – fluid fraction in eclogite, fluid fraction added to the source, and degree of melting in the mantle wedge have some influence on the absolute level of trace element enrichment in the final melt, but they induce only minor variations in the fractionation of trace elements relative to each other.

For fluid salinity, we explored a parameter space up to 10 wt. % Cl in the fluid, which would be equivalent to about 16 wt. % of NaCl. This is well within the range of fluid salinities inferred from the Cl/H_2O ratio in primitive arc basalts (Métrich and Wallace 2008). Experimentally, we have calibrated partition coefficients to about 7 wt. % Cl in the fluid, such that only a minor extrapolation is involved in our modeling. For the fluid fraction in the eclogite, we consider values between 1 and 2 wt. % most plausible, considering that amphibole itself contains only about 2 wt. % water. Higher fluid fractions would likely require some external source (e.g. serpentine dehydration of the hydrated mantle below the basaltic layer). While such an external addition of water is possible, it is also likely that at some distance from the source the fluid flow becomes channelized (e.g. Zack and John 2007, John et al. 2012, Plümper et al. 2017),

such that only a small fraction of the basaltic layer might be affected. Therefore, in our calculations, we mostly assumed a fluid fraction in the eclogite layer of 2 wt. %. Reducing this to 1 wt. % has only a minor effect on the final trace element enrichment pattern. Essentially, at the lower fluid fraction, the abundances of the most fluid-mobile elements (Ba, Sr, Rb, Pb) increase slightly in the final melt composition, while the other elements are hardly affected. This is because at low fluid fraction, for most elements the concentration in the fluid approaches $D^{fluid/eclogite} \cdot c_{MORB}$, i.e. it is nearly independent of fluid fraction. Only for the elements with very high $D^{fluid/eclogite}$, already at low fluid fraction the reservoir becomes strongly depleted in these elements and the aforementioned approximation cannot be used anymore; the concentration in the fluid will then decrease with increasing fluid fraction. For the fluid fraction added to the source, we consider values from 2.5 to 10 wt. %. Plausible values for the degree of melting in the mantle wedge are probably between 10 and 30 %. This parameter has the smallest effect on the final melt composition and therefore, for most calculations, we assumed it to be around 20 %.

In the supplementary online material, we provide a "Subduction calculator" as Excel spreadsheet, which allows a rapid assessment of expected melt composition according to the model outlined above. Calculations with a model fluid released from the basaltic part of the subducted slab at 6 GPa are also possible. The regression coefficients for the fluid/eclogite trace element partitioning at 6 GPa are compiled in Table 8.2. However, 6 GPa is beyond most of the dehydration reactions expected in a subducted slab and a model based solely on a fluid composition produced at such high pressures is not very plausible. The following discussion, is therefore mostly based on the data at 4 GPa and 800 °C.

Figure 8.7 shows arc magma compositions predicted by our model, assuming 2.5 wt. %, 5 wt. %, or 10 wt. % fluid addition to the source of melting in the mantle wedge, with fluid salinities ranging from 0 to 10 wt. % Cl. The data are shown in comparison to a global compilation of average primitive arc magma compositions from Kelemen et al. (2005). This compilation includes data from the Kermadec, Lesser Antilles, Marianas, New Hebrides, Scotia, Tonga, Aleutian, Andean, Cascades, Central America, and Kamchatka arcs. The model data clearly show that metasomatism by a pure aqueous fluid cannot account for the trace element enrichment in arc magmas, as this would only produce minor enrichments of the most fluid-

Table 8.2. *Regression coefficients for the dependence of the fluid/eclogite partition coefficient of trace elements at 6 GPa and 800 ˚C on fluid salinity.*

Trace element	a	b	X^2	R^2
Li	2.449 ± 1.781	-0.008 ± 0.100	28.68	0.004
Be	1.630 ± 0.372	-0.103 ± 0.038	2.84	0.845
B	9.451 ± 1.392	0.137 ± 0.024	0.38	0.973
Rb	7.056 ± 1.517	0.269 ± 0.063	1.38	0.807
Cs	10.227 ± 3.660	0.252 ± 0.093	2.58	0.654
Sr	1.285 ± 0.114	0.356 ± 0.021	0.23	0.982
Ba	2.431 ± 0.518	0.483 ± 0.065	1.37	0.866
Ti	0.209 ± 0.018	-0.114 ± 0.019	0.35	0.972
Nb	0.986 ± 0.140	-0.115 ± 0.027	0.22	0.937
Ta	0.378 ± 0.039	-0.205 ± 0.019	0.09	0.985
La	0.740 ± 0.072	0.274 ± 0.024	0.14	0.978
Ce	1.146 ± 0.066	0.197 ± 0.015	0.07	0.987
Nd	0.396 ± 0.020	0.163 ± 0.010	0.06	0.995
Sm	0.268 ± 0.002	0.044 ± 0.001	0.01	0.999
Eu	0.359 ± 0.057	0.021 ± 0.035.	0.90	0.261
Gd	0.136 ± 0.016	-0.017 ± 0.025	0.39	0.292
Dy	0.098 ± 0.021	-0.158 ± 0.009	0.04	0.995
Er	0.108 ± 0.005	-0.273 ± 0.037	0.47	0.953
Yb	0.099 ± 0.030	-0.329 ± 0.050	0.74	0.922
Lu	0.088 ± 0.026	-0.328 ± 0.051	0.66	0.837
Y	1.583 ± 1.194	-0.463 ± 0.120	0.99	0.734
Sc	0.069 ± 0.034	-0.224 ± 0.077	3.15	0.783
Pb	5.354 ± 2.312	0.081 ± 0.224	5.67	0.069
Th	2.216 ± 1.326	-0.123 ± 0.112	8.79	0.467
U	5.956 ± 3.554	-0.121 ± 0.110	6.35	0.499

For explanation, see Table 8.1

mobile elements Rb, Ba, Sr, and Pb. This result is quite consistent with the frequent view that aqueous fluids are "too dilute" to produce the enrichment seen in arc magmas (e.g. Hermann et al. 2006, Spandler and Pirard 2013). However, the situation changes completely once saline fluids are considered. Already a fluid with 5 wt.% Cl produces an enrichment of Rb, Ba, U, Pb, and Sr that similar to that observed in many arc basalts. Only the light REE (La and Ce) and in

particular Th require higher fluid salinities to match the enrichment observed in natural magmas. The enrichment of La and Ce are well reproduced by salinities between 7 and 10 wt. % Cl. For thorium, the highest salinities near 10 wt. % Cl yield values overlapping with primitive arc basalt compositions. Therefore, the modeling results shown in Figure 8.7 show very clearly that virtually the entire trace element enrichment pattern observed in primitive arc basalts can be reproduced by melting a depleted mantle source metasomatized by saline fluids.
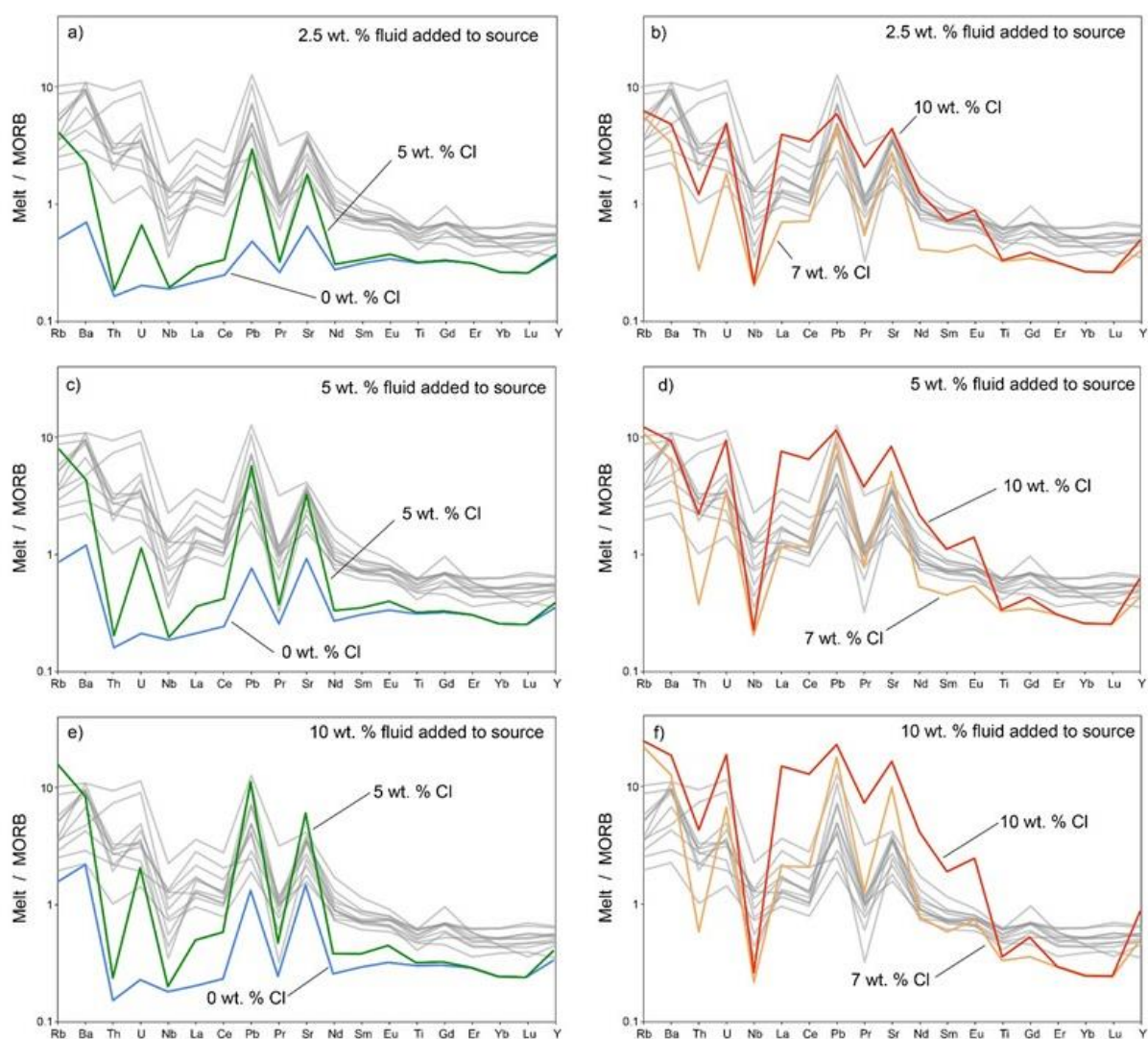
Figure 8.7. Predicted trace element enrichment patterns for partial melts of the mantle wedge enriched by aqueous fluids from the basaltic layer of the subducted slab. Compositions for primitive arc basalts as compiled by Kelemen et al. (2005) are shown as grey lines for comparison. All data were normalized to the "all MORB average" of Gale et al. (2013). Model calculations are shown for 2.5 to 10 wt. % fluid addition to the source and for fluid salinities from 0 to 10 wt. % Cl. Note: The model result for Pr is not directly calculated, but interpolated between Ce and Nd.

For salinities between 7 and 10 wt. % Cl, already 2.5 wt. % fluid addition to the source of melting are sufficient to match most of the arc basalt patterns. High salinities above 7 wt. % Cl are particularly important to match the natural thorium abundances.

When discussing thorium abundances, it is important to note that the appearance of a plot as in Figure 8.7 depends very much on the choice of the MORB composition used for standardization. Here, for consistency, we use the "all MORB average" of 0.404 ppm Th from Gale et al. (2013) for standardization, which was also used for calculating the composition of fluids released from the slab. However, this number is more than two times higher than the often-used N-type MORB abundance of 0.1871 ppm Th from Hofmann (1988). Even the "all normal MORB average" from Gale et al. (2013) is with 0.353 ppm Th still about twice the value quoted by Hofmann (1988). The rather high enrichment of Th in arc magmas suggested by some MORB-normalized diagrams is therefore partially an artifact of normalization to a likely less-representative Th abundance in MORB. Nevertheless, the enrichment of Th in some of the primitive arc basalts would require metasomatism by a very Cl-rich fluid released from the slab at 4 GPa and 800 ˚C. There is, however, an obvious alternative possibility. Pearce et al. (2005) noted in a study of the Mariana arc that the Th/Ba ratio in magmas very much increases with the depth of the slab and they therefore attributed the Th addition mainly to a "deep subduction component". Indeed, in the study of Kessel et al. (2005) in a Cl-free system, increasing the pressure from 4 to 6 GPa at constant temperature of 800 ˚C increases the partitioning of Th into the fluid by about one order of magnitude, while the effect on Ba is more subtle. Our data (Figure 8.4) show a similar enhancement of thorium partitioning into the fluid with pressure for low-salinity fluids. It is therefore entirely plausible that the relatively high Th abundances in some primitive arc basalts may reflect the influence of an additional fluid component released from the slab at higher pressures. Another, perhaps less likely explanation could be that the Th enrichment is due to an additional complexing agent in the fluid, such as fluoride. Fluoride complexing is known to enhance thorium mobility at lower pressures (Keppler and Wyllie 1990) and the recent study of Tsay et al. (2017) showed such an effect also under mantle conditions. However, as noted above, we suspect that the latter study suffered from some incomplete attainment of equilibrium. Moreover, the fluorine abundance in arc magmas is typically one order of magnitude below the chlorine abundance (Straub and Layne 2003), which also makes a significant effect of fluoride complexing on trace element enrichment in arc magmas rather unlikely, although not completely impossible.

A general observation from Figure 8.7 is that our models produce a negative Nb anomaly (and by inference Nb Ta anomaly) that is more pronounced than in most arc basalts. This is, however, the result of assuming 2 wt. % of rutile in the residual eclogite. Reducing the rutile fraction would diminish the magnitude of the negative Nb Ta anomaly. In fact, the data shown in Figure 6 suggest that such an anomaly could also be produced by saline fluid without any rutile in the eclogite residue. The comparison of our modeling results with the observed arc basalt patterns in Figure 8.7 therefore suggests that the fraction of rutile in the eclogite that released the metasomatizing fluid must be rather small.

While the model outlined above is very successful in reproducing the trace element pattern of arc magmas, it contains a number of simplifications. The fluid released from the basaltic part of the slab almost certainly does not have a constant composition. Rather, upon decomposition of amphibole or other hydrous minerals, Cl very likely strongly partitions into the fluid, although there are now experimental data that would allow a quantification of this effect. Therefore, the very first fluid released from the slab likely has high salinity, which then

decreases upon further dehydration. Accordingly, one would expect that the trace element enrichment patter of a real arc magma is a somehow weighed average of the curves for different salinities shown in Figure 8.7. Since, however, the fluid/eclogite partition coefficient of many trace element increases exponentially with salinity, this means that the first aliquot of highly saline fluids contributes a disproportionally high fraction of the trace elements. Therefore, while the curves shown in Figure 8.7 may suggest that the trace element enrichment in arc magmas requires very high salinities, the average salinity of the fluids added to the source may actually be considerably lower. This effect nicely reconciles the fluid salinities required for the trace element enrichment with those inferred from primitive melt inclusions from arc basalts, which range mostly from 5 to 15 wt.% NaCl equivalent (Métrich and Wallace 2008).

Another important effect that is not directly considered in our model is the modification of fluid composition by interaction with the nominally anhydrous minerals of the mantle peridotite during percolation to the zone of melting. According to Mierdel et al. (2007), at temperatures of 800 – 900 ˚C as they are expected in the mantle just above the slab surface, orthopyroxene may dissolve up to 0.5 wt% water. Any aqueous fluid percolating through this part of the mantle wedge will therefore likely lose water and become more concentrated. While this process will not affect the delivery of the incompatible trace elements to the mantle wedge, it is important

to understand the water budget of the entire process. The models shown in Figure 8.7 involve 2.5 – 10 wt. % fluid addition to the source of melting. Assuming that this fluid contained 60 – 70 wt. % water and the water is completely incompatible during melting, this would mean that for 20 % partial melting, the magma generated contains 8 – 32 wt. % of water. While the lower bound of this estimate is entirely realistic for primitive arc basalts (Métrich and Wallace 2008, Goltz et al. 2020), the upper bound is clearly out of the range of water contents observed in nature. However, if some of the water originally present in the fluid has been lost due to interaction with the mantle peridotite before it reaches the zone of melting, this problem disappears. During the "desiccation" of the fluid, the flux of trace elements transported likely would not change, as they are mostly highly incompatible in mantle minerals, as is chlorine (Bernini et al. 2013). The excess solute in the fluid, which is mainly silica, would probably react with olivine to form some orthopyroxene during the percolation process. Evidence for such "desiccated" subduction zone fluids is preserved in highly concentrated, Cl-rich inclusions in diamonds with exceptionally high concentrations of incompatible trace elements (Weiss et al. 2005, Klein BenDavid et al. 2007).

8.5.3. The cause of melting in subduction zones

In order to address the question whether hydrous slab fluids or sediment melts are the essential triggers for arc magmatism, we also calculated the trace element composition of magma produced by partial melting of a mantle source enriched by a few percent of sediment melts. The melt compositions for temperatures that are realistic for a slab surface were taken from the experimental studies of Hermann and Rubatto (2009), Skora and Blundy (2010) and Skora et al. (2015). Hermann and Rubato (2009) experimentally studied a sediment composition close to GLOSS (global subducting sediment, Plank and Langmuir 1988). However, in their experimental starting material, some trace elements were doped at much higher concentration levels than in GLOSS. Therefore, in order to make their experimental results compatible with natural starting material compositions, we multiplied their experimentally derived trace element concentrations in partial melts by a correction factor f_X = (concentration of X in GLOSS) / (concentration of X in experimental starting material). A similar correction factor, relative to natural radiolarian clay composition, was applied to the data from the melting experiments from synthetic radiolarian clay by Skora and Blundy (2010). On the other hand,

no correction was applied to the experimental results of Skora et al. (2015) on natural calcareous clay or marl.

Aside from the compositions of the sediment melts, the assumptions of the model are identical to that described above for fluid metasomatism, i.e. the initial depleted mantle composition is from Salters et al. (2002), the peridotite/basalt partition coefficients are the same as above and a degree of melting of 20 % in the mantle source as assumed. Figure 8.8 shows the results of this calculation. Obviously, the addition of sediment melt to the magma source has only limited success in producing a trace element enrichment pattern that resembles a typical arc basalt. None of the sediment melts produces the required enrichment of the light rare earths La and Ce. Moreover, several of the sediment melts yield an incorrect fractionation of Nb relative to the light rare earths. The GLOSS melts give little fractionation and the calcareous clay or marl melts would even produce an enrichment of Nb relative to La and Ce. Most of the partial melts – with the exception of GLOSS at 4.5 GPa and 800 ˚C – have difficulties to enrich Sr to the required level. Overall, the GLOSS melt is most successful in producing an arc-like pattern. The reason for this, however, is very simple: The bulk composition of GLOSS is similar to average upper continental crust as already noted by Plank and Langmuir (1988). Since the upper continental crust is mostly produced by magmatism in subduction zones, GLOSS has essentially inherited a subduction-like trace-element enrichment pattern. This pattern can, however, not have formed in the first place if it requires the addition of a sediment component, which already contains the required enrichment pattern. In contrast to this, our preferred model of the addition of a saline fluid from a subducted MORB eclogite to the zone of melting in the mantle wedge produces a typical arc-basalt pattern *de novo*, without requiring any other pre-enrichment process.

Another interesting observation from Figure 8.8 is that for thorium, but also for some other elements, the enrichment pattern produced by different sediment melts is very different. While carbonate melts do not enrich thorium at all, partial melts from radiolarian clay are very efficient in doing so. This is a rather curious result, as high thorium enrichments were often considered to be some kind of fingerprint of sediment melts (e.g. Elliott et al. 1997, Class et al. 2000). As our experimental results (Figures 8.3 and 8.4) and models (Figure 8.7) show, a strong thorium enrichment may well be produced by high-salinity fluids, or generally aqueous fluids
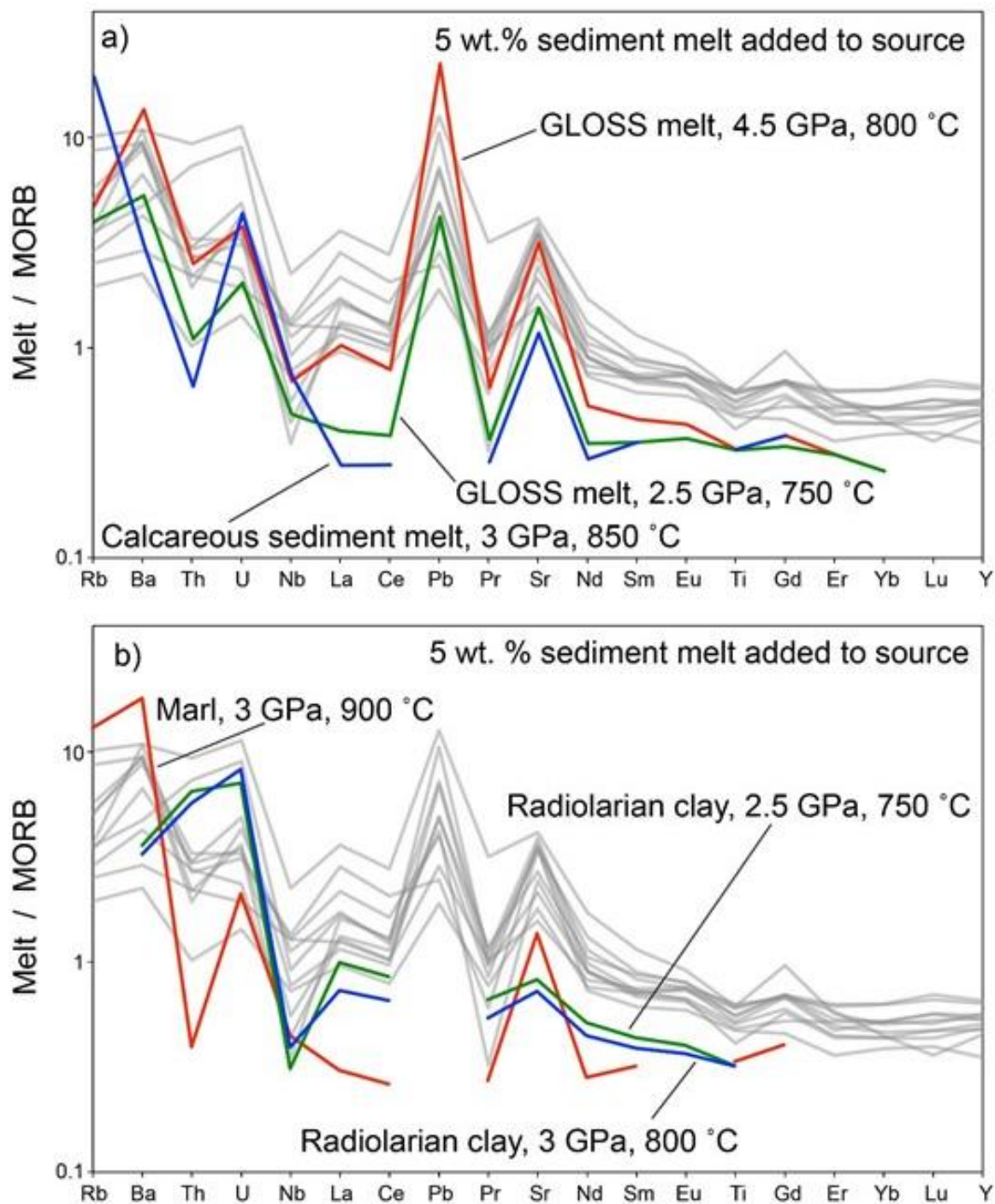
Figure 8.8. *Predicted trace element enrichment patterns for partial melts of the mantle wedge enriched by 5 wt. % of sediment melts. Near-solidus melt compositions were taken from the experimental studies of Hermann and Rubatto (2009) for GLOSS (global subducting sediment), Skora and Blundy (2010) for radiolarian clay and Skora et al. (2015) for calcareous sediment and marl. Compositions for primitive arc basalts as compiled by Kelemen et al. (2005) are shown for comparison as grey lines. All data were normalized to the "all MORB average" of Gale et al. (2013). A few of the rare earth data have been interpolated between neighboring rare earths.*

released above 4 GPa. The strong differences in the enrichment pattern caused by different sediment melts (Figure 8.8) would suggest that if sediment melts contributed strongly to trace element enrichment, it should be easy to distinguish arc basalts produced in subduction zones with mostly carbonate subduction from those with mostly pelite subduction or no sediment subduction. However, this is not so. The compilation of primitive arc basalt composition shown as background in Figures 8.7 and 8.8 includes data from arcs with little or no sediment subduction (e.g. Kamchatka) as well as arcs with massive sediment subduction. Also, the nature of the sediment subducted changes, from mostly pelites (e.g. Tonga) in some arcs to mostly carbonates (e.g. Central America) in other arcs. Nevertheless, the enrichment pattern of trace elements in the different arcs is overall remarkably similar.

Based on the comparison of the modeling results shown in Figures 8.7 and 8.8, we therefore conclude that the sediment melt contribution to primitive arc basalts is negligible and that these magmas are essentially produced by melting of a mantle source enriched by hydrous saline fluids released from the basaltic part of the subducted slab. Our results do not rule out some sediment melt contribution to other types of magmas found in subduction zones; in particular for ultrapotassic melts, such a contribution is plausible (e.g. Mallik et al. 2015). However, numerous geochemical arguments for a sediment contribution to the generation of arc magmas, such as the correlation of trace element (e.g. Th/La) and isotope ratios of magmas and subducted sediments (e.g. Armstrong 1971, Turner and Foden 2001, Plank 2005) do not necessarily involve sediment melting. The experimental data presented here for a basaltic eclogitic system make it rather plausible that saline fluids could transport incompatible trace elements, including thorium from the sediments to the source of melting. This process could also transport Pb, Sr, and Nd isotopic signals. While this hypothesis requires additional experimental testing with sediment lithologies, a recent study by Ferrando et al. (2019) provides direct observational support for this mechanism. They studied aqueous fluid inclusions from subducted kyanite-bearing quartzites from Sulu (China) and observed strong enrichments of Rb, Ba, Sr, Pb, U, Th and the light rare earths in the fluid. We therefore suggest that in particular isotopic "sediment signals" are often transported by saline aqueous fluids. Moreover, as noted above, some elemental enrichments, particularly of thorium that have often been attributed to sediment melts (e.g. Elliott et al. 1997, Class et al. 2000) can be produced by saline fluids released from the basaltic part of the subducted slab alone, without any sediment involvement. We therefore suggest that the importance of sediment melting to the generation

of arc magmas has been greatly overestimated and in reality, this contribution may be rather limited.

8.6. References

Arculus RJ, Powell R (1986) Source component mixing in the regions of arc magma generation. J Geophys Res 91: 5913–5926

Armstrong RL(1971) Isotopic and chemical constraints on models of magma genesis in volcanic arcs. Earth Planet Sci Lett 12: 37–142

Bali E, Audetat A, Keppler H (2011) The mobility of U and Th in subduction zone fluids: an indicator of oxygen fugacity and fluid salinity. Contrib Mineral Petrol 161: 597–613

Bali E, Keppler H, Audetat A (2012) The mobility of W and Mo in subduction zone fluids and the Mo-W-Th-U systematics of island arc magmas. Earth Planet Sci Lett 351: 195–207

Behn MD, Kelemen PB, Hirth G, Hacker BR, Massonne HJ (2011) Diapirs as the source of the sediment signature in arc lavas. Nature Geoscience 4: 641–646

Bernini D, Wiedenbeck M, Dolejs D, Keppler H (2013) Partitioning of halogens between mantle minerals and aqueous fluids: implications for the fluid flow regime in subduction zones. Contrib Mineral Petrol165: 117-128

Brenan JM, Shaw HF, Phinney DL, Ryerson FJ (1994) Rutile-aqueous fluid partitioning of Nb, Ta, Hf, Zr, U and Th: implications for high-field strength element depletions in island arc basalts. Earth Planet Sci Lett 128: 327–339

Brenan JM, Shaw HF, Ryerson FJ, Phinney DL (1995) Mineral-aqueous fluid partitioning of trace elements at 900 °C and 2.0 GPa: Constraints on the trace element chemistry of mantle and deep crustal fluids. Geochim Cosmochim Acta 59: 3331–3350

Bureau H, Keppler H (1999) Complete miscibility between silicate melts and hydrous fluids in the upper mantle: experimental evidence and geochemical implications. Earth Planet Sci Lett 165: 187–196

Carter L., Skora S, Blundy JD, De Hoog JCM, Elliott T (2015) An experimental study of trace element fluxes from subducted oceanic crust. J Petrol 56: 1585–1606

Class C, Miller DM, Goldstein SL, Langmuir CH (2000) Distinguishing melt and fluid subduction components in Umnak Volcanics, Aleutian Arc. Geochem Geophys Geosyst 1: Article Number 1004

Elliott T, Plank T, Zindler A, White W, Bourdon B (1997) Element transport from slab to volcanic front at the Mariana arc. J Geophys Res Solid Earth 102: 14991-15019

Ferrando S, Petrelli M, Frezzotti ML (2019) Gradual and selective trace element enrichment in slab released fluids at sub-arc depths. Scientific Reports 9:16393

Gale A, Dalton CA, Langmuir CH, Su Y, Schilling JG (2013) The mean composition of ocean ridge basalts. Geochem Geophys Geosyst 14: 489–518

Gill J (1981) Orogenic Andesites and Plate Tectonics. Springer, Berlin.

Green TH, Ringwood TE (1968) Genesis of the calc-alkaline igneous rock suite. Contrib Mineral Petrol 18: 105–162

Hawkesworth CJ, Turner SP, McDermott F, Peate DW, van Calsteren P (1997) U-Th isotopes in arc magmas: Implications for element transfer from the subducted crust. Science 276: 551–555.

Hawkesworth C, Cawood PA, Dhuime B (2019) Rates of generation and growth of the continental crust. Geoscience Frontiers 10: 165-173

Hermann J (2002) Allanite: thorium and light rare earth element carrier in subducted crust. Chem Geol 192: 289– 306

Hermann J, Spandler C, Hack A, Korsakov AV (2006) Aqueous fluids and hydrous melts in high-pressure and ultra-high pressure rocks: implications for element transfer in subduction zones. Lithos 92: 399–417

Hermann J, Rubatto D (2009) Accessory phase control on the trace element signature of sediment melts in subduction zones. Chem Geol 265: 512-526

Hofmann AW (1988) Chemical differentiation of the Earth: the relationship between mantle, continental crust, and oceanic crust. Earth Planet Sci Lett 90: 297-394

John T, Gussone N, Podladchikov YY, Bebout GE, Dohmen R, Halama R, Klemd R, Magna T, Seitz HM (2012) Volcanic arcs fed by rapid pulsed fluid flow through subducting slabs. Nature Geosci 5: 489-492

Johnson KTM (1994). Experimental cpx/ and garnet/melt partitioning of REE and other trace elements at high pressures; petrogenetic implications. Mineral Mag 58: 454-455

Johnson MC, Plank T (1999) Dehydration and melting experiments constrain the fate of subducted sediments. Geochemistry, Geophysics, Geosystems 1: Article Number: 1007

Kawamoto T, Mibe K, Bureau H, Reguer S, Mocuta C, Kubsky S, Thiaudiere D, Ono S, Kogiso T (2014) Large-ion lithophile elements delivered by saline fluids to the sub-arc mantle. Earth Planets Space 66: doi:10.1186/1880-5981-66-61

Kelemen PB, Hanghøj K, Greene AR (2005) One view of the geochemistry of subduction-related magmatic arcs, with an emphasis on primitive andesite and lower crust. In R.L. Rudnick, Ed., Treatise of Geochemistry, vol. 3, The Crust: 593-659 (Elsevier, Amsterdam).

Kelley KA, Cottrell E (2009) Water and the oxidation state of subduction zone magmas. Science 325: 605–607.

Keppler H (1996) Constraints from partitioning experiments on the composition of subduction-zone fluids. Nature 380: 237–240.

Keppler H, Wyllie PJ (1990) Role of fluids in transport and fractionation of uranium and thorium in magmatic processes. Nature 348: 531-533

Keppler H, Frost DJ, (2005) Introduction to minerals under extreme conditions. In: Miletich, R. (Ed.), Mineral Behaviour at Extreme Conditions. In: European Mineralogical Union Lecture Notes in Mineralogy, vol. 7, pp. 1–30.

Kessel R, Schmidt MW, Ulmer P, Pettke T (2005) Trace element signature of subduction-zone fluids, melts and supercritical liquids at 120–180 km depth. Nature 437: 724–727

Klein-BenDavid O, Izraeli ES, Hauri E, Navon O (2007) Fluid inclusions in diamonds from the Diavik mine, Canada and the evolution of diamond-forming fluids. Geochim Cosmochim Acta 71: 723–744

Klemme S, Blundy JD, Wood BJ (2002). Experimental constraints on major and trace element partitioning during partial melting of eclogite. Geochim Cosmochim Acta 66: 3109–3123

Konzett J, Frost DJ (2009) The high P-T stability of hydroxyl-apatite in natural and simplified MORB – an experimental study to 15 GPa with implications for transport and storage of phosphorus and halogens in subduction zones. J Petrol 50: 2043–2062

Mallik A, Nelson J, Dasgupta R (2015) Partial melting of fertile peridotite fluxed by hydrous rhyolitic melt at 2-3 GPa: implications for mantle wedge hybridization by sediment melt and generation of ultrapotassic magmas in convergent margins. Contrib Mineral Petrol 169: Article Number 48

Mallmann G, O´Neill HSC (2009) The crystal/melt partitioning of V during mantle melting as a function of oxygen fugacity compared with some other elements (Al, P, Ca, Sc,Ti, Cr, Fe, Ga,Y, Zr and Nb). J Petrol 50: 1765 - 1794

Mandler BE, Grove TL (2016) Controls on the stability and composition of amphibole in the Earth's mantle. Contrib Mineral Petrol 171: Article number 68

Métrich N, Wallace PJ (2008) Volatile abundances in basaltic magmas and their degassing paths tracked by melt inclusions. Rev Mineral Geochem 69: 363–402

Mierdel K, Keppler H, Smyth JR, Langenhorst F (2007) Water solubility in aluminous orthopyroxene and the origin of Earth's asthenosphere. Science 315: 364-368

Peacock SM (1990) Fluid processes in subduction zones. Science 248: 329–337.

Pearce JA, Stern RJ, Bloomer SH, Fryer P (2005) Geochemical mapping of the Mariana arc-basin system: Implications for the nature and distribution of subduction components. Geochemistry, Geophysics, Geosystems 6: Q07006

Plank T (2005) Constraints from thorium/lanthanum on sediment recycling at subduction zones and the evolution of the continents. J Petrol 46: 921–944

Plank T, Langmuir CH (1988) The chemical composition of subducting sediment and its consequences for the crust and mantle. Chem Geol 145: 325–394

Plümper O, John T, Podladchikov YY, Vrijmoed JC, Scambelluri M (2017) Fluid escape from subduction zones controlled by channel-forming reactive porosity. Nature Geosci 10: 150-156

Portnyagin M, Hoernle K, Plechov P, Mironov N, Khubunaya S (2007) Constraints on mantle melting and composition and nature of slab components in volcanic arcs from volatiles (H_2O, S, Cl, F) and trace elements in melt inclusions from the Kamchatka Arc. Earth Planet Sci Lett 255: 53–69

Rapp RP, Shimizu N, Norman MD (2003) Growth of early continental crust by partial melting of eclogite. Nature 425: 605-609

Rustioni G, Audétat A, Keppler H (2019) Experimental evidence for fluid-induced melting in subduction zones. Geochem Persp Lett 11: 49-54

Rustioni G, Audétat A, Keppler H (2020) A systematic assessment of the diamond trap method for measuring fluid compositions in high-pressure experiments. Am Mineral, submitted

Salters VJM, Stracke A (2004), Composition of the depleted mantle. Geochem Geophys Geosyst 5: Article Number 5

Salters VJM, Longhi JE, Bizimis M (2002) Near mantle solidus trace element partitioning at pressures up to 3.4 GPa. Geochem Geophys, Geosyst 3: Article Number 7

Schmidt MW, Poli S (1998) Experimentally based water budgets for dehydrating slabs and consequences for arc magma generation. Earth Planet Sci Lett 163: 361–379

Sisson TW, Kelemen PB (2018) Near-solidus melts of MORB + 4 wt% H_2O at 0.8–2.8 GPa applied to issues of subduction magmatism and continent formation. Contrib Mineral Petrol 173: Article number 70

Skora S, Blundy J (2010) High-pressure hydrous phase relations of radiolarian clay and implications for the involvement of subducted sediment in arc magmatism. J Petrol 51: 2211–2243

Skora S, Blundy J D, Brooker R A, Green ECR, de Hoog JCM, Connolly JAD (2015) Hydrous phase relations and trace element partitioning behaviour in calcareous sediments at subduction-zone conditions. J Petrol 56: 953–980

Spandler C, Pirard C (2013) Element recycling from subducting slabs to arc crust: A review. Lithos 170-171: 208–223

Stalder R, Foley SF, Brey GP, Horn I (1998) Mineral aqueous fluid partitioning of trace elements at 900–1200 °C and 3.0–5.7 GPa: New experimental data for garnet, clinopyroxene, and rutile, and implications for mantle metasomatism. Geochim Cosmochim Acta 62: 1781–1801

Straub SM, Layne GD (2003) The systematics of chlorine, fluorine, and water in Izu arc front volcanic rocks: Implications for volatile recycling in subduction zones. Geochim Cosmochim Acta 67: 4179–4203

Sun C, Liang Y (2012) Distribution of REE between clinopyroxene and basaltic melt along a mantle adiabat: effects of major element composition, water, and temperature. Contr Mineral Petrol 163:807–823

Syracuse EM, van Keken, PE, Abers GA (2010) The global range of subduction zone thermal models. Phys Earth Planet Interiors 183: 73–90

Tatsumi Y (1989) Migration of fluid phases and genesis of basalt magmas in subduction zones. J Geophys Res 94: 4697–4707

Tropper P, Manning CE, Harlov DE (2011) Solubility of $CePO_4$ monazite and YPO_4 xenotime in H_2O and H_2O–NaCl at 800 °C and 1 GPa: Implications for REE and Y transport during high-grade metamorphism. Chem Geol 282: 58–66

Tsay A, Zajacz Z, Sanchez-Valle C (2014) Efficient mobilization and fractionation of rare-earth elements by aqueous fluids upon slab dehydration. Earth Planet Sci Lett 398: 101–112.

Tsay A, Zajacz Z, Ulmer P, Sanchez-Valle C (2017) Mobility of major and trace elements in the eclogite-fluid system and element fluxes upon slab dehydration Geochim Cosmochim Acta 198: 70-91

Turner S, Foden J (2001) U, Th and Ra disequilibria, Sr, Nd and Pb isotope and trace element variations in Sunda arc lavas: predominance of a subducted sediment component. Contrib Mineral Petrol 142: 43–57

Weiss Y, McNeill J, Pearson DG, Nowell GM, Ottley CJ (2015) Highly saline fluids from a subducting slab as the source for fluid-rich diamonds. Nature 524: 339–342

Zack T, John T (2007) An evaluation of reactive fluid flow and trace element mobility in subducting slabs. Chem Geol 239: 199–216

Zamboni D, Gazel E, Ryan JG, Cannatelli C, Lucchi F, Atlas ZD, Trela J, Mazza SE, De Vivo B (2016) Contrasting sediment melt and fluid signatures for magma components in the Aeolian Arc: Implications for numerical modeling of subduction systems. Geochem Geophys Geosyst 17: 2034–2053

8.7. Supplementary tables

Table 8.3. *Summary of experiments.*

Experiment	Pressure (GPa)	Temperature (ºC)	NaCl in fluid (wt. %)	Duration (h)	Capsule material
PC09	4	800	0	84	Au
PC22	4	800	0	120	Pt
PC37	4	800	0	68	Pt
PC38	4	800	0	128	Pt
PC24	4	800	0	144	Pt
PC14	4	800	1	69	Au
PC23	4	800	5	163	Pt
PC10	4	800	5	68	Au
PC27	4	800	10	93	Pt
PC18	4	800	10	52	Pt
PC36	4	800	15	103	Pt
PC39	4	800	15	126	Pt
PC15	4	800	15	63	Au
PC41	4	700	0	123	Pt
PC45	4	700	5	185	Pt
PC42	4	700	10	126	Pt
PC40	4	700	15	127	Pt
PC47	5	800	0	148	Pt
PC49	5	800	5	125	Pt
PC52	5	800	10	79	Pt
PC53	5	800	15	126	Pt
MA08	6	800	0	121	Pt
MA07	6	800	10	76	Pt
MA10	6	800	15	76	Pt

Table 8.4. *Fluid bulk composition*

Experiment	Cl	SiO_2	Al_2O_3	Na_2O	CaO	FeO	MgO	Total solutes
PC09	0	12.0 (3)	1.02 (4)	1.13 (5)	0.61 (2)	0.25 (2)	0.141 (5)	15.1 (4)
PC22	0	5.46 (7)	0.36 (1)	0.48 (1)	0.30 (1)	0.07 (1)	0.068 (1)	6.7 (1)
PC37	0	24.6 (2)	1.82 (1)	2.28 (4)	1.13 (4)	0.5 (3)	0.224 (3)	30.6 (7)
PC38	0	24.5 (5)	1.68 (2)	2.14 (4)	0.75 (2)	0.93 (7)	0.202 (4)	30.2 (6)
PC24	0	7.0 (5)	0.45 (3)	0.65 (4)	0.52 (3)	0.77 (8)	0.142 (5)	9.5 (7)
PC14	0.48 (3)	19 (1)	2.11 (4)	2.00 (5)	1.5 (1)	1.0 (5)	0.4 (1)	27 (2)
PC23	2.3 (2)	27 (2)	1.52 (9)	3.6 (2)	2.7 (2)	1.3 (1)	0.83 (9)	38 (3)
PC10	3.7 (3)	41 (2)	1.9 (1)	3.86 (7)	2.8 (6)	2.8 (1)	1.2 (1)	57 (3)
PC27	4.9 (5)	13.3 (5)	1.61 (3)	3.87 (6)	7.5 (6)	0.74 (3)	0.537 (6)	33 (2)
PC18	4.2 (3)	27.4 (3)	0.65 (9)	3.93 (6)	6.9 (2)	1.26 (5)	0.23 (1)	44 (1)
PC36	6.5 (2)	34.9 (9)	0.93 (3)	5.66 (6)	2.7 (4)	1.24 (8)	0.43 (1)	51 (2)
PC39	6.8 (5)	27 (3)	1.0 (1)	5.74 (8)	2.6 (8)	2.6 (3)	0.76 (8)	45 (5)
PC15	6.9 (8)	13.1 (2)	1.4 (1)	9.1 (4)	9.2 (7)	2.9 (2)	1.62 (9)	43 (3)
PC41	0	5.91 (7)	0.170 (2)	0.37 (1)	0.09 (1)	0.22 (9)	0.061 (3)	6.8 (2)
PC45	2.81 (1)	7.26 (1)	0.30 (1)	2.33 (4)	0.42 (6)	1.16 (5)	0.153 (2)	13.8 (2)
PC42	5.2 (5)	14 (1)	0.28 (2)	4.19 (4)	1.14 (7)	0.83 (9)	0.23 (1)	25 (2)
PC40	7.74 (4)	14.1 (3)	0.22 (2)	5.5 (1)	1.97 (4)	1.4 (2)	0.26 (1)	29.5 (8)
PC47	0	25.9 (4)	1.82 (7)	2.81 (5)	1.18 (6)	0.44 (1)	0.57 (2)	32.7 (6)
PC49	2.73 (1)	9.3 (3)	0.31 (1)	2.06 (3)	0.95 (7)	0.23 (7)	0.17 (1)	15.1 (5)
PC52	4.8 (4)	12 (1)	0.37 (3)	3.0 (3)	1.9 (2)	0.20 (2)	0.30 (3)	21 (2)
PC53	8.11 (3)	8.2 (3)	0.37 (1)	4.89 (9)	3.02 (6)	1.1 (2)	0.47 (1)	24.4 (7)
MA08	0	39 (2)	5.4 (5)	3.3 (1)	1.7 (2)	1.8 (2)	0.78 (8)	52 (3)
MA07	4.87 (8)	20 (2)	1.28 (7)	3.36 (8)	2.8 (2)	0.44 (2)	0.57 (4)	33 (2)
MA10	7.86 (5)	12.0 (7)	0.60 (2)	3.74 (7)	4.1 (2)	0.54 (1)	0.58 (2)	28 (1)

All compositions are given in weight %. Number in parentheses are one standard deviation in the last digit.

Table 8.5. *Trace elements in the fluid*

Experiment	PC41	PC45	PC42	PC40	PC47	PC49	PC52	PC53	MA08	MA07	MA10
Cl (wt. %)	0	2.81 (1)	5.2 (5)	7.74 (4)	0	2.73 (1)	4.8 (4)	8.11 (3)	0	4.87 (8)	7.86 (5)
Li	188 (5)	735 (16)	852 (53)	816 (9)	1300 (36)	892 (25)	794 (74)	836 (22)	1497 (72)	1173 (50)	1365 (16)
Be	58 (1)	56 (1)	97 (8)	99 (1)	316 (8)	195 (8)	266 (24)	215 (9)	776 (82)	682 (63)	316 (16)
B	922 (18)	1822 (5)	4723 (447)	1630 (26	1338 (15)	874 (35)	826 (77)	1077 (34)	1247 (118)	1792 (183)	1870 (92)
Rb	1475 (20)	2852 (26)	4452 (344)	2362 (12)	1588 (57)	1433 (49)	1175 (108)	1154 (33)	1226 (52)	2853 (265)	2831 (96)
Cs	2516 (4)	4420 (153)	6013 (473)	3329 (42)	2047 (5)	1853 (89)	3409 (290	3837 (129)	1924 (40)	4609 (442)	4981 (192)
Sr	83 (8)	1244 (47)	2203 (114)	1993 (30)	519 (20)	581 (32)	980 (97)	1799 (40)	528 (50)	2557 (112)	3577 (70)
Ba	979 (23)	2534 (94)	3304 (143)	2871 (51)	1153 (46)	1369 (54)	2886 (442)	3102 (664)	767 (69)	2940 (206)	3781 (105)
Ti	25.5 (8)	44 (3)	78 (9)	79 (17)	550 (11)	93 (4)	109 (10)	118 (5)	1396 (154)	627 (44)	273 (14)
Nb	1.94 (5)	1.89 (2)	2.7 (3)	2.6 (1)	12.1 (3)	6.5 (2)	6.2 (5)	4.7 (2)	28 (3)	18 (2)	8.5 (5)
Ta	0.58 (5)	0.7 (1)	1.6 (2)	2.0 (2)	1.77 (7)	1.12 (7)	1.5 (1)	1.37 (7)	12 (1)	3.8 (4)	1.35 (4)
La	0.23 (2)	0.5 (1)	1.4 (2)	4.0 (2)	0.45 (2)	5.1 (3)	7.2 (7)	26 (3)	19 (3)	23 (1)	46 (2)
Ce	0.84 (6)	4 (1)	6 (1)	18 (2)	2.9 (1)	19.9 (8)	25 (2)	64 (5)	84 (11)	124 (12)	153 (7)
Nd	0.26 (2)	0.46 (7)	1.5 (4)	3.7 (3)	0.55 (3)	3.5 (2)	6.4 (6)	17 (1)	20 (3)	21 (1)	34 (2)
Sm	0.26 (3)	0.47 (6)	1.1 (1)	3.4 (3)	0.64 (5)	3.0 (2)	6.1 (5)	14.4 (8)	21 (3)	21 (2)	29 (1)
Eu	0.45 (4)	1.1 (1)	1.7 (1)	7.0 (5)	1.25 (4)	5.3 (2)	14 (1)	37 (2)	38 (4)	39 (3)	59 (3)
Gd	0.24 (2)	0.44 (5)	1.2 (2)	3.3 (2)	0.80 (5)	2.4 (1)	5.2 (4)	11.5 (6)	18 (2)	16.0 (8)	18.3 (9)
Dy	0.37 (4)	0.44 (7)	1.4 (1)	2.7 (4)	1.06 (6)	1.24 (7)	2.4 (2)	5.3 (2)	15 (2)	7.8 (5)	5.0 (3)
Er	0.56 (7)	0.7 (1)	2.7 (3)	4.6 (6)	1.2 (2)	0.74 (7)	1.2 (1)	2.9 (1)	17 (3)	4.9 (7)	2.1 (1)
Yb	0.9 (1)	1.6 (2)	7.9 (9)	10 (1)	1.2 (2)	0.50 (7)	0.9 (1)	1.8 (2)	17 (3)	3.7 (7)	1.3 (1)
Lu	0.54 (8)	0.82 (5)	5.6 (5)	7.3 (9)	0.8 (1)	0.33 (4)	0.6 (1	1.27 (9)	12 (2)	2.6 (7)	0.9 (1)
Y	13 (2)	13.8 (4)	43 (4)	30 (4)	4.0 (7)	11 (4)	11 (2)	35 (7)	94 (51)	11 (5)	2.3 (2)
Sc	0.58 (6)	0.97 (5)	2.7 (2)	3.8 (5)	4.1 (2)	0.78 (7)	1.1 (1)	1.8 (1)	12 (1)	5.1 (6)	2.0 (1)
Pb	96 (4)	361 (9)	408 (93)	1118 (35)	534 (12)	377 (19)	435 (44)	343 (19)	386 (14)	367 (39)	1358 (266)
Th	0.37 (2)	0.12 (3)	0.23 (4)	0.6 (1)	0.26 (2)	4.2 (2)	4.3 (4)	2.5 (1)	15 (2)	5.4 (4)	2.7 (1)
U	20 (4)	3.5 (4)	7.7 (9)	20 (3)	17.4 (9)	42 (3)	43 (5)	61 (4)	124 (8)	137 (19)	64 (4)

All compositions are given in ppm by weight, except for Cl (wt.%). Numbers in parentheses are one standard deviation in the last digits.

Table 8.6. *Garnet composition*

Experiment	PC41	PC45	PC42	PC40	PC47	PC49	PC52	PC53	MA08	MA07	MA10
Cl (wt. %)	0	2.81 (1)	5.2 (5)	7.74 (4)	0	2.73 (1)	4.8 (4)	8.11 (3)	0	4.87 (8)	7.86 (5)
Li	114 (9)	96 (7)	126 (14)	87 (6)	159 (11)	125 (21)	149 (22)	152 (17)	147 (51)	222 (27)	116 927)
Be	< 33	35 (6)	110 (20)	44 (2)	66 (4)	92 (22)	63.1 (6)	93 (17)	167 (38)	118 (12)	44 (6)
B	< 82	46 (7)	< 96	23.7 (9)	98 (6)	107 (30)	36.1 (3)	53 (8)	157 (62)	78 (10)	49 (6)
Rb	10 (3)	10 (5)	8 (2)	1.52 (9)	4.1 (9)	15 (4)	8 (4)	8 (2)	19 (8)	11 (3)	33 (22)
Cs	7 (2)	10 (6)	16 (8)	0.67 (4)	3 (1)	14 (3)	4 (2)	6 (3)	18 (3)	7 (2)	54 (37)
Sr	17 (3)	19 (4)	54 (18)	3.7 (7)	4.0 (8)	8 (2).	23 (6)	24 (3)	22 (11)	44 (12)	66 (22)
Ba	7.7 (5)	18 (7)	25 (8)	6 (2)	12.5 (8)	33 (7)	10.3 (1)	9.7 (5)	43 (9)	25 (8)	11 (2)
Ti	3570 (286)	3243 (162)	3371 (202)	1618 (307)	3065 (184)	3353 (268)	4605 (645)	3106 (186)	1148 (402)	7111 (1209)	4083 (1102)
Nb	16 (2)	7 (1)	19 (7)	2.0 (9)	6 (1)	6.2 (8)	25 (8)	9 (2)	25 (18)	43 (17)	30 (11)
Ta	14 (2)	6 (1)	17 (9)	1.7 (5)	5 (1)	7 (1)	19 (6)	6.0 (9)	31 (23)	39 (17)	25 (10)
La	5 (2)	1.6 (3)	9 (4)	1.2 (5)	1.4 (2)	1.5 (2)	3.5 (3)	7 (2)	10 (6)	2.2 (3)	15 (9)
Ce	22 (10)	16 (4)	37 (7)	8 (1)	5.4 (9)	13 (2)	21 (1)	32 (4)	12 (6)	22 (4)	53 (30)
Nd	14 (3)	4.4 (5)	12 (2)	4 (1)	22 (3)	27 (4)	37 (3)	47 (4)	35 (14)	24 (5)	38 (13)
Sm	101 (5)	20 (2)	24 (5)	36 (15)	129 (9)	143 (13)	164 (7)	162 (15)	37 (14)	103 (11)	137 (42)
Eu	216 (9)	54 (5)	47 (6)	79 (26)	232 (23)	235 (17)	305 (12)	291 (24)	30 (14)	195 (15)	214 (56)
Gd	332 (11)	89 (10)	92 (12)	145 (44)	300 (30)	296 (18)	395 (14)	381 (20)	63 (33)	254 (25)	259 (74)
Dy	726 (46)	242 (14)	370 (17)	492 (41)	468 (39)	477 (25)	552 (16)	508 (51)	105 (68)	304 (43)	355 (94)
Er	967 (125)	481 (22)	1074 (80)	1284 (82)	603 (55)	666 (53)	801 (29)	703 (88)	168 (120)	305 (63)	435 (110)
Yb	852 (142)	622 (56)	1498 (155)	2030 (271)	613 (62)	663 (60)	769 (42)	644 (79)	194 (128)	253 (66)	413 (106)
Lu	636 (123)	540 (58)	1361 (163)	1919 (279)	491 (46)	540 (56)	627 (26)	502 (70)	152 (107)	184 (54)	316 (87)
Y	173 (16)	131 (20)	215 (12)	284 (41)	124 (38)	86 (4)	131 (31)	88 (10)	51 (22)	174 (35)	101 (31)
Sc	434 (48)	310 (10)	523 (55)	678 (54)	508 (44)	464 (44)	564 (30)	417 (44)	208 (135)	208 (49)	299 (82)
Pb	9 (2)	8 (2)	16 (3)	2.4 (1)	6 (3)	18 (5)	11 (3)	10 (1)	17 (9)	12 (5)	17 (6)
Th	4 (3)	0.7 (2)	2.6 (7)	2 (1)	2.5 (2)	4.1 (4)	2.5 (2)	7 (1)	8 (4)	2.9 (4)	7 (3)
U	33 (3)	3.4 (4)	7 (2)	6 (2)	53 (7)	57 (6)	52 (5)	68 (10)	15 (9)	21 (3)	61 (18)

All compositions are given in ppm by weight, except for Cl (wt.%). Numbers in parentheses are one standard deviation in the last digits. < Detection limits are reported as maximum values when element concentrations were too low to be measured.

Table 8.7. *Omphacite composition*

Experiment	PC41	PC45	PC42	PC40	PC47	PC49	PC52	PC53	MA08	MA07	MA10
Cl (wt. %)	0	2.81 (1)	5.2 (5)	7.74 (4)	0	2.73 (1)	4.8 (4)	8.11 (3)	0	4.87 (8)	7.86 (5)
Li	1286 (77)	1251 (39)	1221 (55)	1280 (58)	1381 (46)	1315 (41)	914 (30)	871 (23)	646 (42)	1565 (326)	863 (24)
Be	747 (55)	471 (41)	895 (44)	845 (34)	763 (13)	493 (17)	533 (14)	490 (50)	724 (39)	763 (71)	733 (50)
B	212 (40)	205 (32)	223 (30)	309 (17)	167 (21)	40 (5)	198 (14)	117 (12)	130 (28)	95 (16)	85 (16)
Rb	62 (4)	209 (78)	261 (54)	132 (17)	43 (12)	8 (3)	119 (13)	28 (2)	280 (42)	60 (31)	65 (30)
Cs	60 (3	210 (31)	839 (317)	343 (44)	66 (18)	4 (1)	60 (7)	24 (3)	304 (65)	33 (17)	82 (39)
Sr	661 (132)	237 (30)	926 (125)	450 (95)	183 (76)	88 (28)	411 (117)	139 (12)	660 (62)	672 (294)	220 (72)
Ba	182 (22)	183 (39)	269 (162)	21 (2)	75 (11)	51 (11)	250 (132)	51 (14)	481 (47)	264 (128)	35 (14)
Ti	4824 (338)	2549 (535)	4174 (209)	3582 (287)	2002 (60)	1517 (91)	2498 (475)	2532 (354)	10575 (952)	3102 (806)	2948 (766)
Nb	38 (6)	19 (5)	19 (1)	18 (4)	4.1 (5)	2.1 (3)	15 (7)	15 (6)	32 (4)	16 (9)	18 (10)
Ta	37 (8)	14 (5)	13 (1)	1 (3)	2.9 (5)	1.6 (1)	12 (6)	12 (6)	33 (3)	14 (8)	15 (8)
La	57 (13)	3.2 (31)	66 (11)	16 (2)	37 (18)	11 (8)	94 (18)	29 (5)	37 (5)	10 (4)	3 (1)
Ce	282 (55)	37 (22)	470 (75)	146 (11)	117 (46)	34 (24)	269 (52)	88 (13)	115 (11)	48 (18)	15 (3)
Nd	62 (14)	2.3 (20)	58 (11)	16 (4)	41 (18)	16 (9)	111 (20)	47 (7)	63 (5)	22 (6)	16 (1)
Sm	63 (14)	4 (3)	58 (10)	20 (5)	43 (14)	21 (7)	108 (18)	52 (6)	106 (6)	38 (6)	37 (2)
Eu	71 (14)	7 (5)	76 (13)	28 (5)	48 (13	24 (6)	121 (10)	689 (9)	147 (9)	46 (10)	48 (3)
Gd	69 (14)	6 (4)	59 (10)	30 (5)	48 (11)	27 (4)	113 (7)	72 (9)	167 (8)	53 (10)	50 (6)
Dy	68 (14)	9 (7)	64 (8)	43 (8)	52 (11)	20 (4)	134 (10)	76 (14)	168 (14)	53 (14)	40 (10)
Er	75 (17)	13 (10)	82 (9)	63 (12)	68 (16)	16 (5)	171 (18)	81 (22)	191 (19)	53 (17)	43 (18)
Yb	72 (18)	15 (11)	86 (7)	68 (14)	62 (19)	14 (6)	173 (17)	87 (24)	182 (19)	44 (18)	35 (16)
Lu	57 (15)	12 (9)	72 (6)	55 (11)	50 (14)	9 (6)	142 (15)	65 (18)	148 (15)	32 (14)	25 (12)
Y	25 (8)	25 (7)	35 (9)	15 (3)	43 (12)	13 (3)	31 (3)	23 (5)	28 (2)	32 (7)	11 (1)
Sc	110 (10)	92 (7)	107 (6)	113 (15)	91 (11)	40 (6)	161 (14)	100 (15)	198 (10)	85 (9)	114 (10)
Pb	243 (46)	60 (6)	157 (38)	145 (21)	56 (22)	17 (7)	184 (40)	30.4 (3)	106 (16)	108 (66)	26 (7)
Th	14 (2)	1.0 (7)	12 (3)	3.1 (6)	19 (9)	4 (2)	19 (4)	5.3 (7)	8 (1)	2.1 (5)	3 (2)
U	37 (4)	2.3 (22)	48 (4)	15 (2)	30 (11)	6 (2)	31 (3)	18 (1)	27 (5)	11 (4)	13 (5)

All compositions are given in ppm by weight, except for Cl (wt.%). Numbers in parentheses are one standard deviation in the last digits. < Detection limits are reported as maximum values when element concentrations were too low to be measured.

Table 8.8. *Rutile composition*

Experiment	PC41	PC45	PC42	PC40	PC47	PC49	PC52	PC53	MA08	MA07	MA10
Cl (wt. %)	0	2.81 (1)	5.2 (5)	7.74 (4)	0	2.73 (1)	4.8 (4)	8.11 (3)	0	4.87 (8)	7.86 (5)
Li	< 111	< 64	< 525	< 2342	< 107	< 120	< 85	< 95	< 869	< 643	< 499
Be	< 146	< 82	< 151	< 259	< 112	< 152	< 187	< 240	< 1570	< 1134	< 730
B	< 252	< 84	< 938	< 1326	< 254	< 145	< 133	< 171	< 1343	< 1003	< 1512
Rb	< 94	< 48	< 1177	< 783	< 14	< 106	< 82	< 55	< 1180	< 847	< 207
Cs	< 326	< 54	< 2132	< 1569	< 15	< 360	< 165	< 96	< 597	< 465	< 530
Sr	< 98	< 94	< 2637	< 236	< 15	< 55	< 48	< 30	< 927	< 686	< 855
Ba	< 243	< 199	< 283	< 178	< 23	< 44	< 47	< 55	< 1501	< 1034	< 599
Nb	6391 (1300)	5828 (79)	6392 (371)	5706 (34)	6578 (556)	7079 (305)	7922 (287)	7339 (164)	6039 (173)	< 6260	7658 (230)
Ta	5863 (1365)	5287 (347)	6008 (563)	5164 (115)	6982 (681)	6987 (354)	7713 (192)	7254 (158)	5963 (177)	< 6267	7429 (677)
La	< 14	< 18	< 795	< 36	< 5	< 15	< 169	< 5	< 45	< 37	< 55
Ce	< 70	< 64	< 2403	< 81	< 17	< 44	< 444	< 8	< 268	< 215	< 174
Nd	< 32	< 19	< 801	< 27	< 13	< 27	< 182	< 23	< 63	< 55	< 49
Sm	< 17	< 20	< 751	< 53	< 16	< 34	< 121	< 34	< 66	< 56	< 47
Eu	< 19	< 11	< 736	< 133	< 10	< 20	< 61	< 10	< 43	< 32	< 65
Gd	< 28	< 22	< 634	< 151	< 25	< 34	< 77	< 38	< 54	< 47	< 63
Dy	< 20	< 15	< 624	< 267	< 28	< 19	< 35	< 23	< 32	< 30	< 39
Er	< 46	< 22	< 499	< 187	< 42	< 22	< 45	< 26	< 36	< 34	< 28
Yb	< 56	< 13	< 501	< 166	< 50	< 23	< 32	< 33	< 31	< 29	< 35
Lu	< 36	< 6	< 340	< 132	< 37	< 6	< 20	< 9	< 9	< 9	< 15
Y	< 6	< 3	< 78	< 53	< 14	< 4	< 9	< 10	< 12	< 12	< 9
Sc	< 65	< 29	< 245	< 180	< 72	< 85	< 65	< 60	< 117	< 109	< 98
Pb	< 99	< 56	< 766	< 263	< 16	< 36	< 53	< 55	< 488	< 358	< 385
Th	< 7	< 4	< 394	< 9	< 4	< 8	< 170	< 5	< 16	< 14	< 9
U	< 100	< 10	< 463	< 20	< 19	< 51	< 146	< 31	< 70	< 58	< 107

All compositions are given in ppm by weight, except for Cl (wt.%). Numbers in parentheses are one standard deviation in the last digits. < Detection limits are reported as maximum values when element concentrations were too low to be measured.

Table 8.9. *Fluid/eclogite partition coefficients*

Experiment	PC41	PC45	PC42	PC40	PC47	PC49	PC52	PC53	MA08	MA07	MA10
Cl (wt. %)	0	2.81 (1)	5.2 (5)	7.74 (4)	0	2.73 (1)	4.8 (4)	8.11 (3)	0	4.87 (8)	7.86 (5)
Li	0.23 (2)	0.93 (5)	1.09 (11)	1.02 (5)	1.46 (8)	1.06 (6)	1.3 (2)	1.43 (7)	3.4 (4)	1.1 (3)	2.4 (1)
Be	> 0.12	0.19 (2)	0.17 (2)	0.19 (1)	0.65 (3)	0.59 (4)	0.78 (8)	0.65 (8)	1.6 (2)	1.4 (2)	0.69 (8)
B	> 5.8	13 (2)	> 27.4	8.4 (6)	10 (1)	13 (3)	6 (1)	12 (1)	9 (3)	20 (4)	27 (5)
Rb	36 (3)	22 (8)	28 (8)	30 (4)	57 (17)	137 (32)	15 (3)	57 (5)	7 (1)	70 (38)	54 (23)
Cs	65 (4)	34 (6)	12 (5)	16 (2)	50 (13)	242 (59)	88 (18)	229 (32)	10 (2)	203 (105)	70 (30)
Sr	0.2 (1)	8 (1)	3.8 (7)	7 (2)	5 (2)	10 (4)	3 (1)	19 (2)	1.3 (2)	6 (3)	23 (7)
Ba	9 (1)	22 (5)	19 (12)	193 (17)	23 (4)	31 (6)	17 (11)	90 (40)	3 (1)	17 (9)	148 (53)
Ti	0.0016 (1)	0.0031 (2)	0.0053 (4)	0.0064 (6)	0.04 (1)	0.0067 (5)	0.032 (6)	0.0083 (6)	0.21 (3)	0.13 (3)	0.08 (2)
Nb	0.012 (2)	0.014 (1)	0.018 (1)	0.021 (2)	0.089 (9)	0.045 (3)	0.035 (3)	0.029 (2)	0.19 (2)	0.12 (1)	0.048 (4)
Ta	0.004 (1)	0.0057 (7)	0.012 (1)	0.018 (2)	0.012 (2)	0.008 (1)	0.009 (1)	0.009 (1)	0.08 (1)	0.025 (3)	0.008 (1)
La	0.006 (2)	0.20 (18)	0.033 (9)	0.40 (7)	0.02 (1)	0.7 (5)	0.12 (3)	1.3 (3)	0.7 (2)	3 (1)	6 (3)
Ce	0.005 (1)	0.14 (10)	0.021 (7)	0.20 (3)	0.04 (2)	0.8 (5)	0.14 (4)	1.0 (2)	1.1 (2)	3 (1)	5 (2)
Nd	0.006 (2)	0.15 (10)	0.04 (2)	0.3 (1)	0.017 (6)	0.17 (5)	0.07 (2)	0.35 (5)	0.39 (8)	0.9 (2)	1.4 (3)
Sm	0.0033 (6)	0.04 (1)	0.025 (6)	0.13 (4)	0.008 (1)	0.044 (6)	0.045 (6)	0.15 (2)	0.27 (5)	0.33 (5)	0.38 (9)
Eu	0.0035 (5)	0.041 (8)	0.026 (5)	0.15 (4)	0.010 (1)	0.049 (5)	0.070 (7)	0.23 (3)	0.38 (6)	0.37 (5)	0.5 (1)
Gd	0.0014 (1)	0.011 (2)	0.017 (4)	0.04 (1)	0.0054 (7)	0.017 (2)	0.023 (2)	0.059 (5)	0.14 (3)	0.12 (2)	0.14 (4)
Dy	0.0011 (2)	0.0043 (9)	0.0075 (8)	0.012 (3)	0.0048 (6)	0.0061 (6)	0.0080 (8)	0.021 (2)	0.11 (3)	0.051 (9)	0.030 (8)
Er	0.0013 (3)	0.0034 (6)	0.0056 (9)	0.008 (1)	0.0041 (8)	0.0027 (4)	0.0028 (3)	0.009 (1)	0.09 (3)	0.03 (1)	0.011 (3)
Yb	0.0024 (6)	0.006 (1)	0.012 (2)	0.011 (3)	0.0042 (9)	0.0018 (4)	0.0021 (4)	0.006 (1)	0.09 (4)	0.03 (1)	0.007 (2)
Lu	0.0019 (6)	0.0037 (6)	0.010 (2)	0.009 (2)	0.0036 (9)	0.0015 (3)	0.0018 (3)	0.005 (1)	0.08 (3)	0.03 (1)	0.006 (2)
Y	0.16 (4)	0.20 (3)	0.40 (6)	0.24 (6)	0.05 (2)	0.25 (9)	0.15 (5)	0.7 (2)	2.5 (15)	0.12 (7)	0.05 (2)
Sc	0.0024 (4)	0.0054 (4)	0.010 (1)	0.011 (2)	0.016 (2)	0.0037 (6)	0.0035 (5)	0.008 (1)	0.06 (2)	0.038 (9)	0.011 (2)
Pb	0.6 (1)	9 (1)	4 (2)	13 (2)	15 (6)	22 (6)	4 (1)	15 (1)	5 (1)	5 (4)	60 (22)
Th	0.036 (8)	0.13 (9)	0.027 (9)	0.21 (7)	0.02 (1)	1.0 (3)	0.33 (9)	0.42 (6)	1.8 (5)	2.2 (4)	0.6 (2)
U	0.6 (1)	1.3 (7)	0.24 (4)	1.8 (4)	0.4 (1)	1.6 (2)	1.1 (2)	1.6 (3)	6 (1)	9 (2)	2.0 (6)

Numbers in parentheses are one standard deviation in the last digits; > minimum values of D are reported when only maximum concentrations of trace elements were available for garnet and/or omphacite.

9. Appendix: A study of natural melt inclusions from two Japanese volcanoes

The experimental work conducted at the University of Bayreuth was complemented at Tohoku University with a study on natural olivine-hosted melt inclusions (MI) collected from two different arc volcanoes in Japan: Shinmoedake (in the Kirishima volcanic group) and Miyakejima (Figure 9.1).


Figure 9.1. *Location in Japan of Kirishima and Miyakejima volcanoes.*

9.1. Shinmoedake and the 2011 eruption

Shinmoedake is one of the most active volcanoes in the Kirishima volcanic group (Figure 9.2), which is located in southern Kyushu (Figure 9.1). Andesitic pyroclastic material, interlayered with lava flows, constitutes the present Shinmoedake volcanic edifice (Nakada et al. 2013). The volcanic activity of Kirishima lasts since ~ 600 ka, starting with caldera-forming eruptions, then forming about 330 ka ago stratovolcanoes with plinian, vulcanian, strombolian and phreatomagmatic eruptions (Imura, 1992; Nagaoka and Okuno, 2011). The Shinmoedake activity in 1822, 1959 and 1991, was characterized by phreatic explosions (Imura and Kobayashi, 1991; Tsutsui et al., 2005).

The last Shinmoedake eruption took place in 2011, about 300 years after the last magmatic eruption. It started in January 2011 with a phreatomagmatic eruption, followed by sub-plinian eruptions and explosions, lava accumulation in the crater and from February to April repeated vulcanian events (Nakada et al 2013; Suzuki et al 2013).
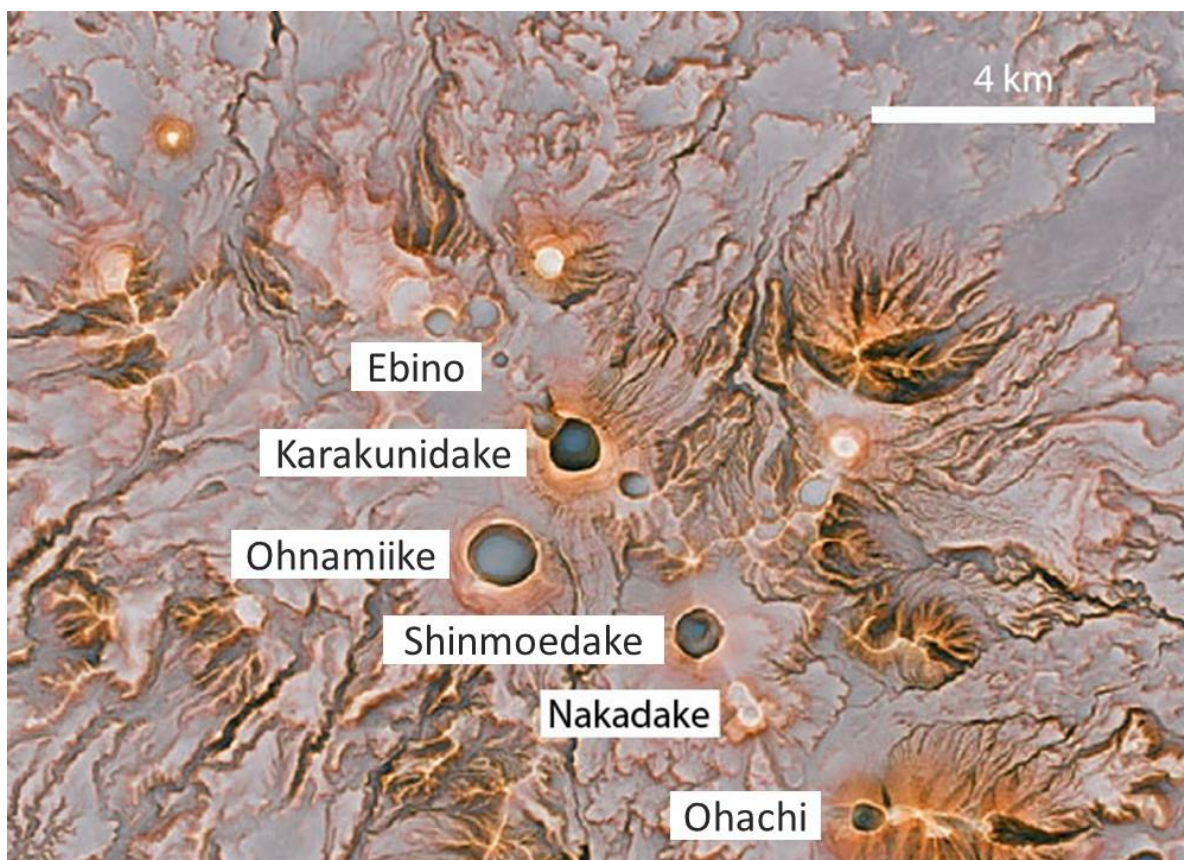
Figure 9.2. Map of the Kirishima volcano group. Modified after Nakada et al. 2013.

The magma erupted in 2011 is andesitic and the composition of the ejecta lie within the range of previous Shinmoedake products. The sub-plinian events produced white, brown and gray pumices, the former having higher SiO_2 content (62 – 63 wt. %) than brown and gray pumices (57 – 58 wt. %, Suzuki et al. 2013). Suzuki et al. (2013) interpreted the white pumices as being representative of a shallower silicic andesite (SA) end-member magma (stored at ~ 870 °C and 120 MPa). Darker pumices on the other hand, would be the product of syn-eruptive magma mixing with a deeper basaltic andesite (BA) magma in a proportion of 30 – 40 % SA with 60 – 70 % BA . The high-temperature BA magma was not erupted directly, but it was estimated to contain 55 wt. % SiO2 and to have been stored in a deeper magma chamber at ~ 1030 °C and 250 MPa.

All the pumices are coarsely plagioclase-phyric, with minor clinopyroxene, orthopyroxene and Fe-Ti oxides. Gray and brown pumices also contain olivine as phenocrysts. Olivines were interpreted by Suzuki et al. (2013) to have formed rapidly from the BA prior to plagioclase and before the mixing event. Reported Mg# [$100 \times$ Mg / (Mg + Fe)] for olivine phenocrysts range between 74.6 – 79.0. Some melt inclusions with andesitic composition (54.1– 57.7 wt. % SiO_2) and average water content of 4.4 wt. % were trapped in olivine due to the rapid crystallization.

9.2. Miyakejima and the Ofunato stage

Miyakejima is a frontal arc volcano of the Izu arc, and is located about 200 km south of Tokyo (Figure 9.1). Miyakejima is a composite volcano with a twofold caldera (Chihara et al., 1984; Hayakawa, 1990). Its volcanic edifice has an average diameter of 20 km, of which about 8 km above sea, with a slight elongation in the north-south direction. Miyakejima is one of the most active Japanese volcanoes, and its eruptive history can be divided into four main stages (Tsukui & Suzuki, 1998; Tsukui et al., 2001; Niihori et al., 2003): the Ofunato stage (10000 – 4000 yBP), the Tsubota stage (4000 – 2500 yBP), the Oyama stage (2500 yBP – 1469 AD) and the Shinmio stage (1469 AD – present).

The main cone was formed during the Ofunato stage, which is regarded as the first phase of the Miyakejima magma plumbing system evolution (Ushioda et al. 2018). Miyakejima ejecta have a wide compositional range within the tholeiitic series, going from basalts (48.5 wt. %

SiO$_2$) to andesite (63 wt. % SiO$_2$, Tsukui et al. 2002). The products of the Ofunato stage represent the least differentiated material erupted over the past 10000 years and consist mostly of basaltic lavas (48.5 - 54.5 wt. % SiO$_2$) and pyroclastic rocks with limited compositional variation (Tsukui et al. 2002, Niihori et al., 2003). The magma chamber conditions of the Ofunato basalts were estimated to be ~ 150 MPa, ~ 1100 °C, and the melt H$_2$O content to be ~ 3 wt. % (Ushioda et al. 2018).

The Ofunato scoria, found in the bottom layer of the Ofunato explosion breccia (Figure 9.3) is the most undifferentiated product of Miyakejima. The bulk rock composition of the Ofunato scoria is: 50.11 wt. % SiO$_2$, 0.92 wt. % TiO$_2$, 18.09 wt. % Al$_2$O$_3$, 11.06 wt. % FeO, 0.21 wt. % MnO, 5.78 wt. % MgO, 11.78 wt. % CaO, 1.85 wt. % Na$_2$O, 0.22 wt. % K$_2$O, 0.01 wt. % P$_2$O$_5$ (Ushioda et al. 2014). The Ofunato scoria contains phenocrysts consisting for 10.9 vol. % of highly calcic plagioclase (> An90) and for 0.7 vol. % of magnesian olivine (~ Fo80, Ushioda et al. 2014, 2018). Basaltic melt inclusions found in olivine are considered to be representative of the melt composition in the magma chamber. A wide range of water content was reported for such MIs, ranging from a maximum of 3.4 wt. % to less than 50 ppm (Ushioda et al. 2018).

9.3. Sample preparation

Samples include gray and brown pumices from the 2011 Shinmoedake eruption and Ofunato scoria from Miyakejima. The pumices were collected at the top of Nakadake crater, a lateral vent of Shinmoedake (Figure 9.2). Detailed sub-unites are not well identified for this location. Ofunato scoria were sampled in the location shown in Figure 9.3.

The two types of samples were separately crushed into coarse grains using a steel mortar. After isolation of the phenocrysts from the groundmass, olivine single crystals were handpicked under an optical microscope while submerged in ethanol. Olivine phenocrysts were then mounted in resin and polished on one side to expose the maximum number of melt inclusions (see Figure 9.4).
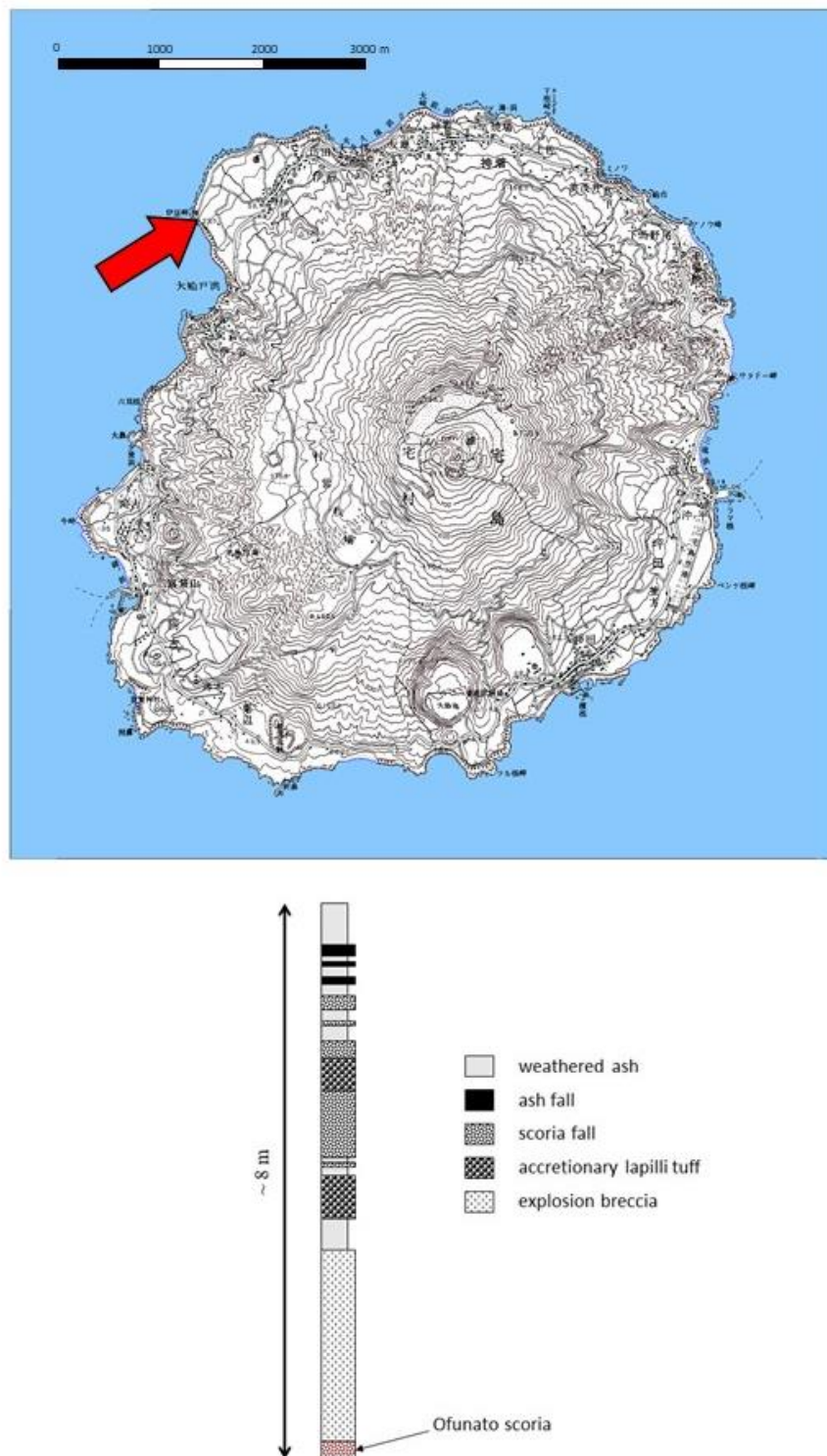
Figure 9.3. Topographic map of Miyakejima modified after the Geospatial Information Authority of Japan. The location of sampling for this study is indicated by a red arrow. A stratigraphic column for the location (after Tsukui and Suzuki 1998) is given below.
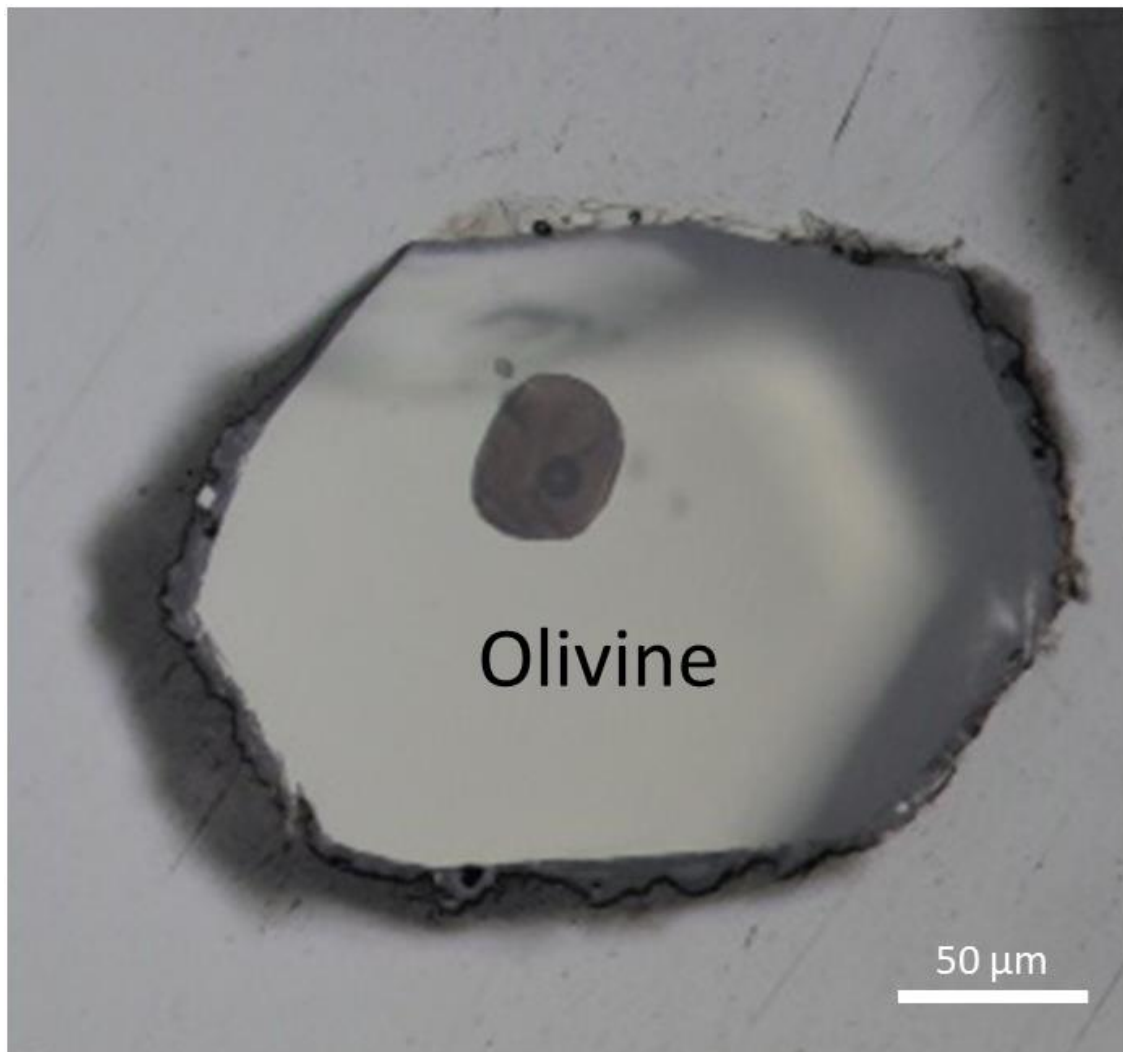
Figure 9.4. *Typical olivine-hosted melt inclusion from the Shinmoedake pumice samples.*

9.4. Analytical methods

9.4.1. Fourier transform infrared spectroscopy

Water contents in the melt inclusions were quantified by Fourier transform infrared (FT-IR) micro-reflectance spectroscopy at the Earthquake Research Institute (ERI), University of Tokyo. Analyses were conducted with a JASCO FT-IR-660 Plus spectrometer equipped with a IRT-30VC microscope. The presence of a vacuum pump that evacuates the entire beam path

greatly improves the signal/noise ratio by eliminating interferences due to atmospheric CO_2 and water vapor. This allows the quantification of water contents even in small samples, such as melt inclusions, by reflectance FT-IR instead of transmission analysis, with considerable advantages in the sample preparation procedures. Reflectance FT-IR spectra were collected for melt inclusions from the polished surface of the olivine mounts. Before each sample analysis, spectra were also acquired from a gold standard. An empirical relationship between H_2O contents and the reflectance intensities in the 3650 cm-1 wavelength region of the collected spectra was used to quantify water concentrations in the melt inclusions. Analysis, calibration and data processing were conducted following the procedure described in Yasuda et al. (2014).

9.4.2. Electron microprobe

The composition of the melt inclusions and the adjacent olivine hosts were measured with a JEOL JXA-8800M electron microprobe at Tohoku University. Analyses of the melt inclusions were performed in two separate cycles: at first only SiO_2, TiO_2, Al_2O_3, FeO, MnO, MgO, CaO, Na_2O and K_2O were measured in order to minimize alkali loss, followed by a second step where Cl, F and P_2O_5 were measured with higher probe current and peak counting times. Analyses were always performed with an accelerating voltage of 15 kV. The first step of MI analyses was done with a probe current of 8 nA and peak counting time of 10 sec. Measurement of Cl, F and P2O5, as well as olivine host analyses were conducted with a probe current of 15 nA and peak counting time of 20 sec. The beam diameter for melt inclusion analyses was 5 μm, while a focused beam was used for olivine.

9.4.3. Laser ablation ICP-MS

Laser ablation ICP-MS measurements were conducted to characterize the melt inclusion compositions in terms of trace elements. Analyses were performed with a GeolasPro 193 nm ArF Excimer Laser (Coherent, USA) equipped with an Elan DRC-e (Perkin Elmer, Canada) at the Bayerisches Geoinstitut. A procedure similar to that described in Chapter 2.6 for synthetic mineral analysis was followed for melt inclusion measurements.

9.5. Results and discussion

9.5.1. Compositions of olivine phenocrysts and melt inclusions

Average measured compositions for olivine hosts and melt inclusions are given in Tables 9.1, 9.2 and 9.3. Olivine host compositions lie in the range previously reported in literature for these samples (Suzuki et al. 2013, Ushioda et al. 2014, 2018), with average Mg# of ~ 76 for Shinmoedake, and ~ 79 for Miyakejima olivines.

Table 9.1. *Average composition for olivine hosts*

Olivine sample	SiO$_2$	TiO$_2$	Al$_2$O$_3$	FeO	MnO	MgO	CaO	NiO	Mg#
Shinmoedake	38.58 (3)	0.017 (2)	0.025 (2)	21.76 (6)	0.334 (5)	39.15 (5)	0.110 (2)	0.045 (4)	76.23 (8)
Miyakejima	38.53 (14)	0.014 (1)	0.020 (3)	19.88 (60)	0.27 (1)	41.05 (49)	0.194 (3)	0.049 (8)	78.62 (72)

Compositions are given in wt. %. Numbers in parentheses are one standard deviation in the last digits. Total iron is given as FeO.

Table 9.2. *Average major element composition for melt inclusions*

MI	n.	SiO$_2$	TiO$_2$	Al$_2$O$_3$	FeO	MnO	MgO	CaO	Na$_2$O	K$_2$O	P$_2$O$_5$	Cl	F	H$_2$O
Shinmoedake	81	53.7 (1)	0.81 (1)	17.17 (7)	7.93 (6)	0.162 (6)	3.13 (6)	8.08 (5)	2.91 (1)	1.08 (2)	0.181 (3)	0.068 (1)	0.032 (4)	3.1 (1)
Myiakejima	9	48.4 (5)	1.01 (6)	15.65 (31)	10.83 (27)	0.162 (18)	5.42 (31)	10.73 (33)	2.17 (15)	0.23 (2)	0.132 (11)	0.047 (4)	0.098 (22)	1.2 (4)

Compositions are given in wt. %. Numbers in parentheses are one standard deviation in the last digits. Total iron is given as FeO. The number of measured inclusions is given under the "n." column.

Table 9.3. *Average trace element composition for melt inclusions*

MI	n.	B	Rb	Sr	Y	Zr	Nb	Cs	Ba	La
Shinmoedake	81	27.3 (5)	36.7 (8)	344.32 (271)	20.1 (3)	72.6 (9)	2.81 (5)	2.349 (48)	211 (3)	9.6 (1)
Myiakejima	9	28.9 (87)	3.4 (2)	0.29 (3)	226.4 (47)	106.2 (87)	0.33 (6)	0.005 (2)	28 (3)	1.9 (3)

| MI	n.	Ce	Nd	Sm	Gd	Yb	Ta	Pb	Th	U
Shinmoedake	81	21.6 (2)	12.2 (2)	3.22 (9)	3.4 (1)	2.12 (4)	0.22 (1)	10.2 (3)	3.01 (7)	0.80 (2)
Myiakejima	9	4.7 (4)	6.3 (12)	1.73 (17)	2.8 (4)	1.76 (18)	17.53 (146)	2.4 (3)	0.15 (3)	0.36 (19)

Compositions are given in ppm. Numbers in parentheses are one standard deviation in the last digits. The number of measured inclusions is given under the "n." column.

Melt inclusions silica contents measured in this study are slightly lower than previously reported data (Suzuki et al. 2013, Ushioda et al. 2018). SiO_2 contents range between 50.0 and 56.3 wt. % with an average of 53.7 wt. % in 81 melt inclusions from Shinmoedake, and between 46.6 and 51.6 wt. % with an average of 48.4 wt. % in 9 melt inclusions from Miyakejima. Water contents measured in melt inclusions from Shinmoedake are also slightly lower than literature data (Suzuki et al. 2013), being on average 3.1 wt. %. In the Miyakejima samples, on the other hand, melt inclusions H_2O contents are generally higher than those reported by Ushioda et al. (2018), having maximum water contents of 4.0 wt. % and a minimum of 0.2 wt. %, with an average value of 1.2 wt. %. Average of measured halogen contents in MIs are 0.068 wt. % of Cl and 0.032 of F in Shinmoedake samples and 0.047 wt. % of Cl and 0.098 wt. % of F in Miyakejima. Cl contents for Miyakejima melt inclusions reported by Ushioda et al. (2018) are in good agreement with those found in this study, while other halogen data are not available in literature for samples from Shinmoedake and Miyakejima. Trace element concentrations were also never quantified before in olivine hosted melt inclusions from Shinmoedake and Miyakejima volcanoes. Averages of trace element contents in melt inclusions collected from both volcanoes are reported in Table 9.3.

9.5.2. La/Yb ratio as a proxy for subduction zone fluids salinity

In order to confirm the experimental results obtained at the Bayerisches Geoinstitut, which indicate a general enhancement of trace element fluid mobility with addition of Cl, information about the salinities of subduction zone fluids that metasomatized the mantle wedge below Shinmoedake and Miyakejima are required. A direct use of measured H_2O and Cl contents in melt inclusions to infer the initial fluid salinity may not yield reliable results due to possible degassing processes that occurred before the entrapment of the inclusions and the fast diffusion of water in the olivine host after entrapment (e.g. Portnyagin et al. 2008, Chen et al, 2011). On the other hand, the diffusion of incompatible trace elements in olivine is very slow, and major changes in the concentrations of such elements should not occur after isolation of the melt inclusions (e.g. Portnyagin et al. 2008). As discussed in Chapter 8, the salinity of the fluid released by the slab is the key parameter that controls the trace element fractionation in primitive arc magmas. Parameters such as the fluid fraction and the degree of mantle melting mostly affect the absolute trace element concentrations with only minor effects on their relative
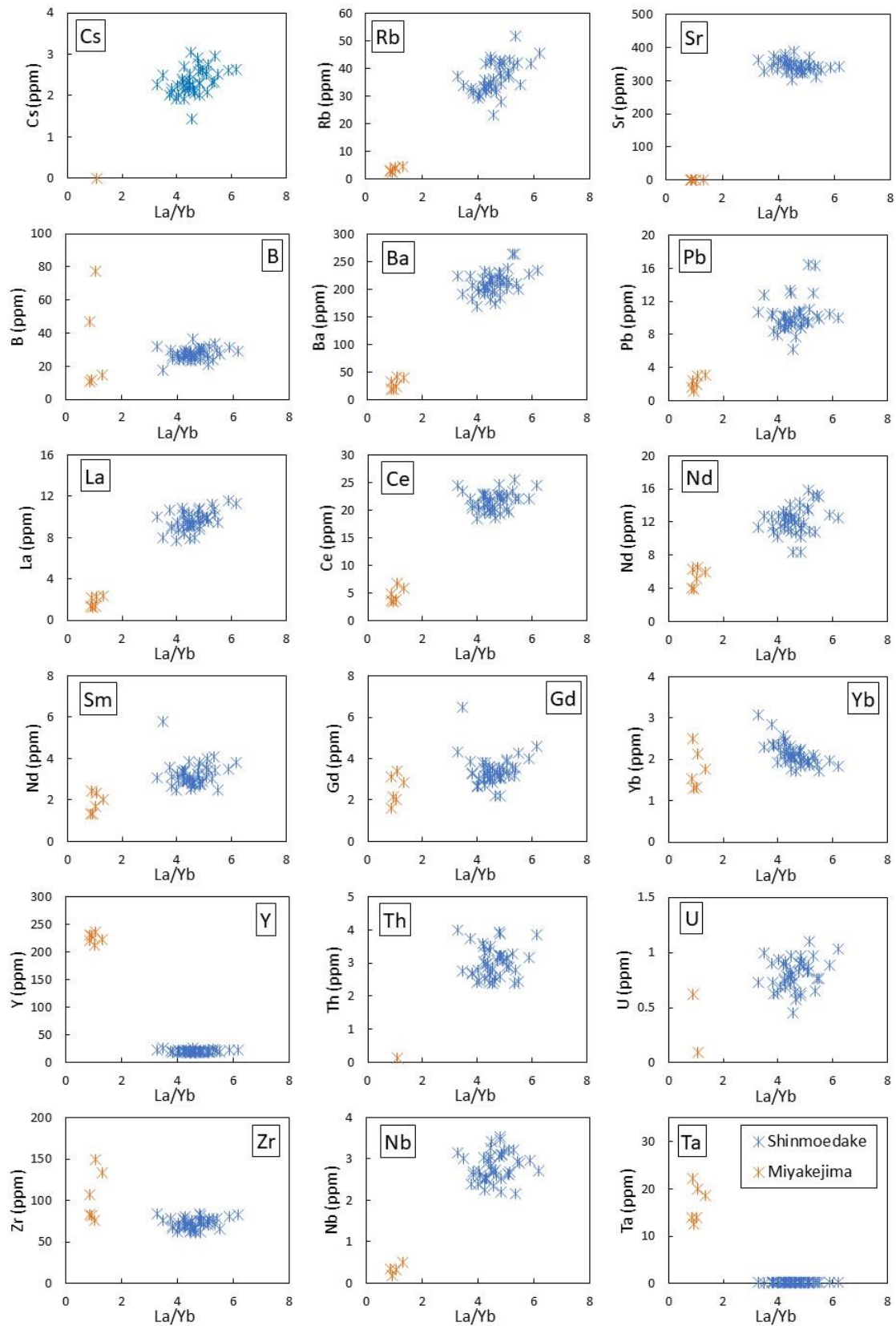
Figure 9.5. *Melt inclusion trace element content against their La/Yb ratio for Shinmoedake (blue symbols) and Miyakejima (orange symbols) samples.*

enrichment pattern. Results from the experimental work conducted in BGI, indicate that at all the investigated pressure and temperature conditions, the addition of Cl strongly enhance light rare earth elements (LREE) fluid solubility, while it does not really affect heavy rare earth elements (HREE) partitioning behavior. Accordingly, the relative enrichment of LREE with respect to HREE may be used as an indicator for the salinity of the fluid released by the subducting slab. In this context, the La/Yb ratio is therefore used as a proxy for subduction zone fluid salinity. Miyakejima samples have lower La/Yb ratios (0.9 – 1.3) than Shinmoedake samples (3.3 – 6.2).

9.5.3. Comparison of natural and experimental results

Trace element concentrations measured in both Shinmoedake and Miyakejima melt inclusions are plotted against their La/Yb ratios in Figure 9.5. Most of the analyzed trace element concentrations in the two volcanoes seem to increase with La/Yb ratios. This correlation is in very good agreement with the experimental data that show a general enhancement of trace element solubility in fluids with increasing fluid salinity. Only Ta, Y and to some extent Zr, have a much higher concentration in the Miyakejima melt inclusion than in Shinmoedake. This result is again consistent with experimental observations that indicate that the solubilities of these elements are almost insensitive to fluid salinity. Their concentrations may therefore be controlled by other parameters such as the presence of rutile in the residual slab mineralogy and the degree of mantle melting. More difficult to reconcile with the experimental results is the positive correlation between Nb and La/Yb, which seem to suggest an enhancement of Nb transport with increasing fluid salinity.

9.6. References

Chen, Y., Provost, A., Schiano, P., & Cluzel, N. (2011). The rate of water loss from olivine-hosted melt inclusions. Contributions to Mineralogy and Petrology, 162(3), 625-636.

Chihara, K., Aoki, S., Yagi, K., Shindo, S. (1984). Caldera of Miyakejima volcano and lava flow control. Bulletin of the Volcanological Society of Japan, 29(2), S335–S342.

Hayakawa, Y. (1990). 276 eruptive history of Miyakejima volcano by tephrochronology and Loesschronometry. Abstract from meeting of the Geological Society of Japan, 97, 416.

Imura R, Kobayashi T (1991) Eruptions of Shinmoedake volcano, Kirishima volcano group, in the last 300 years. Kazan, 36(2), 135-148.

Imura R (1992) Eruptive history of the Kirishima volcano during the past 22,000 years, Geograph. Rep. Tokyo Metropolitan Univ., 27, 71–89.

Nagaoka S, Okuno M (2011) Tephrochronology and eruptive history of Kirishima volcano in southern Japan, Quat. Int., 246, 260–269.

Nakada S, Nagai M, Kaneko T, Suzuki Y, Maeno F (2013) The outline of the 2011 eruption at Shinmoe-dake (Kirishima), Japan. Earth, planets and space, 65(6), 1.

Niihori, K., Tsukui, M., & Kawanabe, Y. (2003). Evolution of magma and magma plumbing system of Miyakejima volcano in the last 10,000 years. Bulletin of the Volcanological Society of Japan, 48(5), 387–405.

Portnyagin, M., Almeev, R., Matveev, S., & Holtz, F. (2008). Experimental evidence for rapid water exchange between melt inclusions in olivine and host magma. Earth and Planetary Science Letters, 272(3-4), 541-552.

Suzuki Y, Yasuda A, Hokanishi N, Kaneko T, Nakada S, Fujii T (2013) Syneruptive deep magma transfer and shallow magma remobilization during the 2011 eruption of Shinmoe-dake, Japan—Constraints from melt inclusions and phase equilibria experiments. Journal of Volcanology and Geothermal Research, 257, 184-204.

Tsukui, M., Suzuki, Y. (1998). Eruptive history of Miyakejima volcano during the last 7000 years. Bulletin of Volcanological Society of Japan, 43, 149–166.

Tsukui, M., Niihori, K., Kawanabe, Y., & Suzuki, Y. (2001). Stratigraphy and formation of Miyakejima volcano. Journal of Geography, 110(2), 156–167.

Tsukui M, Niihroi K, Kawanabe Y (2002) The 2000 AD subsidence caldera at Miyakejima volcano, Izu arc, Japan. Bull Earth Res Inst Univ Tokyo 77:27–42

Tsutsui M, Tomita K, Kobayashi T (2005) Fumarolic activity since December 2003 and volcanic activity during the Meiji and Taisho eras (1880-1923) of Ohachi Volcano, Kirishima Volcano Group, southern Kyushu, Japan. Kazan, 50(6), 475-489.

Ushioda, M., Takahashi, E., Hamada, M., & Suzuki, T. (2014). Water content in arc basaltic magma in the Northeast Japan and Izu arcs: an estimate from Ca/Na partitioning between plagioclase and melt. Earth, Planets and Space, 66(1), 127.

Ushioda, M., Takahashi, E., Hamada, M., Suzuki, T., & Niihori, K. (2018). Evolution of Magma Plumbing System in Miyakejima Volcano: Constraints From Melting Experiments. Journal of Geophysical Research: Solid Earth, 123(10), 8615-8636.

Yasuda A (2014) A new technique using FT-IR micro-reflectance spectroscopy for measurement of water concentrations in melt inclusions. Earth, Planets and Space, 66(1), 34.

(Eidesstattliche) Versicherungen und Erklärungen

(§ 9 Satz 2 Nr. 3 PromO BayNAT)

Hiermit versichere ich eidesstattlich, dass ich die Arbeit selbstständig verfasst und keine anderen als die von mir angegebenen Quellen und Hilfsmittel benutzt habe (vgl. Art. 64 Abs. 1 Satz 6 BayHSchG).

(§ 9 Satz 2 Nr. 3 PromO BayNAT)

Hiermit erkläre ich, dass ich die Dissertation nicht bereits zur Erlangung eines akademischen Grades eingereicht habe und dass ich nicht bereits diese oder eine gleichartige Doktorprüfung endgültig nicht bestanden habe.

(§ 9 Satz 2 Nr. 4 PromO BayNAT)

Hiermit erkläre ich, dass ich Hilfe von gewerblichen Promotionsberatern bzw. -vermittlern oder ähnlichen Dienstleistern weder bisher in Anspruch genommen habe noch künftig in Anspruch nehmen werde.

(§ 9 Satz 2 Nr. 7 PromO BayNAT)

Hiermit erkläre ich mein Einverständnis, dass die elektronische Fassung meiner Dissertation unter Wahrung meiner Urheberrechte und des Datenschutzes einer gesonderten Überprüfung unterzogen werden kann.

(§ 9 Satz 2 Nr. 8 PromO BayNAT)

Hiermit erkläre ich mein Einverständnis, dass bei Verdacht wissenschaftlichen Fehlverhaltens Ermittlungen durch universitätsinterne Organe der wissenschaftlichen Selbstkontrolle stattfinden können.

………………………………………………………………………………………….
Ort, Datum, Unterschrift